Application of Nanomaterials for X-ray Shielding and Dosimetry in Diagnostic Radiology

by

Shruti Nambiar

A thesis
presented to the University of Waterloo
in fulfillment of the
thesis requirement for the degree of
Doctor of Philosophy
in
Systems Design Engineering

Waterloo, Ontario, Canada, 2015

AUTHOR'S DECLARATION

This thesis consists of material all of which I authored or co-authored: see Statement of Contributions included in the thesis. This is a true copy of the thesis, including any required final revisions, as accepted by my examiners.

I understand that my thesis may be made electronically available to the public.

Statement of Contributions

I hereby declare that I have contributed to the majority of research work in this thesis wherein Chapters 3, 5, and 7 include published articles. The reprint permissions of the published work can be found at the end of the thesis.

My contributions to this thesis include design, development, characterization, testing and analysis of nanomaterials/nanocomposites/devices under a wide range of X-ray energies for applications in radiation protection and detection. The contents of my research work reprinted in this thesis include the following co-authors: Dr. John T. W. Yeow (Supervisor) and Dr. Ernest K. Osei (Co-Supervisor). Full citation of the articles along with the corresponding chapters are as follows:

Nambiar, S.; Yeow, J. T., Polymer-composite materials for radiation protection. *ACS applied materials & interfaces* 2012**,** *4* (11), 5717-5726. [**Chapter 3**]

Nambiar, S.; Osei, E. K.; Yeow, J. T. W., Polymer nanocomposite-based shielding against diagnostic X-rays. *Journal of Applied Polymer Science* 2013**,** *127* (6), 4939-4946. [**Chapter 5**]

Nambiar, S.; Osei, E. K.; Yeow, J. T. W., Bismuth Sulfide Nanoflowers for Detection of X-rays in the Mammographic Energy Range. *Sci. Rep.* 2015**,** *5*. [**Chapter 7**]

Abstract

Lead is commonly used in medical radiology departments as a shielding material against X-rays. Lead-based protective materials are also routinely used by clinical personnel and patients during radiological examinations or procedures. However, lead is extremely toxic and prolonged exposure to it can result in serious health concerns. In this thesis, a novel, lead-free, cost-effective nanocomposite was developed for X-ray protection applications. Conformable polymer nanocomposites from polydimethylsiloxane (PDMS) were fabricated using different weight percentages (wt%) of bismuth oxide (BO) nanopowder. BO has a relatively high atomic-number which allowed increased X-ray interactions required for the X-ray photons to deposit energy within the PDMS/BO nanocomposite. The attenuation properties of the nanocomposites were characterized using diagnostic X-ray energies from 40 to 150 kV. The results showed that the PDMS/BO nanocomposite (44.44 wt% of BO and 3.73 mm thick) was capable of attenuating all the scattered X-rays generated at a tube potential of 60 kV.

Another aspect of my thesis-work involves X-ray detection using bismuth sulfide (Bi_2S_3) nanoflowers and organic polymer nanocomposite. There is an increasing demand for real-time, large-area, flexible dosimeters, especially in the biomedical industry. In this thesis, photoelectric response of hydrothermally synthesized Bi_2S_3 nanoflowers was measured under both low X-ray energies (20 to 30 kV), and higher diagnostic X-ray energies (40 to 100 kV). The photoresponse of the nanoflowers clearly showed high sensitivity to changes in X-ray intensities, the capability to operate at relatively low bias voltages (+1 and +1.5 V under X-rays in the mammographic and higher diagnostic energies respectively), and the potential to

perform as a reliable dosimetric material for instantaneous dose measurements over a wide range of diagnostic X-rays. Finally, the nanoflowers were incorporated into a p-type, semiconducting organic polymer (P3HT). The photoelectric response of the both pure P3HT and P3HT/Bi_2S_3-nanocomposite devices was measured under X-rays in the diagnostic energy range. The P3HT/Bi_2S_3-nanoflower composite showed significantly higher sensitivity (~4 times under 100 kV X-rays) compared to that of pure polymer. In summary, the flexible P3HT/Bi_2S_3-nanoflower device could potentially be used over an uneven surface for real-time detection of diagnostic X-rays at a minimal operating voltage of -40 mV.

Acknowledgements

First and foremost, I would like to express my sincere thanks to my supervisor, Prof. John T. W. Yeow who first gave me the opportunity to embark on the Ph.D. journey. His support and enthusiasm has allowed me to try, fail and succeed but, most importantly, to keep trying new ideas without setting boundaries. I would like to express my sincere gratitude for the academic freedom and for some of the most amazing research opportunities, especially the collaborative work with Prof. C. N. R. Rao's laboratory in India, and the Global Nano Innovation contest in Taiwan. I would also like to express my sincerest thanks to my co-supervisor, Dr. Ernest K. Osei, who has been my mentor throughout the Ph.D. program. He is a great teacher from whom I learned the first lessons of radiation physics, and I shall, forever, be grateful for that. Through his relentless support and guidance, I learnt to adapt and resolve many research problems during the program. For his students, his doors are always open for questions, discussions and debates. I have been fortunate to have worked with two great advisors, because of whom I could live my dream of doing top quality research.

I would also like to thank Dr. Johnson Darko (Grand River Regional Cancer Centre), and Prof. Hany Aziz (ECE department, University of Waterloo) for their timely advices and discussions. My sincere thanks to Prof. Arthur Carty (Waterloo Institute for Nanotechnology) for the opportunity to work under the supervision of one of the living legends in material science and chemistry, Prof. C. N. R. Rao (JNCASR, India). I would also like to express my sincere thanks to Prof. Rao for his support and guidance throughout the collaboration program.

I thank all my lab members and my friends (the list is just too long!) for all their support, encouragement and love. I would also like to thank all the lab members at JNCASR (India) for making my stay, in Bangalore, a memorable experience.

I am forever indebted to my parents, Chandrasekhar Nambiar and Dhanalakshmi Nambiar, for their unconditional love and blessings. You both are my strength and motivation. I would like to thank my parents-in-law for their love and encouragement, especially throughout my graduate studies. I would also like to thank my brothers, Shyam and Rupesh. You guys are the best!

I am blessed to have two most wonderful people in my life - my beloved husband, Ratish, and my son, Aryan. Every moment of my life has been meaningful because of you two. Born during the third year of my Ph.D. program, my baby has, in many ways, taught me to be a better researcher – his persistence in trying every move possible to take the first step all by himself, his inquisitiveness, and his innocence in questioning everything – are probably some of the few fundamental lessons that helped me grow as a researcher.

My beloved husband, Ratish, has been my source of strength and motivation throughout all the perfections and craziness. I cannot thank you enough for your unconditional love and support. Especially, during the past few months of thesis-writing, to single-handedly manage a toddler and an anxious graduate student is no ordinary feat! I may never find the right words to express my love and gratitude; I am because you are.

Dedication

To my Ratish.

Table of Contents

List of Figures

List of Tables

Chapter 1
Overview

1.1 Background

A general overview of X-rays used in medical radiological departments is presented. A brief summary of other sources of ionizing (both directly and indirectly ionizing) radiations is discussed. The health risks associated with exposure to ionizing radiation is detailed along with methods of radiation protection , particularly on shielding and detection (or monitoring for safety purposes) of X-rays used in the diagnostic medical radiology. Finally, the research objectives for this thesis are listed along with a brief description on the overall layout of the thesis.

1.1.1 Clinical X-rays – energy range and production

X-rays were discovered by a German physicist, Wilhelm Conrad Röentgen, in 1895 while studying cathode rays (electron beam) in a gas discharge tube. Following this historic discovery, the nature of X-rays has been extensively investigated which has, with time, led to use of X-rays for numerous applications. One of the most significant among them has been in the field of medical radiology wherein X-rays are used for both diagnostic and therapeutic purposes.

X-rays are ionizing electromagnetic radiation, routinely used in the field of medical radiology at energies in the range of 20 keV to 25 MeV. Electron volt (eV) is a unit of energy that equals the kinetic energy gained by an electron when it is accelerated under a potential difference of one volt and it is equal to 1.602×10^{-19} joules. X-rays in the keV range, used in clinical radiological applications such as diagnostic imaging, fluoroscopy and superficial radiotherapy (for e.g., skin lesions), are produced when electrons are accelerated from the cathode of an X-ray tube and are

stopped by hitting the tungsten anode. In contrast, very high energy X-rays in the MeV range, used in treatment of deep-seated tumours, are produced in a linear accelerator in which a waveguide uses microwaves to accelerate electrons at very high velocities and a bending magnet to deflect the high velocity electrons perpendicular to the waveguide. For X-ray treatment, the electrons incident on a thin tungsten target and the forward peaked bremsstrahlung radiation (X-rays produced due to interaction of high-velocity electrons with the tungsten target) is flatten using a flattening filter.

A conventional X-ray tube consists of a cathode and an anode assembly placed in a hermetically sealed chamber (Figure 1.1). The cathode is usually a filament made of a high density material such as tungsten or molybdenum, and the anode is copper rod with tungsten or a tungsten rhenium alloy. When high voltage is applied between the cathode and the anode, the electrons emitted from the filament are accelerated towards the anode and achieve high velocities before striking the anode. X-rays are produced through the sudden deceleration of the electron in the tungsten target.
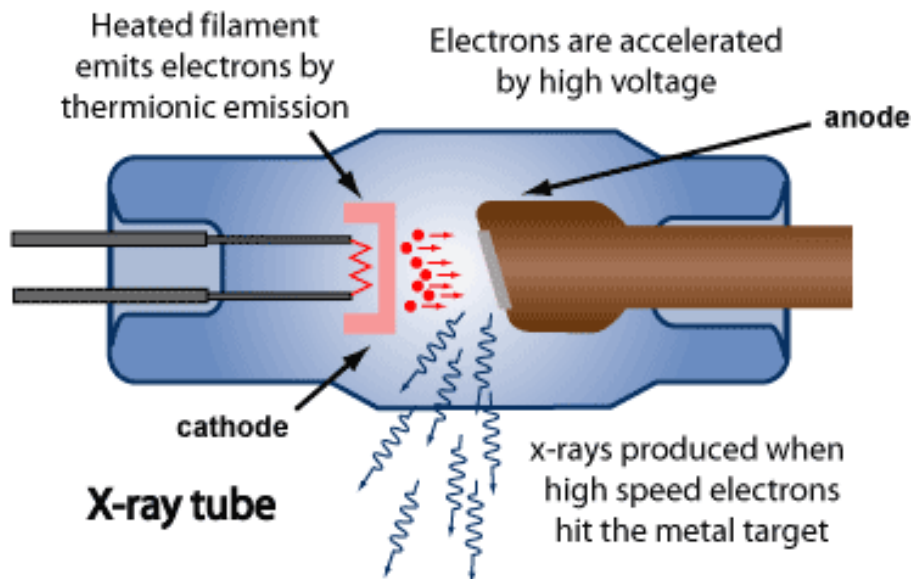
Figure 1.1: Illustration of X-ray generation within an X-ray tube. © Commonwealth of Australia as represented by the Australian Radiation Protection and Nuclear Safety Agency (ARPANSA).

The bombardment of the high-velocity electron with the target (anode) nucleus produces two types of X-rays: (i) *bremsstrahlung* X-rays and (ii) characteristic X-rays. The process of *bremsstrahlung* (braking radiation) is the result of radiative collision between a high-speed electron and a nucleus in which the electron loses a part or all of its energy in the form of electromagnetic radiation consisting of X-ray photons (Figure 1.2). Although the probability of *bremsstrahlung* production depends on the square of the atomic number (Z) of the target material, the efficiency of X-ray production is found to be directly proportional to the first power of the Z and the voltage applied to the tube.
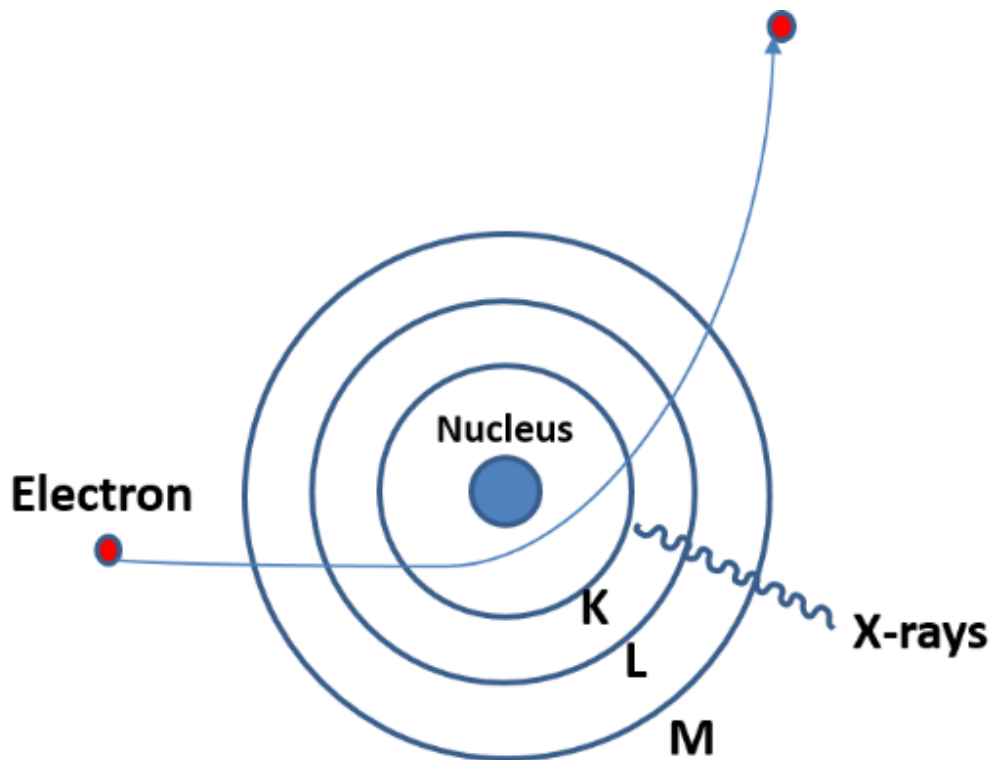
Figure 1.2: Illustration of *bremsstrahlung* production.

Characteristic X-rays are produced when an electron loses its kinetic energy through interaction with the target atom by ejecting an orbital electron (K, L, or M orbital electron) leaving the target

atom ionized. The vacancy created in an inner orbit is then filled by an outer orbital electron through release of radiative energy in the form of characteristic X-rays (Figure 1.3). Unlike *bremsstrahlung*, characteristic X-rays are emitted at discrete energies. Therefore, the overall X-ray spectrum would be a continuous distribution of energies for the *bremsstrahlung* photons superimposed by characteristic X-rays of discrete energies. An example of the X-ray spectrum for 150 kV tube potential is shown in Figure 1.4.
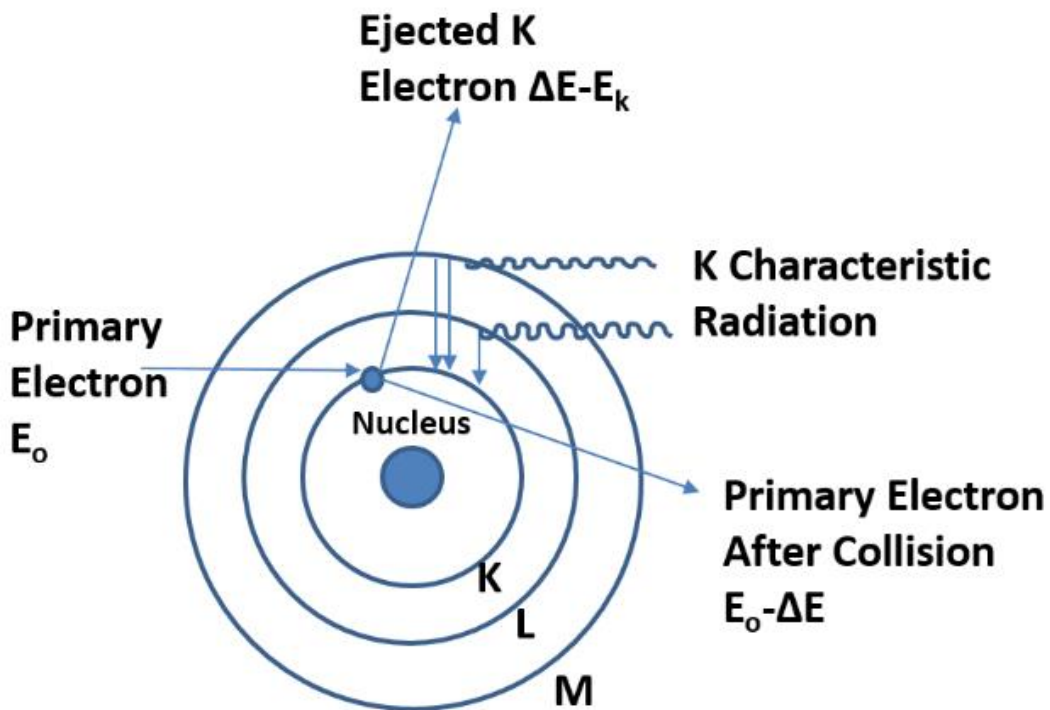
Figure 1.3: Illustration of characteristic X-ray production.
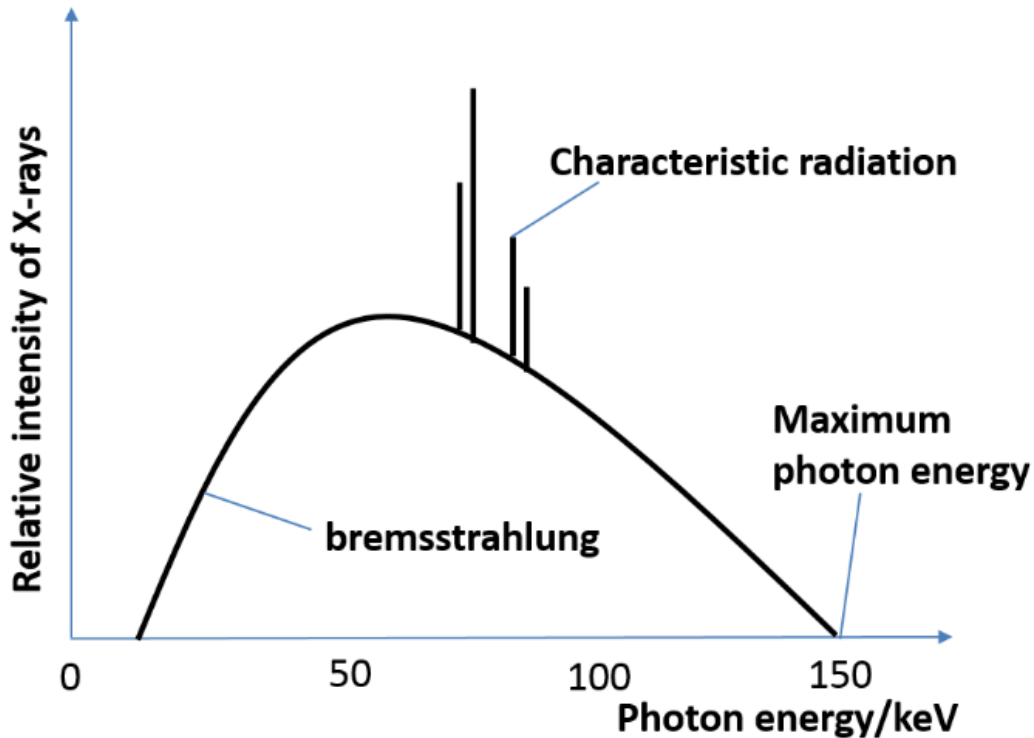
Figure 1.4: X-ray spectrum for a tube potential of 150 kV.

X-rays produced by electrons with kinetic energies between 10 and 100 keV are called diagnostic X-rays, and those with electron kinetic energies between 100 and 500 keV are called orthovoltage X-rays. Based on the application, X-rays of specific energy range are employed, for example, in diagnostic radiography, fluoroscopy (X-ray image-guided surgeries) and superficial radiotherapy, the X-ray tube-voltage (in kV_p) in the range of 10 to 150 kV_p are used while X-rays with energies in the MeV range (6 to 25 MeV) are used in deep-tissue cancer treatment.

1.1.2 Other high-energy radiations

High-energy radiations such as gamma rays, alpha/beta particle emissions, proton, electron, and/or neutron radiation are often employed or encountered (as a by-product) in a wide range of industries that includes healthcare industry, aerospace, and nuclear power plants. Space radiation mainly consists of: galactic cosmic rays (GCRs), solar particle events (SPE) and trapped

energetic radiation.[1] Neutrons are uncharged particles and readily pass through most materials and interact with the nuclei of the target atom resulting in secondary radiations capable of energy transfer in the form of ionization or excitation, and heat. An overview of the various types of radiation associated with hospitals, aerospace industry and nuclear power plants is presented in Table 1.1.

Table 1.1: An overview of the different sources of radiation used or encountered in 3 representative industries. Reprinted with permission from ([2]). Copyright (2012), American Chemical Society.

Industry	Radiation sources	Composition	Typical energy range
Medical radiology: diagnostic, interventional & radiotherapy[3]	(i) X-rays & gamma rays (ii) Protons & electrons	Electromagnetic radiation - wide range of X-rays & gamma rays. Particle radiation for therapeutic purposes.	(i) 10 MeV to 10 GeV (ii) few MeV to 100s of MeV (iii) electrons: few MeV and protons: several 100s of MeV.
Aerospace[4, 5]	(i) Galactic cosmic rays (GCR) (ii) Solar particle events (SPE) (iii)Trapped particle belts	**GCR** consists of high energy protons, alpha particles (helium nuclei), and heavy nuclei account for nearly 85%, 14% & 1% of the total flux respectively. **SPE** consists of transient burst of low to medium energy protons & alpha particles. **Trapped radiation belts** mainly consist of high energy electrons & protons.	Tens of keV to tens of MeV
Nuclear reactors[3]	(i)Particle emissions (ii) Gamma rays	Neutrons, alpha and beta particles, and gamma rays.	(i) 0 to 15 MeV for neutrons, 0 to 4 MeV for alpha and beta particles. (ii)10 keV - 3 MeV

1.1.3 Interaction mechanisms of ionizing radiation with matter

A brief overview of the basic interactions of radiation with matter (target material) is presented in this section. Radiation-target interactions has been categorized into 2 subsections according to the type of radiation: (i) high-energy photon-matter interactions, and (ii) particle-matter

interactions. In each of these subsections, a brief overview of the basic mechanisms of interactions will be presented.

1.1.3.1 High-energy photon (X-rays and gamma rays)-matter interactions

There are 3 main mechanisms of photon interactions: (i) photon scattering (elastic or inelastic), (ii) photoelectric effect, and (iii) pair production.[6] In this sub-section, each of these processes is briefly described along with its effects from a radiation-attenuation point of view.

1.1.3.1.1 Photon scattering

Elastic scattering (or Rayleigh scattering) is one of photon interaction without loss of energy; the incident photon is scattered away with the same energy. Another type of photon scattering is the inelastic scattering (or Compton scattering) during which, the incident photon imparts some of its energy to the orbital electron and gets scattered with reduced energy (increased wavelength). The electron recoils with the energy lost by the incident photon and the photon gets scattered with a new longer wavelength.

1.1.3.2 Photoelectric effect

The photoelectric process consists of an incident photon interacting with an innermost electron and giving all of its energy to the electron, causing it to eject from the target atom. The photon completely disappears and part of its energy is taken up in overcoming the binding energy of the electron and the rest becomes the kinetic energy of the ejected electron (photo-electron). The vacancy created by the ejected electron is usually filled by other electrons from higher energy levels resulting in the emission of characteristic X-rays or Auger electrons. The probability of a photon to undergo photoelectric absorption is proportional to Z^3/E^3, where Z is the atomic number of the target material and E is the incident photon energy.

1.1.3.2.1 Pair and triplet production

If a photon with energy equivalent to or greater than the rest mass of two electrons (i.e. 2×511 keV = 1.02 MeV) interact with an atomic nucleus of the target then it disappears producing an electron-positron pair which results in 'pair production'. On the other hand if the photon interacts with an electron of the target atom then the process is called triplet production. During pair production, the electron deposits its energy in the medium and eventually interacts with a positive ion and becomes part of a neutral atom while the positron may interact with another electron from the target, generating two annihilation photons of equal energies of 511 keV each. These annihilation photons move in opposite directions.

1.1.3.3 Particle-matter interactions

When high-energy, high-Z particles (HZE particles) traverse a medium (or target), for e.g., body of a spacecraft or a tissue, they lose their energy through a number of interactions with the incident material. Of all the possible interactions, the two most important mechanisms from a radiation-shielding point-of-view are interactions that lead to: (i) energy loss (due to radiation, ionization, or excitation of the target material) and (ii) nuclear fragmentation of projectile ions, target material or both.[4, 7]

1.1.3.3.1 Energy loss

Energetic charged particles interact with matter by electrical forces and lose their kinetic energy (inelastic phenomenon) through ionization, excitation and radiative losses. Non-radiative energy loss occurs when charged particles (HZE or beta particles) collide/interact with the electrons of the target resulting in ionization or excitation of the target-atoms along the path traversed by the incident ions. Radiative type of energy loss occurs due to deceleration (slowing down of the

charged particles) as they traverse through a medium. This secondary radiation, the intensity of which is directly proportional to the square of the Z of the target material and inversely related to the mass of the incident particles, is called *bremsstrahlung*. The ratio of the energy loss due to radiation and that is lost through ionization and excitation is proportional to the energy of the particle and to the Z of the target material.

1.1.3.3.2 Nuclear fragmentation

Another important interaction between incident particles and the target material is fragmentation of projectile ions, the target or both. Projectile ion fragmentation involves disintegration of the incident heavy ions into lighter charged particles and neutrons. Nuclear fragmentation of the heavy ion projectile leads to the formation of smaller fragments with the same velocity as the incident ion (i.e. through elastic collision in which the kinetic energy is conserved) but with a lower ionizing power owing to its lower Z. Target fragmentation, on the other hand, results in the production of secondary radiation. Breaking up the heavy ions present in the cosmic rays into smaller fragments (with lower ionizing power) while minimizing target fragmentation is the only practical solution for developing effective shielding materials.[4]

1.1.4 Radiation shielding and dosimetry

Unwanted exposure/s to any of the afore-mentioned ionizing radiations may be hazardous to life. The implications of such exposures are related to a number of factors that include the type of radiation and the energy associated with it, the amount of dose administered (absorbed dose), duration of exposure, etc. Ionizing radiations interact with matter through collisions with the target atoms in which energy is transferred from the photon or particle to the atom. The energy transfer may result in excitation and/or ionization along with heat generation, depending on the

energy of the incident photon or particle and the density of the target material. In other words, radiation interaction with matter especially with biological matter may lead to long term, irreversible health effects. Consequently, radiation shielding and detection (dosimetry) have been the two most important aspects associated with high energy radiation environment. Radiation shielding can be broadly categorized into: (i) protection of personnel or patients in a clinical setting, or of astronauts in space missions, and (ii) structural shielding of machines, components, and buildings. The need for radiation protection for each of these two categories, an overview of current challenges, and possible solutions are discussed in the sections below. Finally, a brief description of conventional dosimeters followed by current challenges and solutions is discussed in Section 1.1.4.3.

1.1.4.1 Personnel radiation protection

1.1.4.1.1 Radiation-induced health risks

In medical radiology, X-rays with energies in both keV (diagnostic use and therapeutic for superficial lesions) and MeV (therapeutic purpose only) are routinely used. Radiation safety and monitoring, thus, becomes crucial for both clinical personnel and patients. For example, X-rays with energies in keV range (~ 60 to 100 kV_p tube voltage) are often employed in interventional procedures (X-ray image-guided procedures) that mandate the use of protective aprons and other garments for both clinical staff and patients in order to avoid unwanted exposure during the procedure. High-energy ionizing radiations (up to tens of MeV), typically produced from a linear accelerator, are used to control tumour growth as part of cancer treatment. It is especially used in treatment of deep-seated tumour. It is also used to treat non-malignant conditions such as severe thyroid disorder, eye disease, abnormal growth of mucousal tissue (pterygium) or bone (heterotopic ossification), aggressive joint lesions, etc. The tissues near the region of treatment

often get exposed to the penetrative X-rays leading to harmful side effects to both internal and superficial organs. One such side-effect which occurs in patients treated for head and neck cancer is xerostomia - a condition that reduces saliva secretion, alters speech, taste, and induces other secondary nutritional deficiencies.[8]

Cosmic radiation imposes important safety concerns for space exploration missions. Several studies have speculated the radiation risks associated with exposure to both galactic cosmic rays (GCR) and solar particle events (SPE). [1, 9] The radiation-induced health risks include carcinogenesis, cardiac problems, cataracts, and other acute radiation syndromes.[1] Damage to neuronal system has been a potential concern related, especially, to the heavy ions present in the GCR.[1] In addition to health hazards, the ionizing radiations may cause degradation of electronic systems and other space payloads especially in manned space missions. Neutrons are uncharged particles commonly used in nuclear reactors for producing nuclear energy. They readily pass through most materials and interact with the nuclei of the target atom. Nuclear plant workers and aircraft crew are most susceptible to occupational exposure of neutrons.[3]

1.1.4.1.2 Protective garments

The composition of the material used for protection against radiation depends on the type of radiation to be blocked or attenuated. The interaction mechanisms of different types of radiations with matter have been well-established, and they form the basis for appropriate selection of shielding material. Considering the scope of this thesis, materials specific to diagnostic X-rays are discussed in this section.

X-rays in the diagnostic range (tens to 100s of keV) can be effectively attenuated using high Z material of appropriate thickness for shielding purposes. This is because the X-ray photons lose their energy through collisions with the high Z target atoms as they traverse through it. High Z

materials such as lead and lead-based alloys are commonly used in protective garments for clinical personnel and patients. The high Z elements are often mixed with polymers to mimic fabric-like conformability. However, lead is toxic and may lead to serious health problems if used for a prolonged period of time. They are often heavy as well which may lead to occupational health hazard such as back pain, improper posture, etc. According to the radiation safety guidelines, during an X-ray image guided interventional procedure, all the clinical personnel present in the room along with the patient should wear protective garments to minimize exposure mainly from scattered X-rays. Several of such procedures are performed routinely and hence, the protective garment plays an important role in providing effective shielding over a prolonged period of exposure to scattered X-rays. Therefore, there is a need for lead-free, conformable, lightweight protective garment. It is important to note that although an ideal protective garment, particularly the ones used in diagnostic radiology, should be "lead-free", they are required to be "lead-equivalent". It is used as a standard to compare the attenuation properties of the protective material with those of pure lead with a certain thickness. For example, the commercial aprons/gear indicate either 0.25 or 0.5 mm lead equivalent value under specified conditions.

Polymer composites can be effectively designed to develop conformable, lead-free yet lead-equivalent shielding against diagnostic X-rays. Polymers reinforced with nanoparticles have been reported to have enhanced material properties such as improved mechanical strength and thermal properties, and enhanced radiation resistance.[10, 11, 12-16] Moreover, both experimental studies and simulations have reported that nanocrystalline materials showed enhanced radiation-resistance when compared to their polycrystalline counterparts.[17-20] Furthermore, few studies have recently investigated the particle size effects of nano- and micro-scale materials. They

reported improved attenuation characteristics of nanoparticles, particularly at lower X-ray energies (i.e. the mammographic energy range: 20 to 30 kV_p), compared to those of microparticles. Hence, polymer nanocomposite made of conformable polymer matrix with non-lead nanoparticles is an ideal candidate to be the next generation of protective garments in medical radiology.

1.1.4.2 Structural shielding

1.1.4.2.1 Radiation-induced effects

In addition to health hazards, the ionizing radiations may cause degradation of electronic systems and other space payloads especially in manned space missions. High energy X-ray source may also produce secondary neutrons. For example, linear accelerators, commonly employed in radiation therapy, may produce secondary neutrons when operated at tube voltages greater than 10 MV through interactions of high energy X-ray photons with the high Z materials used in their collimators. Exposure to neutron radiation is particularly hazardous to body tissues since they are capable of generating a much denser ion path as they lose/deposit their energy within the target material (in this case, body tissues). Interactions with biological matter may also result in the production of other radiations such as gamma rays, protons and alpha particles.

1.1.4.2.2 Structural shielding materials

All units containing any source of ionizing radiation need to be shielded with relatively thick (in centimetres or sometimes in metres) shielding materials for varied reasons; some of which include health and environmental safety concerns, protection of devices with electronics critical for certain applications such as space missions, satellites or stations, isolation of radiation source

particularly during transport, or in case of accidental leakage, and for the convenience of remote monitoring of radiation source for therapy or other applications.

The type of material used for structural shielding depends on the type of radiation source. The principles of radiation interaction remain the same as for those of the protective garments discussed earlier. In diagnostic radiology, structural shielding materials can be found in various parts of the treatment room. For example, lead or lead-equivalent materials are used in the walls, doors, and sometimes lead glass are used in screens/windows/doors for remote monitoring of the room with X-ray source during diagnosis, treatment or machine calibration and other tests. Similar to X-ray protection gear, it is preferred to minimize the use of pure lead or lead-based compounds in structural shielding. Polymer nanocomposite developed using lead-free, high Z materials can be considered as a material for structural shielding in clinical radiology. Owing to their ability to conform over uneven surfaces, ease of fabrication and handling, polymer nanocomposites can be considered as a structural shielding materials for effective protection against X-rays in the keV range.

1.1.4.3 X-ray dosimetry

Accurate radiation dosimetry is essential for radiation detection and monitoring for personnel safety, dose calibration and measurement of delivered dose during X-ray-based diagnoses (using diagnostic X-rays) and treatments (using MV X-rays). Ionization chamber, thermoluminescence dosimeter, solid-state field effect transistor (FET) and radiographic film are most commonly used for radiation detection, monitoring and calibration in clinical radiology. Ionization chamber is the most traditional and reliable dosimeter for point-dose measurements but it requires extremely high operating voltage (typically ± 150 or ± 300 V) and it is not conformable. Thermoluminescence dosimeters are widely used for monitoring personnel radiation dose due to

their ability to store cumulative dose information. However, they require calibration and post-processing using specific equipment in order to estimate any information of exposed dose. FETs operate at much lower voltages than those compared with ionization chamber and may be arranged in a one-dimensional array to obtain point dose information in one dimension. However, the spatial resolution is in the order of mm. Film dosimetry works well for two-dimensional high-spatial resolution (in microns) dose estimation but it is not real-time and reusable; once developed the film is permanently altered. While each of these dosimeters has its own pros & cons and sometimes used in conjunction with each other, there is a significant need to have a single dosimeter for newer radiological applications such as intensity modulated radiation therapy that require detectors to be flexible, capable of delivering real-time dose information over a large area with high spatial resolution (at microns or sub-micron level). A conformable, real-time dosimeter can also be used in in-vivo measurements during diagnostic, interventional or therapeutic procedures.

Recently, organic semiconducting polymers have been investigated in high-energy dosimetric applications. Progress in nanoscale fabrication techniques has allowed development of flexible, polymer-based electronic devices for biomedical applications.[21] In this regard, nanocomposites of semiconducting polymer loaded with high Z nanomaterial can be fabricated on flexible substrate with nanometer thick electrodes for potential dosimetric applications. A relatively small weight percentage of high Z nanomaterials would, in principle, be able to harvest the incident photon energy, and subsequently enhance the overall sensitivity of the device in comparison with that achieved from pure polymer without the nanomaterial. Moreover, the nanomaterial would tend to occupy a relatively larger volume fraction for a specific weight percentage when compared to that obtained from particles of higher dimensions, a property which would be

especially useful in large-area, high spatial resolution dosimetry. Detailed discussion on organic polymer-based dosimetry is presented in Chapters 2 and 4. Some of the potential applications of polymer nanocomposite-based dosimeters include real-time measurements of entrance/exit dose, machine calibrations, large area integrated dosimetry, *in-situ* dose information during radiation therapy and planning, and monitoring exposures for radiation safety purposes. The applications of conformable nano-dosimetry may be extended to other industries as well and hence, are not restricted to medical radiology alone.

1.2 Research Objectives

There is significant demand for the development of novel materials for both X-ray protection and dosimetry especially in clinical radiology. Polymer nanocomposite can be considered as a plausible solution. However, each of the applications require careful selection of both appropriate polymer matrix and nanomaterial in order to develop efficient protective and dosimetric materials. Accordingly, the research objectives for each of the applications are presented in this section.

1.2.1 X-ray Shielding

A. Development of polymer nanocomposite capable of effectively attenuating both primary and scattered X-rays in the diagnostic energy range (40 to 150 kV_p). The nanocomposite should be lead-free, conformable, easily processable, and lightweight.

B. Investigation of particle size effects on X-ray transmission/attenuation properties of nano- and micro-scale materials loaded in polymer matrix. Detailed examination of size effects in terms of various 'mass per unit area' and concentrations (in weight percentage) of the

nano- and micro-particles over a wide range of X-ray energies (20 to 80 kV$_p$) including primary and scattered X-rays.

1.2.2 X-ray dosimetry

A. Synthesis and characterization of high Z, semiconducting nanomaterial for X-ray detection. Fabrication and testing of devices with and without nanomaterial for investigating the real-time X-ray detection based on X-ray induced photocurrent measurements. Verify X-ray detection under different doses, operating voltages, field sizes, and X-ray tube voltages over a wide range of X-ray energies:

   a) 20, 23, 26 and 30 kV$_p$ (mammographic energy range)

   b) 40, 60, 80 and 100 kV$_p$ (higher diagnostic energy range).

B. Investigation of X-ray detection using flexible substrate and organic semiconducting polymer loaded with the tested nanomaterial over X-ray tube voltages in the range of 26 to 100 kV$_p$. Firstly, an insulating polymer need to be selected for deposition of nanometer thick metal (electrode). Secondly, nanocomposite with organic semiconducting polymer and nanomaterial need to be synthesized and deposited on the flexible substrate. Finally to complete the device, another layer of metal need to be deposited on top of the semiconducting nanocomposite layer. Similarly, devices with the organic polymer loaded with and without the nanomaterial need to be fabricated and tested under diagnostic X-rays in order to determine the role of high Z nanomaterial in X-ray detection. The devices need to be assessed under various X-ray tube voltages and doses.

1.3 Thesis Layout

The thesis has been broadly organized into the following:

(i)   Introduction to radiation sources, radiation interaction with matter, the importance of radiation shielding and detection especially in a clinical setting, materials used for the shielding and detection, current challenges, and polymer-based solutions to those challenges. (Chapters 1 and 2)

(ii)   Literature review on polymer composite materials for radiation shielding. (Chapter 3)

(iii)   Literature review on organic semiconducting polymers and their nanocomposites for X-ray or gamma ray dosimetry. (Chapter 4)

(iv)   Research work on development of novel polymer nanocomposite for protection against X-rays in the diagnostic energy range, and the effects of particle size on X-ray transmission/attenuation properties. (Chapters 5 and 6)

(v)   Synthesis, fabrication and testing of semiconducting nanomaterial for detection of X-rays in the diagnostic range. (Chapter 7)

(vi)   Fabrication and testing of semiconducting polymer nanocomposite for clinical dosimetric applications. (Chapter 8)

(vii)   Finally, the overall conclusions of the research work and future directions are presented in Chapter 9.

Chapter 2

Introduction to Materials for Radiation Shielding and Dosimetry

In this chapter, materials and technologies in radiation shielding and dosimetric applications are discussed. Commercially available materials, current challenges, and an introduction to polymer-based materials are presented in Sections 2.1 and 2.2.

2.1 Radiation shielding

2.1.1 Conventional shielding materials

Numerous experimental investigations and theoretical studies have reported the use of a variety of shielding materials (for e.g., aluminum, carbon fibre reinforced plastics (CFRP), metal alloys, concrete, high density concrete, heavy metals such as lead or lead-oxide, composites of lead oxide/tungsten/tin, polymer composites, etc.) for attenuation of the different types of radiations.[7, 22-24] Several of the commercial products for shielding use one or a combination of the listed materials. The shielding effectiveness of a given material largely depends on the type of radiation and the range of energies associated with the radiation.[25]

In space industry, aluminum and metal alloys are commonly used as structural materials in space-vehicles/satellites owing to their excellent mechanical and thermal properties. However, they can produce harmful secondary radiations when exposed to space radiation which would require additional material to attenuate the secondary rays resulting in increased payload, fuel consumption, and hence mission cost. CFRPs are lighter than aluminum-based materials and are often used as structural material. However, they have relatively weak mechanical properties and

require additional material in order to effectively shield the high energy particle radiations in space.

In nuclear plants, neutron radiations are moderated using low Z materials, mainly hydrocarbons such as water, fuel oil, and polymers rich in hydrogen like polyethylene. In order to attenuate the secondary gamma radiations, high Z elements such as lead may be used in conjunction with the low Z materials. Boron and boron carbide containing materials are also often used for neutron shielding in order to minimize the secondary gamma rays.

In healthcare industry, high Z materials mainly including lead or composites of lead are used to attenuate diagnostic X-rays during clinical procedures requiring safety of clinical personnel or patient. They are also used as structural materials of the radiation facility. For example, in the structural components of X-ray machines, or within the walls/doors/window-screens in the radiation room.

2.1.2 Polymer-based radiation shielding

The use of high Z material for shielding against GCR or SPE particles results in emission of highly penetrative *bremsstrahlung* radiation which require additional shielding adding to the total bulk of the material and also to the cost. The production of the *bremsstrahlung* within the target material (i.e. a shielding material) due to radiative energy-loss may pose additional health risks.[26, 27] Therefore, to reduce energy loss due to radiation, low Z materials such as hydrogen are preferred for effective protection. Moreover, for outer space applications, any proposed shielding material must be composed of elements that maximize the probability of projectile fragmentation and minimize the fragmentation of the target material. In this regard, polymers rich in low Z materials especially hydrogen or boron, have shown to be best-suited materials for particle-

radiation shielding. Recent studies[7, 28-30] have shown that elements with low Z tend to provide effective shielding against charged-particle radiations encountered in interstellar space (namely, the GCR and the SPE). Hydrogen being the smallest atomic diameter provides a large number of interaction points in the polymer for projectile fragmentation. Moreover, the absence of elements heavier than carbon minimizes the production of target fragments and hence, the secondary radiations. Thus, a hydrogen-rich polymer - polyethylene has been chosen as a reference material for the accelerator-based radiation testing of multi-function composites currently being developed by NASA.

In medical radiological departments, lead or composites of lead are traditionally used as shielding material. However, lead is toxic resulting in health risks from occupational hazard especially for the clinical workers who routinely use the protective garments, and also environmental concerns for safe disposal of lead-based materials. Consequently, there is a need for lead-free, lightweight, conformable protection gear, as well as lead-free structural material. In summary, there is an increasing demand to develop new shielding materials that can be customized according to specific application (or radiation type).

2.1.2.1 Polymer reinforcement with micro- or nano-materials for radiation shielding applications

Several studies have shown that the composite material exhibit enhanced mechanical strength and higher thermal stability when compared to the polymer without filler/s.[31, 32-34] The enhancement in the material properties has been attributed to the properties of the filler material, uniform dispersion of the filler within the polymer matrix, the type of interaction between the filler and the polymer (interfacial effects), and the size effects of the filler.[30, 35] For example, the properties of carbon nanotubes (CNTs) - exceptionally high elastic-modulus and tensile strength

(~1 TPa and tens or hundreds of GPa respectively) along with excellent thermal and electrical conductivity, and very high resistance to oxidation in air (> 700°C), have shown to improve the material properties of CNT-based polymer composites at relatively low loading of CNTs. [36, 35, 37] Moreover, small-sized filler particles do not create large stress concentrations within the material and helps in retaining the ductility of the polymer.[35]

Upon exposure to ionizing radiation, the process of free-radical formation is responsible for the degradation of the material properties in polymers. Generally, upon photon/particle irradiation, the ionizing energy absorbed by the polymer backbone initiates a free radical process.[38] Subsequently, the polymer then undergoes chain scission (results in reduction of tensile strength and elongation) and crosslinking (increases tensile strength and but reduces elongation), both of which alters the material characteristics of the polymer. For example, in nuclear reactors, polyethylene and borated polyethylene (mixture of polyethylene and boron oxide) are commonly used as neutron shielding materials, however, these polymers have poor mechanical and thermal stability and exhibit poor durability when exposed to continuous radiation.[31, 36]

In this context, reinforcement of polymer with micro- or nano-materials has been reported to not only enhance mechanical and thermal stability but also improve radiation-resistance properties of the composite material.[10, 11] Seo et al. [39] observed radiation-induced interfacial bonding (polar-polar interaction) between epoxy (polymer) and graphite fibre (filler) in their composite material upon exposure to electron beam of 0.5 MeV. Polyimide (PI), commonly used on spacecraft structures, is highly susceptible to atomic oxygen (AO) in Low Earth orbit (LEO) resulting in severe degradation. Incorporation of polyhedral oligosilsesquioxane (POSS), comprised primarily of inorganic silicon-oxygen cage-like structures ranging from 0.5 to 3 nm in diameter, into polyimide significantly improved the oxidation resistance through the formation of a

protective silica layer upon exposure of POSS-PI nanocomposite to high incident fluxes of atomic oxygen in Low Earth orbit.[40] Furthermore, both experimental and simulation studies reported that nanocrystalline materials showed enhanced radiation-resistance when compared to their polycrystalline counterparts. This property of nanomaterials has been attributed to the large volume-fraction of grain boundaries that may serve as effective sinks for defects produced upon irradiation of ions and proton beams.[17-20] Recently, Bai et al.[41] proposed a "self-healing" mechanism especially near the nano-grain boundaries through efficient annihilation of interstitial defects produced upon irradiation.[42] Subsequently, one may hypothesize that incorporation of nanocrystalline materials into polymeric matrix may impart their radiation-resistant behavior to the nanocomposite through "self-healing" mechanisms. Few studies have systematically investigated the enhanced resistance of the polymer/clay nanocomposites under exposure to high-energy radiation.[12-16] Addition of a small weight percentage (wt%) of nano-clay into various polymers resulted in increased radiation resistance through effective grafting of the polymer molecules onto the nano-layered clay.

Based on the advantages offered by the nanomaterials-based fillers, few studies have proposed the use of nanocomposites of a high-performance polymer - polybenzimidazole and carbon nanofibers or other nanomaterials for durable space applications.[32, 33, 43] Carbon-based filler materials such as carbon micro-/nano-fibers and recently, nanotubes used as reinforcements in a variety of polymers (resins and plastics) exhibit high strength-to-weight ratio; rendering the carbon composites as suitable candidates in applications requiring mechanically strong, ultra-lightweight materials.[44, 45] Thus, depending on the type of filler and the application, effective and durable radiation shields can be designed using polymer composites.

In summary, polymer composites are particularly interesting candidates as radiation-shielding materials for varied reasons. Firstly, they offer geometric conformability, a feature particularly useful in protection of various anatomical structures during radiation therapy or procedures. The ability to conform onto uneven structures can also be useful to replace metals or alloys commonly used in space-craft industries. Secondly, polymer composites are lighter than their metal counterparts. This feature is particularly attractive for designing lightweight protective aprons or spacesuits, and also, in decreasing overall space payload resulting in lesser fuel consumption to get to high altitudes or orbits.[46] Finally, polymers can be processed with different types of filler/s to achieve effective shielding for radiations associated with specific industry. Based on the end application, the polymer composite-based shielding materials can be used in: (i) protective aprons/gear for radiation workers or patients, and (ii) structural shielding materials.

2.2 X-ray and Gamma-ray Dosimetry

Ionizing radiation interact with matter resulting in the deposition of energy in the medium which may lead to radiation-induced effects in the material. These effects can be either transitory (for e.g., ionization in gases, fluorescence, and photoconductivity of irradiated material), or relatively permanent (for e.g., thermoluminescence, photographic effect, and chemical effects). In order to determine the radiation-dose delivered to a medium, radiation dosimeters (detectors) make use of the radiation-induced effects in the material. A brief description of the principle of operation of some of the most commonly used X-ray dosimeters, in a clinical setting, is presented in Section 2.2.1. The advantages and disadvantages of each of these detectors are outlined in Table 2.1. The challenges in using conventional dosimeters for radiological applications that require real-time, large area dosimetry are described in Section 2.2.2 along with the introduction of organic semiconducting polymers and its composites as possible solutions. The different photodetection

approaches of the studies reported so far on polymer-based dosimeters are detailed in Section 2.2.2.1.

2.2.1 Current technologies

2.2.1.1 Ionization chamber

There are mainly two types of ionization chambers: free-air ion chambers and thimble ion chamber. The former type is used mainly in Primary Standard Laboratories for primary calibration of ionization chambers, while the thimble chamber is commonly used on the field for patient dosimetry once calibrated. The simplest and most commonly used type of thimble chamber is the Farmer chamber. It consists of an air-filled chamber with three main components: (i) cylindrical capsule with an inner lining of electrically conductive material (i.e. the outer electrode), (ii) an axial (central) electrode (also known as collecting electrode), and (iii) a sensitive volume of air (typically 0.6 cm^3). Upon irradiation, ion pairs are formed and as the collecting voltage is increased, the ions and dissociated electrons move to the electrodes of opposite polarity, under the influence of the high electric field (typical bias voltage applied is ±150 or 300 V), thus creating an ionization current which can be measured by an electrometer. The accumulated charge is proportional to the number of ion pairs created within the chamber volume during the interactions with the incident photons. The continual generation of charge carriers produces an ionization current which represent a measure of the total ionizing dose deposited within the chamber.

Ionization chamber, essentially, gives a measure of the amount of radiation energy transferred to the volume of interest it can be used for the determination of dose absorbed within the volume if designed to achieve an electronic equilibrium based on the Bragg-Gray cavity theory. If the

charged particles escape the irradiated volume without depositing all of their energy, and if they are not compensated for by charged particle originating outside that volume then an electronic equilibrium is not achieved. An ionization chamber needs to be first calibrated before it is used for measurement of absorbed dose. A typical air volume of a thimble chamber is about 0.6 cm^3, and a length of about 2.5 cm. The wall of the chamber (outer electrode) is usually a material which is to be "air-equivalent" such that it has the radiological properties *equivalent* to those of air. Several correction factors also need to be applied to the electrometer reading in order to obtain the absolute dose. In addition to correction for the environment (temperature and pressure), the collection efficiency of the chamber may be adversely affected through ion recombination within the irradiated volume. Ion recombination correction factor depends on chamber design, bias voltage, beam intensity, incident radiation (photon or electron), and beam type (pulsed, pulsed scanned or continuous).

2.2.1.2 Thermoluminescence dosimeter (TLD)

The ionizing radiation dose delivered to a TLD is determine by measuring the amount of visible light emitted from a TLD crystal when the crystal is heated. Most common types of TLD uses calcium fluoride or lithium fluoride doped with one or more impurities to produce trap states for excited electrons. When lithium fluoride is irradiated with X-rays, the absorbed energy excites electrons in the atoms to higher energy levels where they remain trapped within the lattice structure in the intentionally produced trap states. Upon heating the crystal, the electrons return to the ground state and release photon-energy equal to the energy difference between the trap state and the ground state. The energy of the released photons is proportional to the quantity of the radiation originally absorbed.

A basic TLD reader system consists of a holder for placing and heating the TLD, a photomultiplier tube (PMT) to detect the thermoluminescence light emission and convert it into an electrical signal linearly proportional to the detected photon fluence, and an electrometer for recording the PMT signal as a charge or current. For a calibrated TLD system, the charge can then be converted to absorbed dose using the calibration factor.

2.2.1.3 Semiconductor-based dosimeter

Commercially available solid-state dosimeters can be broadly categorized into (i) silicon based photodiodes, and (ii) metal oxide semiconducting transistor (MOSFET). The former is p–n junction diode in which p type or n type silicon is counter-doped at the surface to produce a p-n photodiode. These are referred to as n–Si or p–Si dosimeters, depending upon the base material. For dosimetric applications, the diodes are operated in reverse bias mode to reduce the dark current. Upon irradiation, electron–hole (e–h) pairs are generated and the charges (minority charge carriers) produced in the diode diffuse into the depleted region. They are swept across the depletion region under the action of the electric field due to the intrinsic potential. Consequently, a current is generated in the reverse direction. Diodes are usually operated without an external bias to reduce dark (leakage) current. Diodes are more sensitive and smaller in size than typical ionization chambers. However, they undergo radiation damage over repeated use which adversely affects their sensitivity. They are particularly useful for measurements in phantoms (radiosurgery planning involving smaller field sizes or dose gradient area), and dose depth or distribution in electron beams. They are also used for routine in vivo measurements on patients.

A second type of solid state dosimeter is the metal oxide semiconducting transistor (MOSFET). It is a miniature silicon transistor that offers very little attenuation of the beam due to its small size, particularly useful for in-vivo dosimetry. MOSFET dosimeters are based on the

measurement of the threshold voltage which is linearly proportional to absorbed dose. Ionizing radiation penetrating the oxide generates charge that is permanently trapped, thus causing a change in threshold voltage. The integrated dose may be measured during or after irradiation. Similar to photodiodes, MOSFETs are widely used in radiotherapy applications for in vivo dose measurements or dose distribution measurements in phantoms.

2.2.1.4 Radiographic film

Radiographic film consists of a base of thin plastic with a radiation sensitive emulsion (silver bromide (AgBr) grains suspended in gelatin) coated uniformly on one or both sides of the base. Ionization of AgBr grains, as a result of radiation interaction, forms a latent image in the film which becomes visible (film blackening) and permanent upon processing. Light transmission is a function of the film opacity and can be measured in terms of optical density (OD) with devices called densitometers. The optical density is defined as

$$OD = \log\left(\frac{I_0}{I}\right)$$

I_0 is the initial light intensity and I is the intensity transmitted through the film. If calibrated, the optical density can be converted to absorbed dose using the required dose-optical density curve generated.

Radiographic film gives excellent 2-D spatial resolution and, in a single exposure, provides information about the spatial distribution of radiation in the area of interest or the attenuation of radiation by intervening objects.[6]

Table 2.1: An overview of the features of most commonly used radiation dosimeters.

Types	Advantages	Disadvantages
Ionization chamber	Easy to use Accurate, real-time read-out Recommended for beam calibration	High voltage supply required Low spatial resolution Connecting cables required
Thermoluminescence dosimeter	small, cost effective, robust and easy to use No power supply required	Requires heat processing and read-out is time consuming No real-time read-out Not recommended for beam calibration
MOSFET dosimeter	Real-time read-out, highly sensitive, and good resolution	Requires a bias voltage during irradiation Not suitable for high-spatial resolution applications such IMRT Has limited lifespan
Radiographic film	Permanent record, highly sensitive 2-D spatial resolution Cost effective	Can be used only once Darkroom and processing facilities required Processing difficult to control Cannot be used for beam calibration

2.2.2 Organic semiconducting polymers for radiation detection

Conventional dosimeters, outlined in sub-section 2.2.1, are commonly used in hospitals for monitoring and detection of radiation exposure to clinical personnel and patients. The dosimeters provide reliable measurements but require either very high operating voltages (100s of volts) or post processing techniques. Except for film dosimetry, all others provide limited spatial resolution (in the order of mm). While radiographic film and 3-D gel dosimeters allow for high-resolution, dose distribution measurements in more than one plane, the dosimetric readings are permanent and they require tedious post-processing. Dosimeters based on organic semiconducting polymers, on the other hand, can be potentially designed to provide conformable, portable, real-time, low-power X-ray detection over irregular and a relatively large surface area. They will be especially useful for applications such as point dose measurements and dose depth measurements over a planar region in both diagnostic radiology and radiation

therapy in which conformability of the detector will be an added benefit. Arrays of MOSFETs or ion chambers are commonly used for such purposes. However, the precision of point dose measurements is limited by the spatial resolution of the physical dimensions of the MOSFET dosimeter and the ion chamber which are typically in the mm scale. Hence, there is a demand for conformable dosimeters that can conform to various anatomical contours and also provide high spatial resolution (in the order of microns or sub-microns). In this regard, semiconducting polymers with patterned electronics could be a possible solution. Moreover, organic polymer-based thin film dosimetry would also be useful in radiological procedures wherein real-time dose depth measurements over a two-dimensional region within a phantom allows the physicist or the clinical personnel to determine entrance and transmission dose delivered. It is also important to note that organic semiconductors typically have low effective Z and hence, there will be no significant attenuation of the radiation allowing it to be an ideal candidate for use in real-time dose measurements during radiation therapy. However, the stability of the organic sensing material due to exposure to both the environment and the ionizing radiation remain an area of active research. In summary, organic semiconducting polymers have immense potential to be used in the development of novel dosimeters for ionizing radiation.

Semiconducting organic polymers have been traditionally used in in organic light-emitting devices (OLEDs). Recently, research efforts towards the development of organic polymer-based dosimeters have gained some momentum.[47-56] Most of these studies have used organic semiconducting polymers that have been well-characterized owing to their widespread use in OLEDs. Different design approaches (diode-based, organic field effect transistor (OFET)-based, or optical-based detection) have been adopted by various groups for detection of ionizing

radiation. In this section, studies reported on detection of both X-rays and gamma rays are discussed since both are ionizing radiation, differing only in the source of photon generation.

2.2.2.1 Photodetection approaches

High energy radiation such as X-rays and gamma rays interact with matter mainly through absorption, scattering, or both of these processes. The primary requirement for a material to be used in X-ray or gamma-ray detection is to harvest the high energy radiation as much as possible i.e. capture cross section for efficient photodetection. The capture cross-section (i.e. attenuation of radiation through absorption or scattering) of a given material is dependent on its atomic number and thickness. Since semiconductor polymers typically have low effective Z (equivalent to tissues), the capture cross-section is also low. Consequently, thicker films (in tens of microns) are used in radiation sensors for maximizing the capture of high-energy photons.

Several studies have reported the effects of the ionizing radiation (soft/hard X-rays, or gamma rays) on semiconducting polymers.[47-51] Some of the effects upon irradiation include increased oxidation of polymer chains resulting in polaron formation,[51] significant changes in the effective conjugation length and solubility of the polymers due to chain scission and crosslinking reactions,[49, 50] susceptibility to other degradation mechanisms through reaction with ambient oxygen, etc. These changes, in turn, affect the material characteristics that include optical, electrical, and mechanical properties. The organic semiconductor-based detectors make use of one of these material properties to detect or measure radiation dose.

Based on the type of material-property considered for sensing, the detectors can be mainly categorized into: (i) optical- and (ii) photocurrent-based detection. It should be noted that there may be other parameters specific to the sensing material that could be used for measuring effects of ionizing radiation on the material. For example, Paez-Sierra et al. measured capacitive

impedance from a flexible dosimeter fabricated using a blend of organic semiconducting polymers and organometallic nanostructures.[57]

In optical detection the sensor output is measured as a permanent change in the material characteristics that can be detected by observing the UV-visible absorption or emission spectrum. In this approach, the sensor can be characterized by calibrating the optical change (peak shifts in absorbance or emission spectra) for a given dose of radiation.[49, 50, 52] However, real-time detection of the precise amount of dose is not discernible through this method. An alternate approach is to measure the photocurrent as a function of radiation dose (or dose rate).[51, 53-55] The photophysical processes involved in these two approaches are discussed in the following sub-sections.

2.2.2.1.1 Optical detection

Upon irradiation of X-rays or gamma rays, the polymer chains may undergo one or more physical alterations which may lead to changes in their absorbance or photoluminescence characteristics. For example, an increase in the magnitude of maximum absorption peak along with a blue shift for increasing dosage of gamma rays was observed in the UV-visible spectrum of the irradiated samples of a conjugated polymer, namely, poly [1-methoxy-4-(2-ethylhexyloxy)-phenylenevinylene] (MEH-PPV).[49, 50] These observations, discussed in detail later in Chapter 4, indicated radiation-induced reduction of effective conjugation in the polymer by crosslinking reactions which, in turn, may have enhanced the molar absorptivity (molar mass and/or mass attenuation coefficient) of the polymer. The change in the molar absorptivity is reflected by increase in magnitude along with a blue shift of the maximum absorption peak observed in the UV-vis spectrum. The change in absorption peak has been correlated to the amount of radiation dose accumulated by the conjugated polymer. This relation between the

absorption peak and dosage forms the basis of the sensing mechanism employed by optical-based photodetectors. The efficiency of the sensors can further be improved by optimizing the thickness and/or concentration of the polymer for enhancing the photon cross-section.

Another design-approach of optical-based radiation detectors involves the correlation between the intensity of photoluminescence of organic polymers and the radiation dosage.[52] Radiation induced degradation have been used for facilitating efficient electron transfer between organic polymer and an inorganic heavy atom (or compound) resulting in an increase in photoluminescence quenching of the polymer with dosage (discussed in Chapter 4).

In conclusion, the design criterion of optical-based radiation sensors is to make use of the radiation-induced changes in the UV-vis characteristics of the organic polymer. These changes are permanent in nature and subsequently, give an account of the accumulative dose received by the sensing material.

2.2.2.1.2 Photocurrent detection

Two main design approaches adopted for photocurrent-based detectors include diode-based[53-55] and OFET-based[51, 56] detection of X-rays and gamma rays. A typical diode-based detector consists of an organic semiconductor layer "sandwiched" between the anode (can be a metal or a hole injecting material such as indium tin oxide; ITO) and the cathode (always a metal capable of forming a good Schottky barrier) layers. In order to measure the photon-generated current, the device should be operated in reverse bias mode whereas forward bias favours recombination of the electron-hole pairs (excitons) generated within the organic semiconductor. Hence any material or device-fabrication technique that allows minimum dark current is preferred for developing efficient X-ray (or gamma ray) detectors. Furthermore, the photocurrents generated within the organic semiconductor material upon irradiation of the high-energy electromagnetic

waves such as X-rays and gamma rays are mostly in the range of nano-amperes and consequently, to detect a noticeable change in the photocurrent (i.e. increased sensitivity) as a function of the radiation dose, it is necessary to operate the detector in reverse bias. Presence of dark current (leakage current) at any given reverse bias voltage will amplify the measured photocurrent. However, the leakage current may also induce space charge limited currents due to band bending at the Schottky interface formed between the organic semiconductor and the metal contact.

The operation of OFETs is similar to conventional inorganic FETs. In OFET, the semiconducting layer is typically an organic polymer and the configuration differs from their inorganic counterpart in the sense that localized doping of the polymer is not possible and hence metal contacts are used as source and drain. The OFET-based radiation detector can be designed to detect cumulative dosage as a function of the photocurrent generated at the drain. The increase in the conductivity of the channel upon irradiation is attributed to the changes induced within the organic material that permanently affects its electrical properties. This increase in the conductivity can be measured as the drain current. An OFET-based gamma-ray detector has been reported to show an increase in the OFF current (drain current when transistor is in OFF state i.e. gate voltage is zero) with radiation dose.[51] The authors attributed the increase in conductivity (or OFF current) to the radiation-induced oxidative effects on the polymer molecules rendering it to become a stable polaron. Since the radiation effects were permanent, the cumulative dosage was estimated from the photocurrent measurements (ON current times OFF current). The sensitivity of the detector is proportional to the change in the magnitude of the product of ON-current and OFF-current.[51, 56]

In order to lower the operating voltage, a gate insulator with a higher dielectric constant (k) is often used in OFETs.[56] However, a high k can adversely affect the charge-carrier mobility through localization (traps) of charge-carriers at the interface of the insulator gate and the semiconducting material.[58] The molecular ordering and morphology of the organic semiconducting material are also important factors that can influence the charge transport properties (charge mobility). Smaller grain sizes at the interface between the metal contact and the active organic layer in OFET results in reduction of mobility in comparison to the charge mobility achieved in the channel. In summary, all the above-mentioned factors such as the alignment of the organic molecules, their morphology, and their interaction with the gate insulator layer affect the overall device performance. [58, 59]

Chapter 3

Polymer Composite based Radiation Shielding – Literature Review

In this chapter, a detailed review on polymer micro-/nano-composites for radiation shielding applications is presented. Some of the studies reported in this chapter directly evaluate the attenuation characteristics of a given polymer-composite under one or more types of radiations, while others compare the material performance before and after irradiation by analyzing the material properties such as tensile strength, storage modulus, polymer chain scission or crosslinking, etc. Majority of the research work reported on polymer composite material with micro- or nano-structure/s as filler/s was found to be directed towards outer space applications.

3.1 Different types of micro-/nano-materials used for radiation shielding

The review on polymer composites has been broadly categorized based on the structure of the reinforcements used in the materials: micro-/nano-tubular structures, particles, and platelets.

3.1.1 Polymer reinforced with micro- or nano-whiskers/fibers/tubes

Graphite fibre composites have exceptionally high mechanical strength and hence, they are used as replacements for metals with poor mechanical properties and high densities such as aluminum alloys. Gaier et al.[10] demonstrated the application of graphite microfiber-based epoxy resin composites for shielding against cosmic radiation. They studied the effect of the intercalation of Bromine (Br_2) and iodine monobromide (IBr) on the graphite composites and proposed the use of the composites as electromagnetic interference-shields for power systems in spacecrafts. Br_2 and IBr were intercalated into woven fabrics of graphite microfibers which were then stacked up together with epoxy-resin in between two layers of the intercalated (or pristine in case of control

samples) graphite clothes. They compared the shielding performance of all the composites against high energy photon radiation - X-rays and gamma rays with 13 keV and 46.5 keV energies respectively. The results indicated that equal shielding effectiveness was achieved by 8 mm thick pristine graphite epoxy material, 1.8 mm of Br_2 intercalated graphite epoxy material and less than 1.4 mm thick IBr intercalated graphite epoxy. Thus, intercalated IBr composite significantly reduced the mass of the shield. They concluded that composites with a few heavy atoms within the light matrix acts as a more efficient shield against high energy photons than a uniform, electron rich material. The composite materials were also tested for high-energy electron (100 keV to 1.16 MeV) absorption as a function of areal densities of all composites. Interestingly, they found that regardless of the material being used, the absorption was independent of atomic number of the material and limited by areal density (Figure 3.1). Moreover, intercalation increased the shielding effectiveness due to their higher mass density.
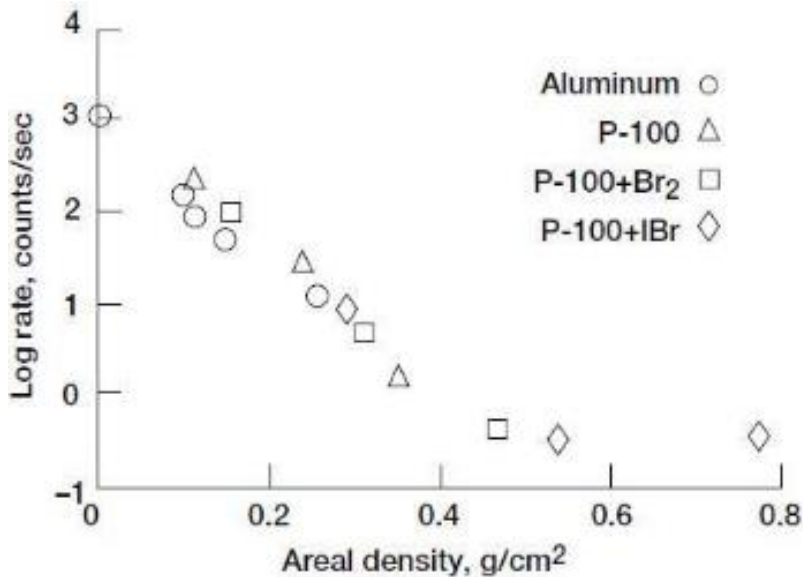
Figure 3.1: Energy absorption as a function of areal density. P-100 is a type of graphite microfiber.[10] Reproduced with permission.

Few researchers have explored the possibility of using CNTs for improving radiation resistance and mechanical strength of hydrogenous polymers.[11, 36, 60] Najafi and Shin[60] reported the high-energy radiation-induced (UV ozone and 20 keV electron beam) effects of CNT-based reinforcements in polymethylmethacrylate (PMMA) polymer matrix. They demonstrated that incorporation of CNTs in PMMA reduced the etch depth of their samples until the percolation threshold of CNT network (at 0.5 wt% of CNTs) within the polymer matrix was achieved, beyond which the etch depth attained saturation (Figure 3.2). The percolation threshold, confirmed from the sheet resistivity measurements, was observed to be the saturation point for the shielding behavior of the CNT network. The authors concluded that the addition of CNT fillers had a dramatic reinforcement effect on the radiation-induced degradation of PMMA and also, in successful dispersion of the radiation.
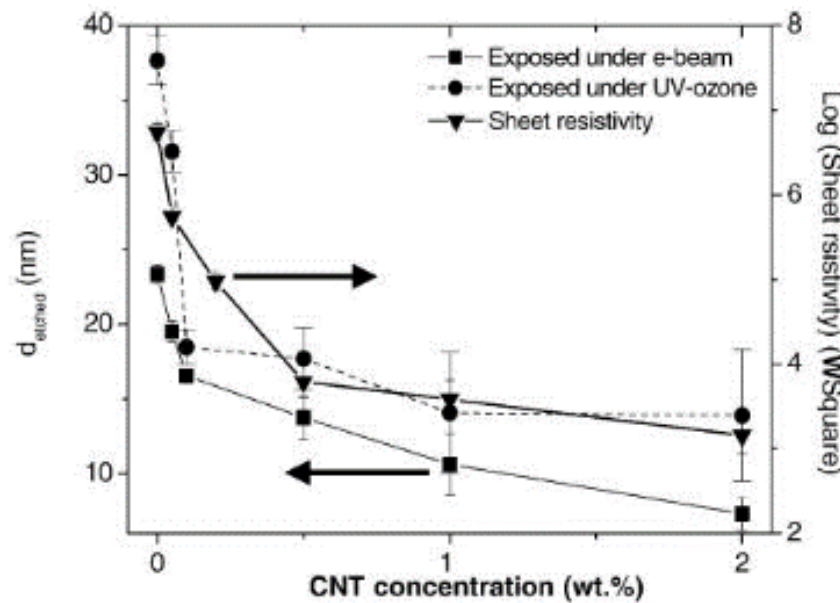
Figure 3.2. Etched depth vs. CNT concentration upon 15 min of exposure under e-beam (closed squares) and UV ozone (closed circles) together with sheet resistivity (closed triangles) of the CNT-PMMA composite thin films. Reprinted from [60], Copyright (2005), with permission from Elsevier.

60

For space applications, the structural materials are required not only to be radiation-resistant, and mechanically strong but also to be able to withstand thermal cycling. Clayton et al.[36] studied the material properties of poly(4-methyl-1-pentene) (PMP) reinforced with 0.5 wt% loading of single-walled CNTs. They proposed the use of PMP, as an alternative to polyethylene for use as a shielding material against GCR, owing to its high performance material properties when compared to that of polyethylene. The dynamic mechanical analysis (DMA) of the neat polymer (PMP) and the composite (PMP+0.5wt% of SWCNTs) showed that the addition of the SWCNTs enhanced the viscoelastic properties of the composite; both the storage and the loss modulus were found to be higher than those of the neat polymer. Moreover, the DMA plots showed that the addition of SWCNTs increased the glass transition temperature of the composite and enhanced the relaxation intensity at the amorphous region of the PMP, both of which indicated that the CNTs improved the crystalline character and mechanical properties of the PMP polymer.

Zhong et al.[29] (2009) reported the radiation shielding performance of ultrahigh molecular weight polyethylene (UHMWPE) fiber-reinforced nano-epoxy composite characterized by radiation tests at the NASA Space Radiation Laboratory. The authors reinforced epoxy matrix with reactive nanofibers of graphite to form 'nano-epoxy' composite and showed that the mechanical (strength, modulus and toughness) and the thermal properties, and wetting and adhesion ability to UHMWPE fibers improved remarkably when compared to UHMWPE fabric alone. Upon testing the material composite against high-energy heavy ion (1 GeV/nucleon) such as the ones encountered in GCR flux, the authors found that the shielding effectiveness was not compromised by the addition of nanofibers into the epoxy/UHMWPE matrix (Figure 3.3). In Figures 3.3a to 3.3d, 'dex1' and 'dey1' denote silicon detectors used to detect the average energy deposited downstream of all the targets materials (a, b, c, and d as listed in the figure caption).
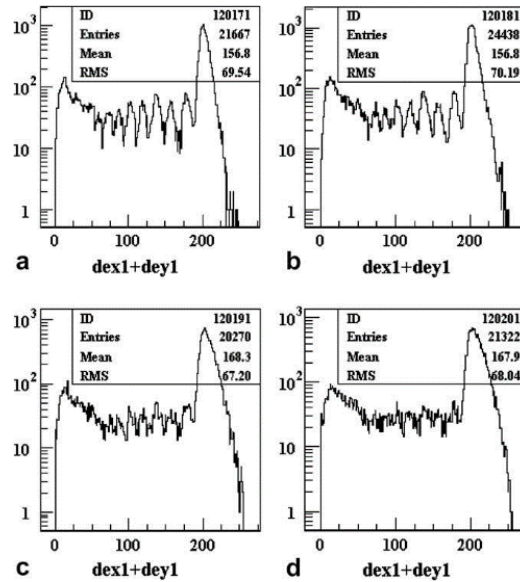
Figure 3.3. Energy loss spectra obtained from the following targets: (a) UHMWPE/nano-epoxy, (b) UHMWPE/pure epoxy, (c) hybrid fiber/nano-epoxy, where 'hybrid fiber' is composed of UHMWPE and S-glass in 2:1 layer ratio and (d) hybrid fiber/pure epoxy. Reprinted from [29], Copyright (2009), with permission from Elsevier.

3.1.2 Polymer reinforced with micro- or nano-particles/powder

Cement or concrete is commonly used in nuclear reactors for blocking neutron flux and gamma rays produced as part of nuclear fission reactions. They are also used in the radiotherapy centers to shield against high energy photons. Gündüz et al.[61] developed several composite materials by impregnating polystyrene into pure concrete (composed of baryte aggregates and cement), concrete loaded with Vitrified Colemanite, VC, ($CaB_3O_4(OH)_3 \cdot H_2O$) in powder form (88 micron in size) and in coarse form (0.833 to 5.613 mm) , and concrete/iron-chunk composites loaded with and without VC. The boron-oxide content in the concrete/VC composites showed improved absorption against thermal neutrons when compared to pure concrete. The composites without the iron chunks blocked the thermal neutrons (secondary emissions produced from primary neutron blockage) efficiently but the γ-rays were not blocked as effectively. However, upon addition of iron chunks, the composite improved attenuation for γ-rays. Finally, the incorporation

of polystyrene into the concrete composites improved the shielding ability towards fast neutron flux.

Polyethylene has been commonly used for shielding purposes in spacecrafts, however, its structural integrity at high pressures and temperature has been of concern. Ashton-Patton et al.[62] reported the use of low density polyethylene (LDPE, bulk density: 924.5 kg.m^{-3}) reinforced with three different types of hollow glass microspheres (HGM) - soda lime borosilicate (bulk density: 170 kg.m^{-3}), borosilicate (bulk density: 150 kg.m^{-3}), and aluminosilicate (bulk density: 160 kg.m^{-3}), all tested against high compression pressures with the following load conditions − A: 6.51 MPa and 110 ± 11 °C, B: 3.9 MPa and 110 ± 11 °C, and C: 3.9 MPa and 120 ± 11 °C. The borosilicate composite, with bulk density 150 kg.m^{-3}, showed the best resistance to breakage for all three conditions. The use of HGM improved the modulus with minimum weight gain. The authors proposed the use of these impact-resistant LDPE/HGM composites as high-energy radiation shields in space exploration studies. Harrison et al.[30] developed composites of high-density polyethylene (HDPE) and boron nitride (BN), and evaluated the materials for mechanical and space-radiation shielding properties. Upon addition of 15 vol. % of neat or functionalized BN to HDPE, the tensile modulus of the composite improved from 588 to 735 MPa and 856 MPa respectively. The authors compared the shielding effectiveness of 2 wt % BN composite with neat HDPE and aluminum (Al) against neutron-beam energies up to 600 MeV, and against 120 GeV protons. Under high-energy neutrons, both neat HDPE and HDPE/BN composites exhibited similar shielding efficiencies to that of Al (Figure 3.4). However, Al proved to be the better shielding material for high-energy protons.
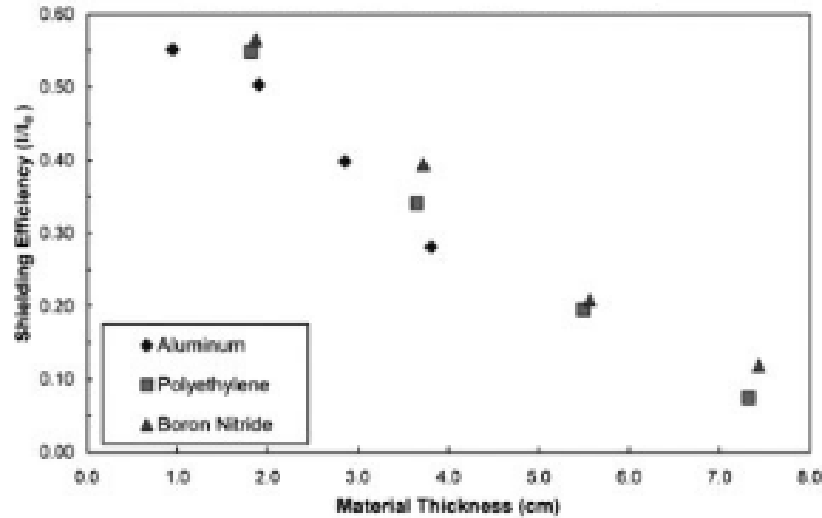
Figure 3.4. Comparison of attenuation results for Al, polyethylene, and polyethylene/BN composites. Reprinted with permission from [30]. Copyright [2008], AIP Publishing LLC.

Silicone rubber is another family of polymers that have been used in spacecraft industry for its excellent electrical insulation properties, performance at wide range of temperatures, and good resistance to aging, chemicals, ozone and particle irradiation. Di et al.[63] compared material properties and high-energy proton irradiation responses of the silicone rubber composites. They tested two composites: (i) silicone rubber reinforced with MQ (M: mono-functional silicon-oxygen units, Q: tetra-functional silicon-oxygen units) silicon resin (represented as M-SR), and (ii) silicone rubber modified with titanium dioxide nanoparticles (nano-TiO_2) based on the M-SR composite (represented as T-SR). Both the composites (M-SR and T-SR) were tested against a range of proton energies – 30 to 200 keV. Analysis of the changes in the surface morphology, mass loss, and mechanical properties of the irradiated composites showed similar crosslinking and degradation effects in both T-SR and M-SR composites. However, the magnitude of degradation in T-SR was found to be lower than M-SR (Figure 3.5). For both the composites, the storage modulus increased upon proton irradiation (fluence = 10^{-14} cm^{-2}) and then decreased for fluence greater than 10^{-14} cm^{-2}. The fluctuation of the modulus was attributed to the sudden

64

increase followed by severe radiation-damage induced decrease in the crosslinking-density for

fluence greater than 10^{-14} cm^{-2}. The authors concluded that the incorporation of nano-TiO$_2$ into

the silicone rubber not only improved the mechanical properties of the rubber but also increased

its resistance to proton radiation.
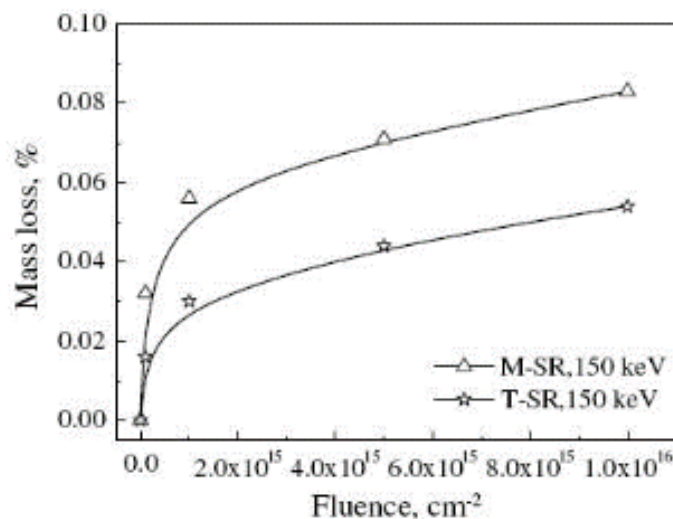
Figure 3.5. Mass loss ratio versus proton fluence for the M-SR and the T-SR composites. Reprinted from [63], Copyright (2006), with permission from Elsevier.

3.1.3 Polymer reinforced with clay platelets

It has been well-established that clay minerals considerably enhance the mechanical, thermal,

electrical, and barrier properties of standard polymers. [13, 64, 65] Moreover, they significantly

reduce flammability of the polymer composite in comparison to that of the pure polymer. The

clay minerals are disc-shaped (platelet) and typically contain a layered structure of tetrahedral

and octahedral sheets. Polymer-clay composites can be broadly categorized into three different

types based on the mode of addition of the clay to the polymer matrix[65]: (i) phase separated

(microcomposite) (ii) Intercalated (nanocomposite), and (iii) Exfoliated (nanocomposite). In

'phase separated' polymer composites, the clay minerals (i.e. layered silicate) are dispersed in

polymer matrix without penetration of the polymer between the layered structures of the clay. However, in both intercalated and exfoliated composites, the polymer penetrates between the interlayer spacing of the clay, resulting in increased interfacial area between the polymer and the filler layers. Both of these types lead to the formation of polymer-clay nanocomposites.

Several studies have investigated the physical and chemical performances of different types of polymer-clay nanocomposites showing remarkable improvements in mechanical properties, thermal stability, and corrosion resistance of the nanocomposites in comparison to the microcomposites and pure polymer.[12, 16] Polymer-clay nanocomposites, therefore, find a wide array of applications in the form of structural materials, heat-resistant coatings, gas-barriers, and electronic materials. In recent years, few groups have explored the radiation-resistant properties of polymer nanocomposites.[12-16] Of the different types of clay minerals, montmorillonite (MMT) has been the most commonly used filler in polymers because of their high surface area and surface reactivity. MMT is a hydrous aluminosilicate clay mineral with an Al octahedral sheet sandwiched between two layers of silicon tetrahedron.[65] Each layered sheet is approximately 1 nm thick with the lateral dimensions on the order of 30 nm to several microns. Studies have shown that different types of MMT-based polymer nanocomposites have enhanced resistance towards high-energy radiation such as gamma rays and HZE particles. Zhang et al.[12] investigated the effects of gamma radiation on nanocomposite based on tri-block copolymer styrene–butadiene–styrene (SBS) intercalated into the layers of organophilic MMT (OMMT). They characterized the radiation-induced effects on SBS/OMMT nanocomposite using X-ray diffraction (XRD), DMA, electron spin resonance (ESR) spectra, and gel fraction measurements as a function of dosage. The XRD data showed that under a dosage of 75 kGy, the SBS/OMMT nanocomposite had higher intensity peaks (i.e. increased ordering of structure) than those

irradiated with a dose of 150 kGy. Based on the XRD data, the authors concluded that the SBS/OMMT nanocomposites may have undergone both crosslinking and main-chain scission when exposed to gamma radiation. The DMA results showed that the storage modulus of both pure SBS and SBS/OMMT nanocomposite decreased with increase in dosage for temperatures above the glass transition temperature of one of the major constituent polymeric blocks in SBS – the polybutadiene (PB). However, the decrease in the storage modulus of the nanocomposite was found to be relatively less than that of the pure SBS. The ESR spectra and the gel fraction measurements showed that the nanocomposites formed more free radicals and favored gel-formation, respectively, compared to the pure polymer. Based on all the characterization techniques, the authors concluded that the OMMT layers protected the SBS chains from irradiation through grafting of the broken chains of SBS on the OMMT. A similar study on another type of polymer/clay composite was conducted by the same research group.[13] Zhang and Fang [13] investigated the effects of gamma radiation on the morphology and material properties of two kinds of clay minerals used as filler materials with ethylene-vinyl acetate (EVA) copolymer. In this study, two different kinds of OMMT were prepared through cationic exchange between the sodium-MMT and a clay-modifying agent in an aqueous solution denoted as HOM (prepared through exchange of 12.5 g of Na-MMT and 4.6 g of hexadecyltrimethylammonium bromide) and DHOM (prepared through exchange of 12.5 g of Na-MMT with 5.8 g of 2-methacryloyloxyethylhexadecyldimethyl-ammonium bromide). XRD analysis of the two kinds of nanocomposites, EVA/HOM and EVA/DHOM, showed that the inter-layer spacing and the peak intensities of the EVA/DHOM were greater than those of the EVA/HOM nanocomposite, indicative of good intercalation and ordered structure of the clay layers of DHOM within the EVA matrix. Similar to their previous study, the mechanical and thermal properties of the

EVA/DHOM nanocomposites showed significant radiation resistance compared to the pure EVA polymer.

Tiwari et al.[14] was the first to report the effects of swift heavy ions (SHI) on poly(vinylidene fluoride) (PVDF)/clay nanocomposites. They studied the structural properties, thermal behavior and morphological changes of the pure polymer and the intercalated PVDF/clay nanocomposites before and after exposure to SHI with various ion fluences. From the XRD results, they concluded that the intercalation of the nano-clay (Cloisite 30B [bis(hydroxyethyl)methyl tallow ammonium ion exchanged montmorillonite]) with the PVDF increased with fluence (i.e. the interlayer spacing between the nanoclay layers increased). Moreover, at higher fluencies, the PVDF/clay nanocomposites were able to re-crystallize (marginal degradation) when compared to the pure PVDF, which completely degraded to form a brittle structure. The crystallinity and the heat of fusion of pristine PVDF significantly reduced after SHI irradiation while the nanocomposites showed relatively small changes even at higher fluences. The damage effects on the surface and bulk of the PVDF and the nanocomposites upon SHI irradiation, as quantified with atomic force microscopy through calculation of the pitting dimensions, showed that the degradation was considerably suppressed in nanocomposites making it a suitable high-energy radiation-resistant thermoplastic polymer.

A similar study was conducted by the same group on a different polymer, poly(vinylidene fluoride-*co*-hexafluoropropylene) (HFP) and the same type of nanofiller.[15] The mechanical, thermal and morphological characterization yielded results similar to those of the PVDF nanocomposites. Additionally, they conducted gel-fraction and molecular weight measurements on both pristine and nanocomposites of HFP. The increased gelation and molecular weight of the nanocomposites at higher fluences indicated that exposure to the SHI mainly induced chain

scission in pure HFP whereas crosslinking was the major phenomenon in nanocomposites. Recently, Tiwari et al.[16] developed multifunctional nanocomposites of poly (vinylidene fluoride-cochlorotrifluoroethylene) (CTFE) with 4 and 8 wt% of nano-clay (Cloisite 30B) that showed significant enhancement in toughness, SHI resistance and piezoelectric properties when compared with pristine CTFE. The authors concluded that the increased radiation resistance of the CTFE/clay nanocomposites, in comparison to the pure polymer, was due to the predominance of the crosslinking mechanism through parallel chain conformation of CTFE molecules onto the surface of the layered nano-clay (i.e. recombination of free radicals formed during SHI exposure).

3.1.4 Conclusions

The shielding effectiveness of any material, in addition to its material properties, is also largely dependent on a variety of factors that include the type of radiation, its origin (cosmos, nuclear reactor, laboratories, natural radioactivity, etc), the range of energies involved, exposure time, secondary radiations and other external parameters such as temperature, pressure, etc. Additional factors involved in selecting an effective shielding material include conformability, cost-effectiveness, weight factor, toxicity, durability, etc. In this regard, polymer composites offer numerous advantages over conventional materials. Based on the studies covered in Section 3.1, we can conclude that polymers reinforced with micro- or nano-scale structures have great potential to be used as radiation shielding materials in all the three industries discussed in this review. Moreover, the general trend seems to be towards development of novel, multifunctional polymer nanocomposites exploiting the properties of nano-fillers. It should be noted that the radiation-resistant properties of the nanomaterials under different types of radiation still remain to be fully understood.

In nuclear industry, low Z materials alone are not often successful in attenuating highly penetrative rays such as gamma rays. One of the emerging solutions is the use of a graded shield material that contains heavy atoms impregnated within hydrogen-rich polymer matrix along with other micro- or nano-materials such as boron, metal oxides, graphitic fibers, metal whiskers, etc. Materials consisting of a mixture of different atomic numbers incorporated within hydrogenous polymer-matrix along with some neutron absorbers are especially suited for shielding applications in nuclear reactors. The inelastic scattering by heavy atoms and elastic scattering by hydrogen could effectively block fast and intermediate neutrons, and the neutron absorbers can reduce secondary gamma radiations and thermal neutrons.[31]

A qualitative comparison between polymer composites and conventional material used in aerospace and healthcare industry is provided in Table 3.1. Overall material properties and their shielding effectiveness are indicated as 'low', 'high' or 'equivalent' in comparison with conventional material.

Heavy metal elements (high Z materials) such as lead, tungsten, bismuth, lead oxide or composites of these materials have been traditionally used for protection against X-rays or gamma rays because of their higher mass densities. The use of lead-based aprons in interventional radiological procedures and related applications tend to cause occupational health hazard due to the toxicity and weight factor associated with lead products. Alternatively, polymer-based shielding materials are lightweight, conformable, and they can be designed to include non-lead, high-Z filler materials that provide effective X-ray protection.[66] The size effects (nanoparticles versus microparticles) on X-ray attenuation properties of copper oxide (CuO) embedded in bee wax has been recently reported by Botelho et al.[67] The CuO nanoparticles showed enhanced attenuation characteristics at the low X-ray energies (26 and 30

kV) when compared to the microparticles. The selective enhancement of radiation attenuation by the nanomaterials at the lower energies was attributed to the increased number of *particles per gram* and grain-size effects. Although such investigations need to be extended to other high Z materials in order to fully understand and exploit the unique properties offered by nano-sized materials, such studies offer a basis for further research efforts on non-lead-based polymer nanocomposites for shielding against low-energy diagnostic applications such as mammography.

Table 3.1: A comparison of polymer composite-based shielding materials with conventional material. Reprinted with permission from ([2]). Copyright (2012), American Chemical Society.

Industry	Material type	Standard material	Material properties compared to standard material				Dose Equivalent compared to standard material
			Mass density	Thermal conductivity & Material strength	Toxicity	Conform-ability	
Aero-space	(**i**)Neat polymers (epoxy, polyethylene, polyether-imide, poly-sulfone, PBI) (**ii**) Polymer + micro-/nano-fillers (carbon/graphite fibers, CNTs, BN, HGM, nano-clay)	Al	Low	Low	-	High	Low
			Low	Equivalent	-	High	Low
Health-care	(**i**) Polymer + lead-based fillers (lead oxide, lead particles) (**ii**) Polymer (LDPE, natural rubber, PDMS) + non-lead based fillers (tungsten, tin, bismuth oxide)	Lead	Low	-	Equivalent, or higher for lead oxide composites.	High	Equivalent
			Low	-	Very Low	High	Equivalent

Aluminum has been traditionally used as a structural material in spacecrafts, however, it is heavy when compared to other shielding materials especially polymers. Moreover, Al provides limited shielding effectiveness because of its low electron density and issues related to production of secondary particles.[68] Subsequently, composites of hydrogen-rich polymers with various fillers began to be investigated. Carbon/graphite fibre reinforced plastics (CFRP) is one such composite material that has been widely used as structural materials due to their high stiffness-to-weight ratio, and superior mechanical and thermal properties. However, high-energy particle radiation in space can accelerate the degradation of CFRP materials if additional shielding technique is not applied.[69] The concept of 'self-healing or self-repair' of micro-cracks has been well explored to address the issues of material degradation in polymers including advanced composites such as CFRPs.[44, 70] Among a number of approaches adopted for self-repair or enhance the impact tolerance of polymers, the most studied is the inclusion of micron sized hollow glass fibers or microcapsules filled with healing agent. [47, 57] While investigations into radiation-induced chemical and structural changes on standalone CNT films (both single-walled and multi-walled) have reported severe bending, decrease in diameter and surface oxidation[71], the use of CNTs as filler material in polymeric matrix has been shown to impart significant reinforcement to the pristine polymer and also improve its resistance towards radiation.[11, 36, 60] As discussed in Section 3.1.1.3, the nano-clay filler materials act as free-radical recombination, enhancing the resistance of polymer nanocomposites under high-energy radiation. With the advancements in nanotechnology, the current trend is towards exploiting the properties of nanoscale structures in creating advanced polymer nanocomposites for effective, lightweight, durable radiation-resistant materials.

Chapter 4

Organic Polymer based X-ray and Gamma-ray Dosimetry - Literature Review

In this chapter, a literature review of organic semiconducting polymer-based X-ray and gamma-ray detectors is presented along with a discussion on the underlying mechanism employed by each study. An overview of the current challenges involved in the development of organic polymer-based radiation detectors is summarized in Section 4.3.

4.1 X-ray detectors

Organic semiconductors have been used for both direct and indirect detection of X-rays. In direct detection, the photo-induced charge-carrier generation and their transportation both takes place within the organic semiconductor (i.e. the sensing element) of the detector, while, in indirect detection the organic material mainly acts as a charge transportation layer in the device. In this section we focus on studies associated with direct detection of X-rays.

The first conjugated polymer-based detector for X-rays was developed by Boroumand et al.[53] They used a diode-based approach for direct detection of photocurrent generated by 17 keV. The structures of the X-ray detector were fabricated by dropcasting toluene solutions of conjugated polymers, namely, MEH-PPV or poly(9,9-dioctylfluorenyl-2,7-diyl) (PFO) onto an ITO-coated glass substrate. The polymer solution was dropcasted 8 times to achieve a thick film of 20 microns. A film with thickness in 10s of microns was used to increase the probability of interaction (or attenuation) of X-rays with the polymer. Finally, a 5×5 mm^2 aluminum (Al) cathode (thickness of 100 nm) was thermally evaporated onto the polymer layer using a metal shadow mask. The electrical performance of the Schottky junction for both the MEH-PPV and

PFO thick film devices was investigated for a range of bias voltages: +200 V to −200 V. The MEH-PPV films showed a lower reverse bias current (a stable dark current of 4 nA/cm^2 under electric field- strength of 25 kV/cm), for voltages ranging from 0 to −200V, when compared to the PFO films.

Dynamic and static monitoring of photocurrent from the MEH-PPV sensor, for a given X-ray dose, showed that the detector output (current) remained consistent over time; indicative of the repeatability and reliability of the detector output (Figure 4.1). The relation between dose rate and photocurrent in the PFO device showed a linear trend starting from 3.79 mGy/s to a maximum dose rate of 18.5 mGy/s (Figure 4.2). The sensitivity increased with the external voltage as shown in Figure 4.2.
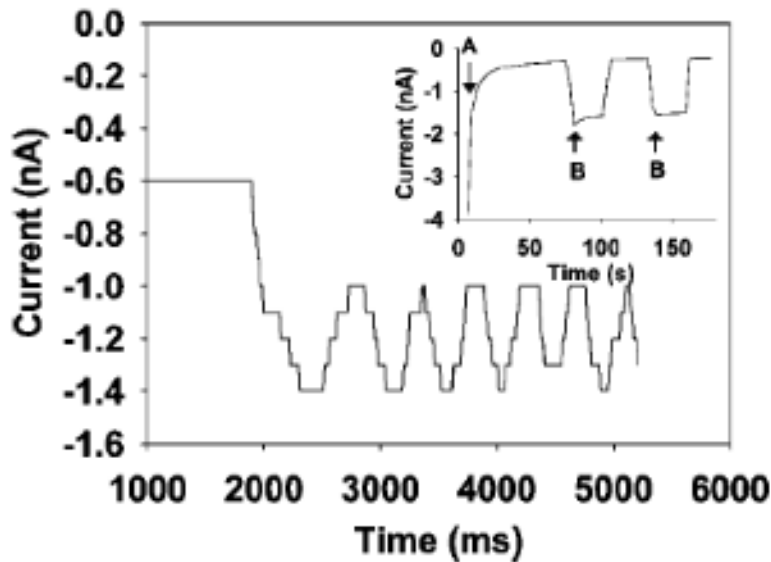
Figure 4.1: Dynamic monitoring of X-ray dose using an MEH-PPV detector. Inset: a static situation where the X-ray source is switched on and off every few seconds. Reprinted with permission from [53], Copyright 2007, AIP Publishing LLC.
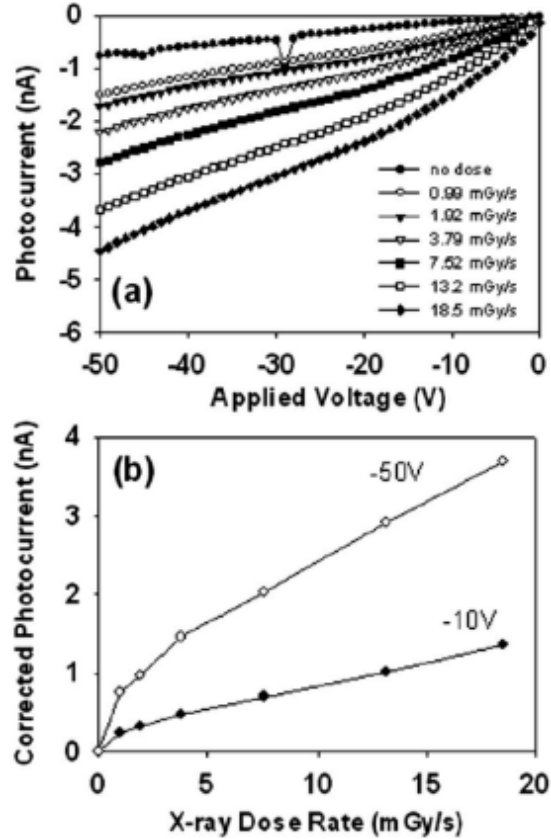
Figure 4.2: X-ray response for PFO device. (a) I-V characteristics for variable X-ray dose rate, and (b) corrected photocurrent of the device from (a) at −10 V and −50 V. Reprinted with permission from [53], Copyright 2007, AIP Publishing LLC.

Intaniwet et al.[54] fabricated poly-(triarylamine) (PTAA)-based X-ray detectors using the diode approach (i.e. polymer sandwiched between ITO and metal contact). The same group reported an extension of their previous work by testing 4 different metal contacts as cathode for the PTAA detector to determine the most suitable one.[55] Of all the 4 metals (aluminum, gold, nickel, palladium), I-V characteristics for PTAA/Al interface showed the minimum leakage current (Figure 4.3a). The leakage current for all PTAA/metal interfaces is dependent on the differences in the Fermi levels of the semiconductor and the contact metal i.e. an ohmic contact (for smaller difference) or a Schottky type contact (for relatively larger difference) may be formed between the HOMO of PTAA and the work function of the metal (Figure 4.3b). If a Schottky contact is

formed then it acts as a hole-injection barrier between the p-type PTAA and the metal contact. The greater the hole-injection barrier, a better diode rectification can be achieved which translates to smaller leakage currents.
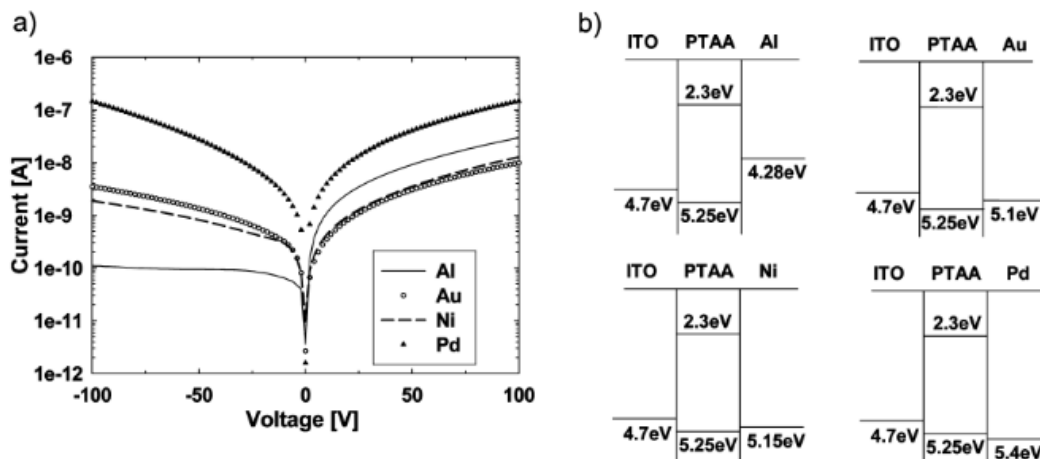
Figure 4.3: (a) Semilog current-voltage characteristics for the ITO/PTAA/metal diodes, with 20 μm thick PTAA layer (b) The corresponding band diagrams for the four ITO/PTAA/metal diodes. Reprinted with permission from ([55]). Copyright (2010) American Chemical Society.

The time-dependent X-ray response of ITO/PTAA/metal (Al, Au or Ni) sensors showed that all the 3 configurations had a fast response to the ON/OFF state of X-rays, and that the Au and Ni contacts had build-up of slow transients during the ON/OFF state (Figure 4.4). High density of X-ray-generated photocarriers causes the build-up of space charge limited currents, the occurrence of which influence the effective Schottky barrier because of band bending at the polymer-metal interface. The PTAA/Al interface, due to the larger effective band gap, showed high resistance to the X-ray induced space charges in comparison with PTAA/Au and PTAA/Ni. A linear relationship between the measured photocurrent and the X-ray dose rate was found for a wide range of bias voltages in ITO/PTAA/Al sensor configuration (Figure 4.5).
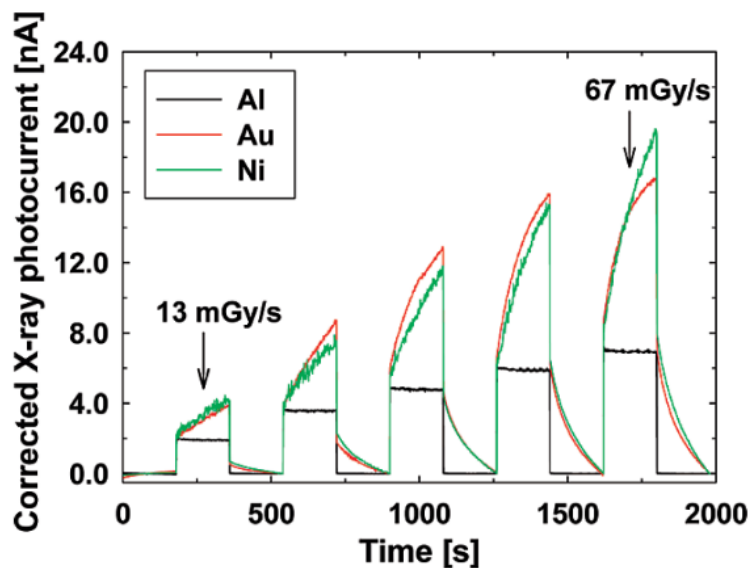
Figure 4.4: X-ray response for the ITO/PTAA/metal sensors, with 20 μm thick PTAA layers, operated at 200 V, exposed to X-rays for 180 s durations through Al, Au, and Ni top contact with dose rates increasing with time (13 to 67 mGy/s). Reprinted with permission from ([55]). Copyright (2010) American Chemical Society.
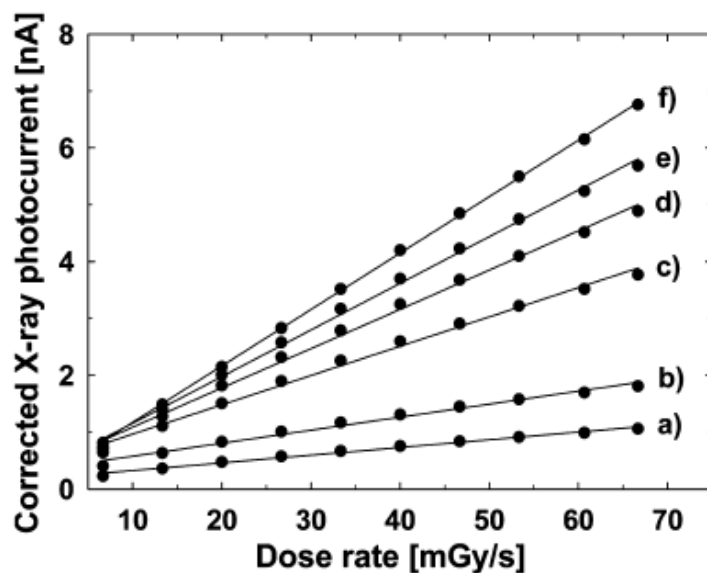
Figure 4.5: X-ray photocurrent as a function of X-ray dose rate for the ITO/PTAA/Al sensor with 30 μm thick PTAA layers. Applied voltages were: (a) 10, (b) 20, (c) 60, (d) 100, (e) 150, and (f) 300 V. Reprinted with permission from ([55]). Copyright (2010) American Chemical Society.

The same group extended their work into PTAA nanocomposite for direct detection of 17.5 keV X-rays.[72] In order to increase the detection sensitivity of the PTAA device, bismuth oxide

(Bi_2O_3) nanoparticles were incorporated into the organic active layer. The introduction of high density nanoparticles having a high Z enhanced the X-ray attenuation characteristics of the device. The reverse bias DC current–voltage characteristics for PTAA–Bi_2O_3 diodes (with ITO and Al contacts) were found to have similar leakage currents to diodes without the nanoparticles (ITO/PTAA/Al). Upon exposure to 17.5 keV X-rays, a PTAA device with 60 wt% Bi_2O_3 nanoparticles showed a sensitivity increase of approximately 2.5 times compared to the pure PTAA device. The authors concluded that the addition of high-Z Bi_2O_3 (Z=83 for Bi) nanoparticles improved the performance of the dosimeters by increasing the X-ray stopping power of the active volume of the diode.

Mills et al.[73] developed flexible X-ray dosimeters using thick films (>1 μm) of the semiconducting polymer poly([9,9-dioctylfluorenyl-2,7-diyl]-co-bithiophene) (F8T2) which was spin-cast over 1.5×1.5 cm^2 Al-coated polyimide substrate, and 50 nm thick gold was thermally evaporated as the top electrode (0.5×0.5 cm^2). A band gap of 2.48 eV was estimated for the polymer from the optical absorption/emission spectra. The diodes when exposed to 17.5 keV X-rays, and operated in reversed bias at -10 and -50 V showed sensitivities of 54 and 158 $nC/mGy/cm^3$ respectively. The authors concluded that a Schottky conduction mechanism occurred in the reverse biased diode, with a barrier to charge injection at the Al electrode. Recently, Mills et al.[74, 75] reported photodetection studies on F8T2 nanocomposites exposed to X-rays in the diagnostic range (17.5 keV) and X-rays in the therapeutic range (6 MV). They reported X-ray induced photocurrents measured in devices with 5 micron thick F8T2 loaded with 30, 42 and 57 wt% of Bi_2O_3 nanoparticles (90-210 nm diameter) and 30 wt% of tantalum (Ta) nanoparticles (<25 nm diameter). The active layer was sandwiched between Al or Au electrodes and ITO-coated substrates; the devices were operated at a reverse bias voltage of -50 V. All

devices (F8T2 with and without nanoparticles) upon exposure to 17.5 keV X-rays showed fairly linear sensitivity to increasing dose rates. The devices with only F8T2 showed the minimum sensitivity compared to those with the high-Z nanoparticles. The devices with the n-type Ta nanoparticles showed higher photocurrents compared to those from the devices with insulator type Bi_2O_3 nanoparticles. Moreover, the devices with Al electrode showed higher photocurrent compared to that from ITO/F8T2+nanoparticles/Au. The authors contributed this to the larger Schottky barrier of the semiconducting polymer with the Al contact which resulted in increased depletion region required for lower dark (or leakage) currents, and subsequently enhanced X-ray sensitivity of the ITO/ F8T2+nanoparticles/Al device. In a similar study but with Linear accelerator X-ray source (6 MV X-rays), Mills et al. developed dosimeters with the same p-type semiconducting organic polymer (F8T2, 10 micron thick film). The devices were fabricated with Al and Au as contact electrodes, and operated at a range of voltages (-50, -100, and -150 V) for 6 MV X-ray measurements. The X-ray response of the F8T2 diode, averaged over a number of X-ray pulses (~30 s at 60 Hz = 1800 pulses), showed fairly linear trend with increase in dose rates from 16.7 to 66.7 mGy/s. The device was found to have X-ray sensitivity of 13.3, 16.6, and 20.4 $C.mGy^{-1}.cm^{-3}$ at a reverse bias voltage of -50, -100 and -150 V respectively.

Recently, Han et al. reported X-ray induced photocurrents measured from SWCNT-based nanocomposite with Au (60 nm) and lithium fluoride (LiF, 5nm)/Al (60 nm) used as contact electrodes.[76] Measurements using 8.06-keV Kα X-rays, generated from a copper target X-ray tube, were performed with and without SWCNTs loaded into the p-type polymer (marketed as "Super Yellow"). Photocurrents of 2.86, 4.46, 10.16 nA were reported for 0, 0.005 and 0.010 wt% loadings of SWCNTs respectively when the devices were operated at -150 V in reverse bias mode. The devices showed fairly linear increase in photocurrent as a function of increasing dose

rate. The device with 0.01 wt% SWCNTs showed the highest sensitivity towards changes in dose rates.

A diode-structure fabricated using a blend of semiconducting organic polymers and organometallic nanostructures with ITO and Al as contact electrodes was reported to show X-ray induced changes in the capacitance of the active layer in the diode.[57] The active layer consisted of blended poly(3-hexylthiophene-2,5-diyl) (P3HT), phenyl-C61-butyric acid methyl ester (PCBM) and the organometallic nanostructure copper(II) 2,2'-bipyridine (Cu(II)BPY). Two types of detectors were developed: PET/ITO/P3HT:PCBM/Al and PET/ITO/P3HT:PCBM:Cu(II)BPY/Al. The devices were exposed to X-rays ranging from 0 to 35 keV, and the impedance spectra for each of the devices was recorded in the frequency range from 20 Hz to 20 kHz and a modulating signal with 50 mV amplitude. The impedance meter measured the alternating current at a fixed modulating signal to deduce the capacitance (C). The capacitance values for the devices, upon irradiation, varied between 3 nF and 15 nF in comparison with those obtained without radiation. It was found that the detectors with P3HT:PCBM:Cu(II)BPY had a dramatic increase of ΔC of about two orders in comparison with those of P3HT:PCBM.

4.2 Gamma-ray detectors

Several different sensing mechanisms (optical shifts in UV-vis characteristics or photocurrent detection using FET) have been adopted in developing organic semiconductor-based gamma ray detectors.[49-52, 56] Silva et al.[49] and Bazani et al.[50] developed optical-based gamma detectors using films and solutions of MEH-PPV (Figures 4.6, 4.7 and 4.8). The underlying mechanism was based on the effects of gamma rays on the UV-vis characteristics of the polymer, MEH-PPV. Effects of radiation on both MEH-PPV thin film and solution from the absorbance peaks were

reported. An increase in the magnitude along with a shift in the maximum peak of absorbance was observed for MEH-PPV solutions as opposed to thin film which showed no such changes upon irradiation. The authors attributed this behaviour to the presence of chlorine atom in the solution to have a larger capture cross-section and to its ability to degrade the MEH-PPV polymer chains by reducing the effective conjugation length which is reflected in the form of optical shifts as observed in Figure 4.6. Increased concentration of MEH-PPV in the solution improved its sensitivity as a gamma sensor, however, for the highest concentration of 0.091 mg/mL the sensitivity dramatically reduced (Figure 4.6). The authors attributed this change of sensitivity to the aggregation of MEH-PPV molecules at higher concentrations, thereby, allowing only fewer molecules to be exposed to the degradation effects induced by the ionized chlorine atoms.
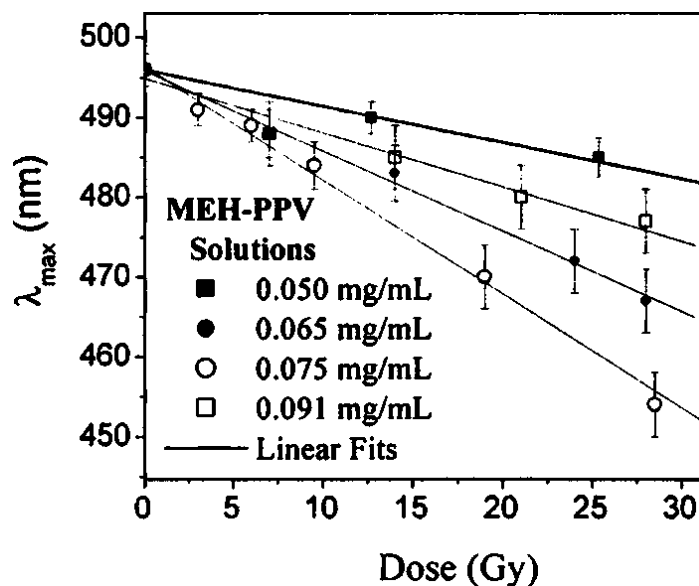
Figure 4.6: Wavelengths of the main peak from the absorbance spectra of the MEH-PPV solutions against applied doses of gamma radiation for different concentrations. Reprinted with permission from [49] Copyright [2005], AIP Publishing LLC.

Bazani et al.[50] showed the effects of gamma radiation on MEH-PPV thin films for higher doses (in kGy) as compared to those reported by Silva et al.[49] Similar to the previous study, the authors attributed the changes in the optical spectrum to the crosslinking effects (by reduction of conjugation length) induced by ionizing gamma radiation (Figures 4.7 and 4.8). They also verified their hypothesis from the Fourier Transform Infrared (FTIR) spectroscopy which revealed no significant degradation by formation of carbonyl defects in the polymer before and after irradiation.
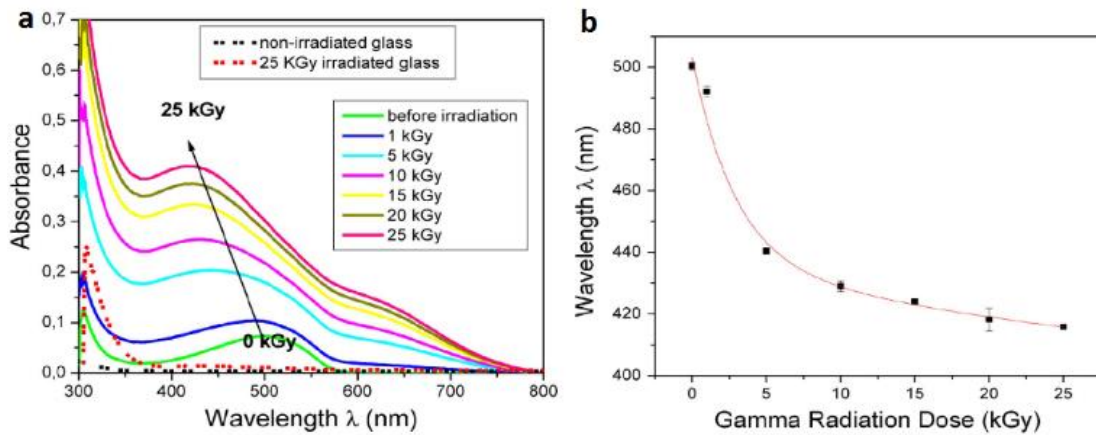
Figure 4.7: Radiation effects on MEH-PPV films: (a) UV-visible absorbance spectra averaged over 3 samples of MEH-PPV thin films of 30 nm thickness, and (b) Wavelength of maximum absorption peak as a function of the gamma radiation dose. © [2009] IEEE. Reprinted, with permission, from [[50]].
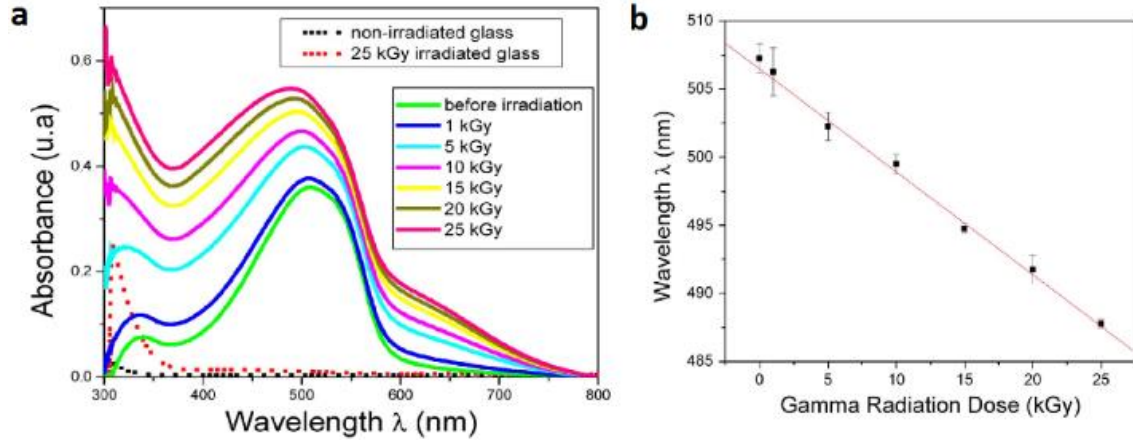
Figure 4.8: Radiation effects on MEH-PPV films: (a) UV-visible absorbance spectra averaged over 3 samples of MEH-PPV thin films of 100 nm thickness, and (b) Wavelength of maximum absorption peak as a function of the gamma radiation dose. © [2009] IEEE. Reprinted, with permission, from [50].

Raval et al.[51, 56] developed OFET-based gamma detector using a solution-processed poly 3-hexylthiophene (P3HT), a p-type organic semiconductor. From the UV-vis spectrum of the P3HT solution, the authors observed an emergence of a peak at a wavelength of 615 nm and the peak amplitude increased with dosage (Figure 4.9). This was attributed to the oxidative effect of ionizing gamma radiation on P3HT molecules indicative of stable polaronic effects. Consequently, the resistance of the material decreased with radiation. In an extension of their work, Raval et al.[56] used a high k material for the gate stack in order to reduce the operating voltage (Figure 4.10a). The magnitude of the drain current (I_{DS}) increased with dose of radiation up to 50 Gy of gamma rays (as observed in the I_{DS}-V_{GS} characteristics of the OFET sensor in Figure 4.10c). The cumulative dose was estimated from the product of I_{OFF} and I_{ON} currents (Figure 4.10d).
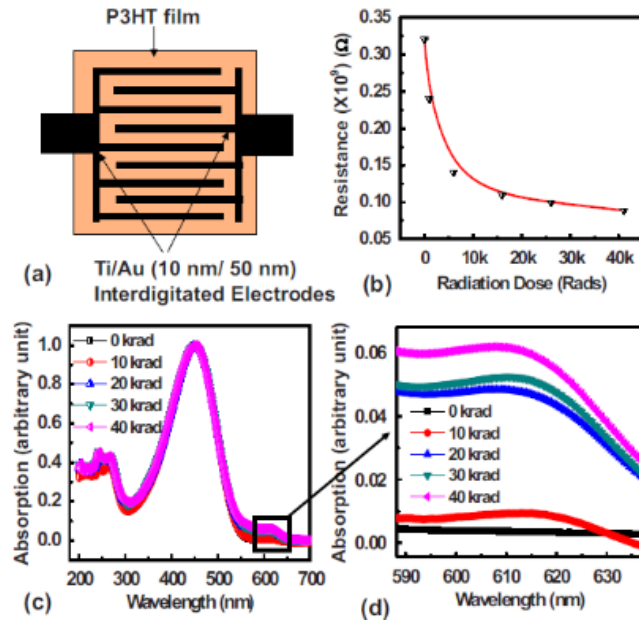
Figure 4.9: (a) Schematic top-view of P3HT-based sensor, (b) Change in the resistivity of the sensor with dose, (c) UV-visible spectrum for the P3HT solution, and (d) The oxidation peak in (c). Copyright [51], AIP Publishing LLC.
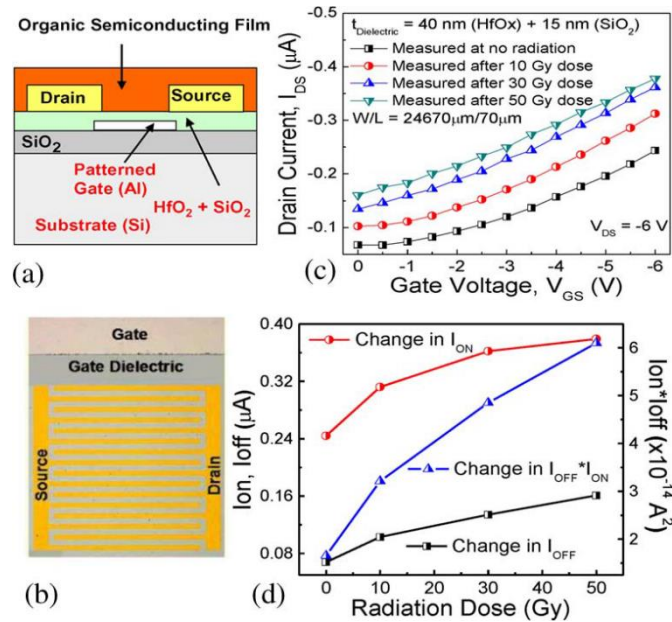
Figure 4.10: (a) Schematic cross section and (b) Top view of the OFET sensor, (c) $I_{DS}-V_{GS}$ characteristics (d) Change in I_{ON} (1.55X) and I_{OFF} (2.37X) with increasing dose of radiation extracted from $I_{DS}-V_{GS}$ characteristics shown in (c).[56]

Another approach of detecting gamma radiation through photoluminescence quenching of conjugated polymer nanocomposite was reported by Zhong et al.[52] The authors developed a ternary composite from poly[9-hexyl-9-(2-ethylhexyl)-fluorene-2,7-diyl] (HEH-PF), bismuth iodide (BiI_3), and oleylamine. The proposed photophysical mechanism for this detector is as follows: before irradiation, oleylamine screens the heavy molecule, BiI_3, and hence prevent photoluminescence quenching of HEH-PF by electron transfer. Upon gamma irradiation, the oleylamine degrades which in turn facilitates efficient electron transfer from exciton on the polymer to the BiI_3. The quenching effect is proportional to the dosage received by the ternary nanocomposite material.

4.3 Summary

Selection of a suitable material is one of the most important factors in the development of an effective sensor. Some of the ideal properties of a material related to its sensing functionality include high sensitivity to radiation dosage, relatively small (in microns) active area for high spatial resolution, and minimal radiation attenuation by the sensing material itself. Most of the organic photocurrent-based dosimeters reported in literature operate at high bias voltages (tens to hundreds of V) which significantly increase the power consumption. Moreover, the smaller photon-capture cross-section of the organic polymers limits the minimum active area (in the lateral direction) of the sensor to 100s of microns or in some cases in 10s of millimetres. One approach to increase the sensitivity and active area is incorporation of inorganic high-Z atoms or molecules containing high-Z elements into the organic semiconducting polymer in order to harvest more photons and hence increase the sensitivity. Since the high-Z composite polymers may significantly attenuate the incident photons and hence the effective dose to be delivered in

applications such as *in-vivo* dose measurements, the relative loadings of the high-Z filler material need to be carefully chosen so as to avoid such deleterious effects.

Other challenges in the field include concerns about batch fabrication and stability issues.[77] Due to involvement of several variables such as the type and quality of polymer (directly impacts material properties), environmental stability and crystallinity of the polymer, solvent (affects printability in solution-based processing), temperature of the substrate (critical in solution-based processing), and/or use of shadow mask for metal contacts of OFETs during the fabrication process of organic photodetectors makes it extremely difficult to establish standard protocols for batch fabrication. Moreover, the ability of conjugated polymers to easily interact with the ambient gases and also to undergo permanent changes upon continuous exposure to ionizing radiation, can significantly impact the shelf-life of the device. However, with the advancements in material science, stable, radiation-hardened, yet highly sensitive materials may improve the integrity and lifetime of organic radiation detectors.

Chapter 5

PDMS/BO Nanocomposite for Shielding against Diagnostic X-rays

5.1 Introduction

High Z materials are capable of attenuating diagnostic X-rays (40 to 150 kV) predominantly through photoelectric effect. For this reason, lead (Z=82) is considered as the most effective material for protection against X-ray exposure. Hence, it is used as structural material in radiological facilities. Lead aprons and other protective garments containing lead are also commonly used by clinical personnel and patients during interventional radiological procedures for protection against direct or scattered X-rays. Protective garments made of high Z materials such as lead, composites of lead or lead-oxide impregnated in polymer matrix,[78, 79] and composites of heavy metals,[80-82] have been developed for protection against X-ray exposure during radiological examinations. However, conventional lead aprons are heavy and cause discomfort to the users, especially during prolonged procedures. Alternatively, polymer composites are lightweight, conformable, cost effective, and can be fabricated to effectively attenuate diagnostic X-rays. Earlier investigations on lead-based polymer composites developed by embedding lead powder into elastomer such as natural rubber showed aging, embrittlement and cracking of the polymer, resulting in drastically shorter lifetime compared to the projected lifetime of 10 years.[83] Moreover, exposure to lead is very hazardous and may lead to several health problems. For example, long term exposure to lead or its salts (e.g., lead oxide, lead acetate, etc.) may result in accumulation of the heavy metal within the body which, in turn, may lead to serious (or fatal depending upon the exposure level) health problems such as neuronal disorders, kidney failure, reduced levels of haemoglobin and red blood cells, etc. Consequently,

efforts to replace the conventional lead-based materials have led to the development of "lead-equivalent" materials which, by definition, have radiation-attenuation characteristics as those of lead of a given thickness (typically 0.25 or 0.5 mm).

The advent of nanotechnology and the subsequent availability of nanomaterials have opened up novel applications in numerous industries. Materials with nanometre dimensions tend to exhibit unique chemical and physical properties relative to the same material with dimensions in microscopic or macroscopic range. Nanomaterials are often used as mechanical reinforcement materials in structural applications, and also as high performance, electromagnetic radiation-resistant materials.[84-87] Few experimental and theoretical studies have proposed the use of polymer nanocomposites (nanomaterials embedded in polymeric matrix) for X-ray and gamma ray shielding applications.[88-90] Nanomaterials have unique properties that make them excellent candidates as fillers in radiation-shielding materials. Recently, some groups have evaluated the radiation resistant properties of the nanocrystalline materials.[20, 41, 91, 92] Owing to the large volume-fraction of grain boundaries, the nanocrystalline materials served as effective sinks for radiation-induced defects. This 'self-healing' behaviour might be particularly useful feature for X-ray protection applications. Currently, the lead aprons used in the radiology departments are required to undergo a mandatory annual test in order to check for the integrity of the material for radiation protection purposes. Furthermore, few studies have reported the size effects (nanoparticles versus microparticles) on X-ray attenuation properties.[67, 93, 94] They have showed that particles in nanometer range had enhanced attenuation characteristics at the low energies (26 and 30 kV) in comparison to those of the microparticles of the same material. The selective enhancement of radiation attenuation by the nanomaterials at the lower energies was attributed to the increased number of *particles per gram*. Therefore, the use of nanomaterials for radiological

protection purposes may have important implications in terms of material durability and effective radiation shielding, all of which can be utilized to replace the toxic lead and lead composites materials.

In this study, the X-ray attenuation characteristics of two different types of nanoparticles (bismuth tungsten oxide and bismuth oxide) were used as filler materials in polydimethylsiloxane (PDMS) and tested against X-rays in the diagnostic energy range (40 to 150 kV).[95] Furthermore, the energy-weighted effective Z of bismuth tungsten oxide and bismuth oxide was calculated using a simulation software called Auto-Zeff that allow fast computation of average atomic numbers and spectrum-weighted mean atomic numbers for any given material.[96] The effective Z of bismuth tungsten oxide and bismuth oxide, for X-ray energies in the range of 10 to 150 keV, was estimated to be in the range of 36.17 to 57.17 and 42.87 to 66.36 respectively. Evidently, the higher effective Z suggested that bismuth oxide would have higher probability of photoelectric interaction with the X-rays in the diagnostic range. Moreover, experimental studies showed that the bismuth-oxide-nanocomposite had relatively better attenuation characteristics and therefore, the bismuth oxide nanoparticles were selected as a filler material for further investigations. Novel, non-lead-based nanocomposite using PDMS and bismuth oxide nanoparticles was studied in detail for shielding against X-ray energies generally employed in interventional radiological procedures and in low-energy diagnostic applications such as mammography.[66] Nanocomposites of polydimethylsiloxane (PDMS) were fabricated with different concentrations of bismuth oxide (denoted as BO) nanoparticles as filler material. The BO-based PDMS nanocomposites are non-toxic (in comparison with the toxicity associated with pure lead), easy to fabricate, cost-effective (~6 times cheaper relative to lead), and they can also be used to coat on uneven surfaces. Attenuation-properties of PDMS-based BO

nanocomposites for both primary beam and scattered X-rays, at tube-voltages ranging from – 40 to 150 kV, are presented in this chapter.

5.2 Materials and Methods

5.2.1 Fabrication

PDMS (Sylgard 184, Dow Corning) is used as the polymeric matrix for embedding filler particles of BO nanopowder (Sigma-Aldrich) with particle size ranging from 90 to 210 nm. Samples with 28.57, 37.73 and 44.44 weight percentage (wt%) of BO in PDMS were prepared such that each sample was approximately 1.3 mm thick. The concentration of the filler material (BO nanopowder) was varied in terms of weight percentage (wt%) which is defined as:

$$\text{Wt\% of BO} = \frac{\text{Weight of BO}}{\text{Weight of PDMS} + \text{Weight of BO}} \times 100$$

For uniform dispersion of the nanopowder, the mixture of PDMS and BO was vortexed for about 15 min. The composite material was then degassed and baked for about 45 min to an hour at 80° C in a vacuum oven. The flexibility of one of the PDMS/BO samples is captured in Figure 5.1. The X-ray attenuation characteristics of the samples were then investigated at X-ray tube-voltages ranging from 40 to 150 kV.
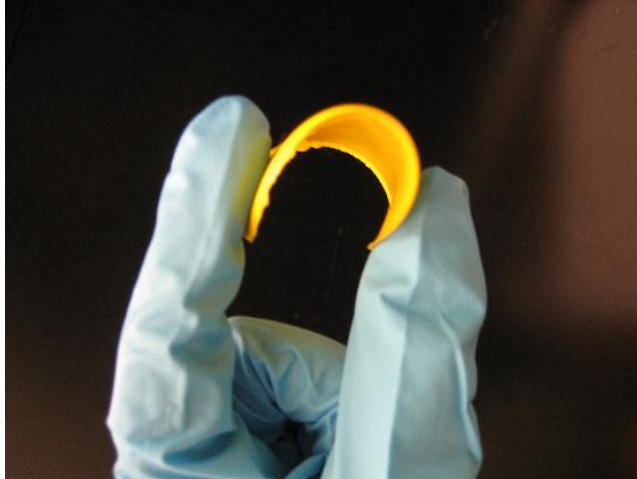
Figure 5.1: Photographic image of PDMS/BO sample.[66]

5.2.2 Characterization

5.2.2.1 Machine characterization

The beam quality of kilovoltage X-rays is usually specified by the first half value layer (HVL) and tube potential (kV_p). Measurements of the HVL of the Ysio diagnostic X-ray machine were determined using technique parameters from 50 to 150 kV_p and 100 mAs in narrow beam geometry. The aluminum attenuators were placed at least 50 cm away from the Farmer chamber (Model: Capintec PR06C, Capintec Inc, Ramsey NJ, USA), and the X-ray collimators (blades) were set at 4 x 4 cm^2 to make a narrow beam measurement. It was ensured that there was no scattering material close to the set-up. The calibration of the 0.6 cc Farmer chamber (Capintec PR06C) together with the electrometer (Capintec 192) is traceable to an accredited National dosimetry laboratory (NRC, Ottawa, Canada). The linearity of mAs and ms with photon intensity were also measured for 3 different tube-voltages: 40, 60 and 81 kV. The tube output as a

function of photon-energy (tube voltage: 40 to 150 kV) was also investigated using mAs=100 and ms=250.

5.2.2.2 Material characterization

The dispersion of the BO nanoparticles in PDMS was characterized using a transmission electron microscope (TEM). The nanocomposites with 37.73 and 44.44 wt% of BO in PDMS were sectioned with a diamond knife on a Reichert Ultracut E ultramicrotome fitted with a cryochamber (model FC 4E, Reichert-Jung, Wien, Austria) at 120°C. The sections were then transferred to 100-mesh Formvar-coated grids. The TEM images of the samples were acquired at 80 kV with a Philips CM10 electron microscope.

5.2.3 Experimental setup

Investigation of the X-ray attenuation by the samples was conducted for both primary and scattered radiation with a diagnostic X-ray machine (Ysio digital diagnostic X-ray machine, Siemens) for tube-voltages ranging from 40 to 150 kV. The milliampere-second (mAs: product of the X-ray tube current (mA) and the beam on time (s)) and the exposure time in millisecond (ms) were 100 mAs and 250 ms respectively. When investigating with the primary X-rays, each sample was placed at a distance of about 20 cm from the X-ray source, and the ion chamber (X-ray detector) was placed at least 50 cm from the floor to avoid backscattered radiation (Figure 5.2a). The field size was maintained at 10 cm x 10 cm. For experiments with scattered X-rays, a lead box was built using a 1 mm thick lead sheet such that it had an opening with dimensions similar to those of the samples (Figure 5.2b). The lead box was used to filter out scattered photons (noise) from the background so as to ensure detection of scattered X-rays originating only from a 10-cm thick solid-water block representing the patient. The lead box was placed

perpendicular with respect to the X-ray source and the solid water block. The 0.6 cc Farmer ion chamber (Model: Capintec PR06C, Capintec Inc, Ramsey NJ, USA) was centred at the opening in the lead box and placed right behind the sample(s). The detector was connected to an electrometer (Capintec 192) which was set to 'medium' mode for the tests with primary X-rays, and to 'low' mode for experiments with scattered X-rays.
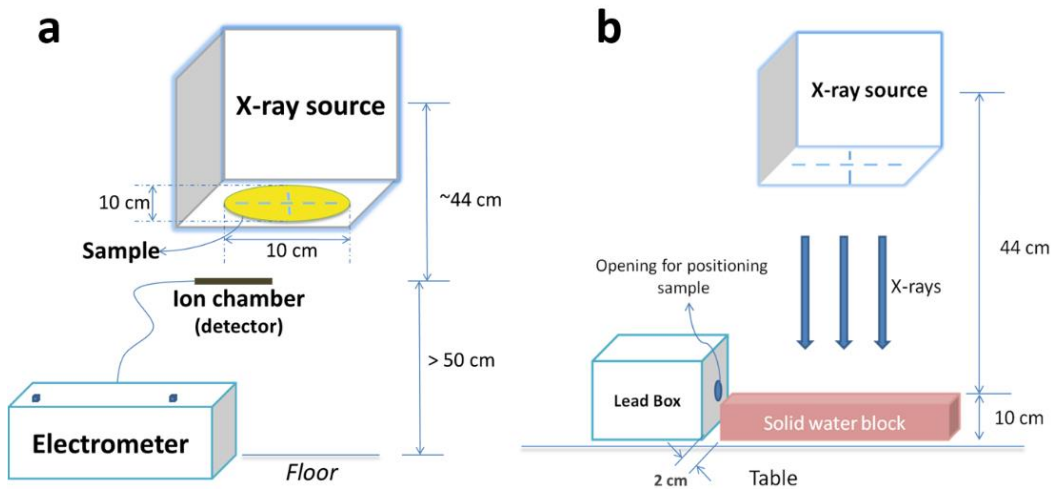
Figure 5.2: Illustration of experimental set-up for (a) primary X-rays, (b) scattered X-rays.[66]

5.2.4 Measurements

All X-ray measurements were taken 'with' and 'without' the samples placed between the X-ray source and the detector. The results were normalized to the electrometer readings obtained without sample between the source and the detector. Percentage attenuation is defined and calculated as follows:

$$\% \text{ attenuation} = \frac{\text{electrometer reading without sample} - \text{electrometer reading with sample}}{\text{electrometer reading without sample}} \times 100$$

The effects of concentration of high-Z material, and material thickness on X-ray attenuation were characterized for all energies of interest (40 to 150 kV). The material thickness was varied by

stacking samples of equal sizes. The measurements were repeated for individual samples to ensure reproducibility of samples for a given concentration.

5.3 Results and Discussion

5.3.1 Machine characterization

The measured half value layers for the Ysio X-ray machine for tube potentials 40 to 150 kV are presented in Table 5.1. Also included in the table is a measured HVL value for 81 kV [20]. The output of the X-ray machine (Ysio, Siemens) showed a linear trend with both mA and ms (Figures 5.3 and 5.4). The electrometer reading as a function of tube potential (40 to 150 kV) is also shown in Figure 5.5.

Table 5.1: First HVL values for tube-voltages 40 to 150 kV produced by Ysio diagnostic X-ray machine.

Tube Voltage (kV)	First HVL (mm)
40	1.25
50	1.8
60	2.35
70	2.6
81	3.1
90	3.425
100	3.75
109	4.2
121	4.6
129	4.9
141	5.275
150	5.55
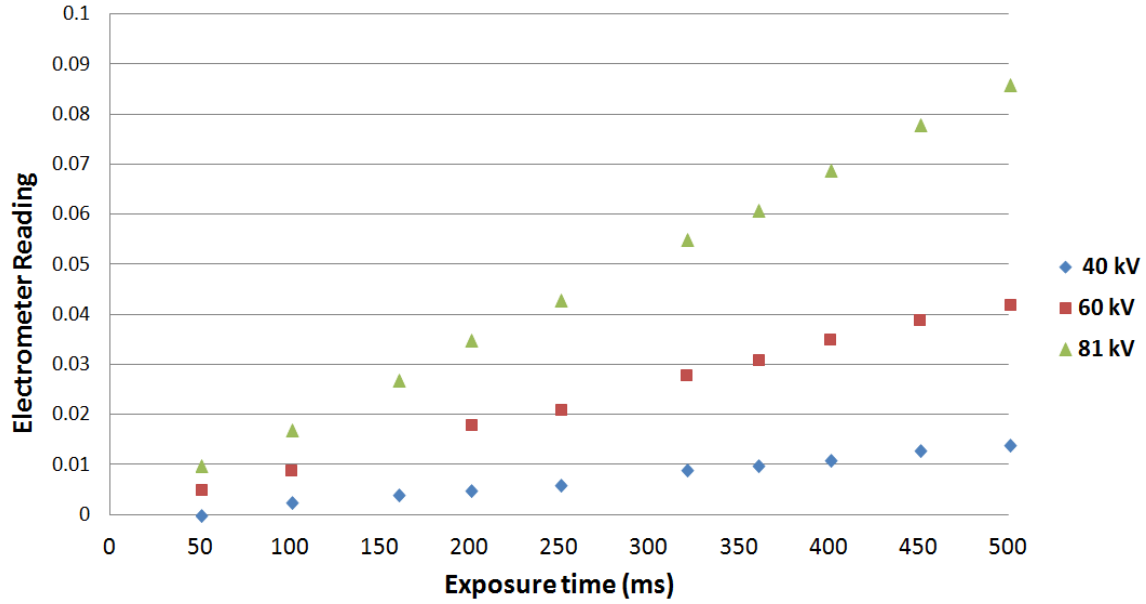
Figure 5.3: X-ray tube-current linearity test with exposure time of 500 ms over a range of 1 to 800 mA for tube potentials – 40, 60 and 81 kV.
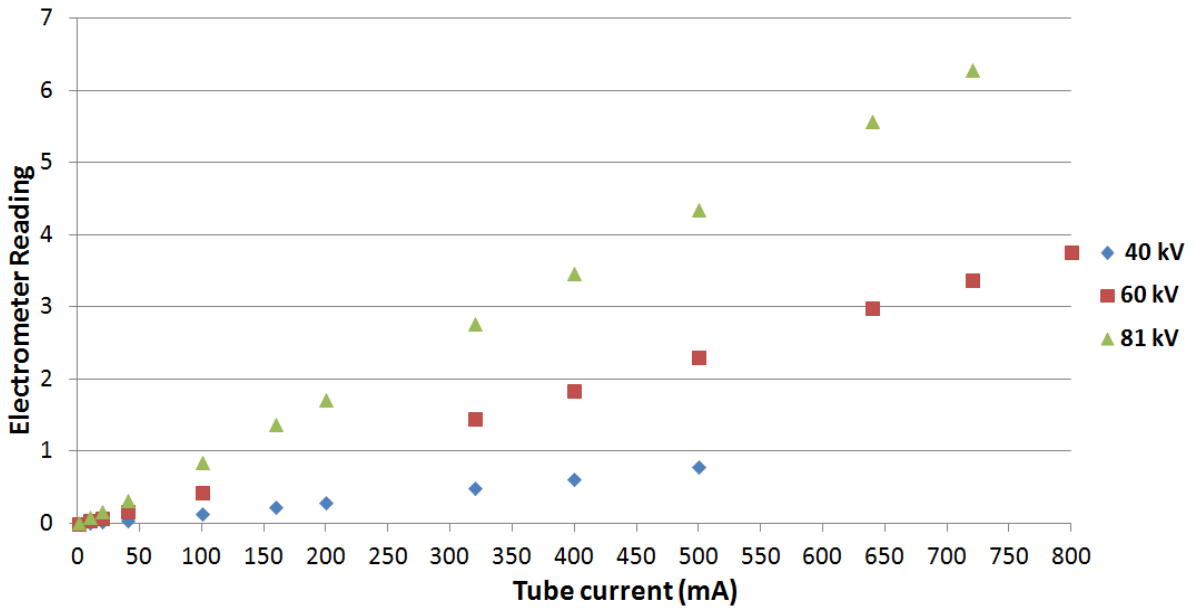
Figure 5.4: Exposure-time linearity test at different tube-potentials (40, 60 and 81 kV) with tube current set to 10 mA.
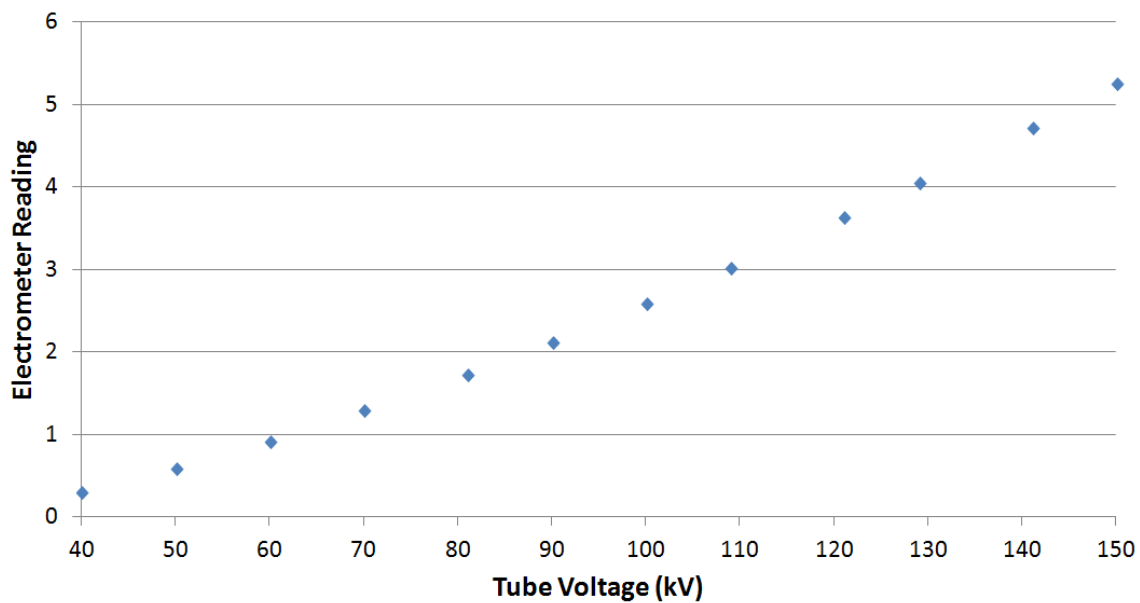
Figure 5.5: Electrometer reading as a function of tube potential (40 to 150 kV) with time-integrated current setting = 100 mAs, and exposure time set to 250 ms.

5.3.2 Material characterization

The TEM images of the samples with 37.73 and 44.44 wt% of BO show spherical morphology of the BO nanoparticles within the size range of 90 to 210 nm (Figure 5.6). The nanoparticles seem to be fairly dispersed within the polymer matrix.
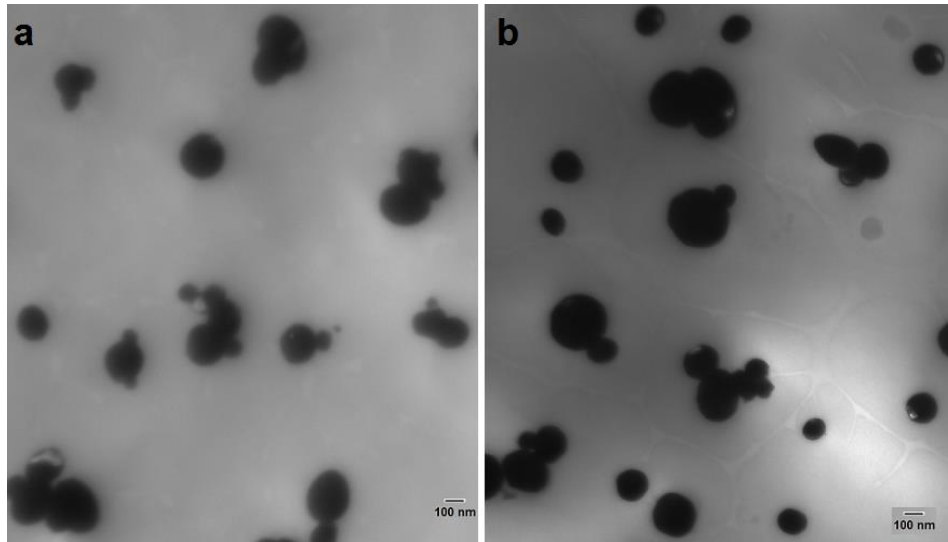
Figure 5.6: TEM images of PDMS/BO nanocomposite with (a) 37.73 wt% and (b) 44.44 wt% of Bi_2O_3 nanoparticles in PDMS.

All the attenuation measurements made with the PDMS/BO nanocomposites indicate that the normalized percentage-attenuation of the X-ray beam decreased with increase in energy for each of the fabricated samples. This is in accordance to the photoelectric interaction between the incident photon and the target material, the attenuation effect decreased with increase in the energy of the incident photons. The effects of the concentration of BO in PDMS, and the sample thickness on X-ray attenuation characteristics are discussed in this section. The attenuation tests (under both primary and scattered X-rays) for individual samples of a given wt% (concentration) and stacked configuration (different thicknesses of samples) were repeated 3 to 4 times and the results were completely reproducible.

5.3.2.1 Effect of concentration of BO in PDMS (under primary X-ray beam)

All samples (of equal thickness) showed an increased attenuation with an increase in the concentration of high Z material (BO). Among all the samples, the nanocomposites with 44.44

wt% of BO (sample: BO 44.44) were the most effective for attenuating the X-ray beam (Figure 5.7).
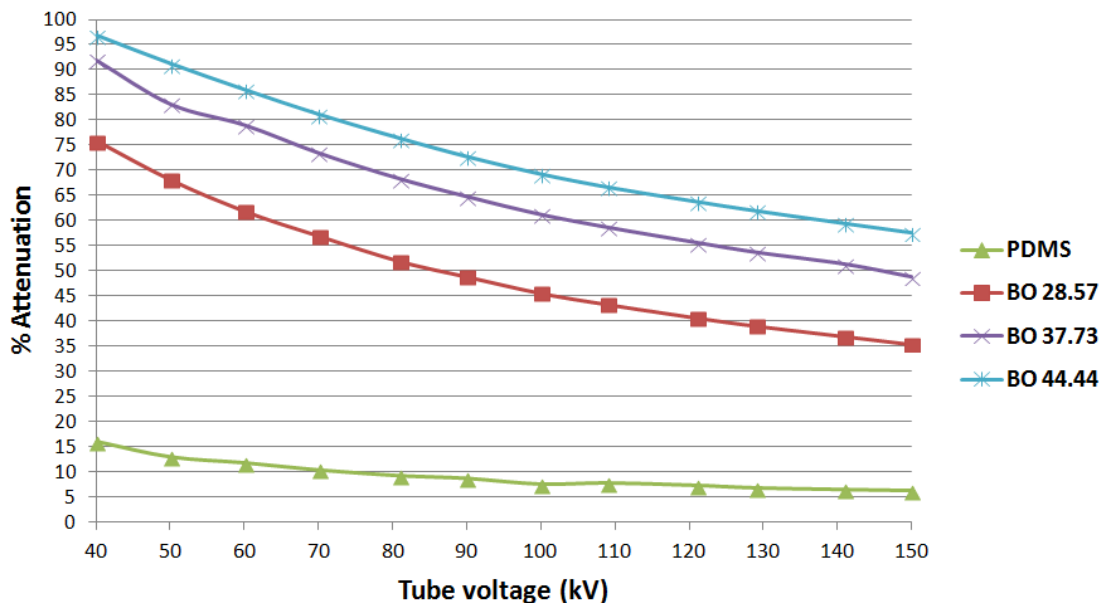
Figure 5.7: Percentage-attenuation of PDMS (control) and PDMS/BO nanocomposites with three different concentrations of BO using primary X-ray beam. The concentration (in terms of wt%) is indicated in the legend.

5.3.2.2 Effect of thickness (under primary and scattered X-rays)

It is a standard practice to indicate a 'lead equivalence value' for a non-lead based X-ray shield. In order to determine the 'lead equivalence' of our nanocomposites, their attenuation characteristics were compared to 0.25 mm pure lead sheet for both primary and scattered X-rays. The attenuation characteristics of PDMS nanocomposites with different thicknesses under primary X-rays are shown in Figures 5.8 and 5.9. The enhanced attenuation by thicker samples of 37.73 and 44.44 wt% of BO in PDMS indicate an increased number of interactions (in the form of absorption or scattering) between the composite material and the X-rays. The percentage attenuation of 'BO 37.73' can be made equivalent to 0.25 mm pure lead sheet for a sample thickness in the range: 4.92 to 6.15 mm (Figure 5.8). Moreover, for a higher wt% composite of

'BO 44.44' the 0.25 mm lead equivalence can be achieved with a 3.73 mm thick 'BO 44.44' (Figure 5.9).
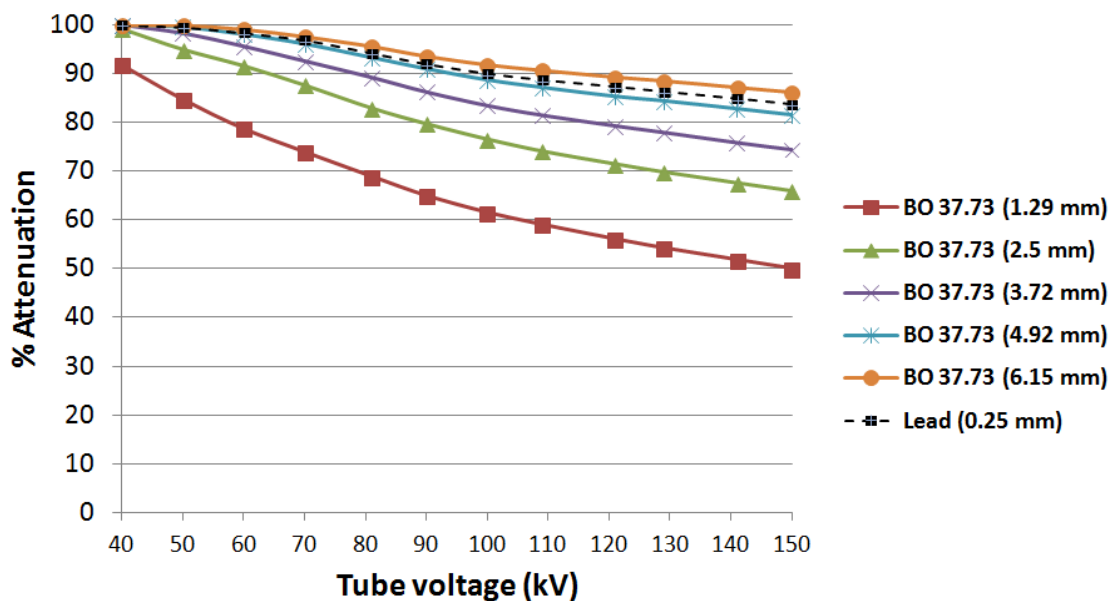
Figure 5.8: Percentage attenuation for different thicknesses (as indicated in the legend) of 'BO 37.73' nanocomposites using primary X-ray beam.
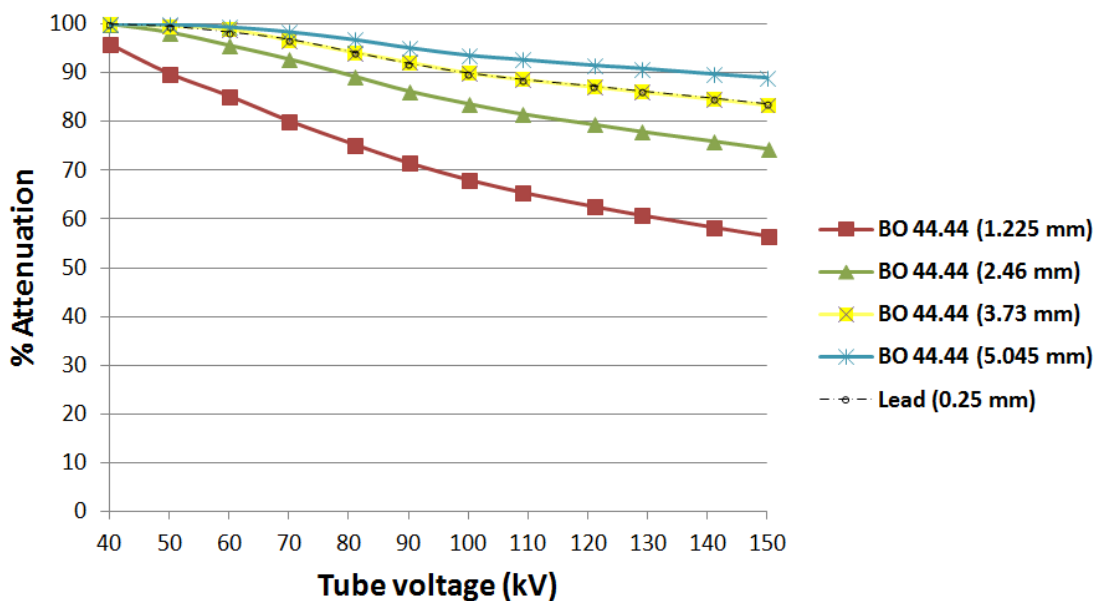
Figure 5.9: Percentage attenuation for different thicknesses (as indicated in the legend) of 'BO 44.44' nanocomposites using primary X-ray beam.

An example of a practical application of X-ray shielding in IVR procedures is the protection of the clinical personnel against X-rays scattered from the patient's body or other objects directly in the path of the primary beam. A 10-cm thick solid-water block, representative of tissue-equivalent material, was placed under the X-ray source to generate scattered X-rays. The percentage attenuation of 'BO 37.73' and 'BO 44.44' nanocomposites exposed to scattered X-rays are shown in Figures 5.10 and 5.11. When compared to the attenuation results under primary X-rays, both 'BO 37.73' and 'BO 44.44' show enhanced attenuation at all energies for a given thickness. This is due to the fact that some of the photons may get absorbed by the water block and only the scattered X-rays actually reach the target material (nanocomposite sample).
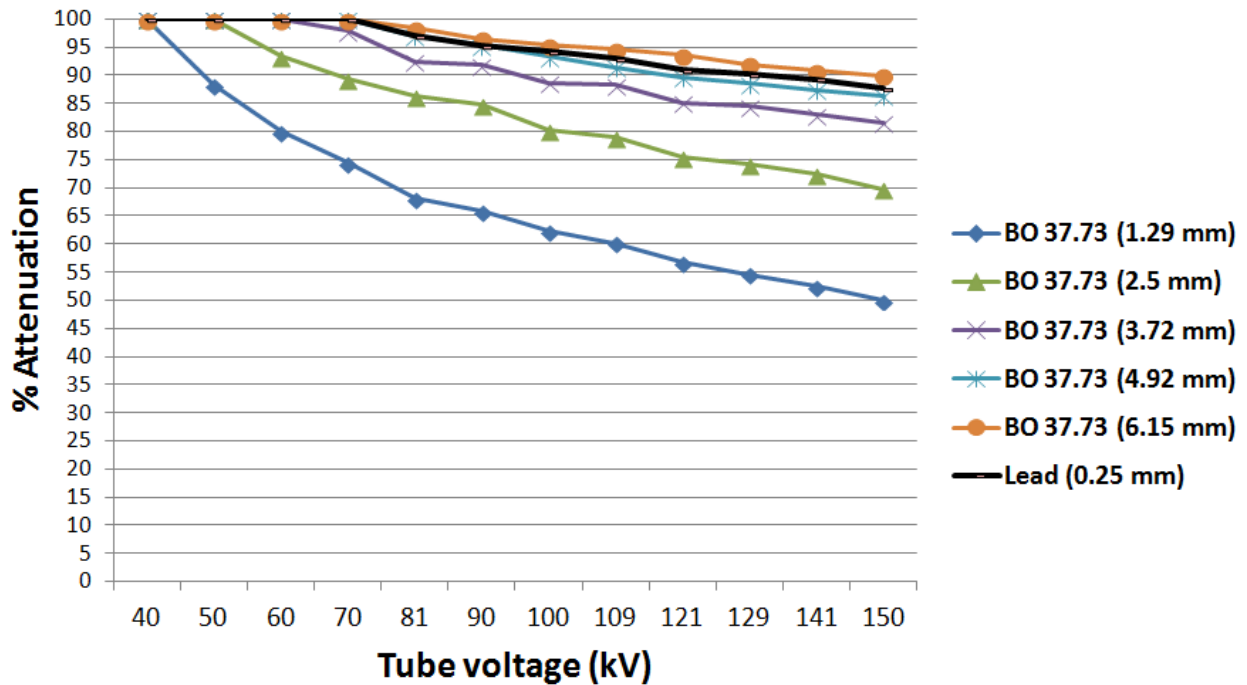
Figure 5.10: Percentage attenuation for different thicknesses (as indicated in the legend) of 'BO 37.73' nanocomposites using scattered X-rays generated at tube potentials ranging from 40-150 kV.
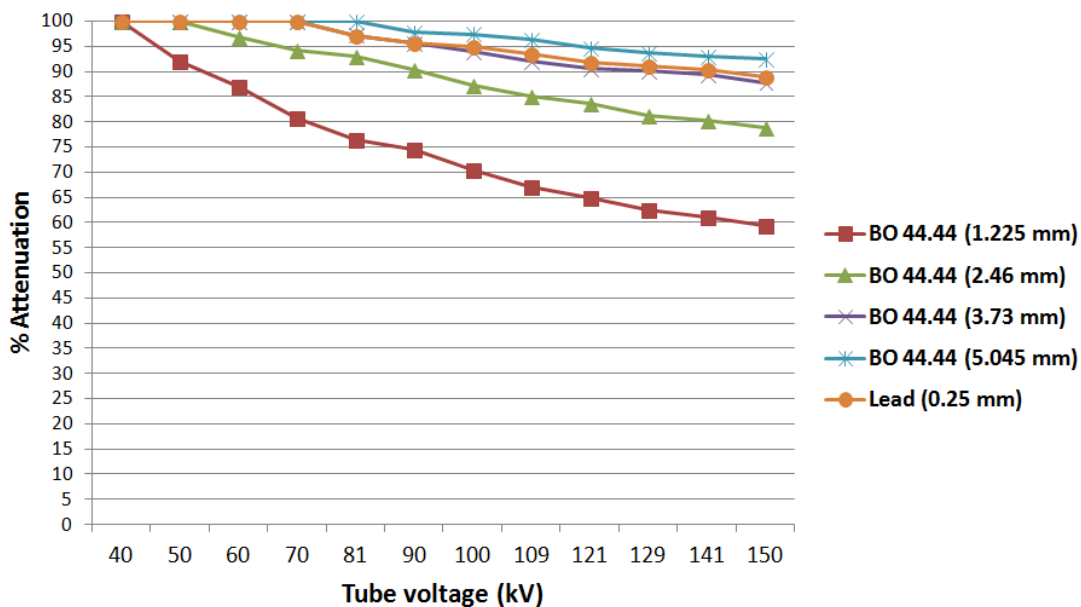
Figure 5.11: Percentage attenuation for different thicknesses (as indicated in the legend) of 'BO 44.44' nanocomposites using scattered X-rays generated at tube potentials ranging from 40-150 kV.

5.4 Conclusions

Novel PDMS nanocomposites were fabricated with different wt% of BO which can potentially be used to attenuate X-rays (primary and phantom-scattered) generated during IVR procedures and hence, can be considered as an alternative to lead-based protective materials. The attenuation characteristics of the polymer nanocomposite showed good repeatability. However, a detailed examination of the radiation-induced damage is essential for long-term usage of PDMS/BO-based radiation shields. Compared to conventional X-ray shielding materials, PDMS nanocomposites are non-toxic, cost-effective, and easy to fabricate (unlike the requirement for industrial-type machineries used for fabrication of most of the commercially available shields). Moreover, 44.44 wt% of BO loadings in PDMS was found to be 0.25 mm lead equivalent at a thickness of 3.73 mm. The percentage-attenuation values reported for the commercially available lead/vinyl-based shields were found to be in the range of 97.5 (0.37 mm lead equivalent) to 98.7% (0.5 mm lead equivalent) for scattered X-rays at 102 kV$_p$ and 80 mAs.[97] In order to

101

achieve the above range of attenuation values, either the wt% of BO or the thickness of the nanocomposites need to be increased.

A 0.25 mm lead-equivalent 'BO 44.44' (3.73 mm thick) nanocomposite weighed twice as much as 0.25 mm pure lead sheet. However, it is important to note that these nanocomposites can be coated or painted and can conform to practically any shape of interest. This feature opens up a range of applications for PDMS/BO nanocomposites; particularly those in which the weight of the protective material is not a significant concern. For example, the lead-based gonad protection worn by patients may be replaced, or conformable thyroid-shielding during mammography can be offered by the PDMS/BO nanocomposites. Moreover, PDMS composites dry off (polymerizes) at room temperature as well and hence, the extra cost and effort of using any additional equipment to dry/shape the material can be avoided. In conclusion, the material-characteristics of the PDMS/BO radio-protective nanocomposite allow it to be used as a filler-material in the walls (bunkers) of radiation treatment facilities, as a protective-coating on electronic devices, and also as protective shields conformable to specific anatomies of patients undergoing radiological procedures.

Chapter 6

Effects of Particle Size on X-ray Transmission Characteristics of PDMS/Ag Nano- and Micro-composites

6.1 Introduction

In recent years, there has been much interest in the radiation-induced effects in nanomaterials; particularly the studies based on ionizing radiations have revealed their potential use in radiological applications as contrast agents in X-ray imaging, radio-sensitizers for localized dose enhancement during radiotherapy, and as filler material in radiation protection garments or structural units.

For protection against diagnostic X-rays, there is an increasing demand for lead-free polymer-based materials. In this regard, polymers loaded with high Z, non-lead particles may be used as alternatives for conventional lead-based materials. Polymers reinforced with nanoparticles have been reported to have enhanced not only the mechanical, electrical and/or thermal material properties but also improved resistance to the degradation effects under ionizing radiation[2]. However, the choice of the optimum particle size for the high Z filler material is not yet well studied in terms of its role in effective attenuation of the desired range of X-ray energies.

A few research groups have compared the X-ray transmission properties of nano- and micro-particles using different loadings of the particles in a polymer matrix for X-ray energies in the diagnostic range.[67, 93, 94] Botelho et al. (2011) reported the particle size effects on X-ray transmission properties of 5 wt% copper oxide (CuO) particles embedded in bee wax for a range of thicknesses (expressed in terms of 'mass per unit area').[67] The CuO nanoparticles (13.4 nm) showed enhanced attenuation characteristics (at least 14% lower transmission over the entire

range of 'mass per unit area') at low X-ray tube voltages (26 and 30 kV) when compared to those of the microparticles (56 μm), however, the transmission characteristics at higher tube voltages (60 and 102 kV) for both the particle sizes were similar. The selective enhancement of radiation attenuation by the nanomaterials at the lower energies was attributed to the increased number of *particles per gram*. The authors suggested that the probability of photoelectric absorption, proportional to Z^3/E^3, dominated at the lower energies and hence, the increased number of particles of nano-sized material compared to the micron-sized material may result in a higher probability for a low energy X-ray photon to interact and to be absorbed in nanostructured composite than for the microstructured composite. In contrast, at higher energies, X-ray scattering phenomenon, weakly dependent on Z and E, would be dominant and hence, produce similar transmission results for both nano- and micro-sized CuO particles.

Künzel and Okuno (2012)[93] further investigated the transmission characteristics of CuO particles in epoxy resin at different loadings (5, 10 and 30 wt%). The authors found similar enhancement effects of attenuation as those reported by Botelho et al. Moreover, they reported improved X-ray absorption in the range of 16% to 33% at varied thicknesses (3 to 10.3 mm), under 25 kV X-rays, for 30 wt% CuO nanocomposites. Noor Azman et al. (2012) reported the effects of particle size, filler loadings (5, 10, 20, 30 and 35 wt%) and X-ray tube potentials on the X-ray transmission in tungsten-oxide/epoxy composites using the mammography unit (25 to 49 kV) and a general radiography unit (40 to 120 kV). Results indicated that the 5 and 10 wt% nano-sized tungsten oxide had better attenuation under X-rays generated by lower tube voltages (25–35 kV) when compared to micro-sized tungsten oxide. The ratio of the X-ray transmission for micro-sized tungsten-oxide/epoxy composite to that for nano-sized tungsten-oxide/epoxy composite was in the range 1.3–3.0 for X-rays generated using the mammographic unit operated at tube potentials

of 25–49 kV. However, there was only negligible X-ray transmission was at the higher X-ray tube voltages (40–120 kV).

In this study, the particle size effects on X-ray transmission at relatively low loadings of silver nano- and micro-sized particles in PDMS has been investigated for a wide range of X-ray voltages (20, 23, 26, 30, 40, 60, and 80 kV).[98] In continuation with the X-ray attenuation capability of PDMS/BO nanocomposite, the investigation of the particle size effects for BO nano- and micro-particles would have been the ideal choice. However, the non-availability of BO particles within the 100 nm range led to the selection of nano- and micron-sized silver particles for comparative study of the role of particle size in X-ray transmission studies. Furthermore, the average energy-weighted, effective Z of BO for the diagnostic X-ray energies is similar to the Z of silver. Energy-weighted effective Z is a range of Z values corresponding to discrete X-ray energies of interest; in this context, the range of energies would be from ~10 to ~30 keV. X-ray transmission properties of both nano- and micro-particles of silver loaded in PDMS were studied for wide range of 'mass per unit area' for each of the three different concentrations. X-ray scatter characteristics of the composites were also measured for all the three different concentrations of particle loading over four different tube potentials (26, 40, 60 and 80 kV). Furthermore, the absorption and scattering characteristics of the composites were studied using thermoluminescent dosimeters.

6.2 Materials and Methods

6.2.1 Materials

Silver (Ag) particles of two different sizes were used as filler material in the fabrication of polymer composites. Ag nanoparticles of average diameter, 20 nm, were purchased from US

Research Nanomaterials, Inc. Ag micro-powder with an average diameter <45 um were purchased from Sigma Aldrich Inc. Polydimethylsiloxane (PDMS, Sylgard 184), purchased from Dow Corning, was used as the polymer matrix.

6.2.1.1 Field Emission Scanning Electron Microscopy

Field Emission Scanning Electron Microscope (FESEM), commonly used to visualize the morphology and particle size distribution at ultra-high magnification (in microns or nanoscale range), was used to verify the characteristics of both nano- and micro-particles of Ag (Figures 6.1 and 6.2). Ag particles of different sizes (average particle size specified by the supplier 20 nm and 45 um) were separately dispersed in ethanol followed by agitation in an ultrasonic water-bath for few minutes to minimize any aggregates. Few μL from each of the Ag-dispersions was individually dropcasted on a piece of aluminum-coated silicon wafer and dried at room temperature. Each of the wafer pieces were then fixed on a FESEM stub using double-sided carbon tape. The stubs were then loaded into the microscope holder, and imaged using FESEM (Zeiss LEO 1550).
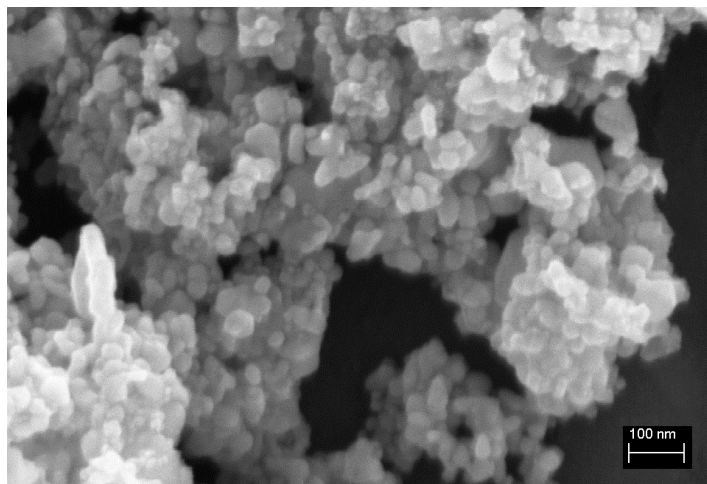
Figure 6.1: FESEM image of as-supplied Ag nanoparticles.
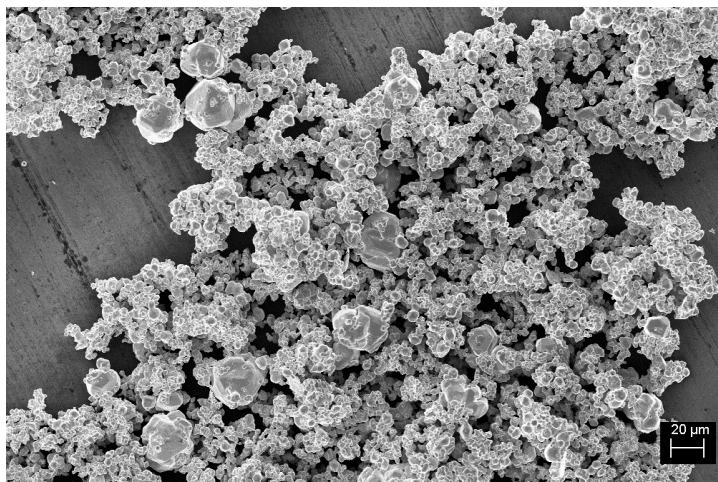
Figure 6.2: FESEM of as-supplied Ag microparticles.

6.2.2 Sample preparation

The following procedure was used to fabricate different wt% of Ag nano- and micro-particles in PDMS (denoted as Ag-nano and Ag-micro respectively): (**i**) 0.138, 0.771, 1.602 g of Ag particles (both nano and micro) were dispersed in 27.5 g of PDMS (pre-polymer + curing agent) to get 0.5, 2.73, and 5.5 wt% of PDMS/Ag composite respectively. (**ii**) Each of the composite was mechanically mixed and vortexed for about 15 min. (**iii**) 4.4 g of the composite was then moulded into a 60x15 mm plastic Petri dish by degassing and curing the samples at 60° C in a vacuum oven. For each of the three different wt% of both Ag-nano and Ag-micro, a total of five samples (each weighing 4.4 g), was prepared. Each of the 4.4 g of PDMS/Ag composite was calculated to have a 'mass per unit area' of 0.2112 g/cm^2.

6.2.3 X-ray transmission setup

Investigation of the X-ray transmission characteristics of the fabricated samples was conducted for both primary and scattered radiation with a Superficial X-ray system (Gulmay Medicals Inc.).

The X-ray transmission characteristics of the samples, for primary beam, were measured at seven tube potentials 20, 23, 26, 30, 40, 60 and 80 kV. The tube current for X-rays in the mammographic range (20 to 30 kV) was set to 20 mA, while 40 and 60 kV were set to 2 mA and 80 kV was set to 1 mA. For scattered (forward & backward) X-rays, tube-potentials of 26, 40, 60 and 80 kV were used. No external filters were used in this study. A cone, of diameter 4 cm, mounted onto the X-ray source was used to define the X-ray field size for all measurements. The transmission characteristics of the samples were recorded using a 0.6 cc Farmer ion chamber (Model: Capintec PR06C, Capintec Inc, Ramsey NJ, USA), centred at the cone opening and placed about 15 cm from it. The detector was connected to an electrometer (Capintec 192) which was set to 'low' (maximum display up to 3 decimal places) or 'medium' (maximum of 2 decimal places) mode with measurement error in the range of ±0.002. The experimental setup is shown in Figure 6.3. The X-ray transmission tests for the forward scatter were conducted with the detector (ion chamber) placed about 1 cm above and away from the periphery of the sample at 45˚ from the edge of the sample (Figure 6.4). For backscatter experiments, the sample was centered on a 1 mm thick lead sheet with a hole of diameter 4 cm and the detector was placed about 2 cm above the lead sheet, about 3 cm away from the centre of the lead sheet (Figure 6.5). The forward scatter setup was such that no primary photons reach the detector but only the photons scattered from the sample in the forward direction were measured. Similarly, the backward scatter setup was such that the detector explicitly measured the scattered photons from the sample but in the backward direction (i.e. on the same side as the source).
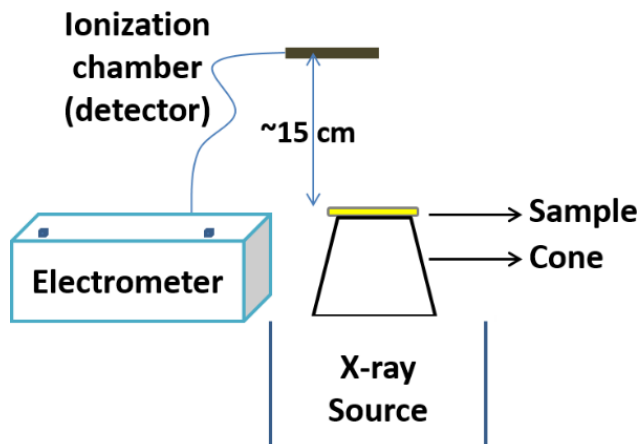
Figure 6.3: Illustration of experimental setup for X-ray transmission studies.
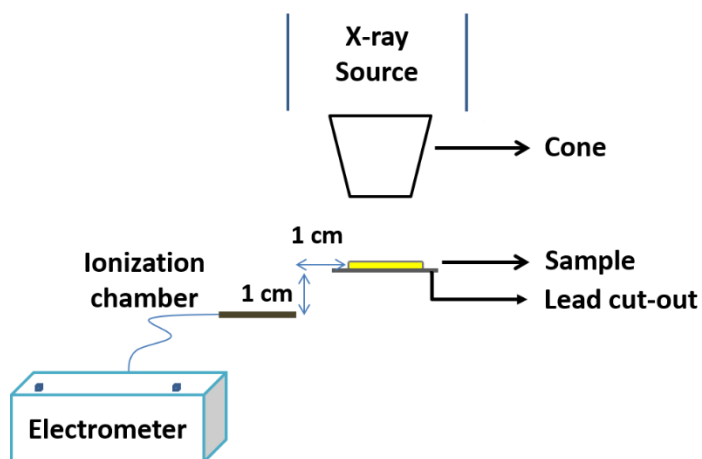
Figure 6.4: Illustration of setup for forward scatter experiments.
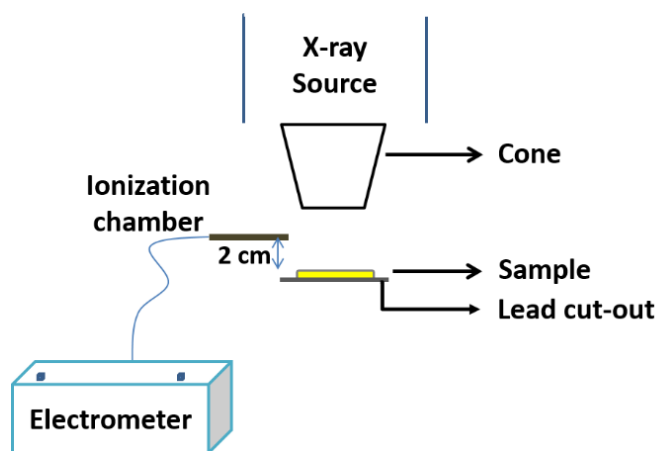
Figure 6.5: Illustration of setup for backward scatter experiments.

6.2.4 X-ray measurements using thermoluminescent dosimeter

Thermoluminescent Dosimeter (TLD) was used to investigate the X-ray attenuation characteristics (comprises of absorption and/or scatter) of Ag-nano and Ag-micro samples. The TLD crystals, exposed to X-rays, store the absorbed X-ray energy and convert it into photons in the visible range when heat is applied. The measurement system consists of: (i) TLD elements for X-ray absorption, and (ii) TLD reader (Harshaw TLD model 5500).

6.2.5 Measurement procedure

The measurements were categorized into two sets based on the applied tube potential: (i) X-rays in the mammographic range (20 to 30 kV), and (ii) X-rays in the higher diagnostic range (40 to 80 kV). An exposure time of 0.3 min was used for all measurements.

6.2.5.1 X-ray transmission characteristics

The effects of particle size on X-ray transmission, as a function of increasing 'mass per unit area' of the sample, was tested by recording transmission of the sample(s) of same physical dimensions stacked up on each other such that the total 'mass per unit area' was increased in steps of 0.2112 g/cm^2 to a maximum of 1.056 g/cm^2 for each of the measurements. This procedure was repeated for all three concentrations (wt%) of PDMS/Ag samples for each of the seven tube potentials (20, 23, 26, 30, 40, 60 and 80 kV). All measurements were repeated at least 2-3 times. The measurements corresponding to the X-ray transmission characteristics of Ag nano- and micro-particles has been denoted as Nano_Tr and Micro_Tr respectively. The ratio of Nano_Tr to Micro_Tr was used as a parameter for comparing the particle size effects on X-ray transmission properties as a function of increasing 'mass per unit area' (in g/cm^2) or concentration (in wt%) for a given 'mass per unit area'. Therefore, at any given 'mass per unit

area' or concentration, a ratio less than unity would indicate that the X-ray transmission properties of the Ag nanoparticles were lower than those of the Ag microparticles and vice-versa for a transmission ratio greater than unity.

6.2.5.2 Investigation of X-ray scatter characteristics

A constant 'mass per unit area' (0.2112 g/cm^2) for nano- and micro-composites was used for all measurements with scattered X-rays. Both forward and backward scatter was measured for all three concentrations of Ag particles in PDMS. Similar to the comparative analysis presented in Section 6.2.5.1, ratios of the forward and backward scatter measurements for a given 'mass per unit area', denoted as 'Nano_Fw/Micro_Fw' and 'Nano_Bk/Micro_Bk' respectively were used to compare the particle concentration effects at four different tube potentials (26, 40, 60 and 80 kV).

6.2.5.3 X-ray attenuation characteristics using thermoluminescent dosimeter

Thermoluminescent dosimeters (TLD-100), lithium fluoride crystals doped with magnesium and titanium, were sandwiched between two sheets of nano-composites (or micro-composites) and exposed to 26 kV (20 mA) X-rays for 0.5 min. Two sets (each set of 3 dosimeters) of TLD-100 were used for each type of composite. In order to account for measurement errors of individual TLDs, the two sets of TLDs used for nano-composites were also used for micro-composites and vice-versa. Two TLDs were kept in the X-ray console room to measure the background radiation. All the TLDs were then carefully placed into a TLD-disk-holder and then inserted into the TLD reader. A software (WinREMS) was used to activate the reader and collect the TLD data (i.e. the charges absorbed by the TLDs). The TLDs were then annealed for 6 hours in an oven (TLDO Annealing Oven, PTW Frieburg) to release the trapped charges. For each set, the

TLD experiments were performed 2-3 times. The readings for each TLD were averaged and the results >3 times the standard deviation were considered. The percentage attenuation of Ag-nano with respect to Ag-micro was determined using the following equation:

$$\% \text{ attenuation} = \frac{\text{TLD reading from Ag\_micro} - \text{TLD reading from Ag\_nano}}{\text{TLD reading from Ag\_micro}} \times 100$$

6.3 Results and Discussion

6.3.1 X-ray transmission characteristics

The ratio of the electrometer reading for Ag-nano to that for Ag-micro was estimated for each of the three particle concentrations and five different 'mass per unit area' considered in this study. In this way, the X-ray transmission characteristics of the Ag nanoparticles could directly be compared with those of the microparticles, eliminating any effects due to the polymer matrix.

6.3.1.1 Effects of particle concentration

The effects of particle concentration (wt% loaded in PDMS matrix) on the relative X-ray transmission of Ag-nano versus Ag-micro were plotted for a constant 'mass per unit area' of 0.2112 g/cm^2. For all the tube potentials in the mammographic range (20 to 30 kV), the X-ray transmission characteristics of Ag-nano decreased significantly with increase in concentration when compared with those of Ag-micro (Figure 6.6a). X-ray transmission properties at higher tube potentials, however, did not show the trend observed for lower kV (Figure 6.6b). In summary, higher concentrations of Ag nanoparticles was found to have enhanced X-ray attenuation properties with respect to Ag microparticles (up to 9% more attenuation, i.e. less transmission reaching the detector) especially at the lowest tube potential (20 kV) considered in this study. Furthermore, it was evident that for all concentrations, the Ag-nano showed an overall

trend of incremental improvement in the attenuation characteristics for the highest to the lowest

tube potentials (i.e. from 80 to 20 kV). These findings are in agreement with the ones reported in

literature.[67, 93, 94] At X-ray energies in the mammographic range (Figure 6.6a), the particle size

effects (i.e. differences in the X-ray transmission properties of a given material due to differences

in unit particle size) increased with particle concentration which may be due to the higher

probability of photoelectric absorption of the incident low-energy photons to interact with the

more number of *particles per gram* in the nanocomposite compared to those of microcomposite.

However, at higher X-ray energies, the relative probability of photoelectric absorption decreases

and therefore, the particle size effects are not as prominent as observed in the lower energy range

(Figure 6.6b).
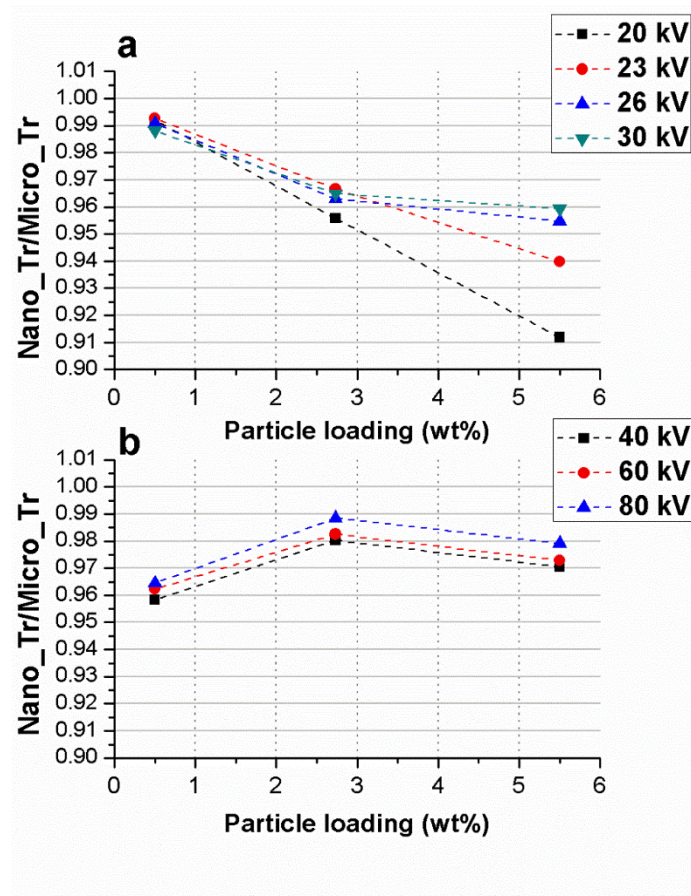
Figure 6.6: X-ray transmission ratio of Ag-nano to Ag-micro as a function of increasing concentrations of Ag particles (0.5, 2.73, and 5.5 wt%) at (a) 20, 23, 26 and 30 kV, and (b) 40, 60 and 80 kV.

6.3.1.2 Effects of 'mass per unit area'

6.3.1.2.1 X-rays in the mammographic energy range

Figures 6.7a to 6.7c show the ratio of the exit dose reading of the Ag-nano to that of the Ag-micro for each of the three concentrations (0.5, 2.73 and 5.5 wt% of Ag loading in PDMS) as a function of increasing 'mass per unit area' for X-rays in the mammographic range (i.e. X-ray tube-potentials of 20, 23, 26 and 30 kV). For all three different concentrations and 'mass per unit area', the Ag nanoparticles showed better overall attenuation (i.e. lower transmission) compared to the Ag microparticles, especially under 20 kV X-rays. For 0.5 wt% of Ag composites, the overall percentage attenuation of Ag nanoparticles at 20 kV was found to be ~2-3% higher than that of the microparticles but fairly negligible improvement of about ≤ 1% at other tube potentials. At the lowest tube-potential (20 kV), the attenuation factor increases to a maximum of 3% for 0.8448 g/cm^2 and decreases to <2% for 1.056 g/cm^2 (Figure 6.7a). When the wt% was increased about 5 times (2.73 wt%), the overall trend for the nanoparticles showed an increase in the attenuation factor: 4 to 6% (Figure 6.7b). At Ag concentrations of 0.5 and 2.73 wt%, the particle size effects (ratios of Nano_Tr to Micro_Tr) were found to be fairly the same for the range of 'mass per unit area' considered in this study. When the concentration of Ag particles was increased 11 times the lowest concentration (5.5 wt%), a maximum of 9% attenuation was observed at the minimum 'mass per unit area' at 20 kV with a dramatic decrease followed by a plateau for the rest of the 'mass per unit area' (Figure 6.7c). The overall trend also seems to be similar but lower than that observed at 20 kV.
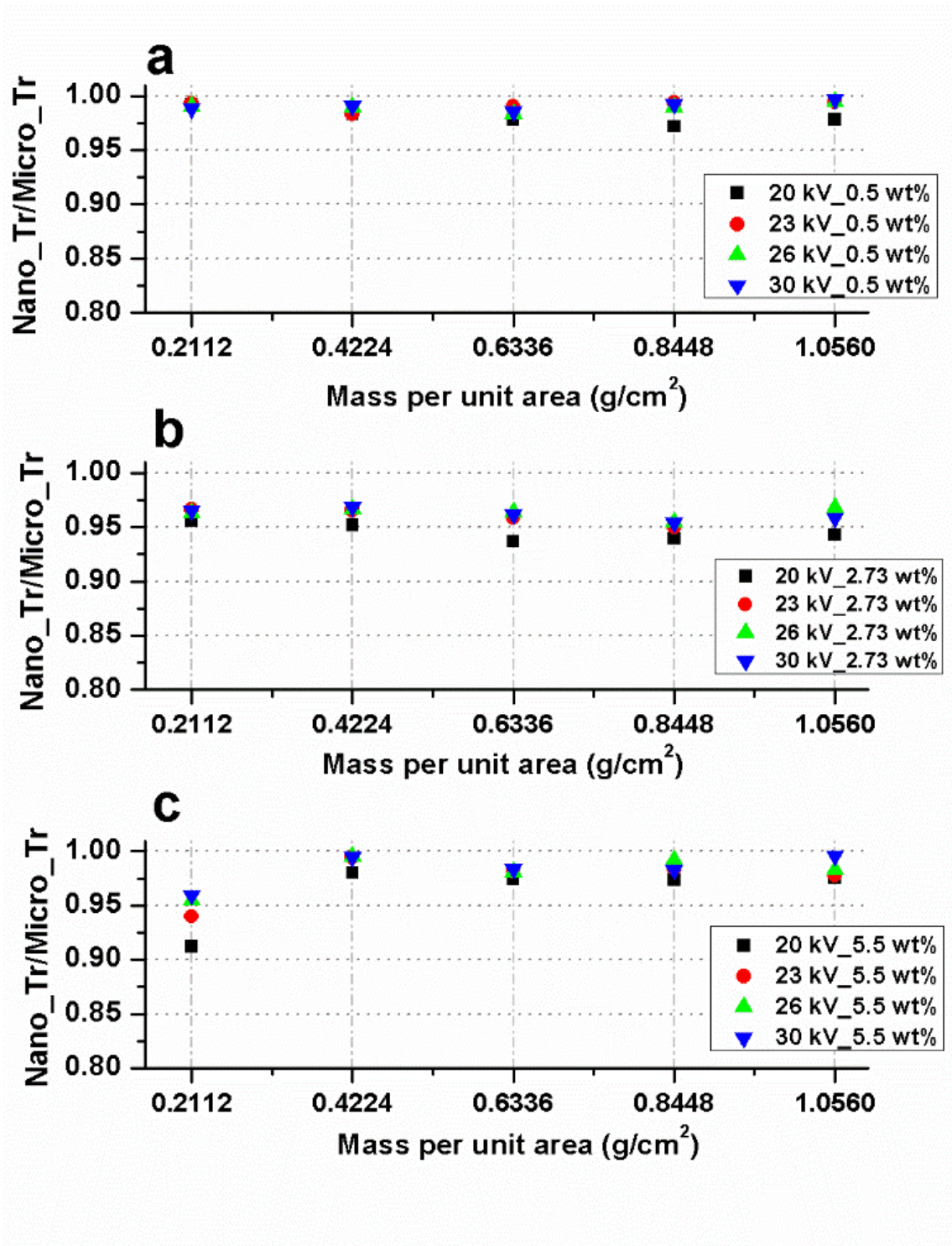
Figure 6.7: X-ray transmission ratio of Ag-nano to Ag-micro as a function of increasing 'mass per unit area' of Ag samples for the mammographic energy range at (a) 0.5 wt%, (b) 2.73 wt%, and 5.5 wt% concentration of Ag particles in PDMS.

6.3.1.2.2 Higher diagnostic X-rays

The X-ray transmission ratio of Ag nanocomposites to Ag microcomposites at 40, 60 and 80 kV are shown Figures 6.8a to 6.8c. The overall trend for all concentrations seems to indicate lower transmission (better attenuation) by Ag-nano for 'mass per unit area' at values less than 0.6336 g/cm^2 compared to those by Ag-micro. For composites with 0.5 wt% Ag particles at 0.2112 g/cm^2, Ag-nano was found to have ~4% better attenuation at all tube potentials compared to Ag-micro. At higher 'mass per unit area' ($\geq$0.6336 g/cm^2), the transmission characteristics showed negligible differences between Ag-nano and Ag-micro. With increase in concentration (2.73 wt%), the attenuation improved, almost uniformly, over the whole range of 'mass per unit area'. For 5.5 wt%, the overall trend was similar to that observed for 0.5 wt%. Moreover, the particle size effects decreased with increase in the tube potentials (from 40 to 80 kV).
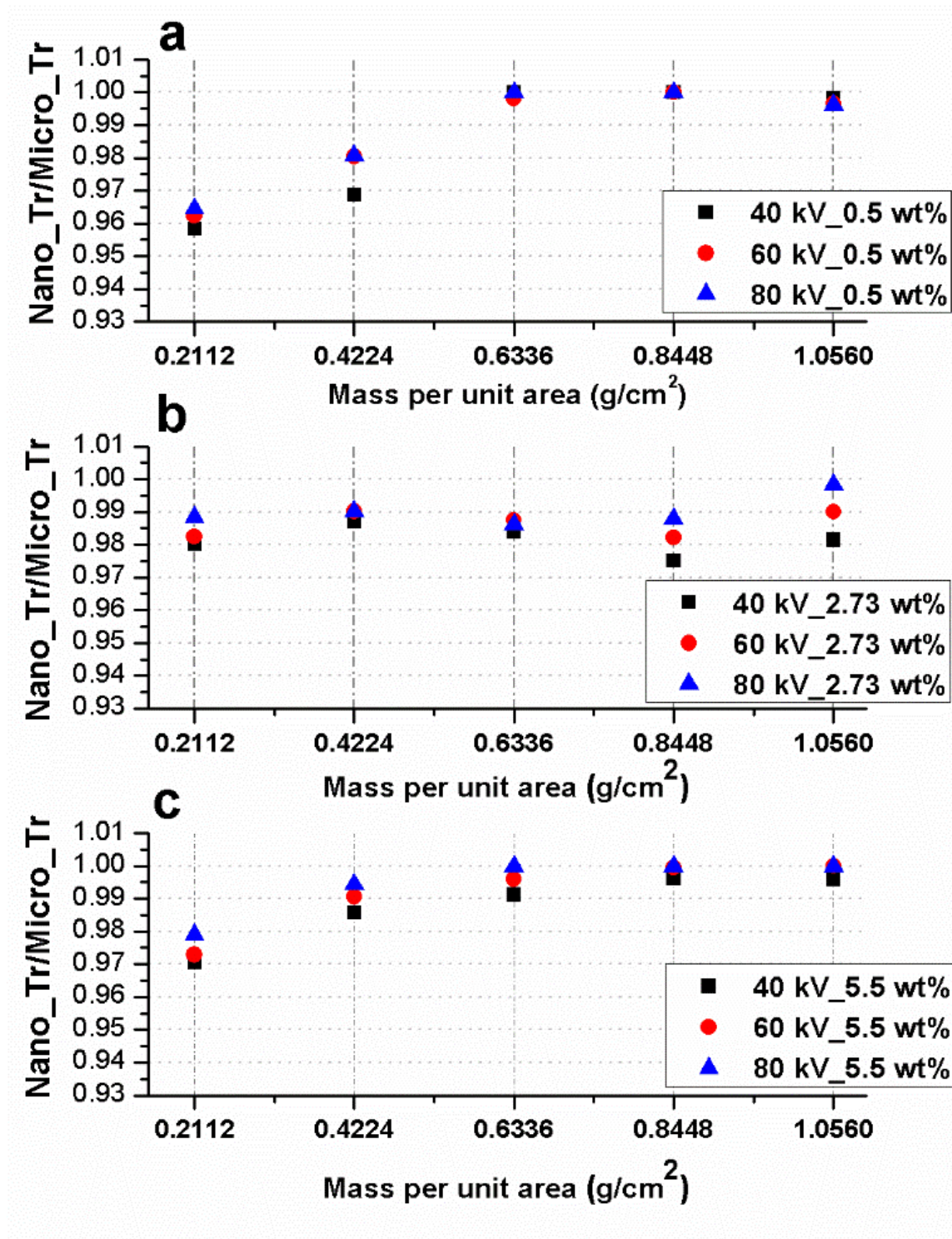
Figure 6.8: X-ray transmission ratio of Ag-nano to Ag-micro as a function of increasing 'mass per unit area' of Ag samples for the higher diagnostic energy range at (a) 0.5 wt%, (b) 2.73 wt%, and 5.5 wt% concentration of Ag particles in PDMS.

6.3.2 Forward and backward scatter characteristics

X-ray attenuation characteristics of a given material is representative of the capability of the material to fully/partially absorb and/or scatter the incident X-ray photons. In order to investigate role of particle size in X-ray scattering, both forward- and back-scattered X-ray measurements from each of the three different concentrations of the Ag-nano and the Ag-micro samples were recorded at four different tube potentials (26, 40, 60 and 80 kV).

Under 26 kV X-rays, the results clearly indicate that the forward scatter characteristics of the Ag-nano sample increased with increase in the particle concentration (i.e. Nano_Fw/Micro_Fw $\leq$ 1 for 0.5 to 5.5. wt% of Ag in PDMS) while the reverse trend was observed at all the higher diagnostic energies (Figure 6.9a). It is interesting to note that the overall forward scatter of Ag-nano sample, for both 60 and 80 kV X-rays, was lower than that for 40 kV X-rays. Moreover, it can be concluded that the Ag-nano sample scattered less X-ray photons in the forward direction in comparison to the Ag-micro sample.

Back scatter results show that for each of the concentrations, the Ag-nano sample scattered more X-ray photons in the backward direction for tube-potentials, 40 to 80 kV, when compared to the scatter characteristics of the Ag-micro sample (Figure 6.9b). For 26 kV X-rays, only 5.5 wt% of Ag-nano showed the least back scatter in comparison to Ag-micro (Figure 6.9b).
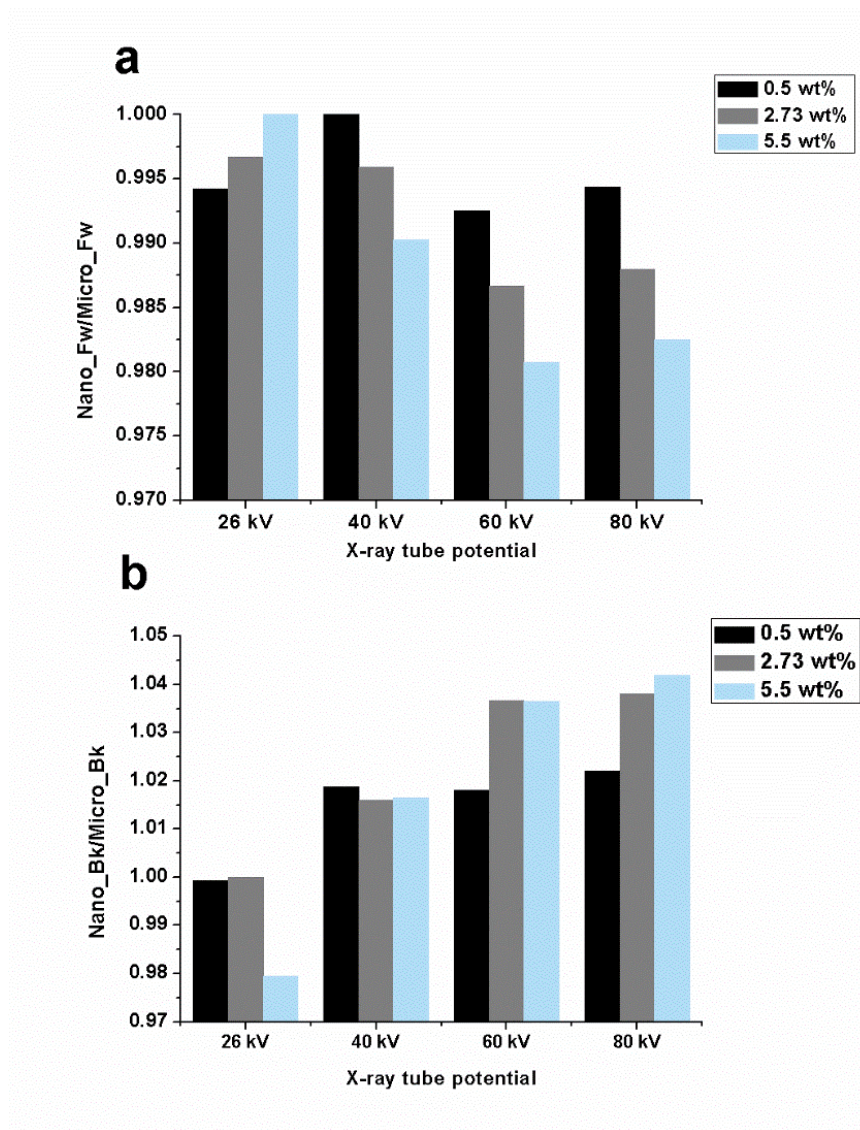
Figure 6.9: X-ray scatter characteristics of three different concentrations of Ag in PDMS for (a) forward, and (b) back scatter experiments.

6.3.3 X-ray attenuation characteristics using TLDs

The X-ray attenuation characteristics of Ag-nano and Ag-micro were studied through comparative analysis of the readings obtained from sets of three TLD elements, each set sandwiched between two Ag-nano (or Ag-micro) samples of 2.73 wt% particle concentration, exposed to 26 kV X-rays. Upon exposure, the X-ray photons transmitted and/or scattered in the

forward direction from the top sample (Ag-nano or Ag-micro) and the backscattered photons from the bottom sample will interact with the TLD elements. In Figure 6.10, all of the six TLD elements show lower TLD-reading when exposed with Ag-nano samples than those with Ag-micro samples. This indicates that the Ag-nano sample (top layer in the sandwiched structure) attenuated more photons in comparison to the Ag-micro sample. Relative difference between the TLD readings obtained from Ag-nano and Ag-micro with respect to Ag-micro (i.e. % attenuation) were estimated using the equation defined in Section 6.2.5.3. The calculated relative difference was found to be about 3.4 to 5.1%. These results are in agreement with the overall transmission characteristics observed for Ag-nano, at 26 kV, in the primary beam (attenuation factor of: 4 to 6%) and X-ray scattering tests (i.e. lower forward scatter and equivalent backward scatter from the top layer of Ag-nano compared to the Ag-micro) discussed in previous sections.
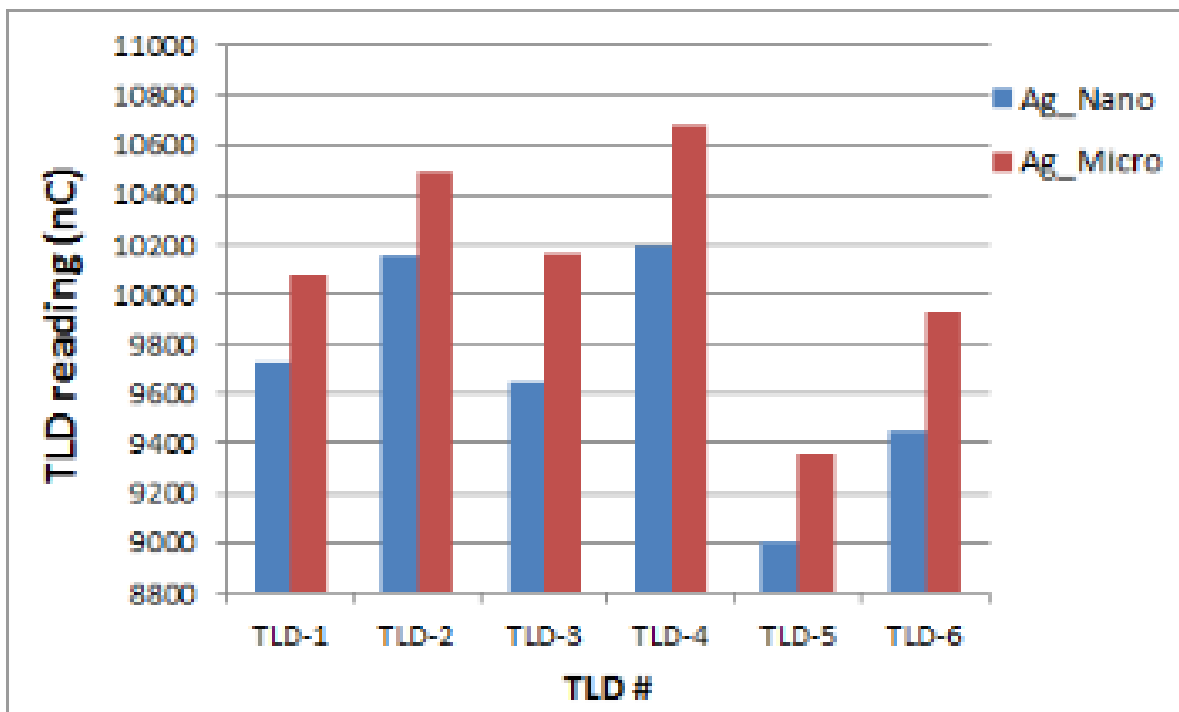
Figure 6.10: TLD readings (nC) for Ag-nano and Ag-micro samples.

6.4 Conclusions

The particle size effects on X-ray transmission characteristics of Ag nano- and micro-composites, under primary beam transmission, were investigated for three different particle concentrations (0.5, 2.73 and 5.5 wt% of Ag in PDMS) and also, for a range of mass per unit area (0.2112 to 1.056 g/cm^2). Ag-nano samples with higher concentration showed about 9 to 6% lower transmission at 20 to 30 kV respectively than the Ag-micro samples at lower photon energies compared to the other energies (about 3 to 2% at 40 to 80 kV respectively).This study clearly demonstrates that the attenuation of diagnostic X-rays can be enhanced at relatively very low loadings of Ag nanoparticles, especially at minimum mass per unit area for energies in the mammographic range. Moreover, the X-ray attenuation behaviour was examined through X-ray scatter tests for all concentrations over four different X-ray energies (26, 40, 60 and 80 kV tube potentials). The forward scatter behaviour of the Ag-nano sample was lower or similar to that of Ag-micro sample at all tube potentials (26, 40, 60 and 80 kV), and the backward scatter characteristics were similar or higher than that of Ag-micro sample for all X-rays in the higher diagnostic energy range (40, 60 and 80 kV). Interestingly, the highest concentration (5.5 wt%) of Ag-nano showed a reduction in the forward scatter (i.e. Nano_Fw < Micro_Fw) and an increase in the backscatter (i.e. Nano_Bkw > Micro_Bkw) as the tube-potential at the higher energy range increased from 40 to 80 kV, while the opposite effects were observed for both forward and backward scatter at the lower energy (26 kV). These results indicate that, compared to microcomposites, nanocomposites with higher loadings of nanoparticles may have an added advantage of minimal forward scatter under higher diagnostic energies, a feature that can be exploited in developing novel X-ray protective aprons using nanomaterials especially for applications such as X-ray image-guided procedures wherein tube-potentials of 60 to 100 kV are

121

commonly employed. Finally, the attenuation behaviour (absorption and/or scatter) of Ag-nano and Ag-micro was further investigated at 26 kV using several TLD elements. The attenuation characteristics of the samples were found to be in agreement with the results obtained from the transmission and the scatter experiments.

Chapter 7

Bismuth Sulfide Nanoflowers for Detection of X-rays in the Diagnostic Energy Range

7.1 Introduction

One dimensional (1-D) nanostructures of metal chalcogenides, especially those of bismuth sulfide (Bi_2S_3), are among the most widely studied. Bi_2S_3 is an n-type crystalline semiconductor with direct bandgap in the range of $1.3 - 1.7$ eV.[99-101] Several studies have reported interesting morphologies of Bi_2S_3 in the form of nanoparticles, nanorods, nanotubes, nanowires, nanoflakes and nanoflowers.[99, 102-107] These 1-D nanostructures of Bi_2S_3 have been reported to exhibit enhanced electrical, thermal and optoelectronic properties and thereby are extensively investigated for a variety of applications such as photovoltaics, thermoelectrics, infrared spectroscopy, and field emission.[106, 107] In a recent study, polymer-coated Bi_2S_3 nanoparticles were used for in vivo X-ray imaging applications as contrast agents in X-ray computed tomography.[108] The nanoparticles showed significantly higher X-ray absorption (five-folds) in comparison to the conventional iodinated contrast agents. The relatively high effective Z of Bi_2S_3 allows it to undergo photoelectric interaction with a wide range of X-ray energies, making it a suitable material for clinical X-ray dosimetry. Subsequently, there is a growing interest to use bismuth-based materials for high-energy dosimetric applications.

Our group has previously reported X-ray photoconductivity measurements from thin films of carbon nanotubes (CNT), and quantum dots (zinc oxide and cadmium telluride) for direct detection of therapeutic X-rays.[109-112] Since the atomic coefficient (i.e. the interaction cross-section) dependence for photoelectric absorption is directly proportional to Z^4,[6] nanomaterials with high Z are most likely to generate detectable charge carriers at very low doses or low-

energy X-rays, improving the sensitivity of the dosimeter. Lobez and Swager reported resistivity-based detection of gamma rays using multi-walled CNTs coated with poly (olefin sulfone) (POS) doped with bismuth. Due to its high Z, bismuth was chosen as a dopant to increase the interaction cross-section of the low Z composite of POS/CNT.[113] Similarly, Zhong et al. reported composites of BiI_3 particles and conjugated polymers to detect gamma rays based on changes in the photoluminescence intensities of the composites upon irradiation.[52] Others have incorporated bismuth oxide nanoparticles into organic semiconducting polymers to increase the absorption cross-section, and thereby the sensitivity, for applications in large-area, X-ray dosimetry.[74, 114] High Z nanoscale materials can occupy more volume fraction of the active detection region at relatively low weight percentage in comparison to the bulk. Moreover, both experimental and simulation studies on different types of nanocrystalline materials exposed to various sources of radiation showed enhanced resistance to radiation-induced material degradation.[18, 41, 91, 115-117] Furthermore, some studies have also reported increased X-ray interactions (i.e. attenuation properties) of nanocomposites in comparison to those of the microcomposites, both irradiated with mammographic X-ray energies as discussed in detail in Chapter 6.[67, 93, 94] High energy photoresponse of high Z nanomaterials such as Bi_2S_3, therefore, has huge technological importance for the development of efficient and durable dosimeters.

In the context of synthesis of Bi_2S_3 nanostructures, solvothermal or hydrothermal method is one of the most commonly used solution-based processes. The hydrothermal technique allows control over the morphology by varying reaction parameters such as reaction time, temperature, precursors, and soft templates (surfactants, complexing agents, biomolecules[107, 118] or polymers).[119] In this study, Bi_2S_3 nanostructures were synthesized through the hydrothermal process using polyethylene glycol (PEG) as a template to obtain flower-like nanostructures. To

the best of our knowledge, this is the first study to report the X-ray photoresponse of the nanoflower-like structures of Bi_2S_3.[120] The photoelectric response of micron-sized Bi_2S_3 units of "flowers" with "petals" of nanorods were measured under: (i) low X-ray energies, 20 to 30 kV, typically used in mammographic tomosynthesis, and (ii) X-ray energies, 40 to 100 kV, typically used in general diagnostic radiology.

7.2 Materials and Methods

7.2.1 Synthesis of Bi_2S_3 nanoflowers

Bismuth nitrate pentahydrate ($Bi(NO_3)_3.5H_2O$ from Sigma Aldrich), thiourea and polyethylene glycol (PEG-4000) were used as precursors for hydrothermal synthesis of Bi_2S_3 nanoflowers. 0.322 g of $Bi(NO_3)_3.5H_2O$ was added to 8 ml of deionized water and stirred well. 1.288 g of PEG-4000 was dissolved in 2 ml of deionized water, and stirred into the above solution. Finally, 1.288 g of thiourea was added and stirred well to obtain a clear, orange colored solution. The solution was then transferred into a 20 mL Teflon-lined stainless steel autoclave and exposed to 180 ℃ for 17.5 hours. Black precipitates, obtained upon hydrothermal reaction, were washed several times with deionized water, and finally with absolute ethanol, and dried overnight at 60 ℃ in an oven.

7.2.2 Characterization of Bi_2S_3 nanoflowers

The samples collected from the hydrothermal reaction were studied using FESEM (Zeiss LEO 1550), energy dispersive spectrometer (EDS) from Oxford Instruments Microanalysis System INCA Energy 350), and powder X-ray diffraction (XRD, Bruker D8 Advance diffractometer using Cu Kα radiation). The bandgap of Bi_2S_3 nanoflowers was determined from the diffuse

reflectance spectra measured using Shimadzu UV-2501PC UV-Vis-NIR spectrophotometer equipped with an integrating sphere accessory, and $BaSO_4$ as reference scatter. The details of the characterization studies can be found in Appendix A.

7.2.3 Device fabrication

Photolithographic techniques were used to fabricate Au/Cr IDE device. Firstly, 200 and 20 nm thick layers of Au and Cr, respectively, were deposited on clean silicon nitride coated wafer using e-beam evaporator (Intlvac Nanochrome™ II UHV system). Photoresist, S1811 (Shipley), was spin-coated on the silicon wafer and baked at 110 ºC for 90 s. A Mylar mask with 16 IDE patterns was used in this study. Each IDE pattern spanned over an area of 1 cm^2 with an electrode spacing and width of 50 microns, and four contact pads, each with an area of 2 mm^2. The patterns were transferred from the mask onto the photoresist-coated wafer by flood exposure to ultraviolet radiation using Suss MA6 Mask Aligner. The photoresist layer was then developed in MF-319 (Shipley's photoresist developer); the wafer was, subsequently, dipped in deionized water and dried with nitrogen gas. Finally, the hydrothermally synthesized Bi_2S_3 nanoflowers were dispersed in ethanol (12.4 mg/200 µL) of which 15 µL was carefully pipetted on the 1 cm^2 area of the IDE pattern using the dropcast method. The film was dried at room temperature. Electrical connections were cold soldered on a pair of contact pads using conductive silver epoxy. Since Bi_2S_3 nanoflowers were found to be photosensitive in the UV-Vis range, the devices were stored in the dark.

7.2.4 Experiment setup

The photoresponse of the Bi_2S_3 nanoflowers on Au/Cr IDE were studied for two sets of diagnostic X-rays categorized based on their energy range: (i) X-rays in the mammographic

range with tube potentials: 20, 23, 26 and 30 kV, and (ii) X-rays with higher energies in the diagnostic range with tube potentials: 40, 60, 80 and 100 kV. The experiments were conducted using a superficial X-ray facility (Gulmay Medical Inc.) at the Grand River Regional Cancer Center (Kitchener, Ontario, Canada). An aperture of diameter 1 cm was used for all measurements. The X-ray tube-current was set to 20 mA for all tube potentials. No external filters were used.

7.2.5 Measurements

7.2.5.1 Detection of X-rays in the mammographic range (20 to 30 kV)

Both dark (leakage) current and X-ray induced currents from the Bi_2S_3 nanoflowers and the substrate (the Au/Cr/SiNx/Si IDE without the nanomaterial) were measured for the following conditions: (i) Four tube potentials in the mammographic range of 20, 23, 26, and 30 kV. (ii) Four different doses were delivered by varying the focus-to-surface distance (FSD) for each of the four tube potentials. (iii) Three different bias voltages: +0.2, +0.4 and +1 V for each of the four tube potentials. (iv) Four different field sizes (0.4, 0.6, 0.8 and 1 cm) for two peak voltages (20 and 30 kV). A picoammeter/voltage-source (Keithley 6487A) was used to record all measurements. A bias voltage of +1 V was used to measure effects of tube-potentials, doses, and field sizes. The dark current for both devices (with and without Bi_2S_3 nanoflowers), for a given bias voltage, was accounted for through subtraction from the picoammeter measurements. All measurements were carried out under ambient conditions but in the dark since Bi_2S_3 nanoflowers were found to be photosensitive in the UV-Vis range. Micro-ionization chamber (Exradin 0.016 cc, model A14) along with an electrometer (Dose-1) was used to measure the dose (i.e. cumulative charge over the exposure period) for all energies. In order to analyze the uniformity

of the field sizes used and the effects of its penumbra, radiographic films (GafChromic EBT3) were exposed to 20 kV X-rays for 18 s with all the four field sizes (using lead cut-outs of diameter 0.4, 0.6, 0.8 and 1 cm). The details of the film dosimetry can be found in Appendix A.

7.2.5.2 Detection of X-rays in the higher diagnostic energy range (40 to 100 kV)

Both dark current and X-ray induced currents from the Bi_2S_3 nanoflowers and the substrate (the Au/Cr/SiNx/Si IDE without the nanomaterial) were measured for the following conditions: (i) Four tube potentials - 40, 60, 80, and 100 kV. (ii) Four different doses were delivered by varying the FSD for each of the four tube potentials. (iii) Three different bias voltages: +1, +1.5 and +2 V for each of the four tube potentials. (iv) Six different field sizes (0.4, 0.6, 0.8, 1, 1.25, and 1.5 cm) for the minimum and maximum peak voltages (40 and 100 kV). Similar to the measurements in the mammographic range, the picoammeter (Keithley 6487A) was used to record all measurements, and the dose delivered at all the four tube potentials was measured using the micro-ionization chamber (Exradin 0.016 cc, model A14) along with an electrometer (Dose-1) that displayed cumulative charges in nano-coulombs. The photoresponse at all tube potentials, doses and field sizes were measured under a constant bias voltage of +1.5 V. The dark current for both devices (with and without Bi_2S_3 nanoflowers) was subtracted from all measurements to determine the X-ray induced currents in the devices.

7.2.6 Simulations

Spekcalc, an open software,[121, 122] calculates X-ray spectra from tungsten anode X-ray tubes over a wide range of tube potentials (20 to 300 kV) and anode angles of 6 to 30°. The SpekCalc utility was used to simulate the X-ray emission spectra for each of the tube-potentials (20 to 100 kV) used in this study. The mean energy estimated from SpekCalc for each tube-potential was

considered as a monoenergetic beam and used to calculate energy-weighted effective Z of Bi_2S_3 nanoflowers using a simulation software called Auto-Zeff that allow fast computation of average atomic numbers and spectrum-weighted mean atomic numbers for any given material.[96] The mass attenuation coefficient (in g/cm^2) of the nanoflowers for each of the mean energies (calculated using SpekCalc for all four tube-potentials) was obtained from another simulation tool called WinXCom.[123] The software calculates X-ray attenuation coefficients for a given material (element, mixture or compound) that can be easily be specified in the program interface. The corresponding linear attenuation coefficients (in cm^{-1}) were calculated by multiplying the density of the Bi_2S_3 nanoflowers with the mass attenuation coefficients. Finally, the penetration depth of the incident photons for each of the tube-potentials was calculated from the reciprocal of the linear attenuation coefficient.

7.3 Results and Discussion

In order to measure the X-ray induced photocurrent, interdigitated electrodes (IDE) of gold/chrome (Au/Cr) were patterned on silicon-nitride-coated silicon (Si) wafer using photolithography. Each IDE had an area of 1 cm^2 with an electrode width and spacing of 50 µm respectively. A film of Bi_2S_3 nanoflowers was deposited on the IDE (Au/Cr/SiNx/Si) using dropcast method. The average unit size of the hydrothermally synthesized Bi_2S_3 nanoflowers was found to be ~4 µm consisting of nanorods with diameters of ~100 nm (Figure 7.1). The X-ray field size was determined with a lead cut-out of 1 cm diameter placed on top of 4 mm thick spacers such that the cut-out exposed only the active area of the IDE to a 1 cm diameter cone attached to the head of the X-ray tube (Figure 7.2).
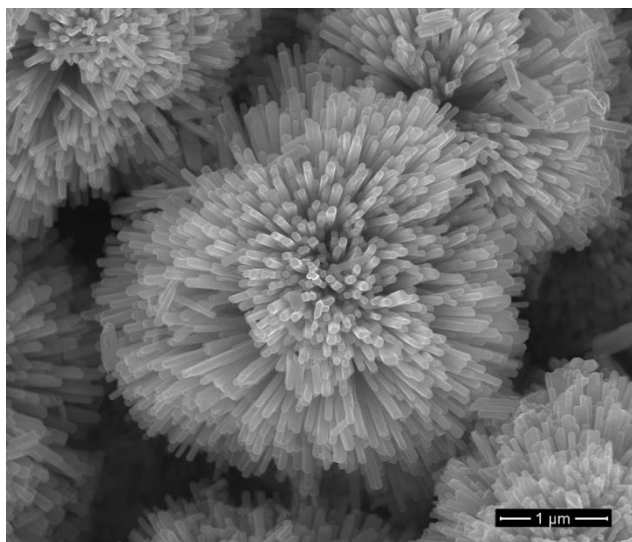
Figure 7.1: FESEM image of Bi_2S_3 nanoflowers.

The photocurrents of the device with and without Bi_2S_3 nanoflowers in response to changes in X-ray beam intensity were measured under

(i)   X-ray tube potentials in the (a) mammographic energy range: 20, 23, 26, and 30 kV, and (b) higher diagnostic energy range: 40, 60, 80, and 100 kV.

(ii)   Four different doses at each of the tube potentials.

(iii) Three operating bias voltages: +0.2, +0.4 and +1 V for the study of X-ray detection in the mammographic energy range, and +1, +1.5, and +2 V for the study of X-ray detection in the higher diagnostic range.

(iv)   Four different field sizes (0.4, 0.6, 0.8 and 1 cm diameter) for two peak voltages (20 and 30 kV), and six different field sizes (0.4, 0.6, 0.8, 1, 1.25 and 1.5 cm diameter) for two peak voltages (40 and 100 kV).
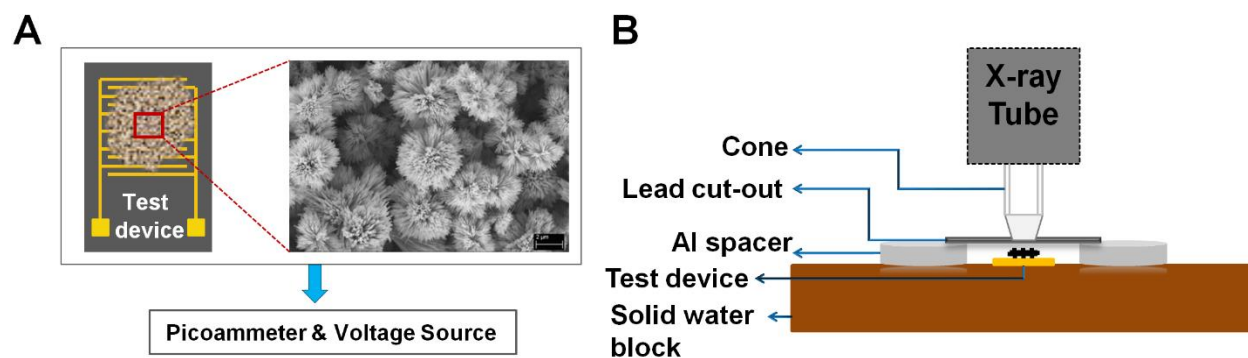
Figure 7.2: Schematic of the: (a) the Au/Cr IDE device with Bi_2S_3 nanoflowers connected to a picoammeter (also a voltage source) for current measurements under a given bias voltage, and (b) experimental setup.[120]

For a given bias voltage, leakage (or dark) currents were recorded for both the Bi_2S_3 (sample) and the reference (substrate) devices. All measurements were conducted after 15 min which was required for stabilization of the transient dark current, and an average of the dark currents recorded just before each exposure, was subtracted from all the measurements to obtain the data presented in Figures 7.3 to 7.18. For all measurements, a ramping-up period of 5-6 s was observed for the X-ray tube to attain the preset tube potential (kV) and intensity (mA). The ramp-up time was also confirmed from ionization chamber (Farmer-type chamber) measurements for all the X-ray energies used in this study.

7.3.1 Effects of tube potential

Figures 7.3a and 7.3b show the effects of X-ray tube potential (in the mammographic range) on the electrical current measurements from the IDE device with and without Bi_2S_3 nanoflowers, respectively, when exposed to X-rays for a duration of 1 min under a bias voltage of +1 V. All the measurements were performed such that the X-ray cone was in contact with the lead cut-out used to set the field size. The initial ramp-up fluctuation was observed for both the devices (with and without the Bi_2S_3 nanoflowers), followed by a very stable photocurrent.
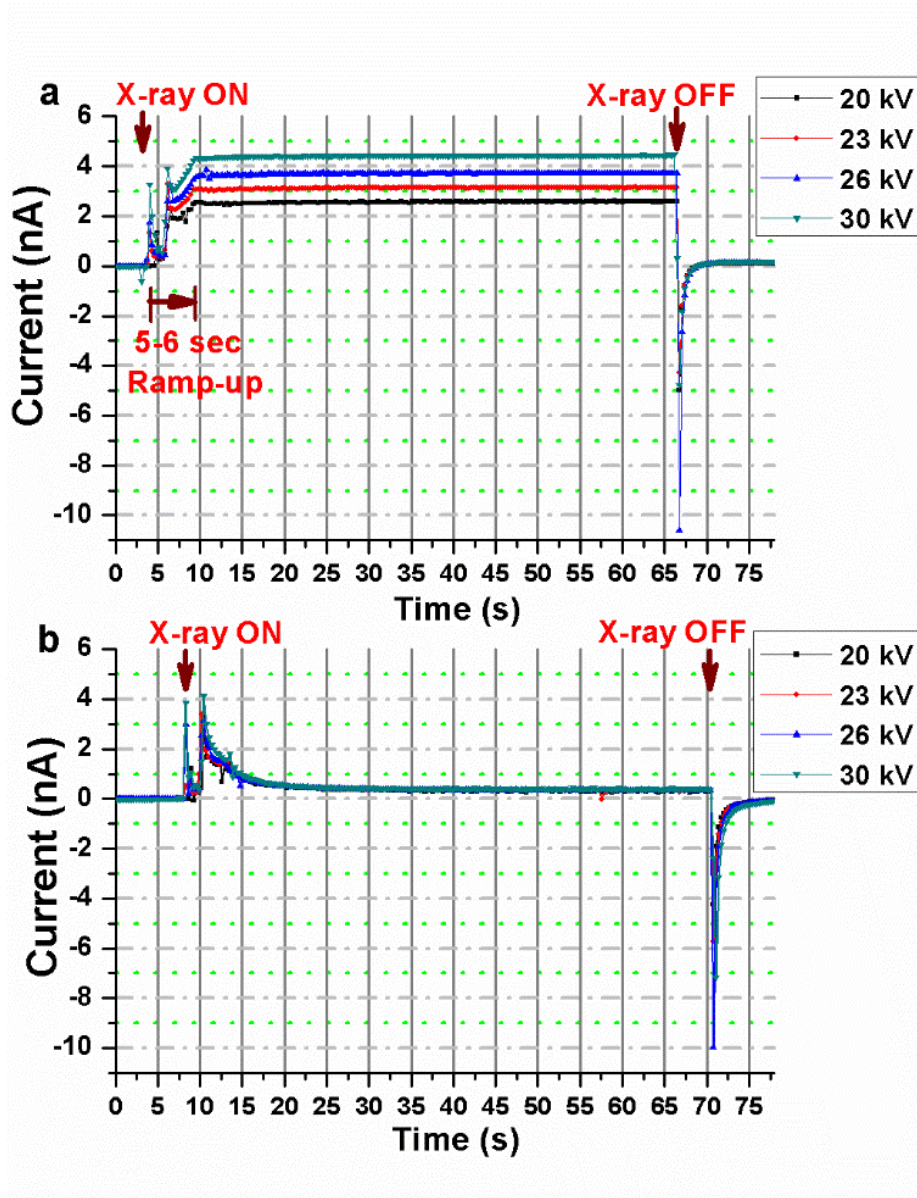
Figure 7.3: X-ray induced current in the IDE device with (a) Bi_2S_3 nanoflowers, and (b) in the substrate (reference device). The IDE devices were operated under a bias voltage of +1 V at four different X-ray tube-potentials of 20, 23, 26 and 30 kV.[120]

The measurements from the Bi_2S_3 device were found to be about 5, 6, 7 and 9 times the photoresponses obtained from the reference device at the 'X-ray ON' state for tube-potentials 20, 23, 26 and 30 kV respectively. For all tube potentials, the reference device showed a rapid loss of charge-carriers for duration of about 18 s, followed by a plateau of steady photoresponse. In

132

contrast, the photoresponses from the Bi_2S_3 device were found to be fairly stable after the initial fluctuation during the ramp-up. A "negative" current or reversal in the current flow, at the instance of 'X-ray OFF' state, was observed for all measurements which may be attributed to the charge trapping and release mechanism(s) from the substrate; also evident from the similar behaviour observed in the reference device at 'X-ray OFF' state (Figure 7.3b).

At the higher diagnostic energies, the X-ray induced photocurrents for the Bi_2S_3 device ('X-ray ON' state) was about 8, 8.5, 8, and 7.4 times the photoresponse of the reference device for the tube potentials 40, 60, 80, and 100 kV respectively (Figures 7.4a and 7.4b). Similar to the results in the mammographic range, both the devices showed the negative peaks at the end of each exposure. Also, overall trend of the responses from the reference device was similar to those obtained in the mammographic range. However, the 'X-ray ON' currents were higher than those recorded for the lower X-ray energies. These differences may, presumably, be attributed to two factors: higher X-ray energies, and relatively higher operating voltage (1.5 V), the former allow more interactions with the substrate to generate more charge carriers and the latter increases the charge collection efficiency under the increased electric field.
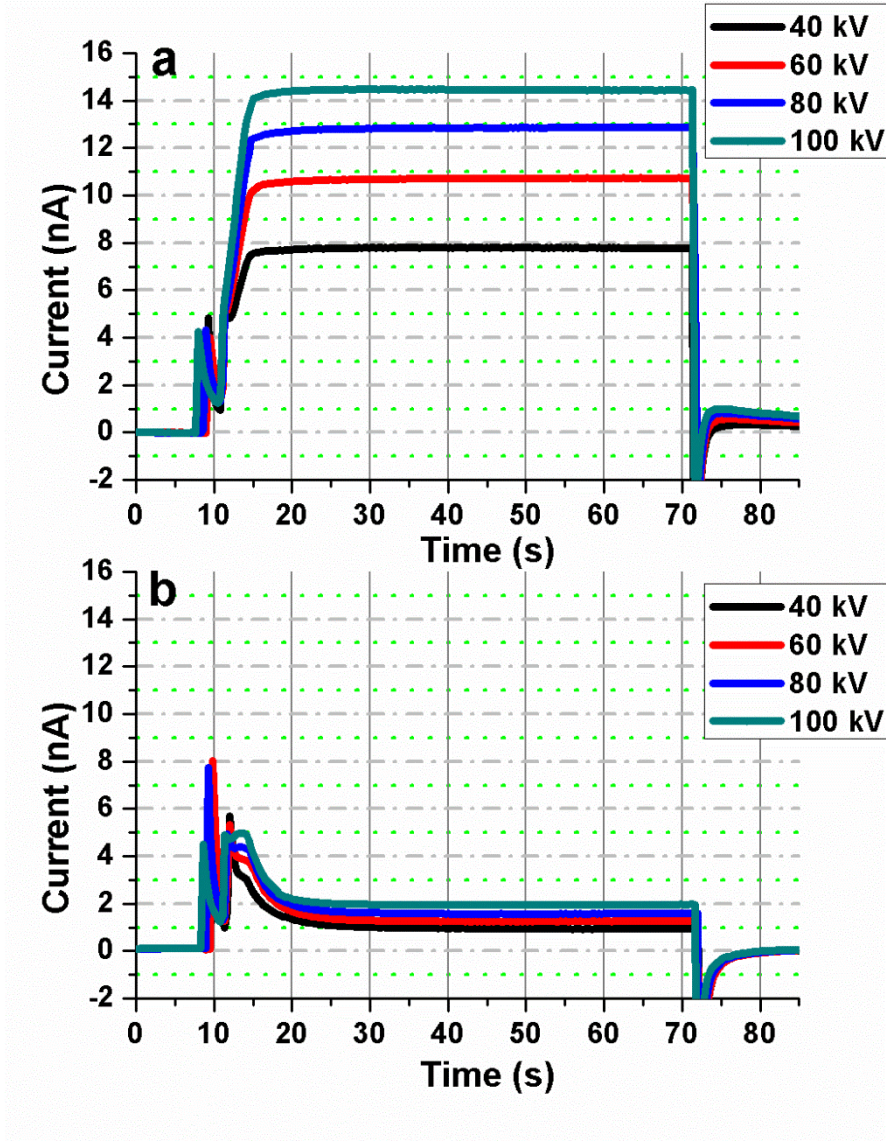
Figure 7.4: X-ray induced current in the (a) IDE device with Bi_2S_3 nanoflowers, and (b) in the substrate (reference device). The devices were operated under a bias voltage of +1.5 V at four different X-ray tube-potentials of 40, 60, 80 and 100 kV.

In order to identify the X-ray interaction processes responsible for the relatively high photocurrents in the Bi_2S_3 nanoflowers, energy-weighted effective Z of Bi_2S_3 was determined using Auto-Zeff simulation software with inputs from an X-ray spectra calculation program known as SpekCalc.[2, 96, 124, 125] The SpekCalc results for the mean energy of the X-ray tube

potentials 20, 23, 26, 30, 40, 60, 80, and 100 kV were 9.78, 10.6, 11.4, 12.4, 14.8, 20, 26.2, and 33.6 keV respectively (see spectra for each of the tube potentials in Appendix A). The energy-weighted effective Z of Bi_2S_3 for monoenergetic beams in the range of 10 to 40 keV, calculated using the Auto-Zeff software, were found to be in the range of 45.06 to 66.47 (see Appendix A). Furthermore, the atomic interaction of X-ray energies <40 keV with an effective Z within the range of 45 to 70 is predominantly photoelectric effect.[6] Based on the incident energy and the thickness of the dropcasted film of Bi_2S_3 nanoflowers exposed to X-rays, the photoelectric effect should allow partial or complete absorption of an incident photon through transfer of energy, typically, by knocking off a core shell electron from Bi_2S_3. The kinetic energy of the knocked off electron is equal to the difference between the incident beam energy and the binding energy of the electron in the core shell. The energetic electron traverse through the medium to interact further via transfer of energy to produce more charge carriers and/or secondary photons which then undergo elastic scattering or photoelectric absorption with the Bi_2S_3 nanoflowers. The secondary interactions also may produce more electron-hole (e-h) pairs, in turn, adding to the overall charge carriers generated due to the incident beam. An external bias voltage establishes an electric field within the film of nanoflowers such that the radiation-induced e-h pairs can be drifted and collected at the electrodes and subsequently measured as electric current by the picoammeter.

The average photocurrent (i.e. the average current at the 'X-ray ON' state) produced in the nanoflowers at each of the tube potentials is listed in Table 7.1. An external bias voltage of +1 and +1.5 V was applied for exposure under the mammographic and higher diagnostic energy range respectively. The photoresponse of the nanoflowers indicate an energy dependent behavior. The measurements were also compared to those recorded from a micro-ionization

135

chamber. The ionization chamber measurements, listed in Table 7.1, confirmed similar trend of increase in the overall dose delivered (in terms of electrometer reading) when the x-ray tube-potential was increased. Evidently, the photocurrent measured from the Bi_2S_3 nanoflowers increased with the overall dose delivered at each of the tube potentials (20 to 100 kV). Detailed dose-dependent characteristics of the nanoflowers are presented in the next section.

Table 7.1: Electrometer measurements using micro-ionization chamber for an exposure time of 18 s for all tube potentials.

Tube Voltage (kV)	Photoresponse of Bi_2S_3 nanoflowers (nA)	Electrometer readout for cumulative charges (nC)
20	2.53	2.12
23	3.1	2.87
26	3.68	3.64
30	4.45	4.72
40	7.8	6.55
60	10.72	10.9
80	12.86	14.47
100	14.47	17.42

7.3.2 Dose Dependence

The dose was varied according to the inverse square law by changing the focus-to-surface distance. The dose was reduced in steps of 1/4th the initial value by increasing the focus-to-surface distance such that the dose of 1, 3/4, 1/2 and 1/4 times of the initial value, denoted as D-

1, D-3/4, D-1/2, and D-1/4 respectively, were obtained for each of the X-ray energies. The measurements at each of the four different doses were compared to those recorded using the micro-ionization chamber. The fabricated devices and the micro-ionization chamber were exposed to both the mammographic (for a duration of 18 s) and the higher diagnostic range (for a duration of 60 s). The overall X-ray dose has been considered in terms of the electrometer readout displayed in units of cumulative charge (in nano-coulomb) as detected by the micro-ionization chamber. For all measurements, the devices were operated at +1 V for X-rays in the mammographic energy range, and +1.5 V external bias voltage for X-rays in the higher diagnostic range. Figure 7.5 shows the X-ray induced photocurrents in Bi_2S_3 nanoflowers as a function of dose (electrometer readout indicated in the figure legends) for each of the four energies in the mammographic range. Figures 7.6 shows the same for reference device.
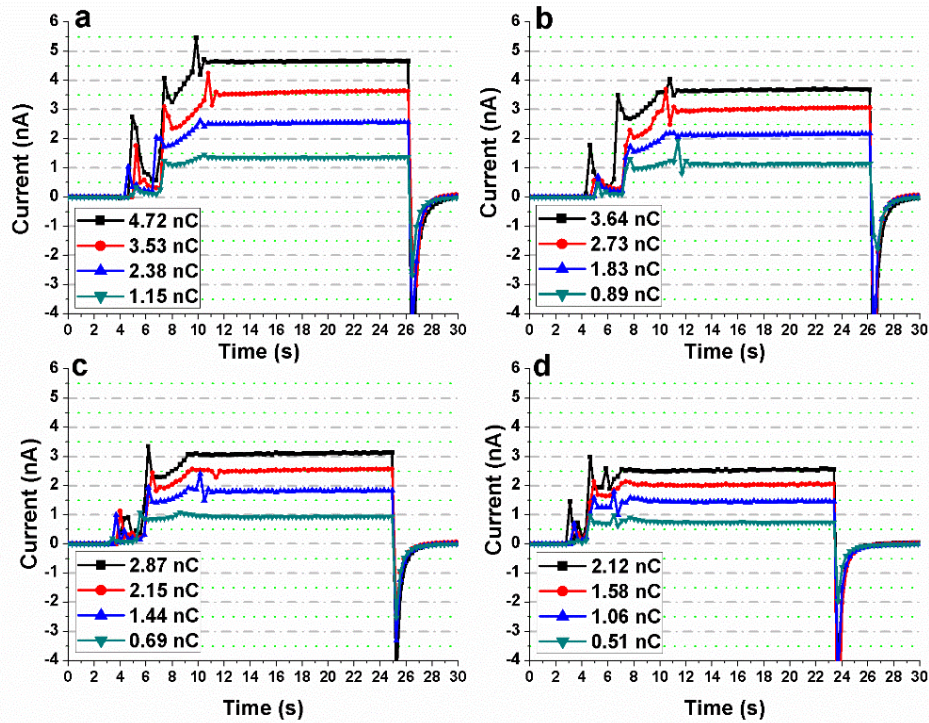
Figure 7.5: Photoresponse of the Bi_2S_3 nanoflowers (in nA) exposed to X-ray dose of D-1, D-3/4, D-1/2, and D-1/4 (corresponding electrometer readout shown in the legend) at a tube potential of (a) 30 kV, (b) 26 kV, (c) 23 kV, and (d) 20 kV.[120]
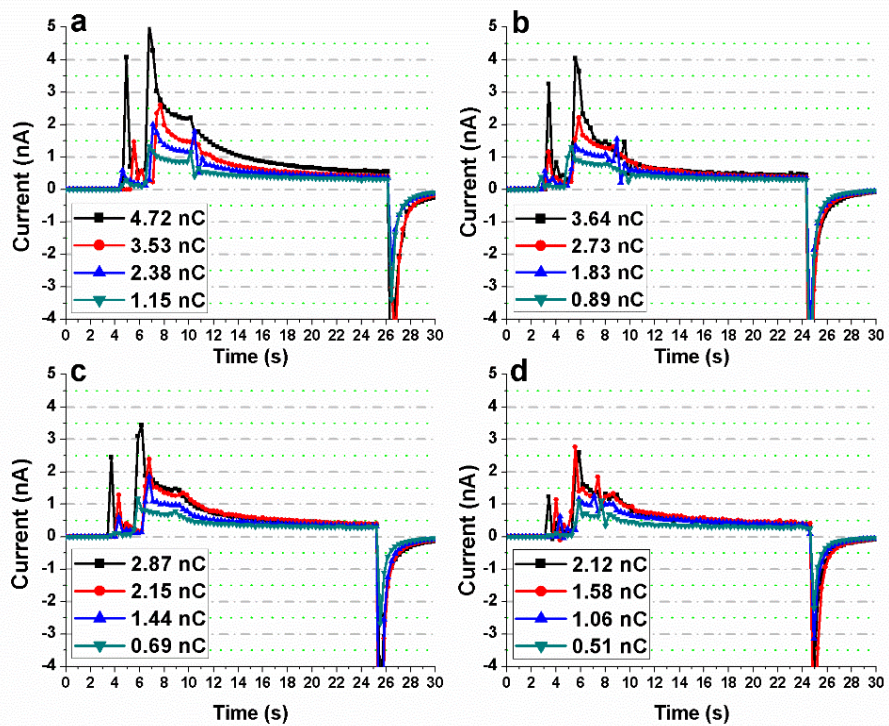
Figure 7.6: Photoresponse of the substrate (reference device) exposed to X-ray dose of D-1, D-3/4, D-1/2, and D-1/4 (corresponding electrometer readout shown in the legend) at a tube potential of (a) 30 kV, (b) 26 kV, (c) 23 kV, and (d) 20 kV.[120]

Figures 7.7 and 7.8 show the X-ray induced response, in the Bi_2S_3 nanoflowers and the reference device respectively, as a function of dose (electrometer readout indicated in the figure legends) for each of the four X-ray tube-potentials in the higher diagnostic range. The nanoflowers showed relatively high, stable photoresponse to changes in delivered dose (about 9X and 7.5X signal amplification at the maximum dose under 30 and 100 kV X-rays, respectively) when compared to the photoresponse of the reference device (Figures 7.5, 7.6, 7.7, and 7.8).
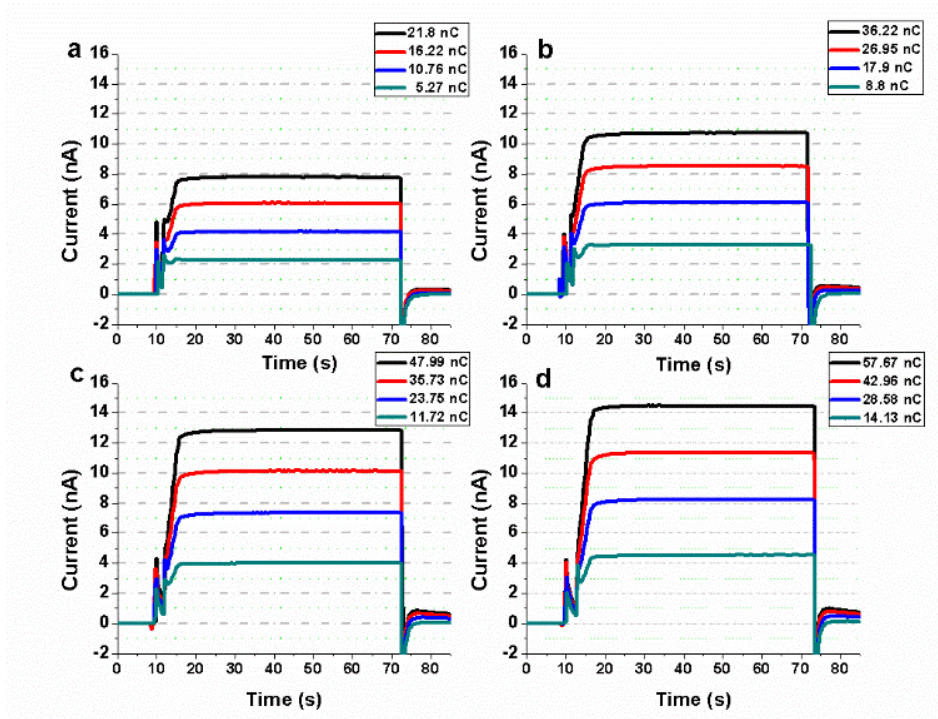
Figure 7.7: Photoresponse of the Bi_2S_3 nanoflowers (in nA) exposed to X-ray dose of D-1, D-3/4, D-1/2, and D-1/4 (corresponding electrometer readout shown in the legend) at a tube potential of (a) 40 kV, (b) 60 kV, (c) 80 kV, and (d) 100 kV.
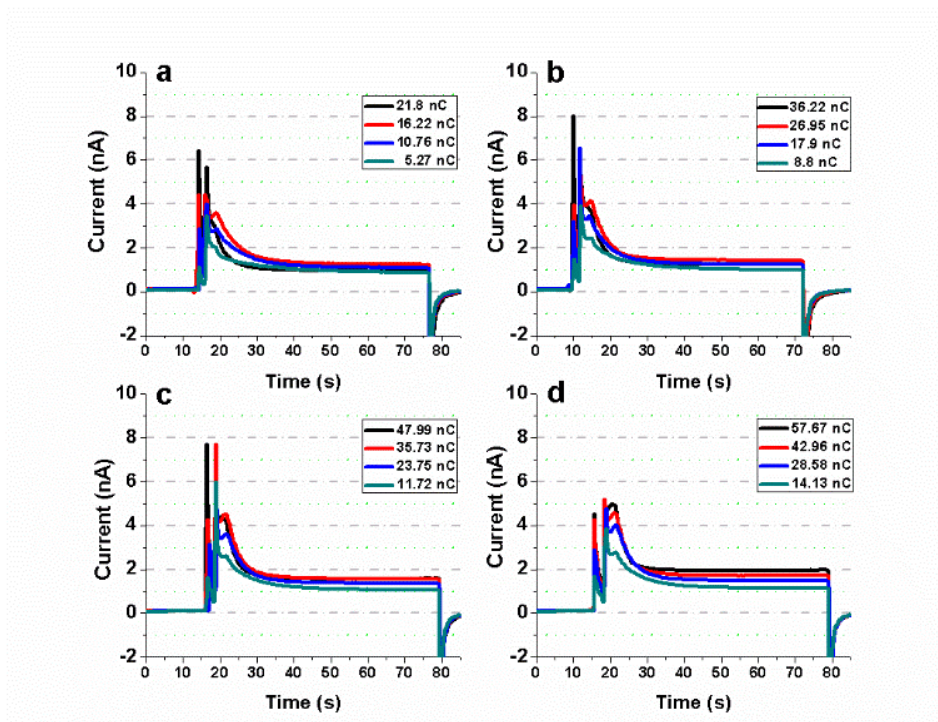
Figure 7.8: Photoresponse of the reference device (in nA) exposed to X-ray dose of D-1, D-3/4, D-1/2, and D-1/4 (corresponding electrometer readout shown in the legend) at a tube potential of (a) 40 kV, (b) 60 kV, (c) 80 kV, and (d) 100 kV.

7.3.3 Field Size Dependence

Average photocurrent from the Bi_2S_3 nanoflowers was used to evaluate the effects of field sizes (exposure area) smaller or greater than the active detection area (i.e. IDE coverage of 1 cm^2). Figure 7.9 shows the average photoresponse of the nanoflowers as a function of field size for 20 and 30 kV X-rays. The incident field was varied by increasing the exposed area on the devices. Circular field sizes of 0.4, 0.6, 0.8, and 1 cm diameter, were determined with circular cut-out of lead sheet placed on top of the IDE with about 4 mm thick aluminum spacers over each side of the device so that the lead sheet was not directly in contact with the test device. The photocurrent in the Figure 7.9, at each of the field sizes, is an average of the measurements recorded over an exposure time of 51 s (obtained from subtraction of the system compensation and the ramp-up time from the exposure interval of 60 s) during the 'X-ray ON' state of the Bi_2S_3 device. Figure 7.10 show the same set of measurements (average current versus exposure area) at higher diagnostic energies (40 and 100 kV) but for field sizes greater than 1 cm lead cut-out (i.e. field sizes defined by 1.25 and 1.5 cm diameter).

It is interesting to note that, at smaller field-sizes (for lead cut-outs ≤ 0.8 cm in diameter), the standard deviations were found to be higher and especially prominent at the maximum tube potential (30 kV in the mammographic range and 100 kV at the higher diagnostic range) than those at other field-sizes. This is because the X-ray induced currents for exposure-areas, relatively smaller than the active detection area, increased with exposure time due to charge build up. In other words, the overall 'X-ray ON' state seemed to depict a space charge limited conduction. In Figure 7.10, the X-ray-induced currents in the nanoflowers increased with exposed area (field-size) until the field size equal to that of the active detection area (0.785 cm^2) was used, beyond which the photocurrent saturated. Furthermore, it is evident that the Bi_2S_3

nanoflowers produced photocurrent for an area of exposure as small as 0.126 cm^2 (i.e. for a field size determined by 0.4 cm diameter lead cut-out) at an X-ray tube-potential as low as 20 kV.
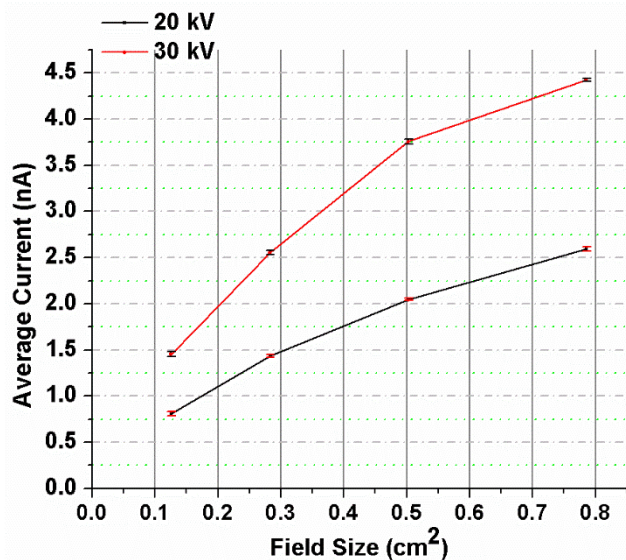
Figure 7.9: Average photocurrent (averaged over 51 s of exposure interval) and standard deviation obtained from the Bi$_2$S$_3$ device under four different field sizes (0.4, 0.6, 0.8 and 1 cm diameter) at 20 and 30 kV X-rays.
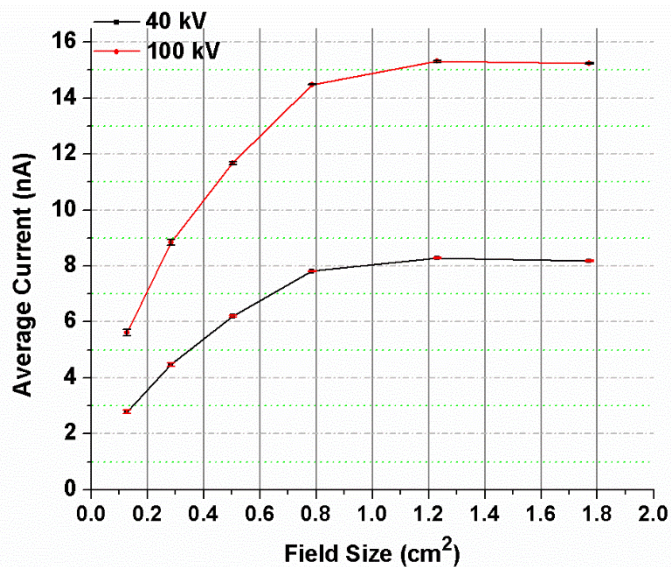
Figure 7.10: Average photocurrent (averaged over 51 s of exposure interval) and standard deviation obtained from the Bi$_2$S$_3$ device under four different field sizes (0.4, 0.6, 0.8, 1, 1.25, and 1.5 cm diameter) at 40 and 100 kV X-rays.

7.3.4 Repeatability of measurements and Dependence on bias voltage

Measurement repeatability and its dependence on the bias voltage were studied for both the Bi_2S_3 nanoflowers and the substrate (without the nanoflowers) at each of the eight X-ray tube potentials.

7.3.4.1 Measurements in the mammographic range (20 to 30 kV X-rays)

Three different bias voltages were tested: +0.2, +0.4 and +1 V. The devices were exposed for an interval of 18 s followed by a longer interval of 1 min in order to assess the repeatability and the stability of the photoresponse of the Bi_2S_3 nanoflowers and the substrate (Figures 7.11 and 7.12). For each of the bias voltages, the photocurrent of the device with Bi_2S_3 nanoflowers was much higher than that of the reference device. Moreover, for all the measurements the magnitude of the "negative currents" at 'X-ray-OFF state' was found to be directly proportional to the applied voltage. In other words, charge trap and release mechanism occurred in the substrate (Au/Cr/SiNx/Si) resulting in storage of charge-carriers generated during irradiation followed by a discharge cycle (or reverse flow of charge-carriers) at the instance of 'X-ray OFF' state.
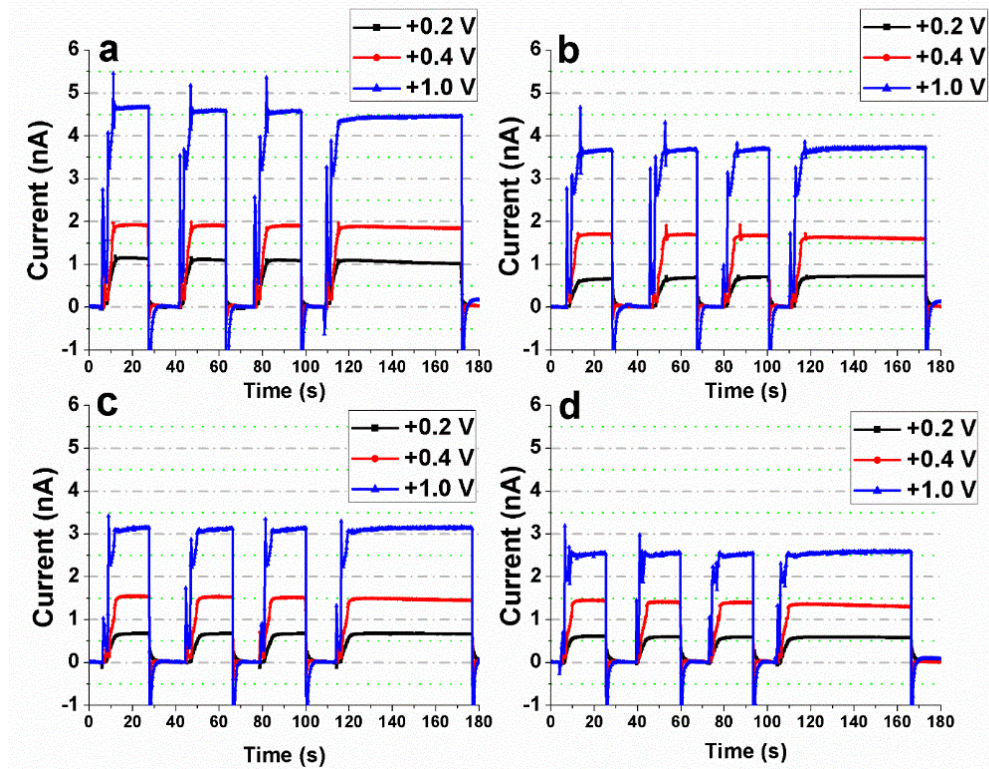
Figure 7.11: Repeatability measurements of the photoresponse from the Bi$_2$S$_3$ nanoflowers exposed to (a) 30 kV, (b) 26 kV, (c) 23 kV, and (d) 20 kV X-rays at different external bias voltages.
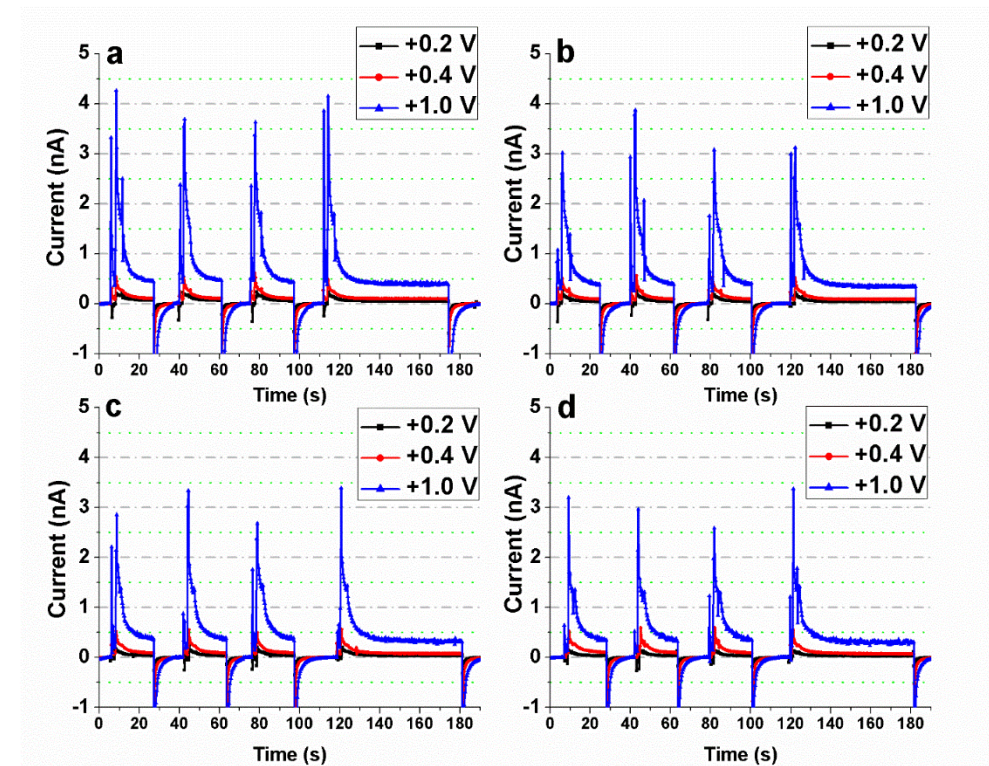
Figure 7.12: Repeatability measurements of the photoresponse from the reference device exposed to (a) 30 kV, (b) 26 kV, (c) 23 kV, and (d) 20 kV X-rays at different external bias voltages.

7.3.4.2 Measurements in the higher diagnostic range (40 to 100 kV X-rays)

Three different bias voltages were tested: +1, +1.5 and +2 V on both the nanoflower and the reference device. They were exposed for an interval of 18 s three times followed by a longer interval of 1 min in order to assess the repeatability and the stability of the photoresponse of the Bi_2S_3 nanoflowers and the substrate (Figures 7.13 and 7.14). Similar to the photoresponse curves for X-rays in the mammographic range, the photocurrent of the device with Bi_2S_3 nanoflowers, for each of the bias voltages, was much higher than that of the reference device. Interestingly, the response at lower external voltage (+1 V) decreased with repeated exposures (overall time-dependent reduction) and showed a temporal decrease at the longer exposure interval (1 min) for all tube potentials. This may be attributed to the loss of charge carriers at the lower bias voltage either due to recombination or trapping. At higher bias voltages (i.e. increased electric field), the photo-generated charge carriers (e-h pairs) could, presumably, lead to improved dissociation of the e-h pairs, and efficient collection at the electrodes resulting in stable photoresponse as observed in Figure 7.13. While the overall temporal loss of photo-carriers was not observed at the higher bias voltages, the highest operating voltage (+2 V) induced a form of space charge limited conduction wherein the photocurrent increased with time for the whole duration of exposure. In other words, the rate of charge injection from the electrodes (i.e. the interdigitated gold electrodes) was relatively higher than the rate of transport or recombination of the photo-carriers. At +1.5 V, the photoresponse was found to be stable and repeatable without the effects observed for +1 V and + 2 V.
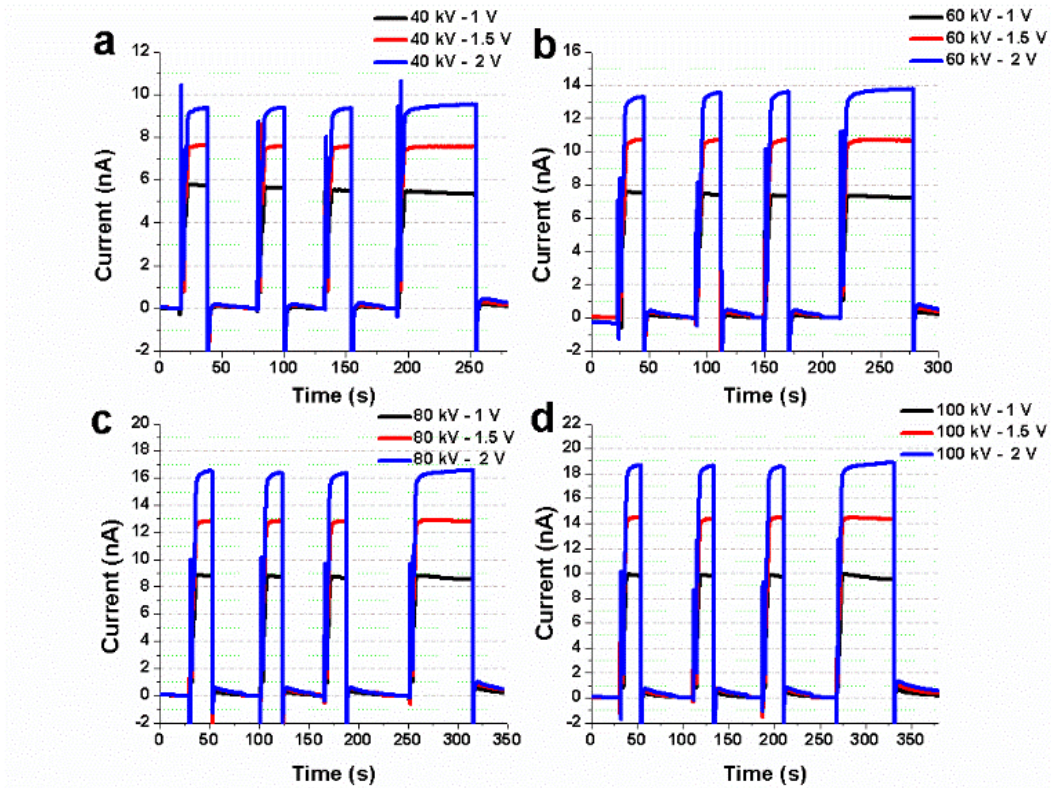
Figure 7.13: Repeatability measurements of the photoresponse from the Bi$_2$S$_3$ nanoflowers exposed to (a) 40 kV, (b) 60 kV, (c) 80 kV, and (d) 100 kV X-rays at different external bias voltages.
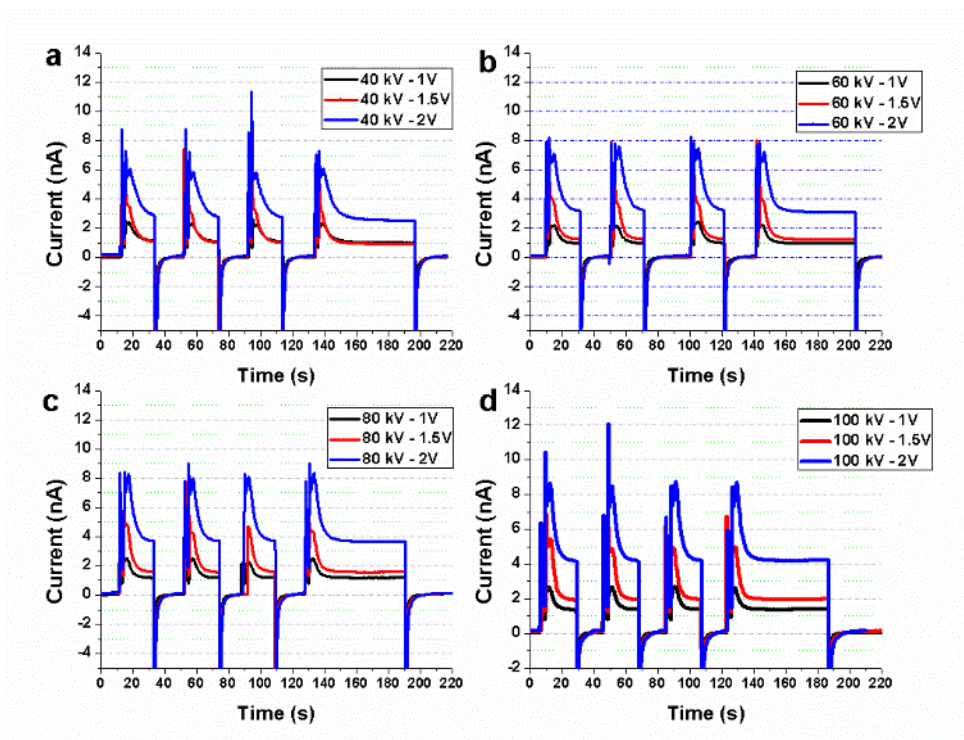
Figure 7.14: Repeatability measurements of the photoresponse from the reference device exposed to (a) 40 kV, (b) 60 kV, (c) 80 kV, and (d) 100 kV X-rays at different external bias voltages.

7.3.5 Sensitivity

In order to evaluate the sensitivity of the Bi_2S_3 nanoflowers with respect to changes in delivered dose, the time-averaged photoresponse of the nanoflowers was plotted as a function of relative dose (D-1/4, D-1/2, D-3/4, and D-1 normalized to D-1 respectively where D-1 is indicative of maximum dose delivered because of the least distance of the X-ray source from the sample). Figures 7.15 and 7.16 show a fairly linear relationship between the photocurrents from the nanoflowers and the relative dose delivered. The photocurrent at each of the doses, shown in the figures, correspond to time-averaged data over 11 and 52 s exposure intervals for the X-rays in the mammographic and higher diagnostic range respectively.

The photoresponse of the nanoflowers increased by about 241%, for both 20 and 30 kV, when the dose was increased by four times the minimum value (i.e. maximum focus-to-surface distance of 30.4 cm from the sample) under a bias voltage of +1 V. The photoresponse of the nanoflowers to 40 and 100 kV X-rays was found to increase by 248% and 220% respectively for the maximum dose response relative to the minimum (i.e. percentage increase in response at D-1/4 to D-1) as shown in Figure 7.16. Moreover, the signal from the Bi_2S_3 nanoflowers shows a dose-dependent behaviour i.e. the photocurrent increased linearly with increase in the X-ray dose (Figures 7.15 and 7.16). The overall photosensitivity of the Bi_2S_3 nanoflowers had a trend similar to the measurements obtained from the micro-ionization chamber showed as an inset in the figures. The photocurrent at 30 kV for the maximum dose was found to vary the most, with a standard deviation of 91 pA, compared to those at other doses and energies.
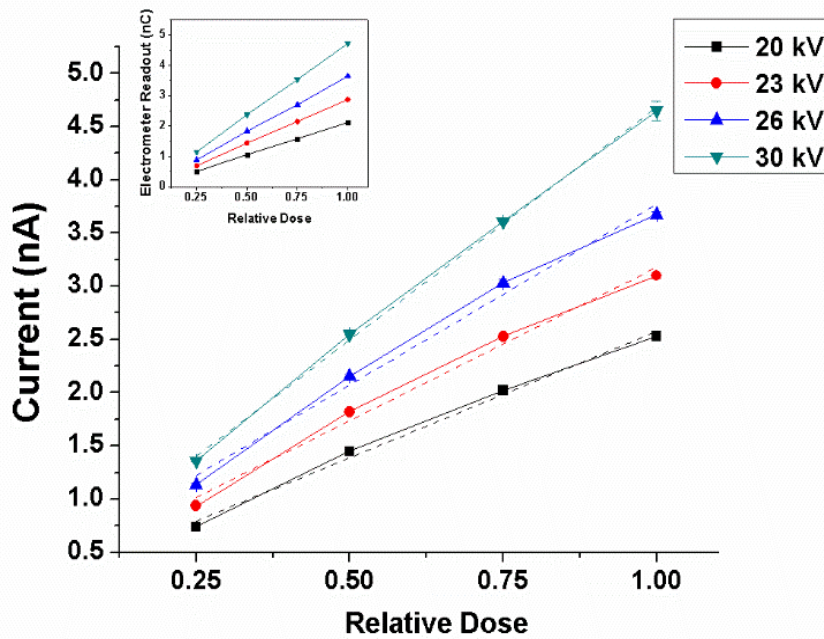
Figure 7.15: X-ray sensitivity curves for Bi_2S_3 nanoflowers at tube-potential of 20 to 30 kV. The photocurrent, at each of the relative doses, correspond to time-averaged data over 11 s of 'X-ray ON' state. The inset shows the dose measurements (electrometer readouts) using the micro-ionization chamber.
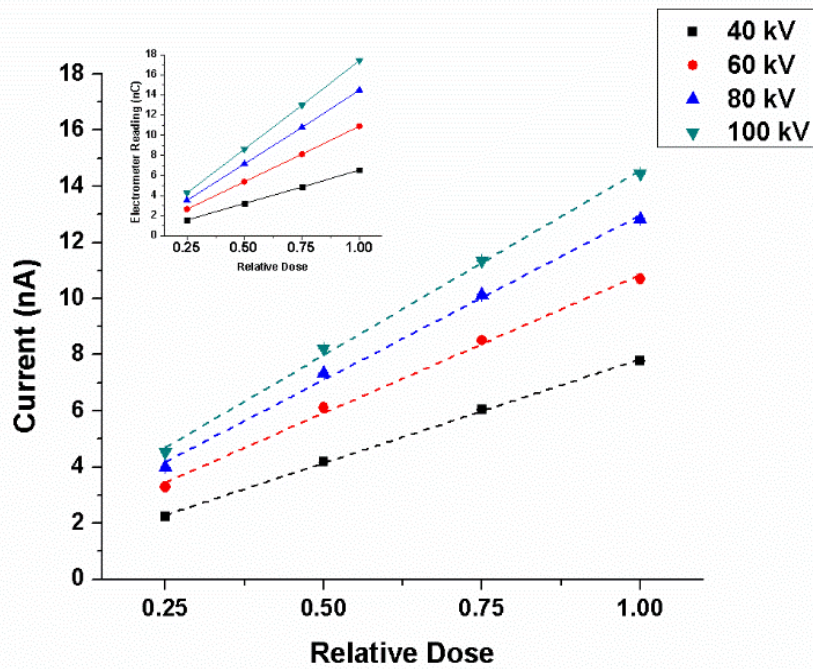
Figure 7.16: X-ray sensitivity curves for Bi_2S_3 nanoflowers at tube-potential of 40 to 100 kV. The photocurrent, at each of the relative doses, correspond to time-averaged data over 52 s of 'X-ray ON' state. The inset shows the dose measurements (electrometer readouts) using the micro-ionization chamber.

147

In order to evaluate the sensitivity of the Bi_2S_3 nanoflowers relative to the substrate, time-averaged photoresponse of the nanoflower device (denoted as 'sample' in Figures 7.17 and 7.18) was plotted along with those of the reference device (denoted as 'control') at the minimum and maximum tube potentials from each of the two sets of X-ray energies considered in this study. It is evident that the photoresponse of the nanoflowers linearly increased with increase in dose such the response was several folds higher compared to the substrate, particularly at the maximum dose.
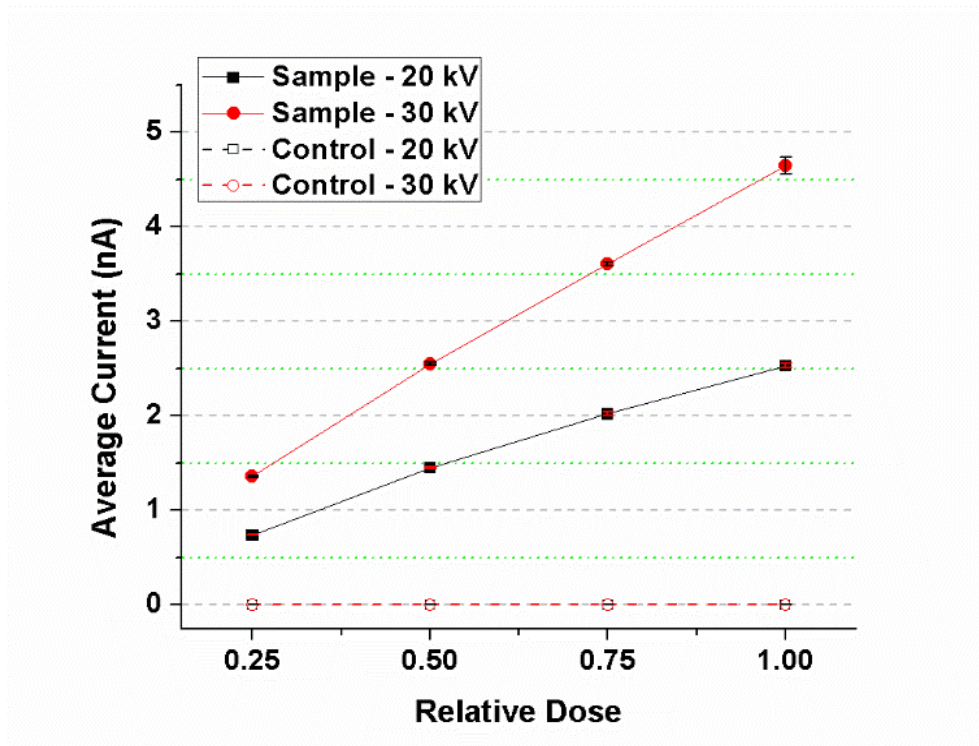
Figure 7.17: Comparison of photocurrents, time-averaged over 11 s, measured from the Bi_2S_3 nanoflowers (sample) and the reference device (control) at tube-potential of 20 and 30 kV.
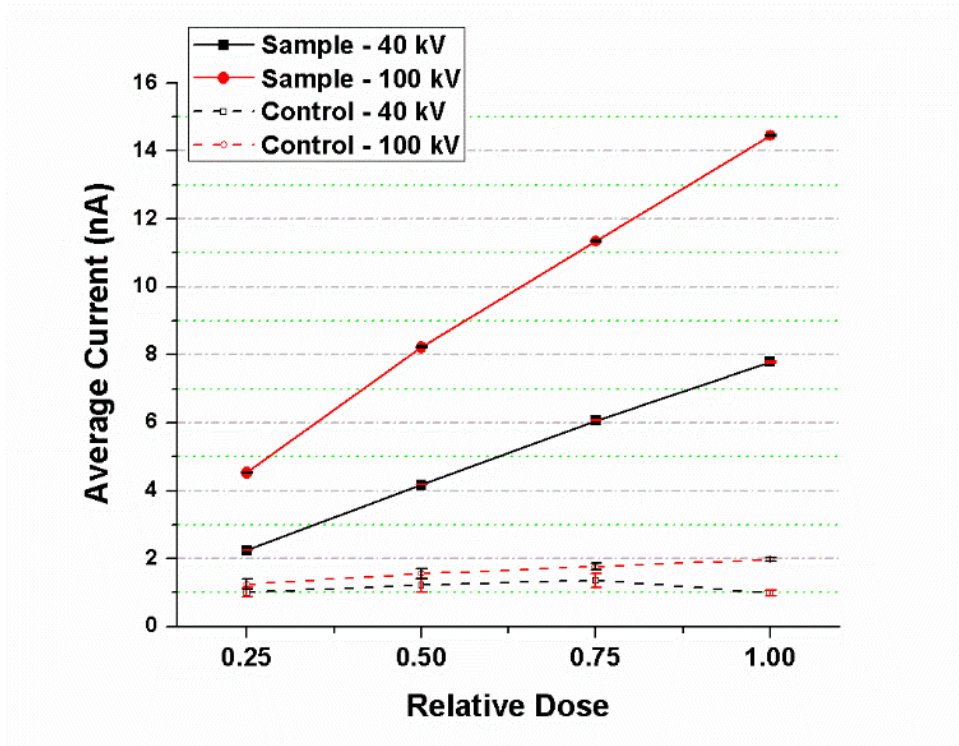
Figure 7.18: Comparison of photocurrents, time-averaged over 52 s, measured from the Bi_2S_3 nanoflowers (sample) and the reference device (control) at tube-potential of 40 and 100 kV.

Three main factors that affect sensitivity of a photoconductor are: (i) amount of radiation attenuated within the material, (ii) generation of charge carriers (i.e. e-h pairs), and (iii) charge collection efficiency.[126] Attenuation of the incident X-rays can be quantified in terms of the quantum efficiency (QE) which is given by the following equation:

$$QE = 1 - e^{-\mu t}$$

where μ is the linear attenuation coefficient and t is the thickness of the photoconductor. The attenuation coefficient is a function of the incident photon energy, Z, and density of the material. The mass attenuation coefficients for the energies of interest (determined from SpekCalc simulations) were calculated using WinXCom software[123] (Table 7.2). A screenshot of the WinXCom software interface is presented in Appendix A (Figure A-6). At lower X-ray energies,

the mass attenuation coefficient of the Bi_2S_3 nanoflowers decreased with increase in the energy (tube potentials 20 to 30 kV) indicative of larger interaction cross-section for the incident photons at 20 kV compared to that at 30 kV (Table 7.2). Similarly, the calculated mass attenuation coefficient of the Bi_2S_3 nanoflowers decreased from 40 to 100 kV (Table 7.3). However, the increase in the photoresponse with increase in the tube potential can be attributed to the interaction between the relatively high-energy incident beam and the nanoflowers. The high energy photons would lose or deposit energy knocking out relatively more number of electrons contributing to increase in photocurrents with increase in tube potential. Another factor to be considered is the penetration depth, defined as the reciprocal of linear attenuation coefficient. The penetration depth needs to be much lower than the thickness of the photoconductor for sufficient interaction (i.e. attenuation) with the incident X-ray photons. The penetration depth for each of the energies is also presented in Tables 7.2 and 7.3.

Table 7.2: Mass attenuation coefficient and the corresponding penetration depth for Bi_2S_3 nanoflowers at each of the tube potentials (20 to 30 kV) as determined from SpekCalc simulations and calculated using WinXCom software.[123]

X-ray tube potential (kV)	Mean energy (keV)	Mass attenuation coefficient (cm^2/g)	Penetration depth (µm)
20	9.78	127	11.6
23	10.6	103	14.32
26	11.4	85.9	17.17
30	12.4	69.3	21.28

Table 7.3: Mass attenuation coefficient and the corresponding penetration depth for Bi_2S_3 nanoflowers at each of the tube potentials (40 to 100 kV) as determined from SpekCalc simulations and calculated using WinXCom software.

X-ray tube potential (kV)	Mean energy (keV)	Mass attenuation coefficient (cm^2/g)	Penetration depth (µm)
40	14.8	101	14.6
60	20	74	19.93
80	26.2	36.8	40.1
100	33.6	19.4	76.03

Although large interaction cross-sections increase the possibility of charge carrier generation through ionization and/or excitation processes, the second factor that determines the sensitivity of the nanoflowers to X-rays is the ability to generate as many collectable charge carriers (e-h pairs) as possible per unit of absorbed radiation. The energy required for a single e-h pair generation, also known as the ionization energy (IE), of the nanoflowers can be roughly estimated from the bandgap energy (E_g) by using the Klein rule for crystalline semiconductors: $IE \approx 3E_g = 3 \times 1.33 \text{ eV} = 3.99 \text{ eV}$.[126] The bandgap of the Bi_2S_3 nanoflowers ($E_g = 1.33$ eV) was obtained from the UV-Vis reflectance measurements. The narrow bandgap of 1.33 eV approximates to a relatively low ionization energy of 3.99 eV for the nanoflowers. In other words, lower value of ionization energy for photoconductor is favored to generate as many e-h pairs as possible upon irradiation thereby allowing higher sensitivity to X-rays. Finally, the last factor that affects the sensitivity is the charge collection efficiency (CCE) of the device. The CCE is directly proportional to the product of the charge carrier (e-h pair generated upon irradiation) drift mobility, its lifetime and the electric field applied across the electrodes (i.e. external bias voltage), and inversely proportional to the thickness of the photoconductor. In order

to maximize CCE, there should be no loss of the charge carriers through recombination or trapping.

Since the Bi_2S_3 nanoflowers were dropcasted on the electrodes, the resultant film was apparently non-uniform in thickness. The reduction in the CCE and the variation in penetration depths for each of the energies have been considered to speculate the gradual loss in sensitivity observed for the repeatability measurements described earlier (Figures 7.11 and 7.13). Of all the energies in the mammographic range and the bias voltages used for that range, only 30 kV at an operating voltage of +1 V was found to have a relatively higher loss in the overall sensitivity for repetitive measurements. From the relatively high photoresponse measured at 30 kV, it is evident that the film of Bi_2S_3 nanoflowers has sufficient penetration depth (at least in some areas of the film) to produce maximum charge carriers (or photocurrent) at the maximum tube potential used in this study. Because of the uneven thickness of the Bi_2S_3 nanoflower film, the higher photoresponse at 30 kV (i.e. generation of more charge carriers) imply a higher possibility of charge trapping or recombination at this energy when compared to rest of the lower X-ray energies considered in this study. Furthermore, an overall temporal loss in the signal at the 'X-ray ON' states for 30 kV could also be attributed to possible reduction in the CCE. The CCE can be adversely affected from localized changes in sensitivity due to previous exposures (i.e. X-ray induced trap centers) and/or recombination of drifting charge-carriers with previously trapped oppositely charged carriers. The overall loss in sensitivity for 30 kV, is thus, speculated to be from the loss of charge carriers (reduction in the mobility $\times$ lifetime product) within the relatively thinner parts of the nanoflower film which possibly act as recombination/trapping sites.

It is interesting to note the effects of applied electric field on the sensitivity of the nanoflowers at lower X-ray energies (tube potentials 20 to 30 kV). When the bias voltage across the IDE was

increased from +0.2 to +1 V, the signal loss within each of the 'X-ray ON' states improved such that the photoresponse at +1 V for each 'X-ray ON' state was observed to be fairly stable in contrast to that at lower bias voltages. The higher electric field led to efficient charge separation and collection avoiding charge loss through bulk recombination thereby improving the CCE, and hence the sensitivity. It may also be presumed that for bias voltages greater than +1 V, the temporal loss of sensitivity at 30 kV may significantly reduce as observed in the repeatability assessment curves of Bi_2S_3 nanoflowers for higher diagnostic energies (Figure 7.13).

7.4 Conclusions

Hydrothermally synthesized nanoflower-like structures of Bi_2S_3 were investigated as a potential candidate for semiconductor-based X-ray sensing material. Recently, nanocrystalline materials have been reported to have interesting properties such as enhanced radiation resistance owing to the large volume fraction of grain boundaries that may serve as effective sinks for defects generated upon irradiation.[41] Reliability and durability are among the important features of an ideal dosimeter. Hence, the 'self-repairing' mechanism of nanomaterials may be exploited by extending their application in the development of novel, nanomaterial-based X-ray dosimeters with increased lifetimes. Moreover, the effective atomic number (Z_{eff}) plays an important role in the interaction mechanisms between the X-rays and the target material. These interactions are directly responsible for the generation of charge carriers required for effective photoconductivity. The relatively high Z_{eff} of the Bi_2S_3 nanoflowers favors photoelectric interaction pathway even at the low X-ray energies and doses considered in this study.

Instantaneous photoresponse of Bi_2S_3 nanoflowers to changes in X-ray energy/dose is evident from the results shown in Figures 7.3 and 7.4. Evaluation of different field sizes, particularly those much smaller than the active region of detection, showed an average photocurrent in the

order of several hundreds of pA at X-ray tube potential as low as 20 kV (Figure 7.9). The results indicate the possibility of using the Bi_2S_3 nanoflowers in miniaturized dosimetric applications. Furthermore, photoresponse of the Bi_2S_3 nanoflowers were found to be repeatable and stable for both short (18 s) and long (1 min) exposures (Figures 7.11 and 7.13). Except for the charge trap/release effects ("negative current" at the instance of 'X-ray OFF' state), the overall response of the substrate to X-rays was found to be negligible in comparison to that measured from the Bi_2S_3 nanoflower device. It is important to note that the overall sensitivity of the Bi_2S_3 nanoflower device showed similar trend to that of a micro-ionization chamber (Figures 7.15 and 7.16) at a minimal operating voltage of +1 or +1.5 V compared to the +300 V required for operating the ionization chamber.

To conclude, the performance of the Bi_2S_3 nanoflowers have been assessed under various conditions such as tube potentials and dose delivered in both the mammographic and the higher diagnostic range, different bias voltages, and X-ray field sizes; all measurements were carried out under ambient conditions. The photoresponse of the nanoflowers clearly showed high sensitivity to changes in X-ray intensities, the capability to operate at a bias voltage as low as +0.2 and +1 V for mammographic and higher diagnostic energies, respectively, and the potential to perform as a reliable dosimetric material for instantaneous dose measurements under the whole range of diagnostic X-rays.

Chapter 8

Direct Detection of X-rays in the Diagnostic Energy Range using Flexible P3HT/Bi$_2$S$_3$-nanoflower Composite Device

8.1 Introduction

X-ray dosimetry is essential in medical radiology for applications such as radiation monitoring for safety purposes, X-ray dose calibrations, treatment planning, X-ray image-guided procedures, etc. For these applications, conventional detectors such as thermoluminescent dosimeters, low spatial-resolution ionization chamber diode array, self-developing radiographic film or high resolution flat panel digital imagers are often used. However, none of these dosimeters allow actual conformability along with high resolution, real-time detection (discussed in detail in Chapter 2). In this regard, polymer-based X-ray detectors can, potentially, be used to develop real-time, conformable, large area dosimetry with high resolution; the features that are especially attractive for radiological applications such as wearable dosimeters for radiation monitoring, dose-depth profile or dose distribution profile over a plane within or on the surface of phantoms generally used in radiation therapy.

In this study, a p-type semiconducting organic polymer, poly(3-hexylthiophene-2,5-diyl) (P3HT) has been investigated for clinical dosimetric applications that use X-rays in the diagnostic energy range. Based on the performance of the Bi$_2$S$_3$ nanoflowers for X-ray detection (presented in Chapter 7), they were used as filler in P3HT to develop novel P3HT/Bi$_2$S$_3$-nanoflower composite. The devices were developed on flexible polyimide substrate coated with chromium and gold (20 and 200 nm thick respectively) to impart conformability feature. The P3HT-based active detection layer was then dropcasted on the substrate followed by e-beam evaporation of top electrode (150 nm thick aluminum layer). The overall thickness of the detector should be

roughly around 150 microns. In order to study the role of Bi_2S_3 nanoflowers in X-ray detection, device with pure P3HT film was also investigated under similar conditions. The devices were exposed to four different tube potentials (26, 40, 60 and 100 kV) under six different operating voltages. Based on the results, the devices were biased with a voltage as low as -40 mV at the gold electrode and exposed to various 'cumulative dose' achieved by increasing the duration of consecutive exposures. Repeatability of the measurements at two different time periods were also assessed for both pure P3HT and P3HT nanocomposite devices.

8.2 Materials and Methods

8.2.1 Sample preparation

High molecular weight, electronic grade, organic semiconducting p-type polymer, poly(3-hexylthiophene-2,5-diyl) (P3HT, Product#: 698997, Sigma-Aldrich Canada Co.) solution was prepared by overnight stirring of 40 mg of P3HT powder in 2 ml of 1, 2-Dichlorobenzene (Product #: 240664, Sigma-Aldrich Canada Co.) at 40 ºC. P3HT nanocomposite was prepared by mixing 10 mg of Bi_2S_3 nanoflowers (synthesized using the hydrothermal method presented in Chapter 7) in 500 µL of P3HT solution followed by ultrasonication for 15 min.

8.2.2 Device fabrication

Pure P3HT and P3HT nanocomposite were used as active sensing materials to fabricate flexible devices on 25.4 micron thick Kapton® polyimide film coated with chromium (30 nm thick) and gold (200 nm thick). The chromium (Cr) and gold (Au) were deposited through e-beam evaporation technique (Intlvac thermal/e-beam evaporator). The Au/Cr polyimide substrate was then cut into 1 square inch pieces for deposition of P3HT solution. In order to minimize

bending/folding of the flexible substrate and to ensure uniform deposition of other layers, the Au/Cr/polyimide sheet was taped onto a microscopic glass slide with Kapton tape. P3HT layer deposition for both pure P3HT and P3HT-nanocomposite devices was achieved by dropcasting 150 μL of the solution on the polyimide/Cr/Au substrates placed on a hotplate heated at ~100 ℃ for about 15 min. For the top electrode, aluminum (Al, ~150 nm thick) was deposited using an e-beam evaporator (Intlvac thermal/e-beam evaporator). The device fabrications steps are presented in Figure 8.1. Finally, Kapton tape, with a small opening to access the top electrode (Al), was used to encapsulate the polymer or the nanocomposite in order to minimize any environmental degradation (such as oxidation) of P3HT. Two micro-positioners (Cascade Microtech), each attached with a tungsten microprobe tip, were used for obtaining contact with each of the electrodes (Au and Al) on the device.
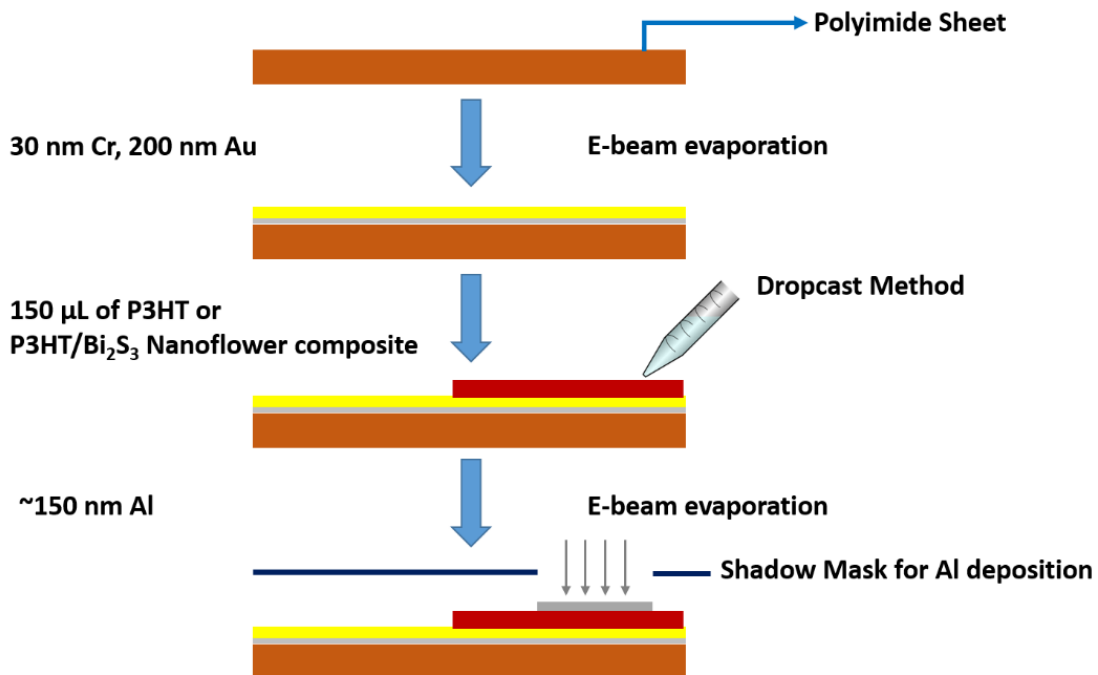
Figure 8.1: Steps involved in fabrication of pure P3HT or P3HT/Bi$_2$S$_3$-nanoflower device on flexible polyimide substrate.

8.2.3 Measurements

All measurements were performed at the superficial X-ray facility (Gulmay Medical Inc.) at the Grand River Regional Cancer Center (Kitchener, Ontario, Canada). An aperture of diameter 1 cm (cone diameter) was used in this study. The X-ray tube-current was set to 20 mA for all tube potentials. No external filters were used. All measurements were performed at a distance of 15.1 cm from the X-ray source (distance estimated by including the preset focus-to-surface distance of 15 cm, and 1 mm air gap between the tip of the cone and the surface of the device). Since both P3HT and Bi_2S_3 nanoflowers were sensitive to light, all measurements were conducted in the dark but at room temperature. The devices were irradiated from the Al electrode side. External bias voltage was applied on the Au electrode.

A micro-ionization chamber (Exradin 0.016 cc, model A14) along with an electrometer (Dose-1) was used to measure the dose (i.e. cumulative charge over the exposure period) for all energies. The ionization chamber readings were used to compare the overall sensitivity of the P3HT devices.

8.3 Results and Discussion

In order to investigate the effects of the Bi_2S_3 nanoflowers on the photoresponse of the devices, both pure P3HT and P3HT-nanocomposite films were exposed to X-rays under the same experimental settings. The response of the P3HT device with and without Bi_2S_3 nanoflowers were measured under:

(i)   Different external bias voltages: ±20, ±40 and ±100 mV.

(ii)   Four different X-ray tube-potentials (26, 40, 60 and 100 kV).

(iii)   X-ray dose by varying exposure intervals (18, 36, 54, and 72 s).

8.3.1 Effects of external bias voltage

The effects of various bias voltages on the pure P3HT device is shown in Figure 8.2. As expected, the dark (or leakage) current of the device increased with increase in the bias voltage (both positive and negative). Based on the performance of Bi_2S_3 nanoflowers for dosimetric applications (detailed in Chapter 7), a polymer nanocomposite was fabricated with 10 mg of nanoflowers dispersed in 20 mg/mL of P3HT solution. The effects of bias voltage were investigated for the P3HT nanocomposite as well (Figure 8.3). Upon irradiation of pure P3HT device with 100 kV X-rays, the photocurrents for all positive bias voltages decreased with respect to the dark current value indicating a photoresponse causing a reversal of current flow. This effect can be attributed to the radiation-induced generation of excess charge carriers (mainly electrons) on the Al electrode (top electrode) through photoelectric interactions with the incident photons. The speculation is validated from the photoresponse observed for P3HT nanocomposite in Figure 8.3 wherein the n-type Bi_2S_3 nanoflowers would also produce relatively higher number of photo-induced electrons resulting in amplification of the photocurrent reversal observed in the pure P3HT device (as seen in the magnitude of the photocurrent in Figures 8.2 and 8.3 at any given positive bias voltage).

In contrast, a negative bias (on Au) favours the flow of high density of the excess photo-carriers generated at the P3HT/Al interface, hence increasing the photocurrent with respect to the corresponding dark current (Figures 8.2 and 8.3). Moreover, the overall differential between the measurements before and after exposure to 100 kV X-rays for the pure P3HT device, operated in positive bias mode, was less than that obtained at negative bias (Table 8.1). In fact, the X-ray sensitivity of the pure P3HT device increased with increase in the negative bias while the opposite effect was observed at higher positive bias (Table 8.1). Similar to the results obtained

for the pure P3HT film, the dark current increased with increase in bias voltage. The photocurrent trend was similar but with an overall higher magnitude for all operating voltages (Table 8.2). The differences between the photo- and dark-currents were found to linearly increase with negative bias voltage (Figure 8.3 and Table 8.2). These results indicate that the p-type P3HT probably forms an ohmic contact with the Au electrode due to similarities in the Fermi level of Au (-5.1 eV) and its 'highest occupied molecular orbital' (HOMO; -5 eV), while at the Al interface the P3HT forms a rectifying type of contact owing to the differences in the Fermi level of Al (-4.1 eV) which results in a depletion region at the Al/P3HT interface. The depletion region in turn leads to band bending that acts as a barrier to hole injection from P3HT to Al. A negative bias applied to the Au electrode further widens the depletion region at the Al/P3HT interface. Upon irradiation, the electrons generated in the semiconducting region (P3HT or P3HT nanocomposite) readily gets attracted towards Al electrode while the holes flow the opposite direction (towards Au) owing to the hole-injection barrier at the Al/P3HT interface. However, the bias voltages used in this study were probably not comparable to the voltages generally reported in organic semiconductor-based diodes operated in reverse bias mode (roughly in the range of -10 to -300 V) for X-ray or gamma ray dosimetric applications.[54, 55, 73-75] Hence, the reduction in dark currents were not very substantial in the range of voltages employed in this study. However, it is important to note that X-ray induced conductivity was favoured in the negative bias mode (i.e. reverse bias) in both the P3HT devices.
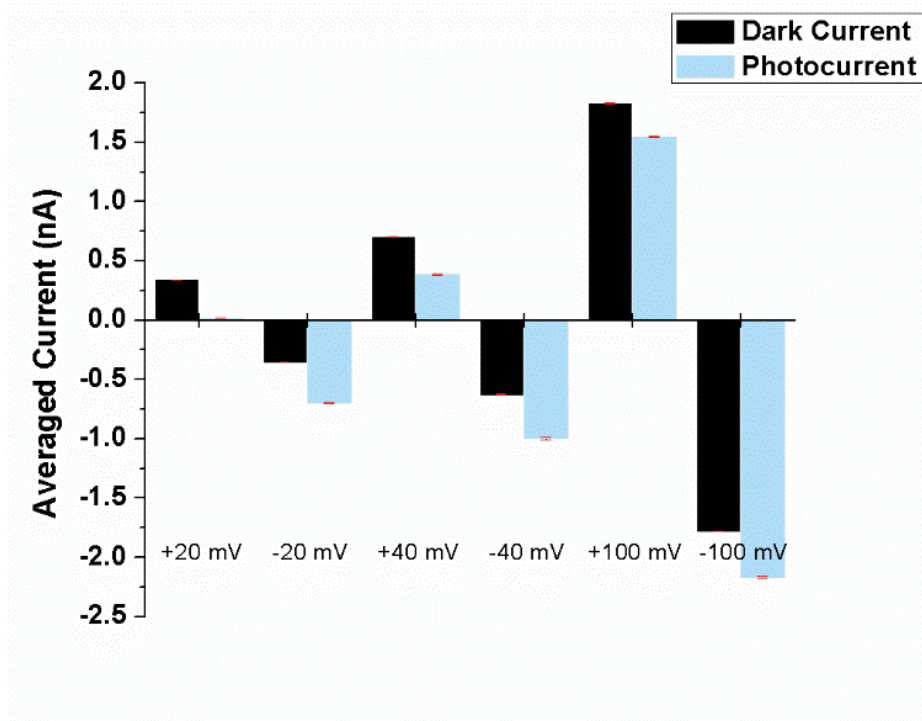
Figure 8.2: Pure P3HT device response, averaged over 13.8 s, at various external bias voltages (+20, -20, +40, -40, +100 and -100 mV). Note that the photocurrent at +20 mV was found to be significantly low (0.0102 nA).
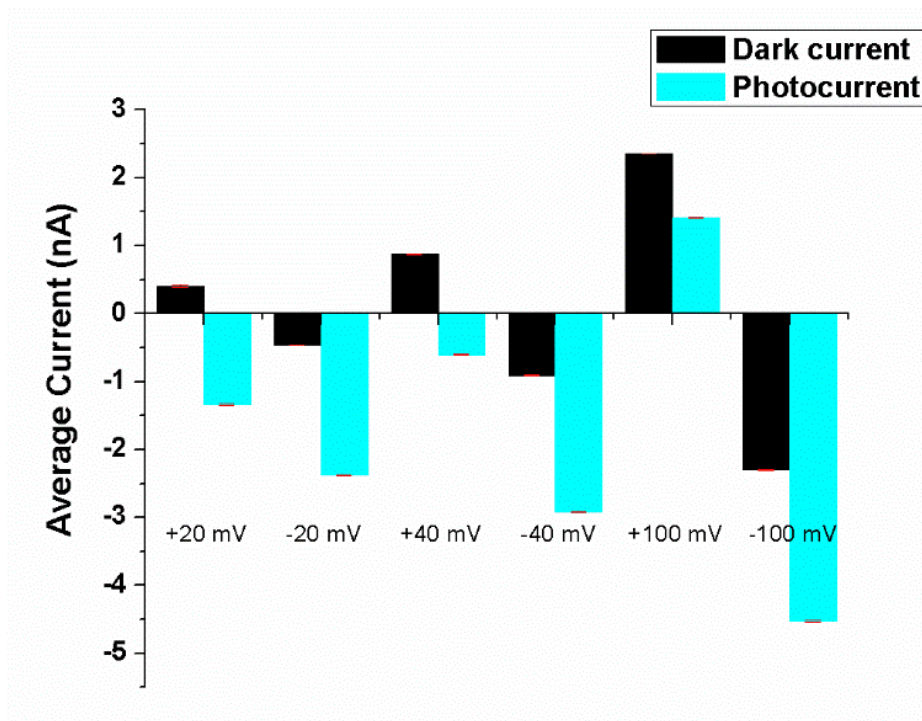
Figure 8.3: P3HT/ Bi$_2$S$_3$-nanoflower device response, averaged over 13.8 s, at various external bias voltages (+20, -20, +40, -40, +100 and -100 mV).

Table 8.1: Effects of external bias voltage on the response of pure P3HT before and after irradiation with 100 kV X-rays.

External bias voltage (mV)	Absolute difference between the photocurrent and dark current measurements (nA)
+20	0.329
+40	0.319
+100	0.282
-20	0.345
-40	0.370
-100	0.387

Table 8.2: Effects of external bias voltage on the response of P3HT/ Bi_2S_3-nanoflower composite before and after irradiation with 100 kV X-rays.

External bias voltage (mV)	Absolute difference between the photocurrent and dark current measurements (nA)
+20	1.75
+40	1.48
+100	0.94
-20	1.93
-40	2.02
-100	2.23

In order to evaluate the role of Bi_2S_3 nanoflowers in signal enhancement, the percentage increase in the photocurrent with respect to pure P3HT was calculated, at each of the bias voltages, based

on the values listed in Tables 8.1 and 8.2. The addition of nanoflowers dramatically increased the overall photosensitivity of the nanocomposite device compared to the pure P3HT device (Table 8.3). Furthermore, the photoresponse of P3HT/Bi$_2$S$_3$-nanoflower composite was greater than 445% at all the negative bias voltages. From all the results, it is evident that both the devices showed a relatively significant improvement in the negative bias mode (i.e. negative potential applied to the Au electrode). For all the measurements presented in sections 8.3.2 to 8.3.4, a bias voltage of -40 mV was used. For ease of comparison of the performance of the P3HT devices under various tube-potentials and doses, dark current measurement was subtracted from the corresponding photocurrent for all measurements to represent the instantaneous change in the response at beam ON/OFF state.

Table 8.3: Percentage increase in the photoresponse of the nanocomposite compared to those of pure P3HT under 100 kV X-rays.

External bias voltage (mV)	Photodetection enhancement factor of nanocomposite with respect to pure P3HT (%)
+20	431.91
+40	363.95
+100	233.33
-20	459.42
-40	445.94
-100	476.23

8.3.2 Effects of X-ray tube potentials

The photoresponse of both the P3HT/Bi$_2$S$_3$-nanoflower and pure P3HT devices were plotted as a function of time under each of the four different X-ray tube potentials representative of both mammographic and higher diagnostic energies (26, 40, 60 and 100 kV). The exposure intervals were varied for each of the tube potentials. The photoresponse of the nanocomposite (Figure 8.4) was relatively more stable and repeatable over varying exposures than those of the pure P3HT film (Figure 8.5). A time interval of 18 s was observed in P3HT/Bi$_2$S$_3$-nanoflower device in order for the X-ray-induced current to stabilize in almost all of the tube potentials, while the photoresponse of pure P3HT device required ~ 21 s at 26 kV to stabilize. Moreover, the magnitude of the X-ray induced photocurrent in the nanocomposite was relatively much greater than those of pure P3HT. The photocurrents measured from the P3HT/Bi$_2$S$_3$-nanoflower device (for an exposure of 36 s) was plotted as a function of tube potential as shown in Figure 8.6. The overall trend is similar to that of the micro-chamber readings measured for an exposure of 36 s. The sensitivity of the nanocomposite with respect to pure P3HT is discussed in the next section.
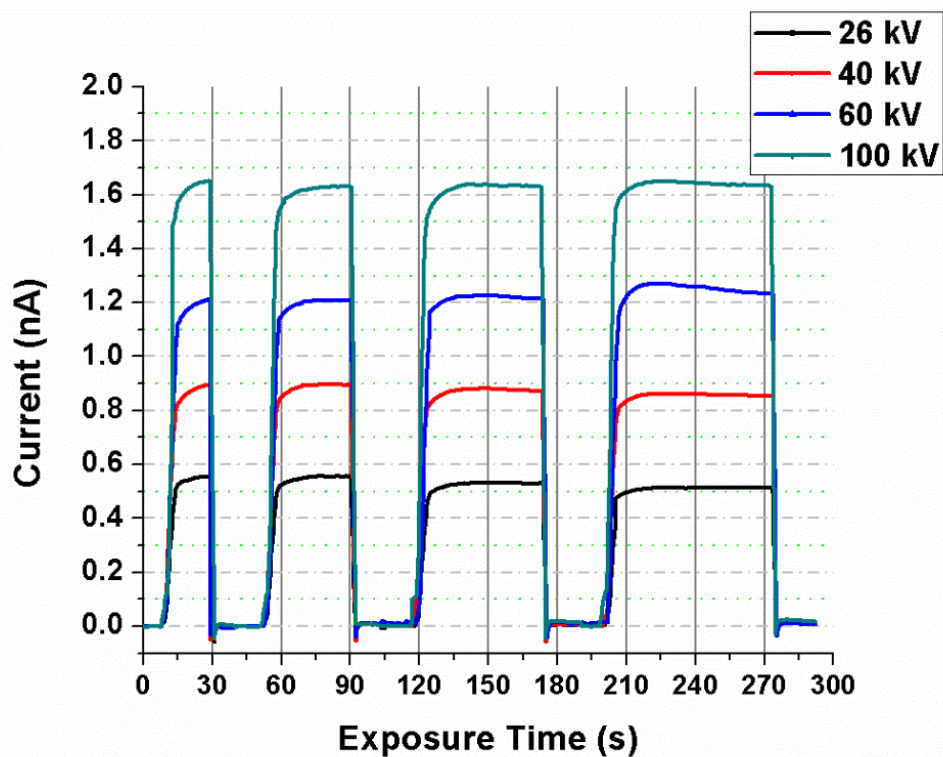
Figure 8.4: P3HT/ Bi_2S_3 -nanoflower device response at various exposure intervals (18, 36, 54, and 72 s) for each of the four tube-potentials (26, 40, 60, and 100 kV).
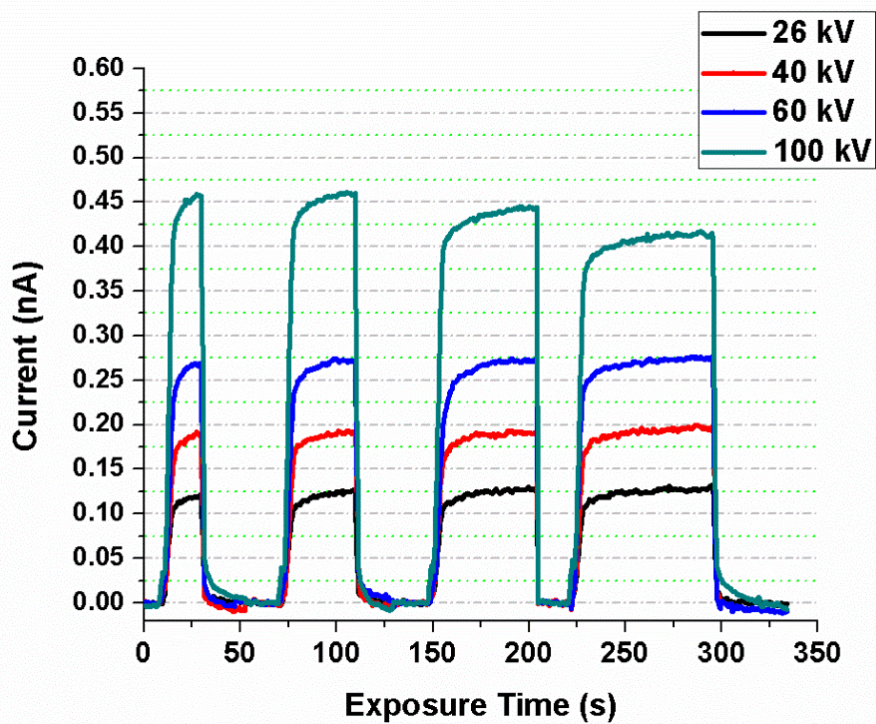
Figure 8.5: Pure P3HT device response at various exposure intervals (18, 36, 54, and 72 s) for each of the four tube-potentials (26, 40, 60, and 100 kV).
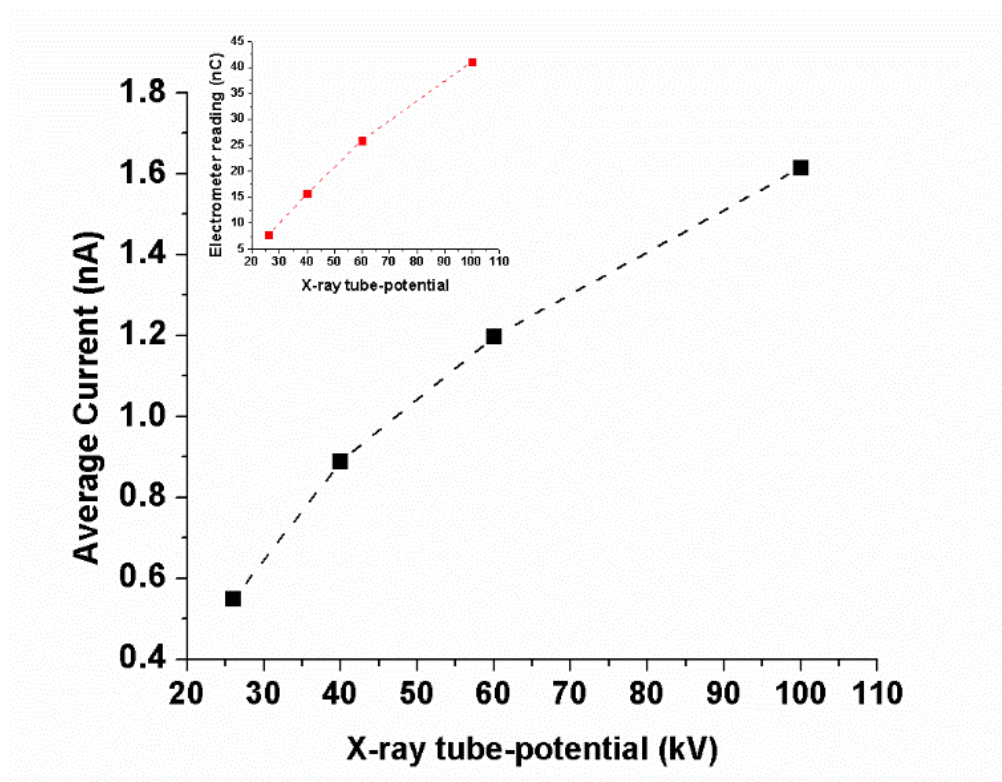
Figure 8.6: Average photocurrent obtained at different tube potentials in the P3HT/Bi$_3$S$_3$-nanoflower composite device. For comparison, micro-chamber readings, in terms of cumulative charge (nC), is shown in the inset.

8.3.3 Dose dependence and Sensitivity

Since the cumulative dose delivered linearly increases with exposure time, the effects of dose dependent variations in the device photoresponse were based on varying the exposure intervals (18, 36, 54 and 72 s). The relative-dose measurement-setup used in the study of X-ray detection using nanoflowers on IDE (Chapter 7) could not be used in this work because of the feasibility issues in restricting the field size with a lead cut-out while using microprobe positioners. Therefore, the cumulative current (dose response) was estimated for each of the four exposure intervals for the nanocomposite device (Figure 8.7). The cumulative current linearly increased with exposure time. At 26 and 100 kV, the relative change in response from the minimum to maximum dose was found to be 332% and 364% respectively. The overall response was also

166

found to be similar to the readings from a micro-ionization chamber (in nC) exposed to different tube potentials and exposure intervals (Figure 8.6).
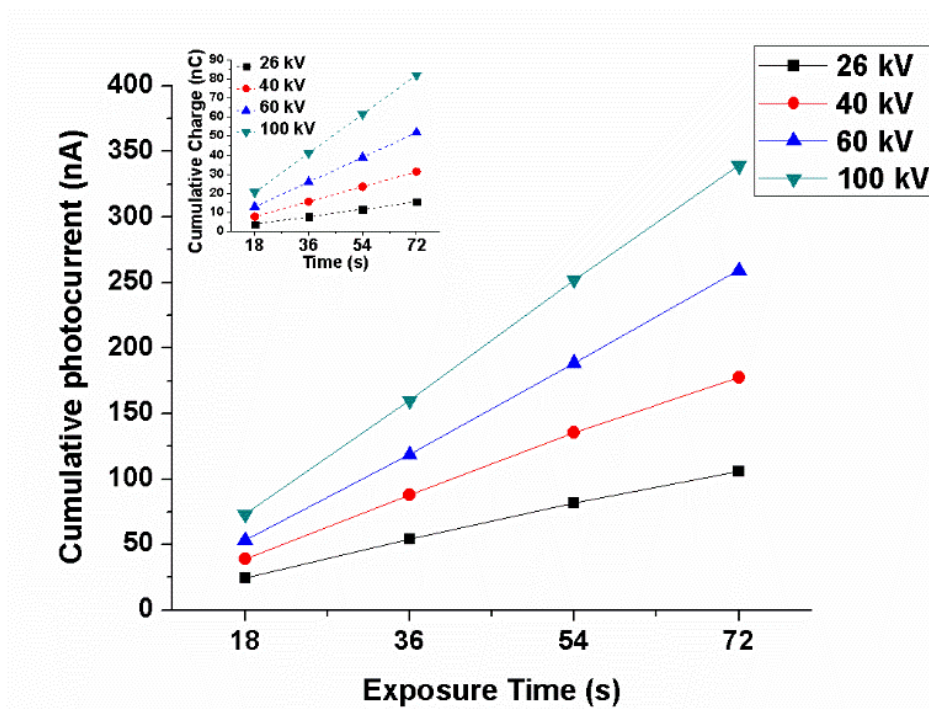
Figure 8.7: Sensitivity curves for P3HT/Bi$_2$S$_3$-nanoflower device exposed to 18, 36, 54, and 72 s. The inset shows micro-chamber readout (cumulative charge) for comparison.

In order to compare the relative enhancement in the photoresponse, the cumulative current from the nanocomposite device was plotted along with that from the pure P3HT (Figure 8.8). Clearly, the magnitude and the overall sensitivity (as observed from the slope of the line joining the data points) of the device with Bi$_2$S$_3$ nanoflowers were much higher than the pure P3HT polymer. For example, at the maximum dose under 100 kV X-rays, the nanocomposite device had 4 times the sensitivity of the pure P3HT device. The enhancement in photoresponse can be attributed to the increased effective atomic-number of the nanocomposite which in turn increase the probability of photoelectric interaction between the incident photons and the target atoms (in this case, P3HT/Bi$_2$S$_3$-nanoflower composite). The ability of the Bi$_2$S$_3$ nanoflowers to harvest more photon

energy increased the overall interaction cross-section and allowed for generation of relatively large number of photo-carriers resulting in dramatic improvement in the X-ray induced current in the P3HT nanocomposite device.
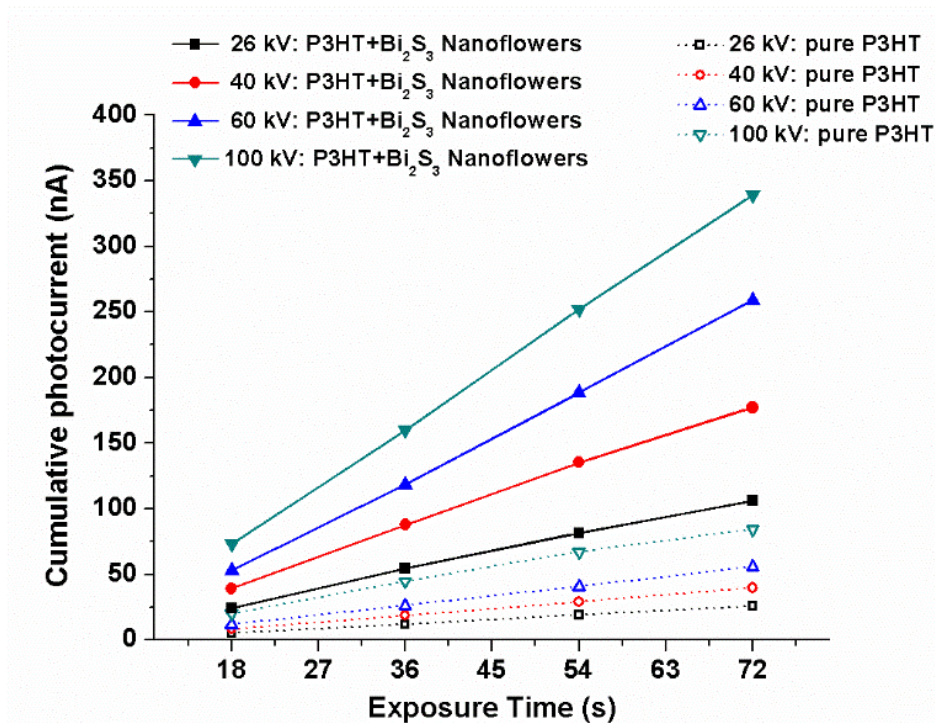
Figure 8.8: Comparison of cumulative photocurrent from P3HT/Bi$_2$S$_3$-nanoflower and pure P3HT device.

Only a few studies have reported the use of P3HT for direct detection of clinical X-rays or gamma rays.[51, 56, 127] Raval et al.[51, 56] reported changes in resistance of P3HT-based organic field effect transistor as a function of dose delivered from Cobalt-60 radiation source. Owing to the differences in the radiation source, dose delivered, and the method of detection, their results cannot be directly compared with our study. However, some comparison on device performance can be drawn from a recent study by Elshahat et al.[127] The authors reported direct detection of diagnostic X-rays from organic photovoltaic device using P3HT along with an n-type organic polymer, phenyl-C61-butyric-acid-methyl-ester (PCBM). The P3HT:PCBM active layer was

sandwiched between aluminum and indium tin oxide, and exposed to 60 to 100 kV X-rays with a time-integrated beam current of 200 mAs. The photocurrent of the Al/P3HT:PCBM/ITO device was reported to range from 0.69 to 2.43 nA/cm^2 as a function of X-ray energy between 60 and 150 kV respectively. In comparison, the photoresponse (in nA/cm^2) measured in our study would be 1.57 and 2.09 nA/cm^2 under X-ray tube potential of 60 and 100 kV respectively. It is important to note that the results can only be roughly compared since the photoresponse can vary with bias voltage, X-ray tube current (mA), exposure time (s), beam quality, and/or backscatter factor.

8.3.4 Repeatability assessment

Two sets of experiments, at two different period of time, were performed to assess the repeatability of the measurements from the P3HT devices such that each set contained continuous beam ON and OFF. The exposure time was set to 18 s. Figures 8.8 and 8.9 show the photoresponse of nanocomposite and pure P3HT device respectively. Within the first and the second set of repetitions, there was no significant signal loss observed in the photoresponse from the nanocomposite device, while there was a difference of about 36 pA observed between the two sets of experiments (Figure 8.9). In contrast, the pure P3HT response showed an overall reduction within each set and a relatively higher signal loss (~80 pA) between each set (Figure 8.10). This may be attributed to X-ray induced degradation effects with the P3HT polymer matrix resulting in increased recombination/trapping centres for the photo-carriers. Based on the results, one may speculate that the Bi$_2$S$_3$ nanoflowers in the P3HT nanocomposite played an important role not only in generation of relatively more charge carriers, but also, in efficient transport/collection of charge-carriers by minimizing any recombination/trapping within the polymer matrix.
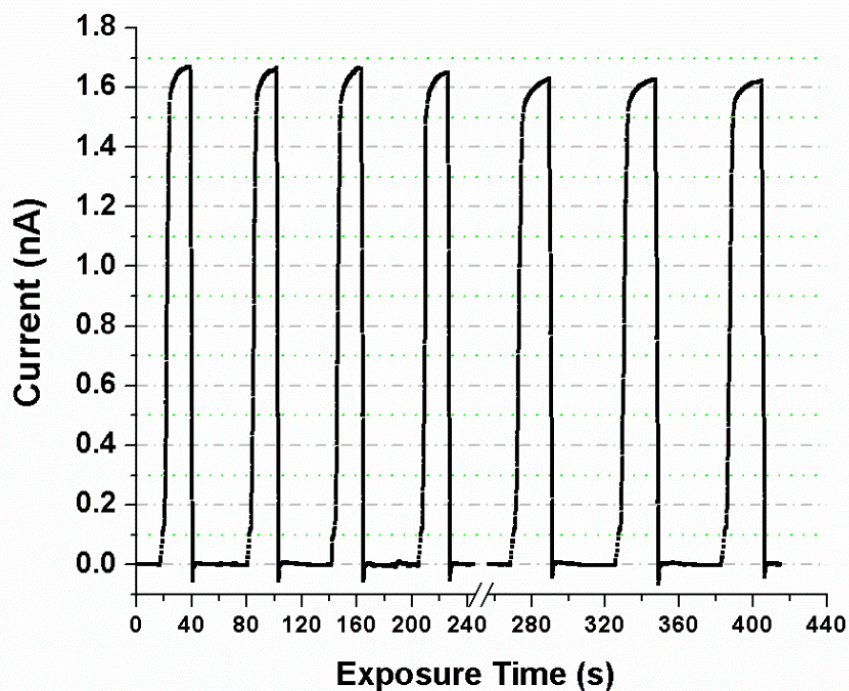
Figure 8.9: Repeatability assessment of P3HT/Bi$_2$S$_3$-nanoflower device exposed to 100 kV X-rays at two different time periods as indicated in the x-axis.
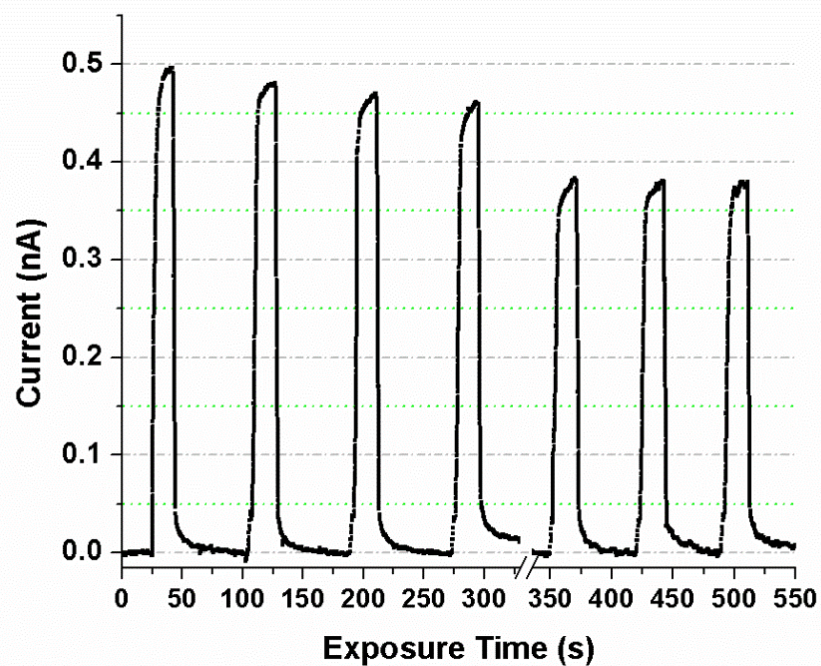
Figure 8.10: Repeatability assessment of P3HT device exposed to 100 kV X-rays at two different time periods as indicated in the x-axis.

8.4 Conclusions

Novel P3HT-based devices were successfully developed and investigated for potential biomedical applications to detect X-ray energies in the diagnostic range. The photoresponse of the P3HT device dramatically improved by a factor of ~4 when Bi_2S_3 nanoflowers were used as filler material. The P3HT/ Bi_2S_3-nanoflower device produced photocurrents in range of 0.52 to 1.64 nA (i.e. 0.66 to 2.09 nA/cm^2) under an X-ray tube potential of 26 to 100 kV respectively. Moreover, both the nanocomposite and the pure P3HT devices could be operated at a bias voltage as low as -40 mV compared to the extremely high bias voltage requirement of standard dosimeter such as the ionization chamber (± 300 V). Furthermore, the X-ray sensitivity of the P3HT/ Bi_2S_3-nanoflower device was found to increase with increase in dose, and significantly so at higher diagnostic energies. More importantly, the photoresponse of the nanocomposite device were fairly stable and repeatable over continuous short-term (18 s) exposures.

The P3HT devices were fabricated with 25.4 micron-thick polyimide substrate along with solution-based semiconducting polymer to impart flexibility which is an added feature that would allow X-ray detection over uneven surfaces such as anatomical contours of patients during diagnostic or interventional procedures. Moreover, the active area of the P3HT devices (with and without nanoflowers) could be easily be extended beyond the area used in this study (1 cm^2), allowing real-time, large-area (two dimensional) dosimetry which would especially be useful in radiotherapy quality assurance tests and dose measurements in phantoms at various depths or uneven surfaces. For commercial applications, the device would need to be encapsulated with a thin layer of material capable of absorbing photons in the UV-Vis range since both P3HT and Bi_2S_3 nanoflowers are light-sensitive materials.

Chapter 9
Summary and Future Directions

9.1 Summary

Key findings of the research work presented in this thesis are summarized here.

9.1.1 PDMS/BO Nanocomposite for Shielding against Diagnostic X-rays

a) Novel nanocomposites using polydimethylsiloxane (PDMS) and bismuth oxide (BO) nanoparticles were fabricated with different concentrations of the nanoparticles. The X-ray attenuation properties of these nanocomposites were investigated under a wide range of diagnostic energies (40 to 150 kV).

b) Results showed that the nanocomposite with the highest concentration of bismuth-oxide nanoparticles (44.44 wt%) could achieve 0.25 mm lead equivalence for both primary and phantom-scattered beam (over the whole range of tube potentials) at a thickness of 3.73 mm.

c) PDMS/BO nanocomposites are cost-effective, and easy to fabricate in laboratory settings (unlike the fabrication processes for most of the commercially available shields that require heavy machinery such as extruders/compressors).

d) A 0.25 mm lead-equivalent 'BO 44.44' (3.73 mm thick) nanocomposite weighed twice as much as 0.25 mm pure lead sheet. However, it is important to note that these nanocomposites can be coated or painted and can conform to practically any shape of interest especially in applications where material weight is not a significant concern. Consequently, they can be used as protective garments by patients during radiological

procedures (diagnostic, interventional or therapeutic procedures using X-rays in the keV range) to minimize unwanted exposures of specific anatomical part/s. For example, some patients prefer thyroid protection during mammographic examinations which require lead-free, conformable material.

9.1.2 Effects of Particle Size on X-ray Transmission Characteristics of PDMS/Ag Nano- and Micro-composites

a) The particle size effects on primary X-ray transmission, scattered X-rays, and attenuation (absorption and/or scatter) characteristics of silver (Ag) nano- and micro-composites (denoted as Ag-nano and Ag-micro respectively) were investigated for relatively low loadings of silver in PDMS.

b) X-ray transmission characteristics of Ag-nano and Ag-micro for three different particle concentrations (0.5, 2.73 and 5.5 wt% of Ag in PDMS) and also, for a range of mass per unit area (0.2112 to 1.056 g/cm^2) were studied. Ag-nano samples with higher concentrations showed about 9 to 6% lower transmission at 20 to 30 kV respectively than the Ag-micro samples at lower photon energies compared to the other energies (about 3 to 2% at 40 to 80 kV respectively).

c) The X-ray scatter properties for highest concentration (5.5 wt%) of Ag-nano showed the reduction in forward scatter and incremental backscatter, in comparison to Ag-micro, as the tube-potential at the higher energy range increased from 40 to 80 kV; the opposite effects were observed for both forward and backward scatter at the lower energy (26 kV).

d) The attenuation behaviour (absorption and/or scatter) of Ag-nano and Ag-micro was further investigated at 26 kV using TLD. The attenuation characteristics of the samples were found to be in agreement with the results obtained from the transmission and the scatter experiments. In summary, the attenuation of diagnostic X-rays can be enhanced at relatively very low loadings of Ag nanoparticles, especially at minimum mass per unit area for energies in the mammographic range.

9.1.3 Bismuth sulfide nanoflowers for direct detection of X-rays in the diagnostic energy range (20 to 100 kV)

a) Hydrothermally synthesized nanoflower-like structures of Bi_2S_3 were investigated as a potential candidate for real-time, semiconductor-based X-ray sensing material. Both the dark currents and the X-ray induced photocurrents of the Bi_2S_3 nanoflowers were measured under various conditions such as tube potentials and dose delivered in both the mammographic (20, 23, 26, and 30 kV) and the higher diagnostic (40, 60, 80, 100 kV) range, different bias voltages, and various X-ray field sizes. For all measurements, the overall response of the substrate to X-rays was found to be negligible in comparison to that measured from the Bi_2S_3 nanoflower device.

b) The photoresponse of the Bi_2S_3 nanoflowers clearly showed high sensitivity to changes in X-ray dose over all tube potentials. For example, the photoresponse of the nanoflowers increased by about 241%, for both 20 and 30 kV, when the dose was increased by four times the minimum value under a bias voltage as low as +1 V. Similarly, the photoresponse of the nanoflowers to 40 and 100 kV X-rays increased by 248% and 220%

respectively for the maximum dose response relative to the minimum. Furthermore, the photocurrent increased linearly with increase in the X-ray dose.

c) Evaluation of different exposure areas, particularly those much smaller than the active region of detection, showed an average photocurrent in the order of several hundreds of pA at X-ray tube potential as low as 20 kV. The results indicate the possibility of using the Bi_2S_3 nanoflowers in miniaturized dosimetric applications.

d) The photoresponse of the Bi_2S_3 nanoflowers were found to be repeatable and stable for both short (18 s) and long (1 min) exposures.

e) The overall sensitivity of the Bi_2S_3 nanoflower device showed similar trend to that of a micro-ionization chamber at a minimal operating voltage of +1 or +1.5 V compared to the +300 V required for operating the ionization chamber.

f) To conclude, Bi_2S_3 nanoflower can be considered as a potential dosimetric material for instantaneous, reliable dose measurements under a wide range of diagnostic X-rays.

9.1.4 Direct detection of X-rays in the diagnostic energy range using flexible P3HT/bismuth-sulfide-nanoflower composite device

a) Novel P3HT-based devices were fabricated on flexible 25.4 micron-thick polyimide substrate with the active layer sandwiched between gold and aluminum electrodes deposited through e-beam technique.

b) Bi_2S_3 nanoflowers were used as filler material to obtain P3HT/ Bi_2S_3-nanoflower composite device. The performance of the P3HT nanocomposite for potential dosimetric

applications to detect X-ray energies in the diagnostic range was compared with that of pure P3HT. The photoresponse of the P3HT/ Bi_2S_3-nanoflower device was found to be significantly higher than (4 times) than that of the pure P3HT device over all the tube potentials.

c) The P3HT/ Bi_2S_3-nanoflower device produced photocurrents in range of 0.52 to 1.64 nA (i.e. 0.66 to 2.09 nA/cm^2) under X-ray tube potential of 26 to 100 kV respectively.

d) Both the nanocomposite and the pure P3HT devices could be operated at a bias voltage as low as -40 mV compared to the extremely high bias voltage required for ionization chamber (±300 V).

e) The X-ray sensitivity of the P3HT/ Bi_2S_3-nanoflower device was found to increase with increase in dose, and significantly so at higher diagnostic energies (i.e. from 26 to 100 kV). Moreover, the photoresponse of the nanocomposite device were fairly stable and repeatable over continuous short-term (18 s) exposures.

f) In summary, the fast photoresponse and the mechanical flexibility of the P3HT/ Bi_2S_3-nanoflower device would potentially allow real-time dosimetric measurements over uneven surfaces such as anatomical parts of patients during diagnostic or interventional procedures. Moreover, the active area of the P3HT devices (with and without nanoflowers) could be easily be extended beyond the area used in this study (1 cm^2), allowing real-time, large-area (two dimensional).

9.2 Future directions

Based on the results and conclusions from the work on X-ray attenuation characteristics of PDMS/BO nanocomposite, it is clear that nanocomposites with concentrations higher than 44.44 wt% of BO dispersed in lighter (in terms of weight) and less viscous polymer than PDMS is most likely to attain the commercially used standard values of lead equivalence. According to the particle size effects on X-ray transmission characteristics of nanocomposites compared to those of microcomposites, it is evident that use of nanoparticles for fabrication of X-ray shielding materials is a better choice than particles of the same material in the micron size range. However, the improvement in attenuation for filler particles of varying sizes in the nano-range is still unclear. The X-ray transmission characteristics for a wide range of elements and compounds, especially, the ones used in fabrication of commercial protective garments or structural shielding materials need to be investigated for varying particle sizes in order to make an optimal selection of the high-Z filler material.

The work on Bi_2S_3 nanoflowers for detection of X-rays in the diagnostic range can be extended to the therapeutic range in order to investigate the performance under the MV range of X-rays generated from linear accelerator. Similarly, P3HT/ Bi_2S_3-nanoflower composite device can also be tested under X-rays in the MV range. Moreover, the effects of different concentrations of Bi_2S_3 nanoflowers in P3HT can be studied in order to determine the wt% required for achieving optimal photoresponse while minimizing the dark currents.

Finally, the ultra-thin nanocomposite-based dosimeter can be integrated onto nanomaterial-based protective garments for real-time monitoring of entrance dose during radiological procedures.

Appendix A

Characterization studies of Bi_2S_3 nanoflowers

Energy dispersive spectrometry

The chemical composition of the nanoflowers was confirmed with energy dispersive spectrometer (EDS, Oxford Instruments Microanalysis System INCA Energy 350) as part of the scanning electron microscope (SEM, JOEL JSM-6460). The sample was dispersed in ethanol and dropcasted on aluminum foil attached to a silicon substrate. Results of the elemental analysis are presented in this section (Figures A-1, A-2, and Table A-1).
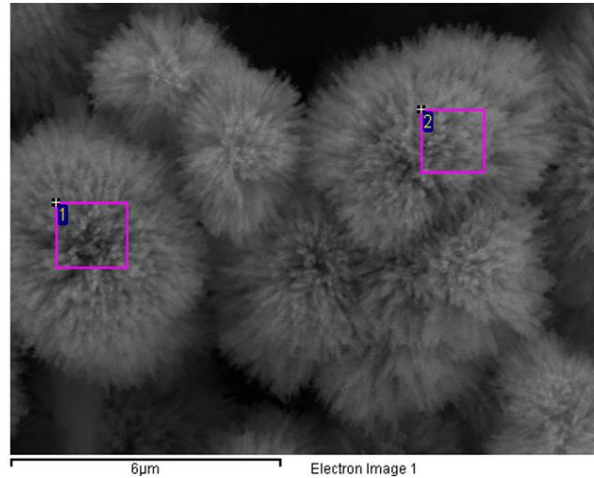
Figure A-1: SEM image of the Bi_2S_3 nanoflowers with two regions (shown as 1 and 2) selected for composition analysis.[120]
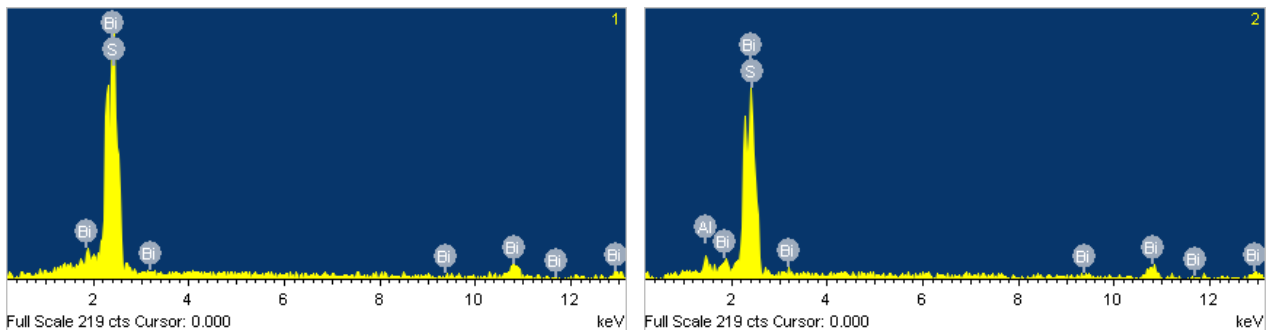
Figure A-2:Energy dispersive spectra showing peaks for (1) Bi and S, and (2) Al (substrate), Bi, and S.[120]

Table A- 1: Quantitative analysis of regions 1 and 2 from EDS analysis.

Spectrum	Al	S	Bi	Total
1		18.77	81.23	100.00
2	1.90	18.11	79.99	100.00
Max.	1.90	18.77	81.23	
Min.	1.90	18.11	79.99	

All results in weight%

Powder X-ray diffraction analysis

Figure A-3 shows the powder X-ray diffraction (XRD) pattern of the nanoflowers recorded on a Bruker D8 Advanced X-ray diffractometer using the parameters listed in Table A-2. The XRD pattern shows polycrystalline nature and all the peaks in the XRD pattern can be indexed to orthorhombic Bi_2S_3 (JCPDS 17-0320) with no indication of impurities (Figure A-3).

Table A-2: Parameters used in XRD study.

Radiation source	Cu Kα
diffraction angle of 2θ	10–70°
Step size	0.019218° 2θ
Specimen Motion	15 rpm
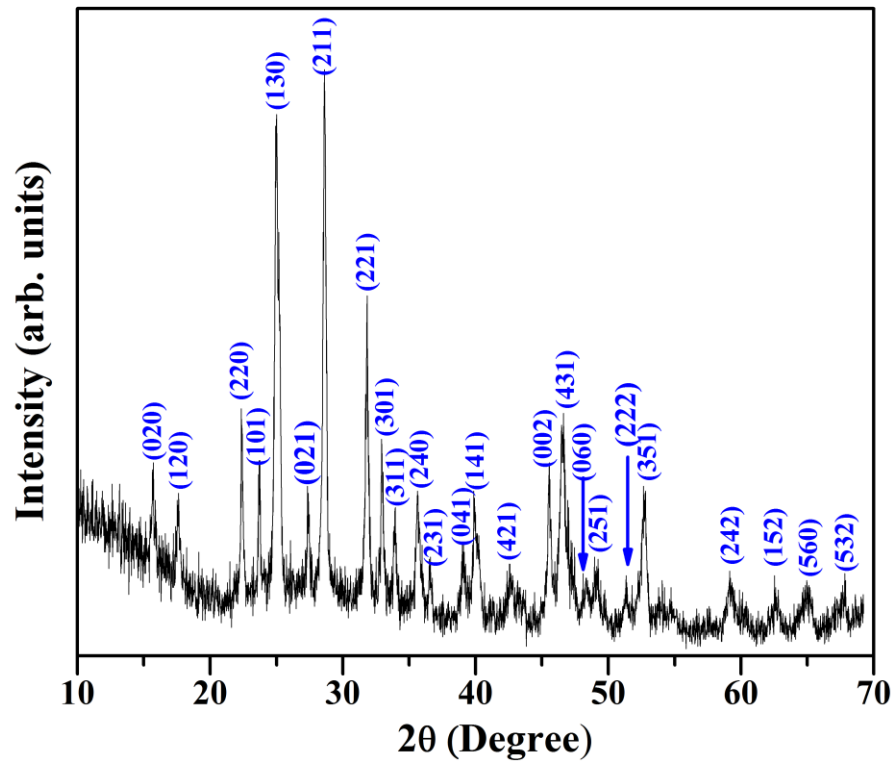
Figure A-3: XRD pattern of the nanoflowers.[120]

SpekCalc simulation

Figure A-4 shows the spectra for X-ray tube-potentials 20 to 30 kV, and Figure A-5 shows the spectra for X-ray tube-potentials 40 to 100 kV using the SpekCalc simulation software. The "air thickness" parameter of 154 mm was used to account for the FSD of 150 mm (from the X-ray setup), and an additional 4 mm from the distance between the tip of the 1 cm cone and the surface of the test device. The mean X-ray energy for each of the tube-potential was also obtained from the simulations.
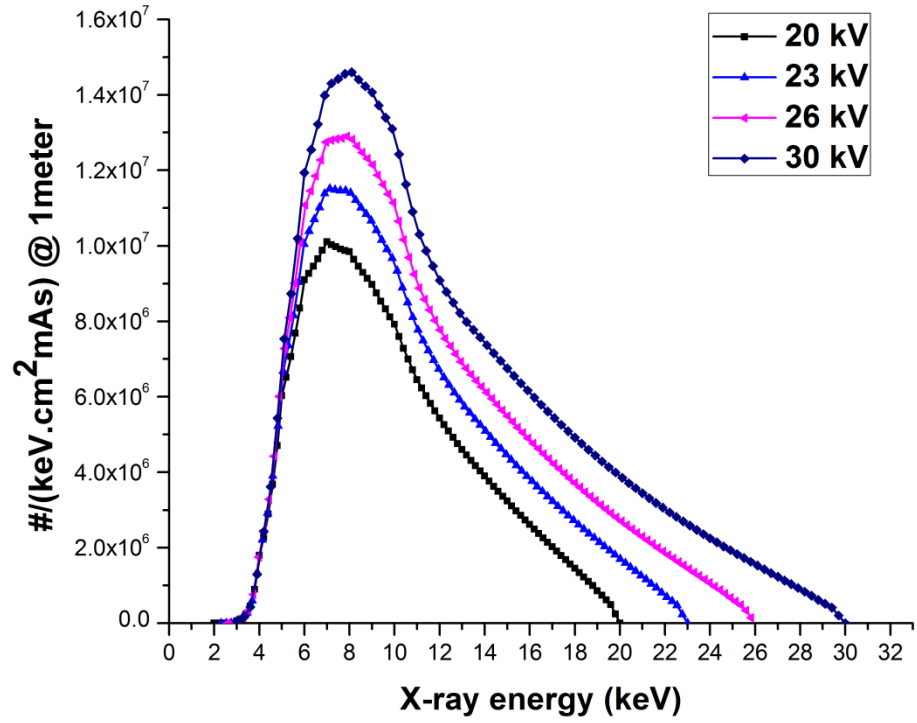
Figure A-4: X-ray spectrum for tube potentials – 20, 23, 26, and 30 kV.
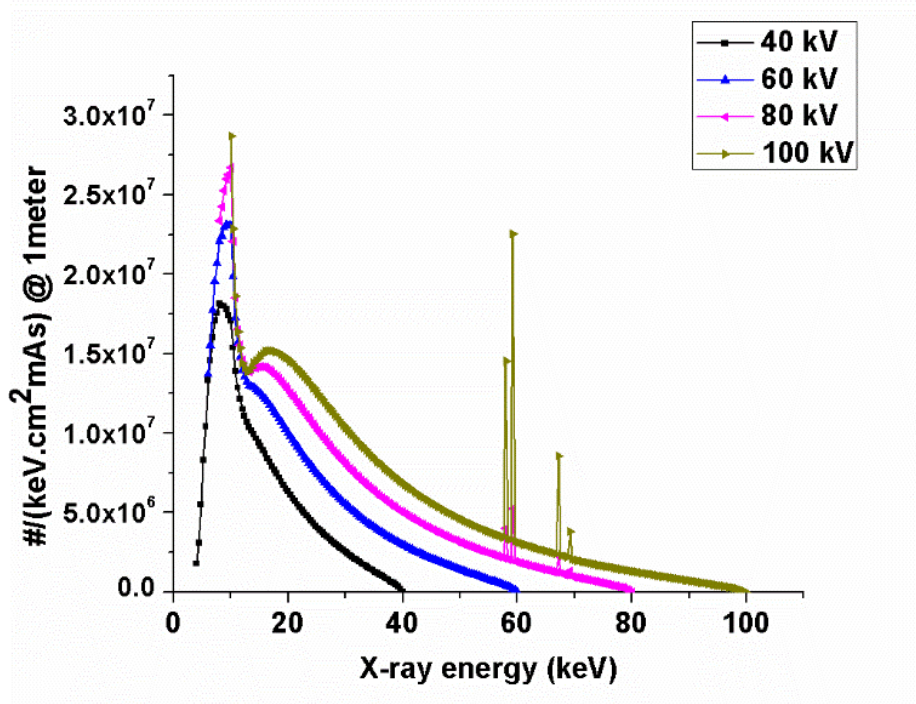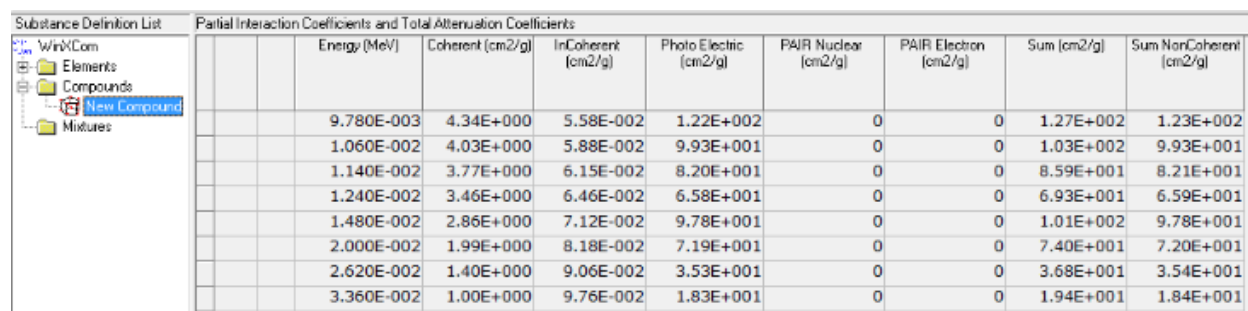
Figure A-5: X-ray spectrum for tube potentials – 40, 60, 80, and 100 kV.

WinXCom simulation

The mass attenuation coefficients (cm^2/g) of Bi_2S_3 for the mean X-ray energies: 9.78, 10.6, 11.4, 12.4, 14.8, 20, 26.2, and 33.6 keV (output from SpekCalc simulations) were obtained using the WinXCom program as shown in Figure A-6.

		Energy (MeV)	Coherent (cm2/g)	InCoherent (cm2/g)	Photo Electric (cm2/g)	PAIR Nuclear (cm2/g)	PAIR Electron (cm2/g)	Sum (cm2/g)	Sum NonCoherent (cm2/g)
		9.780E-003	4.34E+000	5.58E-002	1.22E+002	0	0	1.27E+002	1.23E+002
		1.060E-002	4.03E+000	5.88E-002	9.93E+001	0	0	1.03E+002	9.93E+001
		1.140E-002	3.77E+000	6.15E-002	8.20E+001	0	0	8.59E+001	8.21E+001
		1.240E-002	3.46E+000	6.46E-002	6.58E+001	0	0	6.93E+001	6.59E+001
		1.480E-002	2.86E+000	7.12E-002	9.78E+001	0	0	1.01E+002	9.78E+001
		2.000E-002	1.99E+000	8.18E-002	7.19E+001	0	0	7.40E+001	7.20E+001
		2.620E-002	1.40E+000	9.06E-002	3.53E+001	0	0	3.68E+001	3.54E+001
		3.360E-002	1.00E+000	9.76E-002	1.83E+001	0	0	1.94E+001	1.84E+001

Figure A-6: X-ray interaction cross-sections for each of the input energies as displayed in WinXCom software.

Auto-Zeff simulation

Energy-weighted effective atomic number (Z_{eff}) of Bi_2S_3 nanoflowers was estimated using Auto-Zeff software (Figure A-7). The Z_{eff} was found to be in the range of 45.06 to 66.47 for the X-ray energies used in this study (9.78, 10.6, 11.4, 12.4, 14.8, 20, 26.2, and 33.6 keV).
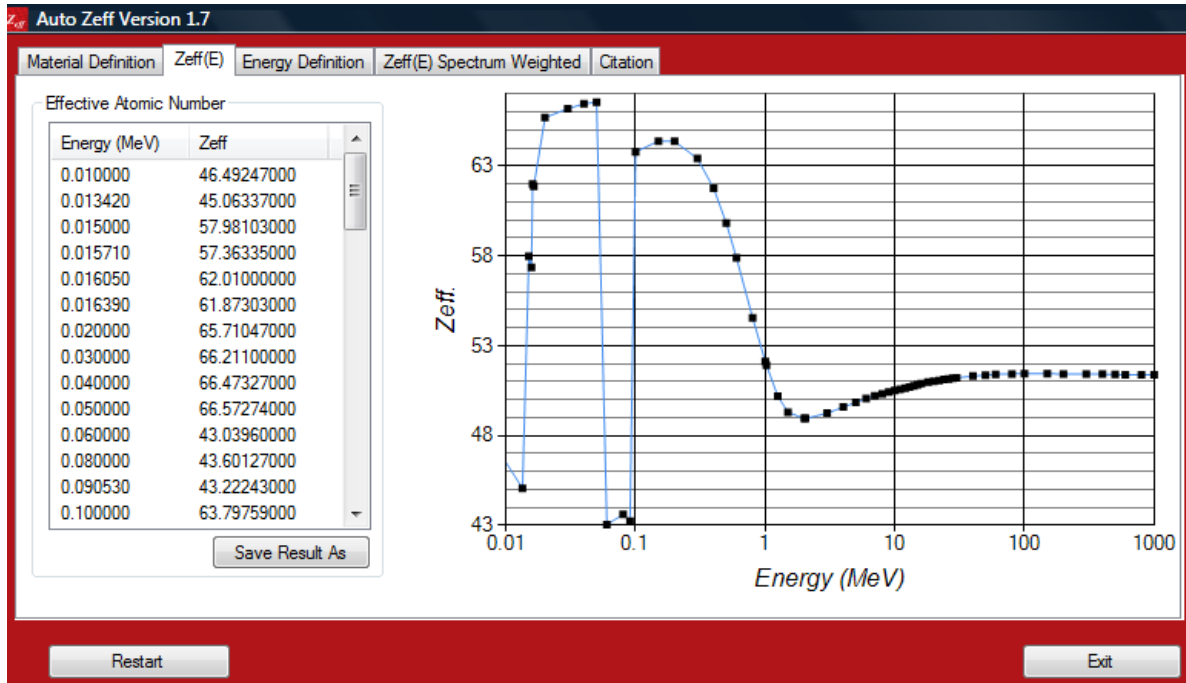
Figure A-7: Energy-weighted Z_{eff} of Bi_2S_3 for X-ray energies from 10 to 100 keV as simulated in Auto-Zeff program.

Energy bandgap calculation

The bandgap of Bi_2S_3 nanoflowers was calculated from the diffuse reflectance spectra (%R versus wavelength) measured using UV-Vis-NIR spectrophotometer (Shimadzu UV-2501PC). The absorbance (F(R)) was calculated from the diffuse reflectance spectrum using the Kubelka-Munk function[128], and the energy bandgap (E_g) was then estimated by substituting F(R) in the Tauc equation.

Kubelka-Munk function is given by:

$$F(R) = \frac{\left(1 - \left(\frac{R}{100}\right)^2\right)}{\left(1 - 2\left(\frac{R}{100}\right)\right)} \qquad (1)$$

where, R is the measured diffuse reflectance.

For the UV-Vis-NIR range, the optical absorption coefficient (α) can be determined by the Tauc equation:

$$\alpha = A \frac{(h\nu - E_g)^n}{h\nu} \qquad (2)$$

where, $h\nu$ is the photon energy, E_g is the bandgap, and A and n are constants.[129] Since Bi_2S_3 is a direct bandgap material, n=1/2. By substituting α with F(R) in equation (2), the Tauc plot $((F(R) * h\nu)^2$ vs. $h\nu)$ was obtained and the energy bandgap (E_g) was then estimated by extrapolating the linear portion of the plot to the energy axis as shown in Figure A-8. The bandgap was found to be 1.33 eV.
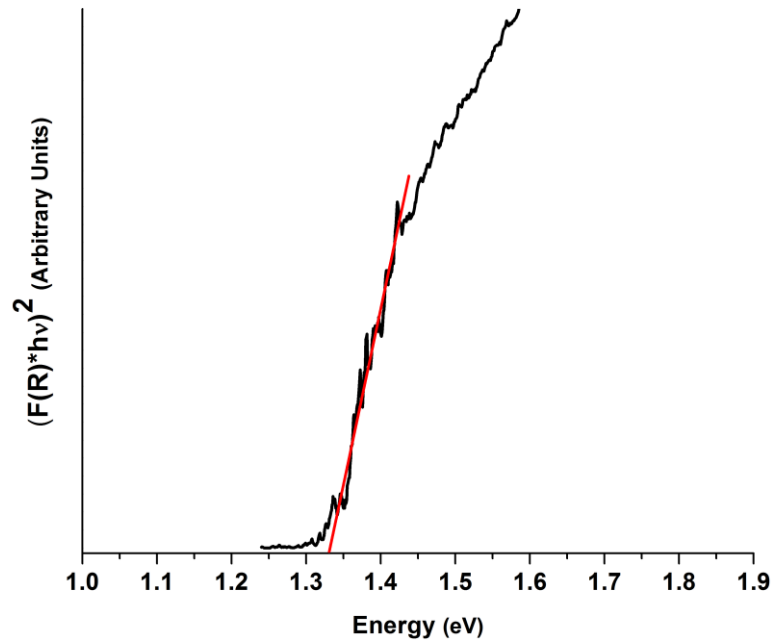
Figure A-8: Tauc plot for Bi_2S_3 nanoflowers.

Film Dosimetry

In order to analyze the uniformity of the field sizes (i.e. the lead cut-outs of diameter 0.4, 0.6, 0.8 and 1 cm) and the effects of its penumbra, radiographic films (GafChromic EBT3) were exposed for 18 s to all the four field sizes under 20 kV X-rays. All the films were converted to digital

184

images using a flatbed scanner (Epson Expression 1000XL). The images (the exposure profile for each field size) were then analyzed using an image processing software (ImageJ) in which a plot profile of a rectangular 'region of interest' passing approximately through the centre of the radiographic image was chosen such that it covered the unexposed areas on either side of the exposed circular field. The plot profile consist of pixel intensity values for 16 bit radiographic image along length of the rectangular 'region of interest'. The image obtained from 20 kV X-rays under 1 cm field size is shown in Figure A-9. The plot profiles of each of the field sizes under 20 kV X-rays are presented in Figure A-10.
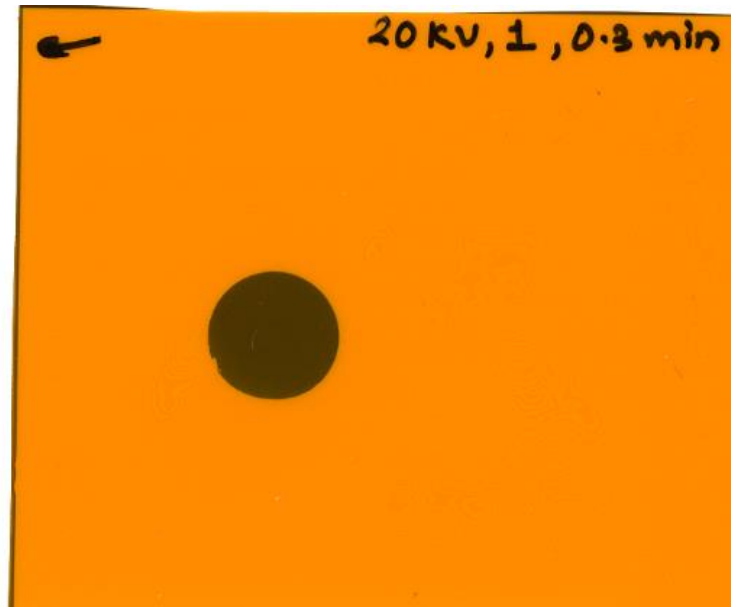
Figure A-9: A self-developing radiographic film exposed to 20 kV X-rays with a 1 cm diameter lead cut-out.
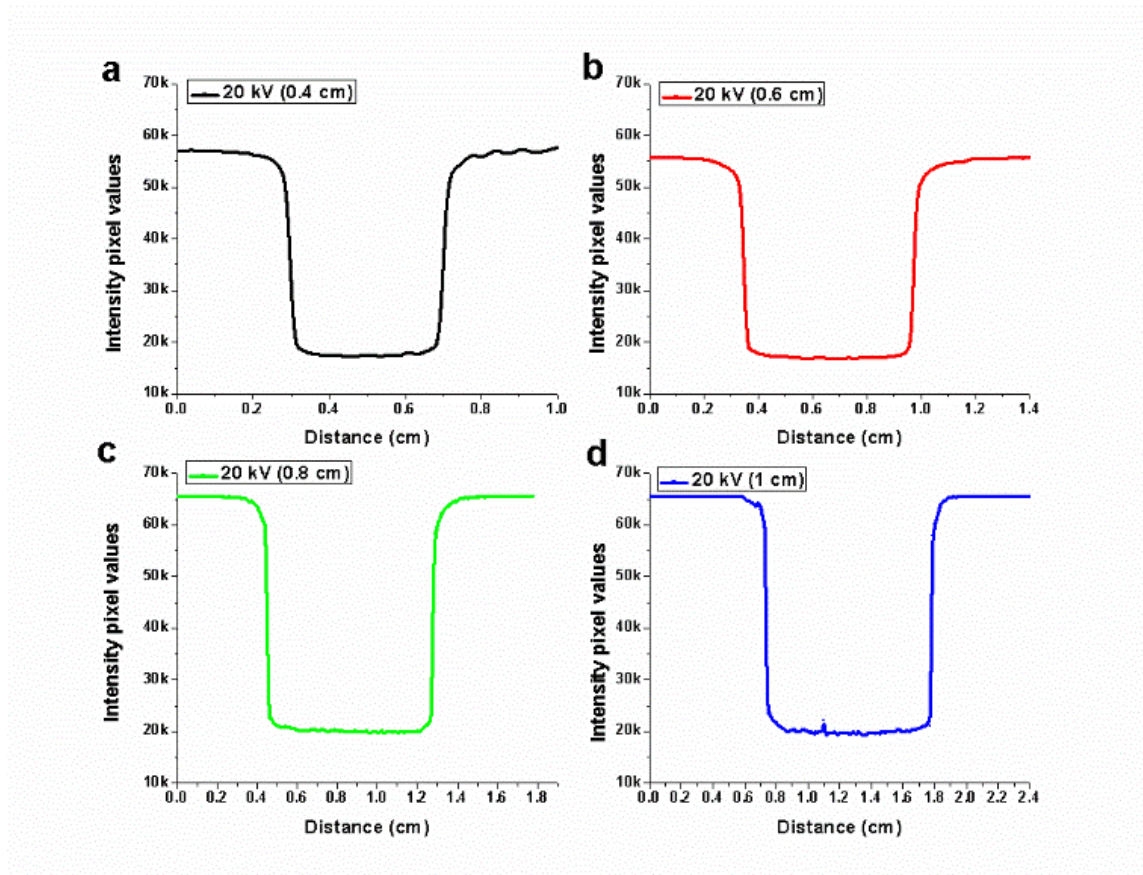
Figure A-10: Profile plot obtained under 20 kV X-rays for lead cut-outs with diameter: (a) 0.4 cm, (b) 0.6 cm, (c) 0.8 cm, and (d) 1 cm.

References

1.   *Report of the task Group on the biological effects of space radiation - radiation hazards to crews on interplanetary mission*; National Academy of Sciences: Washington, D.C., 1996.

2.   Nambiar, S.; Yeow, J. T., Polymer-composite materials for radiation protection. *ACS applied materials & interfaces* **2012,** *4* (11), 5717-5726.

3.   *Report on Carcinogens Background Document for X Radiation & Gamma Radiation and Neutrons*; Technology Planning and Management Corporation (TPMC): Washington, D.C., 2003.

4.   Sen, S. S., E.; O'Dell, J. S.; Deka, L.; Pillay, S.;, The development of a multifunctional composite material for use in human space exploration beyond low-earth orbit. *JOM* **2009,** *61*, 23-31.

5.   Good, R. C.; Shen, S. P.; Dow, N. F. *Active shielding concepts for ionizing radiation in space*; General Electric Company: Philadelphia, PA, 1964.

6.   Podgorsak, E. B., Radiation Oncology Physics: A Handbook for Teachers and Students. *(International Atomic Energy Agency, Vienna, 2005).*

7.   Zeitlin, C.; Guetersloh, S. B.; Heilbronn, L. H.; Miller, J., Measurements of materials shielding properties with 1 GeV/nuc 56Fe. *Nuclear Instruments and Methods in Physics Research Section B: Beam Interactions with Materials and Atoms* **2006,** *252* (2), 308-318.

8.   Chao, K. S. C., Protection of salivary function by intensity-modulated radiation therapy in patients with head and neck cancer. *Semin. Radiat. Oncology* **2002,** *12* (1), 20-25.

9.   Cucinotta, F. A.; Kim, M.-H. Y.; Ren, L., Evaluating shielding effectiveness for reducing space radiation cancer risks. *Radiation Measurements* **2006,** *41* (9-10), 1173-1185.

10.   Gaier, J. R.; Hardebeck, W. C.; Bunch, J. R. T.; Davidson, M. L.; Beery, D. B., Effect of intercalation in graphite epoxy composites on the shielding of high energy radiation. *Journal of Materials Research* **1998,** *13* (08), 2297-2301.

11.   O'Rourke Muisener, P. A.; Clayton, L.; D'Angelo, J.; Harmon, J. P.; Sikder, A. K.; Kumar, A.; Cassell, A. M.; Meyyappan, M., Effects of gamma radiation on poly(methyl methacrylate)/single-wall nanotube composites. *Journal of Materials Research* **2002,** *17* (10), 2507-2513.

12.   Zhang, W.; Zeng, J.; Liu, L.; Fang, Y., A novel property of styrene-butadiene-styrene/clay nanocomposites: radiation resistance. *Journal of Materials Chemistry* **2004,** *14* (2), 209.

13.   Zhang, W.; Fang, Y., Enhancement of radiation-resistant effect in ethylene–vinyl acetate copolymers by the formation of ethylene–vinyl acetate copolymers/clay nanocomposites. *Journal of Applied Polymer Science* **2005,** *98* (6), 2532-2538.

14.   Tiwari, V. K.; Kulriya, P. K.; Avasthi, D. K.; Maiti, P., Radiation-resistant behavior of poly(vinylidene fluoride)/layered silicate nanocomposites. *ACS applied materials & interfaces* **2009,** *1* (2), 311-8.

15.   Tiwari, V. K.; Kulriya, P. K.; Avasthi, D. K.; Maiti, P., Poly(Vinylidene fluoride-co-hexafluoro propylene)/Layered Silicate Nanocomposites: The Effect of Swift Heavy Ion. *The Journal of Physical Chemistry B* **2009,** *113* (34), 11632-11641.

16.   Tiwari, V. K.; Shripathi, T.; Lalla, N. P.; Maiti, P., Nanoparticle induced piezoelectric, super toughened, radiation resistant, multi-functional nanohybrids. *Nanoscale* **2012,** *4* (1), 167-175.

17.   Samaras, M.; Derlet, P. M.; Van Swygenhoven†, H.; Victoria, M., Radiation damage near grain boundaries. *Philosophical Magazine* **2003,** *83* (31-34), 3599-3607.

18.   Chimi, Y.; Iwase, A.; Ishikawa, N.; Kobiyama, M.; Inami, T.; Okuda, S., Accumulation and recovery of defects in ion-irradiated nanocrystalline gold. *J. Nucl. Mater.* **2001,** *297* (3), 355-357.

19.   Chimi, Y.; Iwase, A.; Ishikawa, N.; Kobiyama, M.; Inami, T.; Kambara, T.; Okuda, S., Swift heavy ion irradiation effects in nanocrystalline gold. *Nuclear Instruments and Methods in Physics Research Section B: Beam Interactions with Materials and Atoms* **2006,** *245* (1), 171-175.

20.   Nita, N.; Schaeublin, R.; Victoria, M.; Valiev, R. Z., Effects of irradiation on the microstructure and mechanical properties of nanostructured materials. *Philosophical Magazine* **2005,** *85* (4-7), 723-735.

21.   Nambiar, S.; Yeow, J. T., Conductive polymer-based sensors for biomedical applications. *Biosensors and Bioelectronics* **2011,** *26* (5), 1825-1832.

22.   El-Sayed A., A.; Ali, M. A. M.; Ismail, M. R., Natural fibre high-density polyethylene and lead oxide composites for radiation shielding. *Radiation Physics and Chemistry* **2003,** *66* (3), 185-195.

23.   Tajiri, M.; Tokiya, Y.; Uenishi, J.; Sunaoka, M.; Watanabe, K., New shielding materials for clinical electron beams. *Radiotherapy and oncology : journal of the European Society for Therapeutic Radiology and Oncology* **2006,** *80* (3), 391-3.

24.   Stewart, D. Y.; Harrison, P. F.; Morgan, B.; Ramachers, Y., Radiation shielding for underground low-background experiments. *Nuclear Instruments and Methods in Physics Research Section A: Accelerators, Spectrometers, Detectors and Associated Equipment* **2007,** *571* (3), 651-662.

25.   Erdem, M.; Baykara, O.; Doğru, M.; Kuluöztürk, F., A novel shielding material prepared from solid waste containing lead for gamma ray. *Radiation Physics and Chemistry* **2010,** *79* (9), 917-922.

26.   Wilson, J. W.; Thibeault, S. A.; Cucinotta, F. A.; Shinn, J. L.; Kim, M.; Kiefer, R.; Badavi, F. F., Issues in protection from galactic cosmic rays. *Radiation and environmental biophysics* **1995,** *34* (4), 217-22.

27.   Schimmerling, W.; Cucinotta, F. A.; Wilson, J. W., Radiation risk and human space exploration. *Advances in space research : the official journal of the Committee on Space Research (COSPAR)* **2003,** *31* (1), 27-34.

28.   Guetersloh, S.; Zeitlin, C.; Heilbronn, L.; Miller, J.; Komiyama, T.; Fukumura, A.; Iwata, Y.; Murakami, T.; Bhattacharya, M., Polyethylene as a radiation shielding standard in simulated cosmic-ray environments. *Nuclear Instruments and Methods in Physics Research Section B: Beam Interactions with Materials and Atoms* **2006,** *252* (2), 319-332.

29.   Zhong, W. H.; Sui, G.; Jana, S.; Miller, J., Cosmic radiation shielding tests for UHMWPE fiber/nano-epoxy composites. *Composites Science and Technology* **2009,** *69* (13), 2093-2097.

30.   Harrison, C.; Burgett, E.; Hertel, N.; Grulke, E., Polyethylene/Boron Composites for Radiation Shielding Applications. *AIP Conference Proceedings* **2008,** *969* (1), 484-491.

31.   Hu, H.; Qunshu, W.; Juan, Q.; Yuelei, W.; Tiankui, Z.; Zhongsheng, X.; Xinbiao, J.; Guoguang, Z.; Hu, X.; Xiangyang, Z.; Jing, Z.; Wenhao, L.; Zhenghong, L.; Boping, Z.; Linbo, L.; Zhaohui, S.; Xiaoping, O.; Jun, Z.; Yaolin, Z.; Xiaoqin, M.; Zhengping, D.; Cheng, L.; Zhenyu, J.; Yuanping, Z., Study on composite material for shielding mixed neutron and γ rays. *Nuclear Science, IEEE Transactions on* **2008,** *55* (4), 2376-2384.

32.   Iqbal, H. M. S.; Bhowmik, S.; Benedictus, R.; Moon, J. B.; Kim, C. G.; Mourad, A. H. I., Processing and Characterization of Space-Durable High-Performance Polymeric Nanocomposite. *Journal of Thermophysics and Heat Transfer* **2011,** *25* (1), 87-95.

33.   Bhowmik, S.; Benedictus, R. In *Performance of space durable polymeric nano composite under electromagnetic radiation at Low Earth Orbit*, Applied Electromagnetics Conference, 2007. AEMC 2007. IEEE, 19-20 Dec. 2007; 2007; pp 1-4.

34.   Park, C.; Ounaies, Z.; Watson, K. A.; Pawlowski, K.; Lowther, S. E.; Connell, J. W.; Siochi, E. J.; Harrison, J. S.; Clair, T. L. S., Polymer-Single Wall Carbon Nanotube Composites for Potential Spacecraft Applications. *MRS Online Proceedings Library* **2001,** *706*.

35.   Schadler, L. S., Polymer-Based and Polymer-Filled Nanocomposites. In *Nanocomposite Science and Technology*, Wiley-VCH Verlag GmbH & Co. KGaA: 2004; pp 77-153.

36.   Clayton, L. M.; Gerasimov, T. G.; Cinke, M.; Meyyappan, M.; Harmon, J. P., Dispersion of Single-Walled Carbon Nanotubes in a Non-Polar Polymer, Poly(4-methyl-1-pentene). *Journal of Nanoscience and Nanotechnology* **2006,** *6* (8), 2520-2524.

37.   Ruan, S. L.; Gao, P.; Yang, X. G.; Yu, T. X., Toughening high performance ultrahigh molecular weight polyethylene using multiwalled carbon nanotubes. *Polymer* **2003,** *44* (19), 5643-5654.

38.   Bhattacharya, A., Radiation and industrial polymers. *Progress in Polymer Science* **2000,** *25* (3), 371-401.

39.   Seo, K. S.; Fornes, R. E.; Gilbert, R. D.; Memory, J. D., Effects of ionizing radiation on epoxy, graphite fiber and epoxy/graphite fiber composites. Part I: Surface energy changes. *Journal of Polymer Science Part B: Polymer Physics* **1988,** *26* (2), 245-255.

40.   Tomczak, S. J.; Vij, V.; Minton, T. K.; Brunsvold, A. L.; Marchant, D.; Wright, M. E.; Petteys, B. J.; Guenthner, A. J.; Yandek, G. R.; Mabry, J. M., Comparisons of Polyhedral Oligomeric Silsesquioxane Polyimides as Space-Survivable Materials. In *Polymer Durability and Radiation Effects*, American Chemical Society: 2007; Vol. 978, pp 140-152.

41.   Bai, X. M.; Voter, A. F.; Hoagland, R. G.; Nastasi, M.; Uberuaga, B. P., Efficient annealing of radiation damage near grain boundaries via interstitial emission. *Science* **2010,** *327* (5973), 1631-4.

42.   Ackland, G., Controlling Radiation Damage. *Science (New York, N.Y.)* **2010,** *327* (5973), 1587-1588.

43.   Chen, S.; Nambiar, S.; Li, Z.; Sun, Y.; Gong, S.; Zhu, G. Z.; Yeow, J. T. In *Polymer nanocomposite for space applications*, Nanotechnology (IEEE-NANO), 2014 IEEE 14th International Conference on, IEEE: 2014; pp 685-688.

44.   Williams, G.; Trask, R.; Bond, I., A self-healing carbon fibre reinforced polymer for aerospace applications. *Composites Part A: Applied Science and Manufacturing* **2007,** *38* (6), 1525-1532.

45.   Li, Z.; Nambiar, S.; Zheng, W.; Yeow, J., PDMS/single-walled carbon nanotube composite for proton radiation shielding in space applications. *Materials Letters* **2013,** *108*, 79-83.

46.   Singleterry, R. C., Jr.; Thibeault, S. A. *Materials for Low-Energy Neutron Radiation Shielding*; NASA Langley Technical Report Server: 2000.

47.   Newman, C. R.; Sirringhaus, H.; Blakesley, J. C.; Speller, R., Stability of polymeric thin film transistors for x-ray imaging applications. *Applied Physics Letters* **2007,** *91* (14), 142105.

48.   Keivanidis, P. E.; Greenham, N. C.; Sirringhaus, H.; Friend, R. H.; Blakesley, J. C.; Speller, R.; Campoy–Quiles, M.; Agostinelli, T.; Bradley, D. D. C.; Nelson, J., X-ray stability and response of polymeric photodiodes for imaging applications. *Applied Physics Letters* **2008,** *92* (2), 023304.

49. Silva, E. A. B.; Borin, J. F.; Nicolucci, P.; Graeff, C. F. O.; Netto, T. G.; Bianchi, R. F., Low dose ionizing radiation detection using conjugated polymers. *Applied Physics Letters* **2005,** *86* (13), 131902.

50. Bazani, D. L. M.; Lima, J. P. H.; de Andrade, A. M., MEH-PPV Thin Films for Radiation Sensor Applications. *Sensors Journal, IEEE* **2009,** *9* (7), 748-751.

51. Raval, H. N.; Tiwari, S. P.; Navan, R. R.; Rao, V. R., Determining ionizing radiation using sensors based on organic semiconducting material. *Applied Physics Letters* **2009,** *94* (12), 123304.

52. Zhong, H.; Zhao, Y.; Li, Y.; Pei, Q., Photoluminescence quenching of conjugated polymer nanocomposites for gamma ray detection. *Nanotechnology* **2008,** *19* (50), 505503.

53. Boroumand, F. A.; Zhu, M.; Dalton, A. B.; Keddie, J. L.; Sellin, P. J.; Gutierrez, J. J., Direct x-ray detection with conjugated polymer devices. *Applied Physics Letters* **2007,** *91* (3), 033509.

54. Intaniwet, A.; Mills, C. A.; Shkunov, M.; Thiem, H.; Keddie, J. L.; Sellin, P. J., Characterization of thick film poly(triarylamine) semiconductor diodes for direct x-ray detection. *Journal of Applied Physics* **2009,** *106* (6), 064513.

55. Intaniwet, A.; Mills, C. A.; Sellin, P. J.; Shkunov, M.; Keddie, J. L., Achieving a stable time response in polymeric radiation sensors under charge injection by X-rays. *ACS applied materials & interfaces* **2010,** *2* (6), 1692-9.

56. Raval, H. N.; Ramgopal Rao, V., Low-Operating-Voltage Operation and Improvement in Sensitivity With Passivated OFET Sensors for Determining Total Dose Radiation. *Electron Device Letters, IEEE* **2010,** *31* (12), 1482-1484.

57. Paez-Sierra, B. A.; Rodríguez, H.; Sánchez, J. M.; Rodríguez, M. A.; Pérez, L. D. In *Fabrication of an x-ray detector based on molecular plastic electronics*, SPIE Organic Photonics+ Electronics, International Society for Optics and Photonics: 2014; pp 91851P-91851P-7.

58. Veres, J.; Ogier, S. D.; Leeming, S. W.; Cupertino, D. C.; Mohialdin Khaffaf, S., Low-k Insulators as the Choice of Dielectrics in Organic Field-Effect Transistors. *Advanced Functional Materials* **2003,** *13* (3), 199-204.

59. Tan, H. S.; Mathews, N.; Cahyadi, T.; Zhu, F. R.; Mhaisalkar, S. G., The effect of dielectric constant on device mobilities of high-performance, flexible organic field effect transistors. *Applied Physics Letters* **2009,** *94* (26), 263303-263303-3.

60. Najafi, E.; Shin, K., Radiation resistant polymer–carbon nanotube nanocomposite thin films. *Colloids and Surfaces A: Physicochemical and Engineering Aspects* **2005,** *257-258*, 333-337.

61. GündÜZ, G.; Usanmaz, A., Development of new nuclear shielding materials containing vitrified colemanite and impregnated polymer. *Journal of Nuclear Materials* **1986,** *140* (1), 44-55.

62. Ashton-Patton, M. M.; Hall, M. M.; Shelby, J. E., Formation of low density polyethylene/hollow glass microspheres composites. *Journal of Non-Crystalline Solids* **2006,** *352* (6-7), 615-619.

63. Di, M.; He, S.; Li, R.; Yang, D., Resistance to proton radiation of nano-TiO2 modified silicone rubber. *Nuclear Instruments and Methods in Physics Research Section B: Beam Interactions with Materials and Atoms* **2006,** *252* (2), 212-218.

64. Zeng, Q. H.; Yu, A. B.; Lu, G. Q.; Paul, D. R., Clay-Based Polymer Nanocomposites: Research and Commercial Development. *Journal of Nanoscience and Nanotechnology* **2005,** *5* (10), 1574-1592.

65.   Kurahatti, R. V.; Surendranathan, A. O.; Kori, S. A.; Singh, N.; Kumar, A. V. R.; Srivastava, S., Defence Applications of Polymer Nanocomposites. *Defence Science Journal* **2010,** *60* (5), 551-563.

66.   Nambiar, S.; Osei, E. K.; Yeow, J. T. W., Polymer nanocomposite-based shielding against diagnostic X-rays. *Journal of Applied Polymer Science* **2013,** *127* (6), 4939-4946.

67.   Botelho, M. Z.; Kunzel, R.; Okuno, E.; Levenhagen, R. S.; Basegio, T.; Bergmann, C. P., X-ray transmission through nanostructured and microstructured CuO materials. *Applied radiation and isotopes : including data, instrumentation and methods for use in agriculture, industry and medicine* **2011,** *69* (2), 527-30.

68.   Bell, J.; Lail, D.; Martin, C.; Nguyen, P., Radiation shielding for a lunar base. *National Aeronautics and Space Adiminstration* **2011**.

69.   Sonoda, K., Materials application for spacecraft use in Japan. *Electrical Insulation Magazine, IEEE* **1992,** *8* (2), 18-26.

70.   White, S. R.; Sottos, N. R.; Geubelle, P. H.; Moore, J. S.; Kessler, M. R.; Sriram, S. R.; Brown, E. N.; Viswanathan, S., Autonomic healing of polymer composites. *Nature* **2001,** *409* (6822), 794-797.

71.   Lee, C. O.; Najafi, E.; Kim, J. Y.; Han, S.-H.; Lee, T.; Shin, K., Effects of Protons, Electrons, and UV Radiation on Carbon Nanotubes. In *Polymer Durability and Radiation Effects*, American Chemical Society: 2007; Vol. 978, pp 232-252.

72.   Intaniwet, A.; Mills, C.; Shkunov, M.; Sellin, P.; Keddie, J., Heavy metallic oxide nanoparticles for enhanced sensitivity in semiconducting polymer x-ray detectors. *Nanotechnology* **2012,** *23* (23), 235502.

73.   Mills, C. A.; Intaniwet, A.; Shkunov, M.; Keddie, J. L.; Sellin, P. J. In *Flexible radiation dosimeters incorporating semiconducting polymer thick films*, SPIE Optical Engineering+ Applications, International Society for Optics and Photonics: 2009; pp 74491I-74491I-7.

74.   Mills, C. A.; Al-Otaibi, H.; Intaniwet, A.; Shkunov, M.; Pani, S.; Keddie, J. L.; Sellin, P. J., Enhanced x-ray detection sensitivity in semiconducting polymer diodes containing metallic nanoparticles. *Journal of Physics D: Applied Physics* **2013,** *46* (27), 275102.

75.   Mills, C. A.; Chan, Y.-F.; Intaniwet, A.; Shkunov, M.; Nisbet, A.; Keddie, J. L.; Sellin, P. J., Direct detection of 6 MV x-rays from a medical linear accelerator using a semiconducting polymer diode. *Physics in medicine and biology* **2013,** *58* (13), 4471.

76.   Han, H.; Lee, S.; Seo, J.; Mahata, C.; Cho, S. H.; Han, A.-R.; Hong, K.-S.; Park, J.-H.; Soh, M.-J.; Park, C., Enhancement of X-ray detection by single-walled carbon nanotube enriched flexible polymer composite. *Nanoscale Research Letters* **2014,** *9* (1), 610.

77.   Dimitrakopoulos, C. D.; Malenfant, P. R., Organic thin film transistors for large area electronics. *Advanced Materials* **2002,** *14* (2), 99.

78.   Abdel-Aziz, M.; Badran, A.; Abdel-Hakem, A.; Helaly, F.; Moustafa, A., Styrene–butadiene rubber/lead oxide composites as gamma radiation shields. *Journal of Applied Polymer Science* **1991,** *42* (4), 1073-1080.

79.   Harish, V.; Nagaiah, N.; Prabhu, T. N.; Varughese, K., Preparation and characterization of lead monoxide filled unsaturated polyester based polymer composites for gamma radiation shielding applications. *Journal of Applied Polymer Science* **2009,** *112* (3), 1503-1508.

80.   Attix, F. H., *Introduction to Radiological Physics and Radiation Dosimetry*. Wiley Interscience: Hoboken, NJ, 1986.

81. McCaffrey, J. P.; Mainegra-Hing, E.; Shen, H., Optimizing non-Pb radiation shielding materials using bilayers. *Medical physics* **2009,** *36* (12), 5586-94.

82. Yue, K.; Luo, W.; Dong, X.; Wang, C.; Wu, G.; Jiang, M.; Zha, Y., A new lead-free radiation shielding material for radiotherapy. *Radiat Prot Dosimetry* **2009,** *133* (4), 256-60.

83. McCaffrey, J.; Shen, H.; Downton, B.; Mainegra-Hing, E., Radiation attenuation by lead and nonlead materials used in radiation shielding garments. *Medical physics* **2007,** *34* (2), 530-537.

84. Kim, H.; Kim, K.; Lee, C.; Joo, J.; Cho, S.; Yoon, H.; Pejaković, D.; Yoo, J.; Epstein, A., Electrical conductivity and electromagnetic interference shielding of multiwalled carbon nanotube composites containing Fe catalyst. *Applied Physics Letters* **2004,** *84* (4), 589-591.

85. Lines, M., Nanomaterials for practical functional uses. *Journal of Alloys and Compounds* **2008,** *449* (1), 242-245.

86. Niu, Y., Electromagnetic interference shielding with polyaniline nanofibers composite coatings. *Polymer Engineering & Science* **2008,** *48* (2), 355-359.

87. Poole, C. P., Jr.; Owens., F. J., *Introduction to Nanotechnology*. Wiley-Interscience: Hoboken, New Jersey, USA, 2004.

88. El Haber, F.; Rocquefelte, X.; Andraud, C.; Amrani, B.; Jobic, S.; Chauvet, O.; Froyer, G., Prediction of the transparency in the visible range of x-ray absorbing nanocomposites built upon the assembly of LaF3 or LaPO4 nanoparticles with poly(methyl methacrylate). *J. Opt. Soc. Am. B* **2012,** *29* (3), 305-311.

89. Friedman, H.; Singh, M., *Radiation transmission measurements for demron fabric*. United States. Department of Energy: 2003.

90. Taylor, E. W. In *Organics, polymers and nanotechnology for radiation hardening and shielding applications*, Optical Engineering+ Applications, International Society for Optics and Photonics: 2007; pp 671307-671307-10.

91. Ackland, G., Materials science. Controlling radiation damage. *Science (New York, N.Y.)* **2010,** *327* (5973), 1587-8.

92. Samaras, M.; Derlet, P. M.; Van Swygenhoven, H.; Victoria, M., Radiation damage near grain boundaries. *Philosophical Magazine* **2003,** *83* (31-34), 3599-3607.

93. Kunzel, R.; Okuno, E., Effects of the particle sizes and concentrations on the X-ray absorption by CuO compounds. *Applied radiation and isotopes : including data, instrumentation and methods for use in agriculture, industry and medicine* **2012,** *70* (4), 781-4.

94. Noor Azman, N. Z.; Siddiqui, S. A.; Hart, R.; Low, I. M., Effect of particle size, filler loadings and x-ray tube voltage on the transmitted x-ray transmission in tungsten oxide-epoxy composites. *Applied radiation and isotopes : including data, instrumentation and methods for use in agriculture, industry and medicine* **2013,** *71* (1), 62-7.

95. Nambiar, S.; Osei, E.; Yeow, J., MO-F-BRA-01: Polymer Composite-Based Shielding of Diagnostic X-Rays. *Medical physics* **2011,** *38* (6), 3720-3720.

96. Taylor, M. L.; Smith, R. L.; Dossing, F.; Franich, R. D., Robust calculation of effective atomic numbers: The Auto-Zeff software. *Medical physics* **2012,** *39* (4), 1769-1778.

97. Hubbert, T. E.; Vucich, J. J.; Armstrong, M. R., Lightweight aprons for protection against scattered radiation during fluoroscopy. *American Journal of Roentgenology* **1993,** *161* (5), 1079-1081.

98.   Nambiar, S.; Osei, E. K.; Yeow, J., Effects of Particle Size on X-ray Transmission Characteristics of PDMS/Ag Nano- and Micro-composites. In *IEEE NANO*, Rome, Italy, 2015.

99.   Yu, X.; Cao, C., Photoresponse and Field-Emission Properties of Bismuth Sulfide Nanoflowers. *Cryst. Growth Des.* **2008,** *8* (11), 3951-3955.

100.   Liao, H.-C.; Wu, M.-C.; Jao, M.-H.; Chuang, C.-M.; Chen, Y.-F.; Su, W.-F., Synthesis, optical and photovoltaic properties of bismuth sulfide nanorods. *CrystEngComm* **2012,** *14* (10), 3645.

101.   Suarez; R.; Nair; K., P.; Kamat; V., P., Photoelectrochemical behavior of Bi_2S_3 nanoclusters and nanostructured thin films. *Langmuir* **1998,** *14* (12), 3236-3241.

102.   Bao, H.; Cui, X.; Li, C. M.; Gan, Y.; Zhang, J.; Guo, J., Photoswitchable Semiconductor Bismuth Sulfide (Bi_2S_3) Nanowires and Their Self-Supported Nanowire Arrays. *J. Phys. Chem. C* **2007,** *111* (33), 12279-12283.

103.   Phuruangrat, A.; Thongtem, T.; Thongtem, S., Characterization of Bi2S3 nanorods and nano-structured flowers prepared by a hydrothermal method. *Materials Letters* **2009,** *63* (17), 1496-1498.

104.   Tang, C.; Wang, C.; Su, F.; Zang, C.; Yang, Y.; Zong, Z.; Zhang, Y., Controlled synthesis of urchin-like Bi2S3 via hydrothermal method. *Solid State Sciences* **2010,** *12* (8), 1352-1356.

105.   Thongtem; Titipun; Phuruangrat; Anukorn; Wannapop; Surangkana; Somchai; Thongtem, Characterization of Bi_2S_3 with different morphologies synthesized using microwave radiation. *Mater. Lett.* **2010,** *64*, 122-124.

106.   Warule, S.; Kashid, R.; Shinde, D.; Chaudhari, N.; Kale, B.; More, M., Architectured Bi_2S_3 nanoflowers: photoenhanced field emission study. *J. Nanopart. Res.* **2012,** *14* (6), 1-13.

107.   Zhong, J.; Xiang, W.; Liu, L.; Yang, X.; Cai, W.; Zhang, J.; Liang, X., Biomolecule-assisted Solvothermal Synthesis of Bismuth Sulfide Nanorods. *J. Mater. Sci. Technol.* **2010,** *26* (5), 417-422.

108.   Rabin, O.; Manuel Perez, J.; Grimm, J.; Wojtkiewicz, G.; Weissleder, R., An X-ray computed tomography imaging agent based on long-circulating bismuth sulphide nanoparticles. *Nature materials* **2006,** *5* (2), 118-22.

109.   Ma, J.; Yeow, J. T.; Chow, J. C.; Barnett, R. B., A Customized Radiation Sensor for Ionization Collection. *IEEE Sens. J.* **2006,** *6* (6), 1523-1530.

110.   Ma, J.; Yeow, J. T. W.; Chow, J. C. L.; Barnett, R. B., A carbon nanotube-based radiation sensor. *Int. J. Robot. Autom.* **2007,** *22* (1), 49-58.

111.   Gao, X.; Kang, Q. S.; Yeow, J. T.; Barnett, R., Design and evaluation of quantum dot sensors for making superficial x-ray energy radiation measurements. *Nanotechnology* **2010,** *21* (28), 285502.

112.   Kang, Q.; Yeow, J. T.; Barnett, R., The use of semiconducting single-walled carbon nanotube films to measure X-ray dose. *Carbon* **2012,** *50* (6), 2197-2201.

113.   Lobez, J. M.; Swager, T. M., Radiation detection: resistivity responses in functional poly(olefin sulfone)/carbon nanotube composites. *Angew Chem Int Ed Engl* **2010,** *49* (1), 95-8.

114.   Intaniwet, A.; Mills, C. A.; Shkunov, M.; Sellin, P. J.; Keddie, J. L., Heavy metallic oxide nanoparticles for enhanced sensitivity in semiconducting polymer x-ray detectors. *Nanotechnology* **2012,** *23* (23), 235502.

115.   Samaras, M.; Derlet, P.; Van Swygenhoven, H.; Victoria, M., Radiation damage near grain boundaries. *Philos. Mag.* **2003,** *83* (31-34), 3599-3607.

116.   Nita, N.; Schaeublin, R.; Victoria, M.; Valiev, R., Effects of irradiation on the microstructure and mechanical properties of nanostructured materials. *Philos. Mag.* **2005,** *85* (4-7), 723-735.

117.   Chimi, Y.; Iwase, A.; Ishikawa, N.; Kobiyama, M.; Inami, T.; Kambara, T.; Okuda, S., Swift heavy ion irradiation effects in nanocrystalline gold. *Nucl. Instr. Meth. Phys. Res. B* **2006,** *245* (1), 171-175.

118.   Zhang, B.; Ye, X.; Hou, W.; Zhao, Y.; Xie, Y., Biomolecule-assisted synthesis and electrochemical hydrogen storage of Bi_2S_3 flowerlike patterns with well-aligned nanorods. *J. Phys. Chem. B* **2006,** *110* (18), 8978-8985.

119.   Panigrahi, P. K.; Pathak, A., The Growth of Bismuth Sulfide Nanorods from Spherical-Shaped Amorphous Precursor Particles under Hydrothermal Condition. *J. Nanopart.* **2013,** *2013*, 11.

120.   Nambiar, S.; Osei, E. K.; Yeow, J. T. W., Bismuth Sulfide Nanoflowers for Detection of X-rays in the Mammographic Energy Range. *Sci. Rep.* **2015,** *5*.

121.   Poludniowski, G. G.; Evans, P. M., Calculation of x-ray spectra emerging from an x-ray tube. Part I. Electron penetration characteristics in x-ray targets. *Medical physics* **2007,** *34* (6), 2164-2174.

122.   Poludniowski, G. G., Calculation of x-ray spectra emerging from an x-ray tube. Part II. X-ray production and filtration in x-ray targets. *Medical physics* **2007,** *34* (6), 2175-2186.

123.   Gerward, L.; Guilbert, N.; Jensen, K. B.; Leving, H., WinXCom – a program for calculating x-ray attenuation coefficients. *Radiation Physics and Chemistry* **2004,** *71*, 653-654.

124.   Poludniowski, G. G.; Evans, P. M., Calculation of x-ray spectra emerging from an x-ray tube. Part I. Electron penetration characteristics in x-ray targets. *Med. Phys.* **2007,** *34* (6), 2164-2174.

125.   Poludniowski, G. G., Calculation of x-ray spectra emerging from an x-ray tube. Part II. X-ray production and filtration in x-ray targets. *Med. Phys.* **2007,** *34* (6), 2175-2186.

126.   Kasap, S.; Frey, J. B.; Belev, G.; Tousignant, O.; Mani, H.; Greenspan, J.; Laperriere, L.; Bubon, O.; Reznik, A.; DeCrescenzo, G.; Karim, K. S.; Rowlands, J. A., Amorphous and polycrystalline photoconductors for direct conversion flat panel x-ray image sensors. *Sensors (Basel)* **2011,** *11* (5), 5112-57.

127.   Elshahat, B.; Filipyev, I.; Shrestha, S.; Hesser, J.; Gill, H.; Kumar, J.; Karellas, A.; Zygmanski, P.; Sajo, E., SU-E-CAMPUS-I-01: Nanometric Organic Photovoltaic Thin Film X-Ray Detectors for Clinical KVp Beams. *Medical physics* **2014,** *41* (6), 384-385.

128.   Kubelka, P.; Munk, F., Ein Beitrag zur Optik der Farbanstriche. *Zeits. f. Techn. Physik* **1931,** *12*, 593–601.

129.   Mane, R. S.; Sankapal, B. R.; Lokhande, C. D., Studies on chemically deposited nanocrystalline Bi_2S_3 thin films. *Mater. Res. Bull.* **2000,** *35* (4), 587-601.

Letters of copyright permission

JOHN WILEY AND SONS LICENSE
TERMS AND CONDITIONS

May 14, 2015

This Agreement between Shruti Nambiar ("You") and John Wiley and Sons ("John Wiley and Sons") consists of your license details and the terms and conditions provided by John Wiley and Sons and Copyright Clearance Center.

License Number	3627810149214
License date	May 14, 2015
Licensed Content Publisher	John Wiley and Sons
Licensed Content Publication	Journal of Applied Polymer Science
Licensed Content Title	Polymer nanocomposite-based shielding against diagnostic X-rays
Licensed Content Author	Shruti Nambiar,Ernest K. Osei,John T. W. Yeow
Licensed Content Date	Jun 14, 2012
Pages	8
Type of use	Dissertation/Thesis
Requestor type	Author of this Wiley article
Format	Print and electronic
Portion	Full article
Will you be translating?	No
Title of your thesis / dissertation	Application of Nanomaterials for X-ray Shielding and Detection in Diagnostic Radiology
Expected completion date	May 2015
Expected size (number of pages)	200
Requestor Location	Shruti Nambiar E2-1303F, 200 University Avenue West Waterloo, ON N2L3G1 Canada Attn: Shruti Nambiar
Billing Type	Invoice
Billing Address	Shruti Nambiar E2-1303F, 200 University Avenue West Waterloo, ON N2L3G1 Canada Attn: Shruti Nambiar
Total	0.00 CAD

Terms and Conditions

transaction, you agree that the following terms and conditions apply to this transaction (along with the billing and payment terms and conditions established by the Copyright Clearance Center Inc., ("CCC's Billing and Payment terms and conditions"), at the time that you opened your Rightslink account (these are available at any time at http://myaccount.copyright.com).

Copyright Clearance Center

RightsLink®

Home | Create Account | Help | Live Chat

nature publishing group

Title: Bismuth Sulfide Nanoflowers for Detection of X-rays in the Mammographic Energy Range

Author: Shruti Nambiar, Ernest K. Osei, John T. W. Yeow

Publication: Scientific Reports

Publisher: Nature Publishing Group

Date: Mar 24, 2015

Copyright © 2015, Rights Managed by Nature Publishing Group

Author Use

Authors of NPG articles do not require permission to use content from their article in most cases as stated in the author's guidelines.

Authors wishing to use their article for commercial purposes must request permission in the normal way.

For further questions, please contact NPG's permissions department: permissions@nature.com

BACK | CLOSE WINDOW

CAMBRIDGE UNIVERSITY PRESS LICENSE
TERMS AND CONDITIONS

Mar 02, 2015

This is a License Agreement between Shruti Nambiar ("You") and Cambridge University Press ("Cambridge University Press") provided by Copyright Clearance Center ("CCC"). The license consists of your order details, the terms and conditions provided by Cambridge University Press, and the payment terms and conditions.

All payments must be made in full to CCC. For payment instructions, please see information listed at the bottom of this form.

License Number	3580800901226
License date	Mar 02, 2015
Licensed content publisher	Cambridge University Press
Licensed content publication	Journal of Materials Research
Licensed content title	Effect of intercalation in graphite epoxy composites on the shielding of high energy radiation
Licensed content author	James R. Gaier, Wendie C. Hardebeck, Jennifer R. Terry Bunch, Michelle L. Davidson and Dwight B. Beery
Licensed content date	Jan 31, 2011
Volume number	13
Issue number	08
Start page	2297
End page	2301
Type of Use	Dissertation/Thesis
Requestor type	Not-for-profit
Portion	Text extract
Number of pages requested	1
Order reference number	None
Territory for reuse	World
Title of your thesis / dissertation	Nanomaterial-based X-ray Shielding and Detection
Expected completion date	May 2015
Estimated size(pages)	200
Billing Type	Invoice
Billing Address	Shruti Nambiar E2-1303F, 200 University Avenue West Waterloo, ON N2L3G1 Canada Attn: Shruti Nambiar
TAX (0.00%)	0.00 USD
Total	0.00 USD

TERMS & CONDITIONS

Cambridge University Press grants the Licensee permission on a non-exclusive non-transferable basis to reproduce, make available or otherwise use the Licensed content 'Content' in the named territory 'Territory' for the purpose listed 'the Use' on Page 1 of this Agreement subject to the following terms and conditions.

1. The License is limited to the permission granted and the Content detailed herein and does not extend to any other permission or content.
2. Cambridge gives no warranty or indemnity in respect of any third-party copyright material included in the Content, for which the Licensee should seek separate permission clearance.
3. The integrity of the Content must be ensured.
4. The License does extend to any edition published specifically for the use of handicapped or reading-impaired individuals.
5. The Licensee shall provide a prominent acknowledgement in the following format: author/s, title of article, name of journal, volume number, issue number, page references, , reproduced with permission.

Other terms and conditions: None

v1.0

Questions? customercare@copyright.com or +1-855-239-3415 (toll free in the US) or +1-978-646-2777.

Gratis licenses (referencing $0 in the Total field) are free. Please retain this printable license for your reference. No payment is required.

ELSEVIER LICENSE
TERMS AND CONDITIONS

Mar 02, 2015

This is a License Agreement between Shruti Nambiar ("You") and Elsevier ("Elsevier") provided by Copyright Clearance Center ("CCC"). The license consists of your order details, the terms and conditions provided by Elsevier, and the payment terms and conditions.

All payments must be made in full to CCC. For payment instructions, please see information listed at the bottom of this form.

Supplier	Elsevier Limited The Boulevard,Langford Lane Kidlington,Oxford,OX5 1GB,UK
Registered Company Number	1982084
Customer name	Shruti Nambiar
Customer address	E2-1303F, 200 University Avenue West
	Waterloo, ON N2L3G1
License number	3580801167253
License date	Mar 02, 2015
Licensed content publisher	Elsevier
Licensed content publication	Colloids and Surfaces A: Physicochemical and Engineering Aspects
Licensed content title	Radiation resistant polymer–carbon nanotube nanocomposite thin films
Licensed content author	Ebrahim Najafi,Kwanwoo Shin
Licensed content date	5 May 2005
Licensed content volume number	257
Licensed content issue number	n/a
Number of pages	5
Start Page	333
End Page	337
Type of Use	reuse in a thesis/dissertation
Intended publisher of new work	other
Portion	figures/tables/illustrations
Number of figures/tables /illustrations	1
Format	both print and electronic
Are you the author of this Elsevier article?	No
Will you be translating?	No
Original figure numbers	1

Title of your thesis/dissertation	Nanomaterial-based X-ray Shielding and Detection
Expected completion date	May 2015
Estimated size (number of pages)	200
Elsevier VAT number	GB 494 6272 12
Permissions price	0.00 CAD
VAT/Local Sales Tax	0.00 CAD / 0.00 GBP
Total	0.00 CAD
Terms and Conditions	

INTRODUCTION

1. The publisher for this copyrighted material is Elsevier. By clicking "accept" in connection with completing this licensing transaction, you agree that the following terms and conditions apply to this transaction (along with the Billing and Payment terms and conditions established by Copyright Clearance Center, Inc. ("CCC"), at the time that you opened your Rightslink account and that are available at any time at http://myaccount.copyright.com).

GENERAL TERMS

2. Elsevier hereby grants you permission to reproduce the aforementioned material subject to the terms and conditions indicated.

3. Acknowledgement: If any part of the material to be used (for example, figures) has appeared in our publication with credit or acknowledgement to another source, permission must also be sought from that source. If such permission is not obtained then that material may not be included in your publication/copies. Suitable acknowledgement to the source must be made, either as a footnote or in a reference list at the end of your publication, as follows:

"Reprinted from Publication title, Vol /edition number, Author(s), Title of article / title of chapter, Pages No., Copyright (Year), with permission from Elsevier [OR APPLICABLE SOCIETY COPYRIGHT OWNER]." Also Lancet special credit - "Reprinted from The Lancet, Vol. number, Author(s), Title of article, Pages No., Copyright (Year), with permission from Elsevier."

4. Reproduction of this material is confined to the purpose and/or media for which permission is hereby given.

5. Altering/Modifying Material: Not Permitted. However figures and illustrations may be altered/adapted minimally to serve your work. Any other abbreviations, additions, deletions and/or any other alterations shall be made only with prior written authorization of Elsevier Ltd. (Please contact Elsevier at permissions@elsevier.com)

6. If the permission fee for the requested use of our material is waived in this instance, please be advised that your future requests for Elsevier materials may attract a fee.

7. Reservation of Rights: Publisher reserves all rights not specifically granted in the combination of (i) the license details provided by you and accepted in the course of this

licensing transaction, (ii) these terms and conditions and (iii) CCC's Billing and Payment terms and conditions.

8. License Contingent Upon Payment: While you may exercise the rights licensed immediately upon issuance of the license at the end of the licensing process for the transaction, provided that you have disclosed complete and accurate details of your proposed use, no license is finally effective unless and until full payment is received from you (either by publisher or by CCC) as provided in CCC's Billing and Payment terms and conditions. If full payment is not received on a timely basis, then any license preliminarily granted shall be deemed automatically revoked and shall be void as if never granted. Further, in the event that you breach any of these terms and conditions or any of CCC's Billing and Payment terms and conditions, the license is automatically revoked and shall be void as if never granted. Use of materials as described in a revoked license, as well as any use of the materials beyond the scope of an unrevoked license, may constitute copyright infringement and publisher reserves the right to take any and all action to protect its copyright in the materials.

9. Warranties: Publisher makes no representations or warranties with respect to the licensed material.

10. Indemnity: You hereby indemnify and agree to hold harmless publisher and CCC, and their respective officers, directors, employees and agents, from and against any and all claims arising out of your use of the licensed material other than as specifically authorized pursuant to this license.

11. No Transfer of License: This license is personal to you and may not be sublicensed, assigned, or transferred by you to any other person without publisher's written permission.

12. No Amendment Except in Writing: This license may not be amended except in a writing signed by both parties (or, in the case of publisher, by CCC on publisher's behalf).

13. Objection to Contrary Terms: Publisher hereby objects to any terms contained in any purchase order, acknowledgment, check endorsement or other writing prepared by you, which terms are inconsistent with these terms and conditions or CCC's Billing and Payment terms and conditions. These terms and conditions, together with CCC's Billing and Payment terms and conditions (which are incorporated herein), comprise the entire agreement between you and publisher (and CCC) concerning this licensing transaction. In the event of any conflict between your obligations established by these terms and conditions and those established by CCC's Billing and Payment terms and conditions, these terms and conditions shall control.

14. Revocation: Elsevier or Copyright Clearance Center may deny the permissions described in this License at their sole discretion, for any reason or no reason, with a full refund payable to you. Notice of such denial will be made using the contact information provided by you. Failure to receive such notice will not alter or invalidate the denial. In no event will Elsevier or Copyright Clearance Center be responsible or liable for any costs, expenses or damage incurred by you as a result of a denial of your permission request, other than a refund of the amount(s) paid by you to Elsevier and/or Copyright Clearance Center for denied permissions.

LIMITED LICENSE

The following terms and conditions apply only to specific license types:

15. **Translation**: This permission is granted for non-exclusive world **English** rights only unless your license was granted for translation rights. If you licensed translation rights you may only translate this content into the languages you requested. A professional translator must perform all translations and reproduce the content word for word preserving the integrity of the article. If this license is to re-use 1 or 2 figures then permission is granted for non-exclusive world rights in all languages.

16. **Posting licensed content on any Website**: The following terms and conditions apply as follows: Licensing material from an Elsevier journal: All content posted to the web site must maintain the copyright information line on the bottom of each image; A hyper-text must be included to the Homepage of the journal from which you are licensing at http://www.sciencedirect.com/science/journal/xxxxx or the Elsevier homepage for books at http://www.elsevier.com; Central Storage: This license does not include permission for a scanned version of the material to be stored in a central repository such as that provided by Heron/XanEdu.

Licensing material from an Elsevier book: A hyper-text link must be included to the Elsevier homepage at http://www.elsevier.com . All content posted to the web site must maintain the copyright information line on the bottom of each image.

Posting licensed content on Electronic reserve: In addition to the above the following clauses are applicable: The web site must be password-protected and made available only to bona fide students registered on a relevant course. This permission is granted for 1 year only. You may obtain a new license for future website posting.

17. **For journal authors:** the following clauses are applicable in addition to the above:

Preprints:

A preprint is an author's own write-up of research results and analysis, it has not been peer-reviewed, nor has it had any other value added to it by a publisher (such as formatting, copyright, technical enhancement etc.).

Authors can share their preprints anywhere at any time. Preprints should not be added to or enhanced in any way in order to appear more like, or to substitute for, the final versions of articles however authors can update their preprints on arXiv or RePEc with their Accepted Author Manuscript (see below).

If accepted for publication, we encourage authors to link from the preprint to their formal publication via its DOI. Millions of researchers have access to the formal publications on ScienceDirect, and so links will help users to find, access, cite and use the best available version. Please note that Cell Press, The Lancet and some society-owned have different preprint policies. Information on these policies is available on the journal homepage.

Accepted Author Manuscripts: An accepted author manuscript is the manuscript of an article that has been accepted for publication and which typically includes author-incorporated changes suggested during submission, peer review and editor-author communications.

Authors can share their accepted author manuscript:

- immediately

    ○ via their non-commercial person homepage or blog

    ○ by updating a preprint in arXiv or RePEc with the accepted manuscript

    ○ via their research institute or institutional repository for internal institutional uses or as part of an invitation-only research collaboration work-group

    ○ directly by providing copies to their students or to research collaborators for their personal use

    ○ for private scholarly sharing as part of an invitation-only work group on commercial sites with which Elsevier has an agreement

- after the embargo period

    ○ via non-commercial hosting platforms such as their institutional repository

    ○ via commercial sites with which Elsevier has an agreement

In all cases accepted manuscripts should:

- link to the formal publication via its DOI

- bear a CC-BY-NC-ND license - this is easy to do

- if aggregated with other manuscripts, for example in a repository or other site, be shared in alignment with our hosting policy not be added to or enhanced in any way to appear more like, or to substitute for, the published journal article.

Published journal article (JPA): A published journal article (PJA) is the definitive final record of published research that appears or will appear in the journal and embodies all value-adding publishing activities including peer review co-ordination, copy-editing, formatting, (if relevant) pagination and online enrichment.

Policies for sharing publishing journal articles differ for subscription and gold open access articles:

<u>Subscription Articles:</u> If you are an author, please share a link to your article rather than the full-text. Millions of researchers have access to the formal publications on ScienceDirect, and so links will help your users to find, access, cite, and use the best available version.

Theses and dissertations which contain embedded PJAs as part of the formal submission can be posted publicly by the awarding institution with DOI links back to the formal publications on ScienceDirect.

If you are affiliated with a library that subscribes to ScienceDirect you have additional private sharing rights for others' research accessed under that agreement. This includes use for classroom teaching and internal training at the institution (including use in course packs and courseware programs), and inclusion of the article for grant funding purposes.

Gold Open Access Articles: May be shared according to the author-selected end-user license and should contain a [CrossMark logo](#), the end user license, and a DOI link to the formal publication on ScienceDirect.

Please refer to Elsevier's [posting policy](#) for further information.

18. **For book authors** the following clauses are applicable in addition to the above: Authors are permitted to place a brief summary of their work online only. You are not allowed to download and post the published electronic version of your chapter, nor may you scan the printed edition to create an electronic version. **Posting to a repository:** Authors are permitted to post a summary of their chapter only in their institution's repository.

19. **Thesis/Dissertation**: If your license is for use in a thesis/dissertation your thesis may be submitted to your institution in either print or electronic form. Should your thesis be published commercially, please reapply for permission. These requirements include permission for the Library and Archives of Canada to supply single copies, on demand, of the complete thesis and include permission for Proquest/UMI to supply single copies, on demand, of the complete thesis. Should your thesis be published commercially, please reapply for permission. Theses and dissertations which contain embedded PJAs as part of the formal submission can be posted publicly by the awarding institution with DOI links back to the formal publications on ScienceDirect.

Elsevier Open Access Terms and Conditions

You can publish open access with Elsevier in hundreds of open access journals or in nearly 2000 established subscription journals that support open access publishing. Permitted third party re-use of these open access articles is defined by the author's choice of Creative Commons user license. See our [open access license policy](#) for more information.

Terms & Conditions applicable to all Open Access articles published with Elsevier:

Any reuse of the article must not represent the author as endorsing the adaptation of the article nor should the article be modified in such a way as to damage the author's honour or reputation. If any changes have been made, such changes must be clearly indicated.

The author(s) must be appropriately credited and we ask that you include the end user license and a DOI link to the formal publication on ScienceDirect.

If any part of the material to be used (for example, figures) has appeared in our publication with credit or acknowledgement to another source it is the responsibility of the user to ensure their reuse complies with the terms and conditions determined by the rights holder.

Additional Terms & Conditions applicable to each Creative Commons user license:

CC BY: The CC-BY license allows users to copy, to create extracts, abstracts and new works from the Article, to alter and revise the Article and to make commercial use of the Article (including reuse and/or resale of the Article by commercial entities), provided the user gives appropriate credit (with a link to the formal publication through the relevant DOI), provides a link to the license, indicates if changes were made and the licensor is not represented as endorsing the use made of the work. The full details of the license are

available at http://creativecommons.org/licenses/by/4.0.

CC BY NC SA: The CC BY-NC-SA license allows users to copy, to create extracts, abstracts and new works from the Article, to alter and revise the Article, provided this is not done for commercial purposes, and that the user gives appropriate credit (with a link to the formal publication through the relevant DOI), provides a link to the license, indicates if changes were made and the licensor is not represented as endorsing the use made of the work. Further, any new works must be made available on the same conditions. The full details of the license are available at http://creativecommons.org/licenses/by-nc-sa/4.0.

CC BY NC ND: The CC BY-NC-ND license allows users to copy and distribute the Article, provided this is not done for commercial purposes and further does not permit distribution of the Article if it is changed or edited in any way, and provided the user gives appropriate credit (with a link to the formal publication through the relevant DOI), provides a link to the license, and that the licensor is not represented as endorsing the use made of the work. The full details of the license are available at http://creativecommons.org/licenses/by-nc-nd/4.0. Any commercial reuse of Open Access articles published with a CC BY NC SA or CC BY NC ND license requires permission from Elsevier and will be subject to a fee.

Commercial reuse includes:

- Associating advertising with the full text of the Article

- Charging fees for document delivery or access

- Article aggregation

- Systematic distribution via e-mail lists or share buttons

Posting or linking by commercial companies for use by customers of those companies.

20. **Other Conditions**:

ELSEVIER LICENSE
TERMS AND CONDITIONS

Mar 02, 2015

This is a License Agreement between Shruti Nambiar ("You") and Elsevier ("Elsevier") provided by Copyright Clearance Center ("CCC"). The license consists of your order details, the terms and conditions provided by Elsevier, and the payment terms and conditions.

All payments must be made in full to CCC. For payment instructions, please see information listed at the bottom of this form.

Supplier	Elsevier Limited The Boulevard,Langford Lane Kidlington,Oxford,OX5 1GB,UK
Registered Company Number	1982084
Customer name	Shruti Nambiar
Customer address	E2-1303F, 200 University Avenue West
	Waterloo, ON N2L3G1
License number	3580810425862
License date	Mar 02, 2015
Licensed content publisher	Elsevier
Licensed content publication	Nuclear Instruments and Methods in Physics Research Section B: Beam Interactions with Materials and Atoms
Licensed content title	Resistance to proton radiation of nano-TiO2 modified silicone rubber
Licensed content author	Mingwei Di,Shiyu He,Ruiqi Li,Dezhuang Yang
Licensed content date	November 2006
Licensed content volume number	252
Licensed content issue number	2
Number of pages	7
Start Page	212
End Page	218
Type of Use	reuse in a thesis/dissertation
Intended publisher of new work	other
Portion	figures/tables/illustrations
Number of figures/tables /illustrations	1
Format	both print and electronic
Are you the author of this Elsevier article?	No
Will you be translating?	No
Original figure numbers	Fig. 3

Title of your thesis/dissertation	Nanomaterial-based X-ray Shielding and Detection
Expected completion date	May 2015
Estimated size (number of pages)	200
Elsevier VAT number	GB 494 6272 12
Permissions price	0.00 CAD
VAT/Local Sales Tax	0.00 CAD / 0.00 GBP
Total	0.00 CAD
Terms and Conditions	

INTRODUCTION

1. The publisher for this copyrighted material is Elsevier. By clicking "accept" in connection with completing this licensing transaction, you agree that the following terms and conditions apply to this transaction (along with the Billing and Payment terms and conditions established by Copyright Clearance Center, Inc. ("CCC"), at the time that you opened your Rightslink account and that are available at any time at http://myaccount.copyright.com).

GENERAL TERMS

2. Elsevier hereby grants you permission to reproduce the aforementioned material subject to the terms and conditions indicated.

3. Acknowledgement: If any part of the material to be used (for example, figures) has appeared in our publication with credit or acknowledgement to another source, permission must also be sought from that source. If such permission is not obtained then that material may not be included in your publication/copies. Suitable acknowledgement to the source must be made, either as a footnote or in a reference list at the end of your publication, as follows:

"Reprinted from Publication title, Vol /edition number, Author(s), Title of article / title of chapter, Pages No., Copyright (Year), with permission from Elsevier [OR APPLICABLE SOCIETY COPYRIGHT OWNER]." Also Lancet special credit - "Reprinted from The Lancet, Vol. number, Author(s), Title of article, Pages No., Copyright (Year), with permission from Elsevier."

4. Reproduction of this material is confined to the purpose and/or media for which permission is hereby given.

5. Altering/Modifying Material: Not Permitted. However figures and illustrations may be altered/adapted minimally to serve your work. Any other abbreviations, additions, deletions and/or any other alterations shall be made only with prior written authorization of Elsevier Ltd. (Please contact Elsevier at permissions@elsevier.com)

6. If the permission fee for the requested use of our material is waived in this instance, please be advised that your future requests for Elsevier materials may attract a fee.

7. Reservation of Rights: Publisher reserves all rights not specifically granted in the combination of (i) the license details provided by you and accepted in the course of this

licensing transaction, (ii) these terms and conditions and (iii) CCC's Billing and Payment terms and conditions.

8. License Contingent Upon Payment: While you may exercise the rights licensed immediately upon issuance of the license at the end of the licensing process for the transaction, provided that you have disclosed complete and accurate details of your proposed use, no license is finally effective unless and until full payment is received from you (either by publisher or by CCC) as provided in CCC's Billing and Payment terms and conditions. If full payment is not received on a timely basis, then any license preliminarily granted shall be deemed automatically revoked and shall be void as if never granted. Further, in the event that you breach any of these terms and conditions or any of CCC's Billing and Payment terms and conditions, the license is automatically revoked and shall be void as if never granted. Use of materials as described in a revoked license, as well as any use of the materials beyond the scope of an unrevoked license, may constitute copyright infringement and publisher reserves the right to take any and all action to protect its copyright in the materials.

9. Warranties: Publisher makes no representations or warranties with respect to the licensed material.

10. Indemnity: You hereby indemnify and agree to hold harmless publisher and CCC, and their respective officers, directors, employees and agents, from and against any and all claims arising out of your use of the licensed material other than as specifically authorized pursuant to this license.

11. No Transfer of License: This license is personal to you and may not be sublicensed, assigned, or transferred by you to any other person without publisher's written permission.

12. No Amendment Except in Writing: This license may not be amended except in a writing signed by both parties (or, in the case of publisher, by CCC on publisher's behalf).

13. Objection to Contrary Terms: Publisher hereby objects to any terms contained in any purchase order, acknowledgment, check endorsement or other writing prepared by you, which terms are inconsistent with these terms and conditions or CCC's Billing and Payment terms and conditions. These terms and conditions, together with CCC's Billing and Payment terms and conditions (which are incorporated herein), comprise the entire agreement between you and publisher (and CCC) concerning this licensing transaction. In the event of any conflict between your obligations established by these terms and conditions and those established by CCC's Billing and Payment terms and conditions, these terms and conditions shall control.

14. Revocation: Elsevier or Copyright Clearance Center may deny the permissions described in this License at their sole discretion, for any reason or no reason, with a full refund payable to you. Notice of such denial will be made using the contact information provided by you. Failure to receive such notice will not alter or invalidate the denial. In no event will Elsevier or Copyright Clearance Center be responsible or liable for any costs, expenses or damage incurred by you as a result of a denial of your permission request, other than a refund of the amount(s) paid by you to Elsevier and/or Copyright Clearance Center for denied permissions.

LIMITED LICENSE

The following terms and conditions apply only to specific license types:

15. **Translation**: This permission is granted for non-exclusive world **English** rights only unless your license was granted for translation rights. If you licensed translation rights you may only translate this content into the languages you requested. A professional translator must perform all translations and reproduce the content word for word preserving the integrity of the article. If this license is to re-use 1 or 2 figures then permission is granted for non-exclusive world rights in all languages.

16. **Posting licensed content on any Website**: The following terms and conditions apply as follows: Licensing material from an Elsevier journal: All content posted to the web site must maintain the copyright information line on the bottom of each image; A hyper-text must be included to the Homepage of the journal from which you are licensing at http://www.sciencedirect.com/science/journal/xxxxx or the Elsevier homepage for books at http://www.elsevier.com; Central Storage: This license does not include permission for a scanned version of the material to be stored in a central repository such as that provided by Heron/XanEdu.

Licensing material from an Elsevier book: A hyper-text link must be included to the Elsevier homepage at http://www.elsevier.com . All content posted to the web site must maintain the copyright information line on the bottom of each image.

Posting licensed content on Electronic reserve: In addition to the above the following clauses are applicable: The web site must be password-protected and made available only to bona fide students registered on a relevant course. This permission is granted for 1 year only. You may obtain a new license for future website posting.

17. **For journal authors:** the following clauses are applicable in addition to the above:

Preprints:

A preprint is an author's own write-up of research results and analysis, it has not been peer-reviewed, nor has it had any other value added to it by a publisher (such as formatting, copyright, technical enhancement etc.).

Authors can share their preprints anywhere at any time. Preprints should not be added to or enhanced in any way in order to appear more like, or to substitute for, the final versions of articles however authors can update their preprints on arXiv or RePEc with their Accepted Author Manuscript (see below).

If accepted for publication, we encourage authors to link from the preprint to their formal publication via its DOI. Millions of researchers have access to the formal publications on ScienceDirect, and so links will help users to find, access, cite and use the best available version. Please note that Cell Press, The Lancet and some society-owned have different preprint policies. Information on these policies is available on the journal homepage.

Accepted Author Manuscripts: An accepted author manuscript is the manuscript of an article that has been accepted for publication and which typically includes author-incorporated changes suggested during submission, peer review and editor-author communications.

Authors can share their accepted author manuscript:

- immediately

    ○ via their non-commercial person homepage or blog

    ○ by updating a preprint in arXiv or RePEc with the accepted manuscript

    ○ via their research institute or institutional repository for internal institutional uses or as part of an invitation-only research collaboration work-group

    ○ directly by providing copies to their students or to research collaborators for their personal use

    ○ for private scholarly sharing as part of an invitation-only work group on commercial sites with which Elsevier has an agreement

- after the embargo period

    ○ via non-commercial hosting platforms such as their institutional repository

    ○ via commercial sites with which Elsevier has an agreement

In all cases accepted manuscripts should:

- link to the formal publication via its DOI

- bear a CC-BY-NC-ND license - this is easy to do

- if aggregated with other manuscripts, for example in a repository or other site, be shared in alignment with our hosting policy not be added to or enhanced in any way to appear more like, or to substitute for, the published journal article.

Published journal article (JPA): A published journal article (PJA) is the definitive final record of published research that appears or will appear in the journal and embodies all value-adding publishing activities including peer review co-ordination, copy-editing, formatting, (if relevant) pagination and online enrichment.

Policies for sharing publishing journal articles differ for subscription and gold open access articles:

<u>**Subscription Articles:**</u> If you are an author, please share a link to your article rather than the full-text. Millions of researchers have access to the formal publications on ScienceDirect, and so links will help your users to find, access, cite, and use the best available version.

Theses and dissertations which contain embedded PJAs as part of the formal submission can be posted publicly by the awarding institution with DOI links back to the formal publications on ScienceDirect.

If you are affiliated with a library that subscribes to ScienceDirect you have additional private sharing rights for others' research accessed under that agreement. This includes use for classroom teaching and internal training at the institution (including use in course packs and courseware programs), and inclusion of the article for grant funding purposes.

Gold Open Access Articles: May be shared according to the author-selected end-user license and should contain a CrossMark logo, the end user license, and a DOI link to the formal publication on ScienceDirect.

Please refer to Elsevier's posting policy for further information.

18. **For book authors** the following clauses are applicable in addition to the above: Authors are permitted to place a brief summary of their work online only. You are not allowed to download and post the published electronic version of your chapter, nor may you scan the printed edition to create an electronic version. **Posting to a repository:** Authors are permitted to post a summary of their chapter only in their institution's repository.

19. **Thesis/Dissertation**: If your license is for use in a thesis/dissertation your thesis may be submitted to your institution in either print or electronic form. Should your thesis be published commercially, please reapply for permission. These requirements include permission for the Library and Archives of Canada to supply single copies, on demand, of the complete thesis and include permission for Proquest/UMI to supply single copies, on demand, of the complete thesis. Should your thesis be published commercially, please reapply for permission. Theses and dissertations which contain embedded PJAs as part of the formal submission can be posted publicly by the awarding institution with DOI links back to the formal publications on ScienceDirect.

Elsevier Open Access Terms and Conditions

You can publish open access with Elsevier in hundreds of open access journals or in nearly 2000 established subscription journals that support open access publishing. Permitted third party re-use of these open access articles is defined by the author's choice of Creative Commons user license. See our open access license policy for more information.

Terms & Conditions applicable to all Open Access articles published with Elsevier:

Any reuse of the article must not represent the author as endorsing the adaptation of the article nor should the article be modified in such a way as to damage the author's honour or reputation. If any changes have been made, such changes must be clearly indicated.

The author(s) must be appropriately credited and we ask that you include the end user license and a DOI link to the formal publication on ScienceDirect.

If any part of the material to be used (for example, figures) has appeared in our publication with credit or acknowledgement to another source it is the responsibility of the user to ensure their reuse complies with the terms and conditions determined by the rights holder.

Additional Terms & Conditions applicable to each Creative Commons user license:

CC BY: The CC-BY license allows users to copy, to create extracts, abstracts and new works from the Article, to alter and revise the Article and to make commercial use of the Article (including reuse and/or resale of the Article by commercial entities), provided the user gives appropriate credit (with a link to the formal publication through the relevant DOI), provides a link to the license, indicates if changes were made and the licensor is not represented as endorsing the use made of the work. The full details of the license are

available at http://creativecommons.org/licenses/by/4.0.

CC BY NC SA: The CC BY-NC-SA license allows users to copy, to create extracts, abstracts and new works from the Article, to alter and revise the Article, provided this is not done for commercial purposes, and that the user gives appropriate credit (with a link to the formal publication through the relevant DOI), provides a link to the license, indicates if changes were made and the licensor is not represented as endorsing the use made of the work. Further, any new works must be made available on the same conditions. The full details of the license are available at http://creativecommons.org/licenses/by-nc-sa/4.0.

CC BY NC ND: The CC BY-NC-ND license allows users to copy and distribute the Article, provided this is not done for commercial purposes and further does not permit distribution of the Article if it is changed or edited in any way, and provided the user gives appropriate credit (with a link to the formal publication through the relevant DOI), provides a link to the license, and that the licensor is not represented as endorsing the use made of the work. The full details of the license are available at http://creativecommons.org/licenses/by-nc-nd/4.0. Any commercial reuse of Open Access articles published with a CC BY NC SA or CC BY NC ND license requires permission from Elsevier and will be subject to a fee.

Commercial reuse includes:

- Associating advertising with the full text of the Article

- Charging fees for document delivery or access

- Article aggregation

- Systematic distribution via e-mail lists or share buttons

Posting or linking by commercial companies for use by customers of those companies.

20. **Other Conditions**:

Questions? customercare@copyright.com or +1-855-239-3415 (toll free in the US) or +1-978-646-2777.

Gratis licenses (referencing $0 in the Total field) are free. Please retain this printable license for your reference. No payment is required.

ELSEVIER LICENSE
TERMS AND CONDITIONS

Mar 02, 2015

This is a License Agreement between Shruti Nambiar ("You") and Elsevier ("Elsevier") provided by Copyright Clearance Center ("CCC"). The license consists of your order details, the terms and conditions provided by Elsevier, and the payment terms and conditions.

All payments must be made in full to CCC. For payment instructions, please see information listed at the bottom of this form.

Supplier	Elsevier Limited The Boulevard,Langford Lane Kidlington,Oxford,OX5 1GB,UK
Registered Company Number	1982084
Customer name	Shruti Nambiar
Customer address	E2-1303F, 200 University Avenue West
	Waterloo, ON N2L3G1
License number	3580810658858
License date	Mar 02, 2015
Licensed content publisher	Elsevier
Licensed content publication	Composites Science and Technology
Licensed content title	Cosmic radiation shielding tests for UHMWPE fiber/nano-epoxy composites
Licensed content author	W.H. Zhong,G. Sui,S. Jana,J. Miller
Licensed content date	October 2009
Licensed content volume number	69
Licensed content issue number	13
Number of pages	5
Start Page	2093
End Page	2097
Type of Use	reuse in a thesis/dissertation
Intended publisher of new work	other
Portion	figures/tables/illustrations
Number of figures/tables /illustrations	1
Format	both print and electronic
Are you the author of this Elsevier article?	No
Will you be translating?	No
Original figure numbers	Fig. 5

Title of your thesis/dissertation	Nanomaterial-based X-ray Shielding and Detection
Expected completion date	May 2015
Estimated size (number of pages)	200
Elsevier VAT number	GB 494 6272 12
Permissions price	0.00 CAD
VAT/Local Sales Tax	0.00 CAD / 0.00 GBP
Total	0.00 CAD
Terms and Conditions	

INTRODUCTION

1. The publisher for this copyrighted material is Elsevier. By clicking "accept" in connection with completing this licensing transaction, you agree that the following terms and conditions apply to this transaction (along with the Billing and Payment terms and conditions established by Copyright Clearance Center, Inc. ("CCC"), at the time that you opened your Rightslink account and that are available at any time at http://myaccount.copyright.com).

GENERAL TERMS

2. Elsevier hereby grants you permission to reproduce the aforementioned material subject to the terms and conditions indicated.

3. Acknowledgement: If any part of the material to be used (for example, figures) has appeared in our publication with credit or acknowledgement to another source, permission must also be sought from that source. If such permission is not obtained then that material may not be included in your publication/copies. Suitable acknowledgement to the source must be made, either as a footnote or in a reference list at the end of your publication, as follows:

"Reprinted from Publication title, Vol /edition number, Author(s), Title of article / title of chapter, Pages No., Copyright (Year), with permission from Elsevier [OR APPLICABLE SOCIETY COPYRIGHT OWNER]." Also Lancet special credit - "Reprinted from The Lancet, Vol. number, Author(s), Title of article, Pages No., Copyright (Year), with permission from Elsevier."

4. Reproduction of this material is confined to the purpose and/or media for which permission is hereby given.

5. Altering/Modifying Material: Not Permitted. However figures and illustrations may be altered/adapted minimally to serve your work. Any other abbreviations, additions, deletions and/or any other alterations shall be made only with prior written authorization of Elsevier Ltd. (Please contact Elsevier at permissions@elsevier.com)

6. If the permission fee for the requested use of our material is waived in this instance, please be advised that your future requests for Elsevier materials may attract a fee.

7. Reservation of Rights: Publisher reserves all rights not specifically granted in the combination of (i) the license details provided by you and accepted in the course of this

licensing transaction, (ii) these terms and conditions and (iii) CCC's Billing and Payment terms and conditions.

8. License Contingent Upon Payment: While you may exercise the rights licensed immediately upon issuance of the license at the end of the licensing process for the transaction, provided that you have disclosed complete and accurate details of your proposed use, no license is finally effective unless and until full payment is received from you (either by publisher or by CCC) as provided in CCC's Billing and Payment terms and conditions. If full payment is not received on a timely basis, then any license preliminarily granted shall be deemed automatically revoked and shall be void as if never granted. Further, in the event that you breach any of these terms and conditions or any of CCC's Billing and Payment terms and conditions, the license is automatically revoked and shall be void as if never granted. Use of materials as described in a revoked license, as well as any use of the materials beyond the scope of an unrevoked license, may constitute copyright infringement and publisher reserves the right to take any and all action to protect its copyright in the materials.

9. Warranties: Publisher makes no representations or warranties with respect to the licensed material.

10. Indemnity: You hereby indemnify and agree to hold harmless publisher and CCC, and their respective officers, directors, employees and agents, from and against any and all claims arising out of your use of the licensed material other than as specifically authorized pursuant to this license.

11. No Transfer of License: This license is personal to you and may not be sublicensed, assigned, or transferred by you to any other person without publisher's written permission.

12. No Amendment Except in Writing: This license may not be amended except in a writing signed by both parties (or, in the case of publisher, by CCC on publisher's behalf).

13. Objection to Contrary Terms: Publisher hereby objects to any terms contained in any purchase order, acknowledgment, check endorsement or other writing prepared by you, which terms are inconsistent with these terms and conditions or CCC's Billing and Payment terms and conditions. These terms and conditions, together with CCC's Billing and Payment terms and conditions (which are incorporated herein), comprise the entire agreement between you and publisher (and CCC) concerning this licensing transaction. In the event of any conflict between your obligations established by these terms and conditions and those established by CCC's Billing and Payment terms and conditions, these terms and conditions shall control.

14. Revocation: Elsevier or Copyright Clearance Center may deny the permissions described in this License at their sole discretion, for any reason or no reason, with a full refund payable to you. Notice of such denial will be made using the contact information provided by you. Failure to receive such notice will not alter or invalidate the denial. In no event will Elsevier or Copyright Clearance Center be responsible or liable for any costs, expenses or damage incurred by you as a result of a denial of your permission request, other than a refund of the amount(s) paid by you to Elsevier and/or Copyright Clearance Center for denied permissions.

LIMITED LICENSE

The following terms and conditions apply only to specific license types:

15. **Translation**: This permission is granted for non-exclusive world **English** rights only unless your license was granted for translation rights. If you licensed translation rights you may only translate this content into the languages you requested. A professional translator must perform all translations and reproduce the content word for word preserving the integrity of the article. If this license is to re-use 1 or 2 figures then permission is granted for non-exclusive world rights in all languages.

16. **Posting licensed content on any Website**: The following terms and conditions apply as follows: Licensing material from an Elsevier journal: All content posted to the web site must maintain the copyright information line on the bottom of each image; A hyper-text must be included to the Homepage of the journal from which you are licensing at http://www.sciencedirect.com/science/journal/xxxxx or the Elsevier homepage for books at http://www.elsevier.com; Central Storage: This license does not include permission for a scanned version of the material to be stored in a central repository such as that provided by Heron/XanEdu.

Licensing material from an Elsevier book: A hyper-text link must be included to the Elsevier homepage at http://www.elsevier.com . All content posted to the web site must maintain the copyright information line on the bottom of each image.

Posting licensed content on Electronic reserve: In addition to the above the following clauses are applicable: The web site must be password-protected and made available only to bona fide students registered on a relevant course. This permission is granted for 1 year only. You may obtain a new license for future website posting.

17. **For journal authors:** the following clauses are applicable in addition to the above:

Preprints:

A preprint is an author's own write-up of research results and analysis, it has not been peer-reviewed, nor has it had any other value added to it by a publisher (such as formatting, copyright, technical enhancement etc.).

Authors can share their preprints anywhere at any time. Preprints should not be added to or enhanced in any way in order to appear more like, or to substitute for, the final versions of articles however authors can update their preprints on arXiv or RePEc with their Accepted Author Manuscript (see below).

If accepted for publication, we encourage authors to link from the preprint to their formal publication via its DOI. Millions of researchers have access to the formal publications on ScienceDirect, and so links will help users to find, access, cite and use the best available version. Please note that Cell Press, The Lancet and some society-owned have different preprint policies. Information on these policies is available on the journal homepage.

Accepted Author Manuscripts: An accepted author manuscript is the manuscript of an article that has been accepted for publication and which typically includes author-incorporated changes suggested during submission, peer review and editor-author communications.

Authors can share their accepted author manuscript:

- immediately

    ○ via their non-commercial person homepage or blog

    ○ by updating a preprint in arXiv or RePEc with the accepted manuscript

    ○ via their research institute or institutional repository for internal institutional uses or as part of an invitation-only research collaboration work-group

    ○ directly by providing copies to their students or to research collaborators for their personal use

    ○ for private scholarly sharing as part of an invitation-only work group on commercial sites with which Elsevier has an agreement

- after the embargo period

    ○ via non-commercial hosting platforms such as their institutional repository

    ○ via commercial sites with which Elsevier has an agreement

In all cases accepted manuscripts should:

- link to the formal publication via its DOI

- bear a CC-BY-NC-ND license - this is easy to do

- if aggregated with other manuscripts, for example in a repository or other site, be shared in alignment with our hosting policy not be added to or enhanced in any way to appear more like, or to substitute for, the published journal article.

Published journal article (JPA): A published journal article (PJA) is the definitive final record of published research that appears or will appear in the journal and embodies all value-adding publishing activities including peer review co-ordination, copy-editing, formatting, (if relevant) pagination and online enrichment.

Policies for sharing publishing journal articles differ for subscription and gold open access articles:

Subscription Articles: If you are an author, please share a link to your article rather than the full-text. Millions of researchers have access to the formal publications on ScienceDirect, and so links will help your users to find, access, cite, and use the best available version.

Theses and dissertations which contain embedded PJAs as part of the formal submission can be posted publicly by the awarding institution with DOI links back to the formal publications on ScienceDirect.

If you are affiliated with a library that subscribes to ScienceDirect you have additional private sharing rights for others' research accessed under that agreement. This includes use for classroom teaching and internal training at the institution (including use in course packs and courseware programs), and inclusion of the article for grant funding purposes.

Gold Open Access Articles: May be shared according to the author-selected end-user license and should contain a CrossMark logo, the end user license, and a DOI link to the formal publication on ScienceDirect.

Please refer to Elsevier's posting policy for further information.

18. **For book authors** the following clauses are applicable in addition to the above: Authors are permitted to place a brief summary of their work online only. You are not allowed to download and post the published electronic version of your chapter, nor may you scan the printed edition to create an electronic version. **Posting to a repository:** Authors are permitted to post a summary of their chapter only in their institution's repository.

19. **Thesis/Dissertation**: If your license is for use in a thesis/dissertation your thesis may be submitted to your institution in either print or electronic form. Should your thesis be published commercially, please reapply for permission. These requirements include permission for the Library and Archives of Canada to supply single copies, on demand, of the complete thesis and include permission for Proquest/UMI to supply single copies, on demand, of the complete thesis. Should your thesis be published commercially, please reapply for permission. Theses and dissertations which contain embedded PJAs as part of the formal submission can be posted publicly by the awarding institution with DOI links back to the formal publications on ScienceDirect.

Elsevier Open Access Terms and Conditions

You can publish open access with Elsevier in hundreds of open access journals or in nearly 2000 established subscription journals that support open access publishing. Permitted third party re-use of these open access articles is defined by the author's choice of Creative Commons user license. See our open access license policy for more information.

Terms & Conditions applicable to all Open Access articles published with Elsevier:

Any reuse of the article must not represent the author as endorsing the adaptation of the article nor should the article be modified in such a way as to damage the author's honour or reputation. If any changes have been made, such changes must be clearly indicated.

The author(s) must be appropriately credited and we ask that you include the end user license and a DOI link to the formal publication on ScienceDirect.

If any part of the material to be used (for example, figures) has appeared in our publication with credit or acknowledgement to another source it is the responsibility of the user to ensure their reuse complies with the terms and conditions determined by the rights holder.

Additional Terms & Conditions applicable to each Creative Commons user license:

CC BY: The CC-BY license allows users to copy, to create extracts, abstracts and new works from the Article, to alter and revise the Article and to make commercial use of the Article (including reuse and/or resale of the Article by commercial entities), provided the user gives appropriate credit (with a link to the formal publication through the relevant DOI), provides a link to the license, indicates if changes were made and the licensor is not represented as endorsing the use made of the work. The full details of the license are

available at http://creativecommons.org/licenses/by/4.0.

CC BY NC SA: The CC BY-NC-SA license allows users to copy, to create extracts, abstracts and new works from the Article, to alter and revise the Article, provided this is not done for commercial purposes, and that the user gives appropriate credit (with a link to the formal publication through the relevant DOI), provides a link to the license, indicates if changes were made and the licensor is not represented as endorsing the use made of the work. Further, any new works must be made available on the same conditions. The full details of the license are available at http://creativecommons.org/licenses/by-nc-sa/4.0.

CC BY NC ND: The CC BY-NC-ND license allows users to copy and distribute the Article, provided this is not done for commercial purposes and further does not permit distribution of the Article if it is changed or edited in any way, and provided the user gives appropriate credit (with a link to the formal publication through the relevant DOI), provides a link to the license, and that the licensor is not represented as endorsing the use made of the work. The full details of the license are available at http://creativecommons.org/licenses/by-nc-nd/4.0. Any commercial reuse of Open Access articles published with a CC BY NC SA or CC BY NC ND license requires permission from Elsevier and will be subject to a fee.

Commercial reuse includes:

- Associating advertising with the full text of the Article

- Charging fees for document delivery or access

- Article aggregation

- Systematic distribution via e-mail lists or share buttons

Posting or linking by commercial companies for use by customers of those companies.

20. **Other Conditions**:

Questions? customercare@copyright.com or +1-855-239-3415 (toll free in the US) or +1-978-646-2777.

Gratis licenses (referencing $0 in the Total field) are free. Please retain this printable license for your reference. No payment is required.

AIP PUBLISHING LLC LICENSE
TERMS AND CONDITIONS

Feb 25, 2015

All payments must be made in full to CCC. For payment instructions, please see information listed at the bottom of this form.

License Number	3576080945325
Order Date	Feb 25, 2015
Publisher	AIP Publishing LLC
Publication	Applied Physics Letters
Article Title	Direct x-ray detection with conjugated polymer devices
Author	F. A. Boroumand,M. Zhu,A. B. Dalton, et al.
Online Publication Date	Jul 18, 2007
Volume number	91
Issue number	3
Type of Use	Thesis/Dissertation
Requestor type	Student
Format	Print and electronic
Portion	Figure/Table
Number of figures/tables	3
Title of your thesis / dissertation	Nanomaterial-based X-ray Shielding and Detection
Expected completion date	May 2015
Estimated size (number of pages)	200
Total	0.00 CAD

Terms and Conditions

AIP Publishing LLC -- Terms and Conditions: Permissions Uses

AIP Publishing LLC ("AIPP"") hereby grants to you the non-exclusive right and license to use and/or distribute the Material according to the use specified in your order, on a one-time basis, for the specified term, with a maximum distribution equal to the number that you have ordered. Any links or other content accompanying the Material are not the subject of this license.

1. You agree to include the following copyright and permission notice with the reproduction of the Material:"Reprinted with permission from [FULL CITATION]. Copyright [PUBLICATION YEAR], AIP Publishing LLC." For an article, the copyright and permission notice must be printed on the first page of the article or book chapter. For photographs, covers, or tables, the copyright and permission notice may appear with the Material, in a footnote, or in the reference list.
2. If you have licensed reuse of a figure, photograph, cover, or table, it is your responsibility to ensure that the material is original to AIPP and does not contain the copyright of another entity, and that the copyright notice of the figure, photograph, cover, or table does not indicate that it was reprinted by AIPP, with permission, from another source. Under no circumstances does AIPP, purport or intend to grant permission to reuse material to which it does not hold copyright.
3. You may not alter or modify the Material in any manner. You may translate the Material into another language only if you have licensed translation rights. You may not use the Material for promotional purposes. AIPP reserves all rights not specifically granted herein.
4. The foregoing license shall not take effect unless and until AIPP or its agent, Copyright Clearance Center, receives the Payment in accordance with Copyright Clearance Center Billing and Payment Terms and Conditions, which are incorporated herein by reference.

5. AIPP or the Copyright Clearance Center may, within two business days of granting this license, revoke the license for any reason whatsoever, with a full refund payable to you. Should you violate the terms of this license at any time, AIPP, AIP Publishing LLC, or Copyright Clearance Center may revoke the license with no refund to you. Notice of such revocation will be made using the contact information provided by you. Failure to receive such notice will not nullify the revocation.

6. AIPP makes no representations or warranties with respect to the Material. You agree to indemnify and hold harmless AIPP, AIP Publishing LLC, and their officers, directors, employees or agents from and against any and all claims arising out of your use of the Material other than as specifically authorized herein.

7. The permission granted herein is personal to you and is not transferable or assignable without the prior written permission of AIPP. This license may not be amended except in a writing signed by the party to be charged.

8. If purchase orders, acknowledgments or check endorsements are issued on any forms containing terms and conditions which are inconsistent with these provisions, such inconsistent terms and conditions shall be of no force and effect. This document, including the CCC Billing and Payment Terms and Conditions, shall be the entire agreement between the parties relating to the subject matter hereof.

This Agreement shall be governed by and construed in accordance with the laws of the State of New York. Both parties hereby submit to the jurisdiction of the courts of New York County for purposes of resolving any disputes that may arise hereunder.

Questions? customercare@copyright.com or +1-855-239-3415 (toll free in the US) or +1-978-646-2777.

Gratis licenses (referencing $0 in the Total field) are free. Please retain this printable license for your reference. No payment is required.

AIP PUBLISHING LLC LICENSE
TERMS AND CONDITIONS

Feb 25, 2015

All payments must be made in full to CCC. For payment instructions, please see information listed at the bottom of this form.

License Number	3576091340573
Order Date	Feb 25, 2015
Publisher	AIP Publishing LLC
Publication	Applied Physics Letters
Article Title	Low dose ionizing radiation detection using conjugated polymers
Author	E. A. B. Silva,J. F. Borin,P. Nicolucci, et al.
Online Publication Date	Mar 21, 2005
Volume number	86
Issue number	13
Type of Use	Thesis/Dissertation
Requestor type	Student
Format	Print and electronic
Portion	Figure/Table
Number of figures/tables	1
Title of your thesis / dissertation	Nanomaterial-based X-ray Shielding and Detection
Expected completion date	May 2015
Estimated size (number of pages)	200
Total	0.00 CAD

Terms and Conditions

AIP Publishing LLC -- Terms and Conditions: Permissions Uses

AIP Publishing LLC ("AIPP"") hereby grants to you the non-exclusive right and license to use and/or distribute the Material according to the use specified in your order, on a one-time basis, for the specified term, with a maximum distribution equal to the number that you have ordered. Any links or other content accompanying the Material are not the subject of this license.

1. You agree to include the following copyright and permission notice with the reproduction of the Material:"Reprinted with permission from [FULL CITATION]. Copyright [PUBLICATION YEAR], AIP Publishing LLC." For an article, the copyright and permission notice must be printed on the first page of the article or book chapter. For photographs, covers, or tables, the copyright and permission notice may appear with the Material, in a footnote, or in the reference list.
2. If you have licensed reuse of a figure, photograph, cover, or table, it is your responsibility to ensure that the material is original to AIPP and does not contain the copyright of another entity, and that the copyright notice of the figure, photograph, cover, or table does not indicate that it was reprinted by AIPP, with permission, from another source. Under no circumstances does AIPP, purport or intend to grant permission to reuse material to which it does not hold copyright.
3. You may not alter or modify the Material in any manner. You may translate the Material into another language only if you have licensed translation rights. You may not use the Material for promotional purposes. AIPP reserves all rights not specifically granted herein.
4. The foregoing license shall not take effect unless and until AIPP or its agent, Copyright Clearance Center, receives the Payment in accordance with Copyright Clearance Center Billing and Payment Terms and Conditions, which are incorporated herein by reference.

5. AIPP or the Copyright Clearance Center may, within two business days of granting this license, revoke the license for any reason whatsoever, with a full refund payable to you. Should you violate the terms of this license at any time, AIPP, AIP Publishing LLC, or Copyright Clearance Center may revoke the license with no refund to you. Notice of such revocation will be made using the contact information provided by you. Failure to receive such notice will not nullify the revocation.

6. AIPP makes no representations or warranties with respect to the Material. You agree to indemnify and hold harmless AIPP, AIP Publishing LLC, and their officers, directors, employees or agents from and against any and all claims arising out of your use of the Material other than as specifically authorized herein.

7. The permission granted herein is personal to you and is not transferable or assignable without the prior written permission of AIPP. This license may not be amended except in a writing signed by the party to be charged.

8. If purchase orders, acknowledgments or check endorsements are issued on any forms containing terms and conditions which are inconsistent with these provisions, such inconsistent terms and conditions shall be of no force and effect. This document, including the CCC Billing and Payment Terms and Conditions, shall be the entire agreement between the parties relating to the subject matter hereof.

This Agreement shall be governed by and construed in accordance with the laws of the State of New York. Both parties hereby submit to the jurisdiction of the courts of New York County for purposes of resolving any disputes that may arise hereunder.

Questions? customercare@copyright.com or +1-855-239-3415 (toll free in the US) or +1-978-646-2777.

Gratis licenses (referencing $0 in the Total field) are free. Please retain this printable license for your reference. No payment is required.

Copyright Clearance Center

RightsLink®

Home | Account Info | Help | Live Chat

IEEE
Requesting permission to reuse content from an IEEE publication

Title: MEH-PPV Thin Films for Radiation Sensor Applications

Author: Bazani, D.L.M.; Lima, J.P.H.; de Andrade, A.M.

Publication: IEEE Sensors Journal

Publisher: IEEE

Date: July 2009

Copyright © 2009, IEEE

Logged in as:
Shruti Nambiar

Account #:
3000583583

LOGOUT

Thesis / Dissertation Reuse

The IEEE does not require individuals working on a thesis to obtain a formal reuse license, however, you may print out this statement to be used as a permission grant:

Requirements to be followed when using any portion (e.g., figure, graph, table, or textual material) of an IEEE copyrighted paper in a thesis:

1) In the case of textual material (e.g., using short quotes or referring to the work within these papers) users must give full credit to the original source (author, paper, publication) followed by the IEEE copyright line © 2011 IEEE.
2) In the case of illustrations or tabular material, we require that the copyright line © [Year of original publication] IEEE appear prominently with each reprinted figure and/or table.
3) If a substantial portion of the original paper is to be used, and if you are not the senior author, also obtain the senior author's approval.

Requirements to be followed when using an entire IEEE copyrighted paper in a thesis:

1) The following IEEE copyright/ credit notice should be placed prominently in the references: © [year of original publication] IEEE. Reprinted, with permission, from [author names, paper title, IEEE publication title, and month/year of publication]
2) Only the accepted version of an IEEE copyrighted paper can be used when posting the paper or your thesis on-line.
3) In placing the thesis on the author's university website, please display the following message in a prominent place on the website: In reference to IEEE copyrighted material which is used with permission in this thesis, the IEEE does not endorse any of [university/educational entity's name goes here]'s products or services. Internal or personal use of this material is permitted. If interested in reprinting/republishing IEEE copyrighted material for advertising or promotional purposes or for creating new collective works for resale or redistribution, please go to http://www.ieee.org/publications_standards/publications/rights/rights_link.html to learn how to obtain a License from RightsLink.

If applicable, University Microfilms and/or ProQuest Library, or the Archives of Canada may supply single copies of the dissertation.

BACK | CLOSE WINDOW

AIP PUBLISHING LLC LICENSE
TERMS AND CONDITIONS

Feb 25, 2015

All payments must be made in full to CCC. For payment instructions, please see information listed at the bottom of this form.

License Number	3576101271009
Order Date	Feb 25, 2015
Publisher	AIP Publishing LLC
Publication	Applied Physics Letters
Article Title	Determining ionizing radiation using sensors based on organic semiconducting material
Author	Harshil N. Raval,Shree Prakash Tiwari,Ramesh R. Navan, et al.
Online Publication Date	Mar 26, 2009
Volume number	94
Issue number	12
Type of Use	Thesis/Dissertation
Requestor type	Student
Format	Print and electronic
Portion	Figure/Table
Number of figures/tables	1
Title of your thesis / dissertation	Nanomaterial-based X-ray Shielding and Detection
Expected completion date	May 2015
Estimated size (number of pages)	200
Total	0.00 CAD

Terms and Conditions

AIP Publishing LLC -- Terms and Conditions: Permissions Uses

AIP Publishing LLC ("AIPP"") hereby grants to you the non-exclusive right and license to use and/or distribute the Material according to the use specified in your order, on a one-time basis, for the specified term, with a maximum distribution equal to the number that you have ordered. Any links or other content accompanying the Material are not the subject of this license.

1. You agree to include the following copyright and permission notice with the reproduction of the Material:"Reprinted with permission from [FULL CITATION]. Copyright [PUBLICATION YEAR], AIP Publishing LLC." For an article, the copyright and permission notice must be printed on the first page of the article or book chapter. For photographs, covers, or tables, the copyright and permission notice may appear with the Material, in a footnote, or in the reference list.
2. If you have licensed reuse of a figure, photograph, cover, or table, it is your responsibility to ensure that the material is original to AIPP and does not contain the copyright of another entity, and that the copyright notice of the figure, photograph, cover, or table does not indicate that it was reprinted by AIPP, with permission, from another source. Under no circumstances does AIPP, purport or intend to grant permission to reuse material to which it does not hold copyright.
3. You may not alter or modify the Material in any manner. You may translate the Material into another language only if you have licensed translation rights. You may not use the Material for promotional purposes. AIPP reserves all rights not specifically granted herein.

Print This Page

RightsLink®

Copyright Clearance Center

Home | Account Info | Help | Live Chat

IEEE
Requesting permission to reuse content from an IEEE publication

Title: Low-Operating-Voltage Operation and Improvement in Sensitivity With Passivated OFET Sensors for Determining Total Dose Radiation

Author: Raval, H.N.; Ramgopal Rao, V.

Publication: IEEE Electron Device Letters

Publisher: IEEE

Date: Dec. 2010

Copyright © 2010, IEEE

Logged in as:
Shruti Nambiar
Account #:
3000583583

LOGOUT

Thesis / Dissertation Reuse

The IEEE does not require individuals working on a thesis to obtain a formal reuse license, however, you may print out this statement to be used as a permission grant:

Requirements to be followed when using any portion (e.g., figure, graph, table, or textual material) of an IEEE copyrighted paper in a thesis:

1) In the case of textual material (e.g., using short quotes or referring to the work within these papers) users must give full credit to the original source (author, paper, publication) followed by the IEEE copyright line © 2011 IEEE.
2) In the case of illustrations or tabular material, we require that the copyright line © [Year of original publication] IEEE appear prominently with each reprinted figure and/or table.
3) If a substantial portion of the original paper is to be used, and if you are not the senior author, also obtain the senior author's approval.

Requirements to be followed when using an entire IEEE copyrighted paper in a thesis:

1) The following IEEE copyright/ credit notice should be placed prominently in the references: © [year of original publication] IEEE. Reprinted, with permission, from [author names, paper title, IEEE publication title, and month/year of publication]
2) Only the accepted version of an IEEE copyrighted paper can be used when posting the paper or your thesis on-line.
3) In placing the thesis on the author's university website, please display the following message in a prominent place on the website: In reference to IEEE copyrighted material which is used with permission in this thesis, the IEEE does not endorse any of [university/educational entity's name goes here]'s products or services. Internal or personal use of this material is permitted. If interested in reprinting/republishing IEEE copyrighted material for advertising or promotional purposes or for creating new collective works for resale or redistribution, please go to http://www.ieee.org/publications_standards/publications/rights/rights_link.html to learn how to obtain a License from RightsLink.

If applicable, University Microfilms and/or ProQuest Library, or the Archives of Canada may supply single copies of the dissertation.

BACK | CLOSE WINDOW